



Università degli Studi di Cagliari

**Ph.D. Degree in Chemical Sciences and Technologies**

Cycle XXXIII

# **Bio-surfactants-based lipid architectures as nanomedicine platforms**

Scientific Disciplinary Sector:  
**CHIM/02 – Physical Chemistry**

Ph.D. Student: Marco Fornasier  
Ph.D. Coordinator: Prof. Stefano Enzo  
Supervisor: Prof. Sergio Murgia

Final exam. Academic Year 2019 – 2020

Thesis defence: February 2021 Session



Marco Fornasier gratefully acknowledges Sardinian Regional Government for the financial support of his Ph.D. scholarship (P.O.R. Sardegna F.S.E. - Operational Programme of the Autonomous Region of Sardinia, European Social Fund 2014-2020 - Axis III Education and training, Thematic goal 10, Investment Priority 10ii, Specific goal 10.5).



## Abstract

The use of nanocarriers for drug delivery and imaging purposes have highly increased in the last decades. Both hard and soft matter-based formulations can provide selective and efficient treatment in several administration routes. Indeed, the biocompatibility and the biodegradability of the formulations represent a key requirement in order to translate the *in vitro* studies into *in vivo* investigations. Therefore, lipids are a safe choice as building blocks to formulate a large variety of liquid crystalline architectures in water.

Vesicles, hexosomes and cubosomes have been adopted as nanomedicine platforms providing excellent biological performances. However, several drawbacks may impact the application of these carriers: the poor stability in the physiological environment and the biodegradability of the stabilizing agent required to sterically stabilize the nanoparticles (NPs) are few examples. Given the importance these materials have acquired nowadays in the nanomedicine field, this thesis is devoted to investigating on the factors that can enhance the physico-chemical and biological performances of these nanoparticles for systemic and topical administration. Most of the formulations presented in this thesis were prepared using monoolein as building block, given its biocompatibility and lower cytotoxicity in comparison with other surfactants. However, the potential application of cell-derived nanoparticles known as nanoerythrocytes for medical imaging was also explored. Therefore, the thesis evaluated different approaches:

**(i)** evaluation of the effect of various stabilizers (modified poloxamers, hemicellulose and polyphosphoesters) on monoolein-based cubosomes features, in order to formulate nanoparticles suitable for systemic administration. This investigation was focused on the physico-chemical (bulk and surface) characterization of the empty carriers and of those loaded with antioxidants or fluorophores suitable for *in vitro* imaging. Bioassays (viability and uptake experiments) were conducted in order to evaluate the biological performance of the differently stabilized cubosomes.

**(ii)** the effect of permeation enhancers and edge activators on monoolein-based vesicles and hexosomes for topical administration. *In vitro* permeation tests were performed to show the efficacy of these carriers into overcoming the stratum corneum, the first layer of the skin, to deliver antioxidants.

**(iii)** the potential role of nanoparticles derived from red blood cells, nanoerythrocytes, as personal medicine for application in optical imaging. Cross-linking and Click Chemistry were employed to decorate the surface of the nanoparticles and their emission properties in a physiological buffer were evaluate.

# List of Papers

This thesis is based on the following papers:

## Paper I

*“Multifunctional cubic liquid crystalline nanoparticles for chemo- and photodynamic synergistic cancer therapy”*

By: S. Jenni, G. Picci, **M. Fornasier**, M. Mamusa, J. Schmidt, Y. Talmon, A. Sour, V. Heitz, S. Murgia, C. Caltagirone;

Paper published in: Photochemical & Photobiological Sciences, 2020, 19, 674-680.

**DOI: 10.1039/c9pp00449a**

## Paper II

*“Bicontinuous cubic liquid crystalline phase nanoparticles stabilized by softwood hemicellulose”*

By: P. Naidjonoka\*, **M. Fornasier\***, D. Pålsson, G. Rudolph, B. Al-Rudainy, S. Murgia, T. Nylander;

\* These authors equally contributed to the study.

Manuscript submitted to Colloids and Surfaces B, 2020.

## Paper III

*“Cubosomes stabilized by a polyphosphoester-analog of Pluronic F127 with reduced cytotoxicity”*

By: **M. Fornasier**, S. Biffi, B. Bortot, P. Macor, A. Manhart, F. R. Wurm, S. Murgia;

Paper published in: Journal of Colloid and Interface Science, 2020, 580, 286-297.

**DOI: 10.1016/j.jcis.2020.07.038**

## Paper IV

*“3-Hydroxycoumarin Loaded Vesicles for Recombinant Human Tyrosinase Inhibition in Topical Applications”*

By: M. Schlich\*, **M. Fornasier\***, M. Nieddu, C. Sinico, S. Murgia, A. Rescigno;

\* These authors equally contributed to the study.

Paper published in: Colloids and Surfaces B, 2018, 171, 675-681.

**DOI: 10.1016/j.colsurfb.2018.08.008**

## **Paper V**

*“Tuning lipid structure by bile salts: hexosomes for topical administration of catechin”*

By: **M. Fornasier**, R. Pireddu, A. Del Giudice, C. Sinico, T. Nylander, K. Schillén, L. Galantini, S. Murgia;

Paper published in: Colloids and Surfaces B, 2021, 199, 111564

**DOI:10.106/j.colsurfb.2021.111564**

## **Paper VI**

*“Surface-modified nanoerythroosomes for potential optical imaging diagnostics”*

By: **M. Fornasier**, A. Porcheddu, A. Casu, S. R. Raghavan, P. Jönsson, K. Schillén, S. Murgia;

Paper published in: Journal of Colloid and Interface Science, 2021, 582, 246-253.

**DOI: 10.1016/j.jcis.2020.08.032**

## **Paper VII**

*“Bioimaging Applications of Non-Lamellar Liquid Crystalline Nanoparticles”*

By: S. Murgia, S. Biffi, **M. Fornasier**, V. Lippolis, G. Picci, C. Caltagirone;

Paper published in: Journal of Nanoscience and Nanotechnology, 2021, 21, 1-18.

**DOI: 10.1166/jnn.2021.19064**

## Papers not included in this PhD Thesis

*“Branched alkyl dimethylamine oxide surfactants: An effective strategy for the design of high concentration/low viscosity surfactant formulations”*

By: A. Fabozzi, I. Russo Krauss, R. Vitiello, **M. Fornasier**, L. Sicignano, S. King, S. Guido, C. Jones, L. Paduano, S. Murgia, G. D’Errico;

Paper published in: Journal of Colloid and Interface Science, 2019, 552, 448-463.

**DOI: 10.1016/j.jcis.2019.05.052**

*“Effect of tail branching on the phase behavior and the rheological properties of amine oxide/ethoxysulfate surfactant mixtures”*

By: L. Savignano, A. Fabozzi, R. Vitiello, **M. Fornasier**, S. Murgia, S. Guido, V. Guida, L. Paduano, G. D’Errico;

Paper published in: Colloids and Surfaces A, 2020, in press.

**DOI: 10.1016/j.colsurfa.2020.126091**

## **Author's contributions**

### **Paper I**

I prepared the cubosomes dispersions and characterized them by means of SAXS, ELS and DLS. I contributed to the writing of the paper (Introduction, Material and Methods and Results and Discussion).

### **Paper II**

P.N. and I conceptualized the study and designed the experiments. I performed the analysis of the experimental data. I wrote the manuscript with the input of all the co-authors.

### **Paper III**

I designed the experiments, prepared the samples and performed the SAXS, DLS, ELS, cryo-TEM and encapsulation measurements. I contributed to the writing of the paper (Introduction, Materials and Methods, Results and Discussion, Conclusions).

### **Paper IV**

I designed the experiments, prepared the liquid and gel vesicles and performed the SAXS, DLS and ELS experiments. I conducted the *in vitro* penetration tests with the help of MS. I contributed to the writing of the paper (Material and Methods, Results and Discussion).

### **Paper V**

I conceptualized and designed the study with the input of the other co-authors. I prepared the samples and run the SAXS, DLS, ELS, cryo-TEM and *in vitro* penetration tests. I wrote the manuscript with the input of the other co-authors.

### **Paper VI**

I conceptualized and designed the study. I prepared the NERs samples and functionalized them with the help of AP. I characterized the systems by means of DLS, ELS and UV-Vis and fluorescence spectroscopy. I wrote the manuscript with the input of the other co-authors.

## **Paper VII**

I searched for the references and designed Figures 1 and 2. I contributed to the writing of the paper (first two sections).



## *Acknowledgements*

First, all of this work would have not been reachable without the support and encouragements from my family, to whom this thesis is dedicated. Thanks to their sacrifice and continuous love, I have realized step more towards one of my dreams. I love you with all my heart.

### **Regarding the people who helped me during this journey in Cagliari.**

I cherish the time spent with and the teachings by my PhD Supervisor, Prof. Sergio Murgia. I would like to thank you for the guidance during these almost four years together and to push me to get the best out of everything. I have learnt a lot from you, and I hope that the end of my PhD would be just the beginning of a long and fruitful collaboration.

I think that I would not have tried pursuing a PhD position without the trust and the pushes from my old Master Supervisor, Prof. Claudia Caltagirone. Thank you for seeing something in a young and naïve student and for your tips and collaboration in the last five years. For the same reason, I would like to thank Dr. Giacomo Picci as well: we have started our PhD journey together and shared the same passion about the research. Maybe, without your pushes and friendship, many things would have been different.

The “PhD life” in Cagliari would have not been the same without the friends from “Lo Studio Bellissimo”: thank you, Mariangela, Noemi, Rosita, Johanna, and Suchitra for the wonderful time spent together. The laughter and the experiences that we shared lighted these years up.

A special thank is mandatory for Mari, Noe and Rosi since they had to handle me in the last months of my PhD, not an easy task.

Indeed, I would like to thank all the PhD colleagues, the professors and the researchers at the Dept. of Chemical and Geological Sciences. A special thank for Antonio, Roberto, Greta, Alessandra and all the crew from the administration.

My “second” supervisors are quite dispersed in different places.

In Lund University: Tommy and Karin, thank you for everything. You welcomed me in the Division of Physical Chemistry, making me feel at home in any moment. Both of you helped me both with my research and in my daily life. You are indeed special, and I would like to thank you again for your precious help and important friendship.

In Rome, Sapienza University: Luciano, I would like to thank you for all the times that you have invited me to perform measurements or just to spend time in your lab speaking about projects and collaborations. I have indeed appreciated the chats and the meetings.

In Wroclaw, University of Science and Technology: I have to be honest, my stay in Wroclaw was quite short, due to the pandemic, but I have felt at home thanks to the warmth of Prof. Urszula Bazylińska. Thank you for your help and your collaboration, even though its fruit are not a part of this thesis.

Last, but not the very least, Prof. José Campos-Téran: you welcomed me in your home in an extreme moment of need. You decided to take care of me as a student of your own and, I would say, as a part of your family. I will never forget the help, the kindness, the professionalism and the friendship that you demonstrated towards me.

I would like to thank all the co-authors involved in the projects that I have worked on; Prof. Chiara Sinico, Prof. Andrea Porcheddu, Dr. Michele Schlich, Dr. Rosa Pireddu, Dr. Alessandra del Giudice, Prof. Friederik Wurm, Prof. Srinivasa Raghavan, Prof. Peter Jönsson, Dr. Anna Casu, Prof. Valerie Heiz. Thank you for your valuable work!

A special thank for the students that I had the pleasure to co-supervise; Michele, Edoardo and especially Francesca, who made my life so much easier given her passion and her cheerful attitude.

**Indeed, my time in the dark and cold Sweden would have not been warm if I had not met several important people.**

My wonderful officemates: Alexis, Jen and Polina, you made my Swedish experience one of the most beautiful and memorable of my life. I cannot say “thank you” enough times to express my gratitude for the laughter, dinners, board games and all the time that we have shared together. Even though 2020 should be a year to be forgotten worldwide, this time away from home showed me how friends can become a part of your family.

Vicky, Marta, João, Ben, Jonas, Pierfrancesco, Jasper, Maria, Tommy, Dora, Axel, Guanqun, Hong, Johan, Madeleine, Marija, Veronica, Erika (and all the other colleagues at the Division of Physical Chemistry in Lund), I thank you for all the moments shared during the “fikas”, the parties and the collaborations.

I would like to thank all the people working at the Division of Physical Chemistry in Lund University that contributed to make my life in Sweden easy and smooth: Helena, Maria S., Maria L, Chris, Peter J., Ulf, Emma, Caroline, thank you all.

A special thank is mandatory for some of the above-mentioned people. I would like to thank deeply Marta and João for the help when the pandemic started, by hosting me without making me feel uneasy or uncomfortable. I loved our time together as “flat-mates” and attempts in trying to mix the Portuguese and the Italian cousins.

Vicky, thank you so much for teaching me how to handle cells, for your precious help and collaboration. All the game nights spent with you and Alexis were undeletable moments, such as my aiming skills.

Polina deserves another special thank as well: being on the finishing line of the PhD together, we supported each other, cheering us up when needed. Thank you for being a special friend as you are!

**Old and new friends had always my back and shared my joy during these years.**

Michela and Simone, you are my two oldest (stress on the old) and dearest friends. We shared all kinds of moments together: the work related to this thesis was possible thank to your immeasurable support.

Angelica, Silvia, Francesco, Daniele, Anna, Noemi, Andrea, Michela, thank you all for your patience, your warmth and your true friendship.

Jessica and Tiziana, my life would be indeed sad without all the funny and crazy moments with you. The Layù is strong on us all.

My friends and colleagues from the Summer School in Catania – Emilia, Valentina, Giorgio and Vincenzo – were absolutely the best. Looking forward to sharing another experience with all of you! A special thank for Emilia is mandatory: our trips from Giulianello to Sapienza (the topics!) and all the time together will be unforgettable!

To close this very long acknowledgements section, I thank Mariangela, my “sorella”. We shared everything in the last three years, ranging from joyful moments to tears and sadness. My life would not be the same without you and I still thank the moment which we started to discuss about an ugly presentation.

# Table of contents

<b>Chapter 1 – Introduction: Soft Matter and Nanomedicine</b>	page 1
1.1. Surfactants and self-assembly	page 3
1.2. Liquid crystalline phases	page 5
1.2.1. Bulk phases	page 5
1.2.1.1. Lamellar phases	page 6
1.2.1.2. Hexagonal phases	page 7
1.2.1.3. Bicontinuous cubic phases	page 8
1.2.1.4. Sponge phase	page 9
1.2.1.5. Mesh phases	page 10
1.3. Dispersions of liquid crystalline bulk phases	page 10
1.3.1. Vesicles	page 11
1.3.2. Hexosomes and Cubosomes	page 12
1.3.3. Stability of LCNPs	page 12
1.4. Monoolein, a versatile building block	page 13
1.5. GMO-based LLCNPs as nanomedicine platforms	page 15
1.5.1. Drug Delivery: an overview	page 15
1.5.2. Bioimaging: an overview	page 17
1.5.3. Theranostics and targeting	page 18
1.6. Administration routes	page 20
1.6.1. Oral administration	page 21
1.6.2. Intravenous administration	page 22
1.6.3. Dermal/transdermal release	page 23
1.7. Vesicles, hexosomes and cubosomes: a comparative highlight	page 25
1.8. Objectives of the PhD thesis	page 28
1.9. References	page 30
<b>Chapter 2 – Experimental characterization of LLCNPs</b>	page 39
2.1. Bulk Techniques	page 42
2.1.1. Scattering Techniques	page 42
2.1.1.1. Light Scattering	page 43
2.1.1.2. Electrophoretic Light Scattering	page 45
2.1.1.3. Small angle X-ray scattering	page 48
2.1.1.4. Small angle neutron scattering	page 51
2.1.2. Microscopy Techniques	page 51
2.1.2.1. Fluorescence microscopy	page 51
2.1.2.2. Electron Microscopy: cryo-TEM	page 52
Surface Techniques	page 53
2.2.1. QCM-D	page 53
2.2.2. Ellipsometry	page 54

2.2.2.1. Null Ellipsometry	page 55
2.2.2.2. Spectroscopic Ellipsometry	page 56
2.3. Bioassays and biological characterization	page 57
2.3.1. <i>In vitro</i> studies	page 58
2.3.2. <i>In vivo</i> studies	page 59
2.4. Techniques employed in the papers	page 60
2.5. References	page 61

## **Chapter 3 – The effect of stabilizers on cubosomes for systemic**

<b>administrations</b>	page 65
3.1. Cubosomes functionalized with a photosensitizer for application PDT	page 68
3.2. Hemicellulose as stabilizer for bicontinuous cubic phase dispersions	page 70
3.3. Stabilization of cubosomes by a polyphosphoester analog of Pluronic F127	page 73
3.4. Surface characterization of PPE-stabilized cubosomes	page 78
3.5. Conclusions and future perspectives	page 80
3.6. References	page 82

## **Chapter 4 – Topical administration of LLCNPs**

4.1. Effect of LCh on the penetration properties	page 91
4.2. BSs as edge activators in LLCNPs	page 93
4.3. Conclusions and Future Perspectives	page 96
4.4. References	page 98

## **Chapter 5 – Cell-inspired nanovectors for imaging applications**

5.1. NERs stability and functionalization routes	page 104
5.2. Conclusions and future perspectives	page 107
5.3. References	page 108

## **Concluding remarks**

page 111

## **Annex**

Disclosure

Paper I

Paper II

Paper III

Paper IV  
Paper V  
Paper VI  
Paper VII





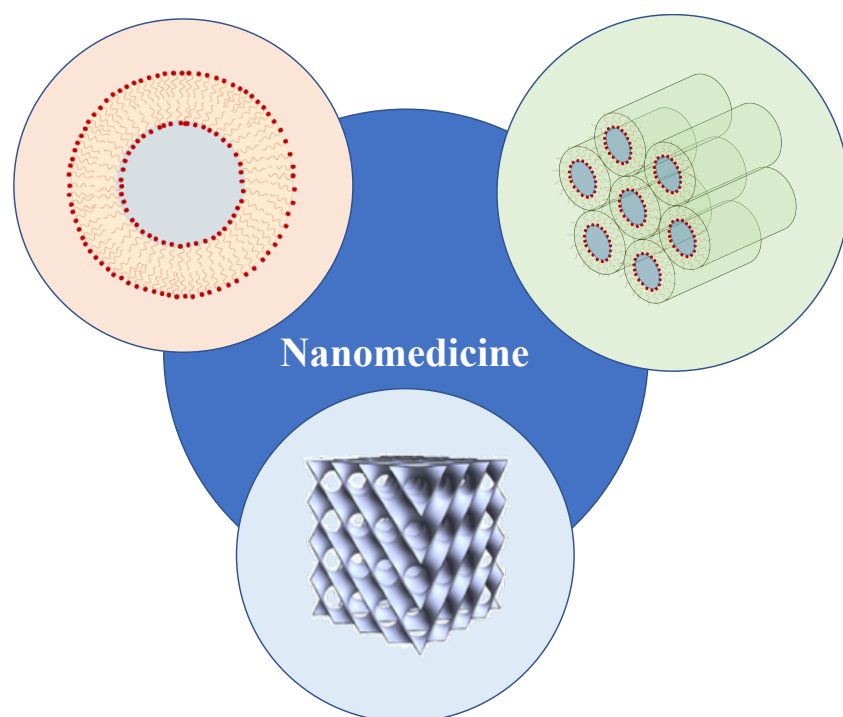


*To my family, who always encouraged me  
to follow and fulfill my dreams*



*Bio-surfactants-based lipid  
architectures as nanomedicine  
platforms*

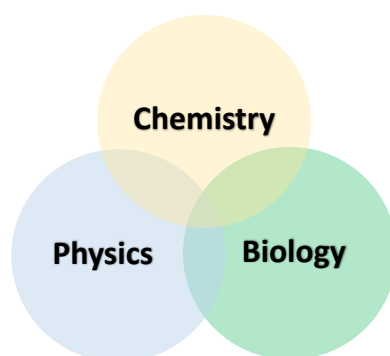
*Marco Fornasier*





# 1

## Introduction: Soft Matter and Nanomedicine



### Chapter 1 – Table of contents

- 1.1. Surfactants and self-assembly
  - 1.2. Liquid crystalline phases
    - 1.2.1. Bulk phases
      - 1.2.1.1. Lamellar phases
      - 1.2.1.2. Hexagonal phases
      - 1.2.1.3. Bicontinuous cubic phases
      - 1.2.1.4. Sponge phase
      - 1.2.1.5. Mesh phases
  - 1.3. Dispersions of liquid crystalline bulk phases
    - 1.3.1. Vesicles
    - 1.3.2. Hexosomes and Cubosomes
    - 1.3.3. Stability of LCNPs
  - 1.4. Monoolein, a versatile building block
  - 1.5. GMO-based LLCNPs as nanomedicine platforms
    - 1.5.1. Drug Delivery: an overview
    - 1.5.2. Bioimaging: an overview
    - 1.5.3. Theranostics and targeting
  - 1.6. Administration routes
    - 1.6.1. Oral administration
    - 1.6.2. Intravenous administration
    - 1.6.3. Dermal/transdermal release
  - 1.7. Vesicles, hexosomes and cubosomes: a comparative highlight
  - 1.8. Objectives of the PhD thesis
  - 1.9. References
- 

Surfactants are among the most versatile products of the chemical industry. They are contained in a wide variety of everyday products, ranging from motor oils used in automobiles to pharmaceuticals, cosmetics and detergents. Indeed, surfactants have changed the chemical and pharmaceutical industry, having remarkable consequences on our daily life.

The phenomenon of detergency related to surfactant molecules was well known for centuries, but the mechanism underlying the removal of dirt was speculated in the last century, given the knowledge of surfactant self-assembly. J.W. McBain suggested the idea of colloidal ions in sodium palmitate solutions in 1913, the first proof of a surfactant aggregate. Starting from this speculation, the design of supramolecular aggregates through self-assembly processes increased highly and opened new routes of application.

Liquid crystalline nanoparticles, derived from self-assembly of surfactants such as lipids, have been mostly used as drug carriers, given the possibility of loading them with hydrophilic and hydrophobic bio-actives.

In this chapter, the phenomenon of self-assembly and the history of lipid liquid crystalline nanoparticles (cubosomes, hexosomes and vesicles) will be described, highlighting their application in the drug delivery and imaging field.

## 1.1. Surfactants and self-assembly

Surfactants are interesting molecules that have the peculiar feature of self-organizing in solution to reduce non-favorable interactions. The word surfactant derives from the contraction of the surface-active agent, indicating the modification of surface or interfacial free energy when a low concentration of surfactant is adsorbed. Fig. 1.1 shows the typical structure of a surfactant molecule.

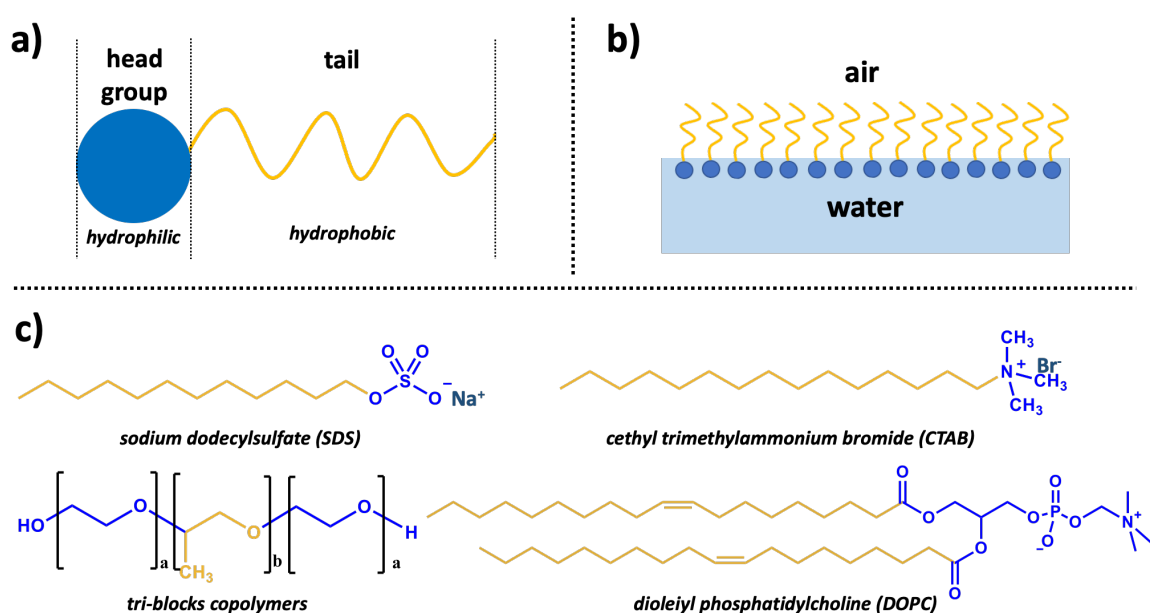


**Figure 1.1.** a) General structure of a surfactant molecule. b) Surfactant molecules arranged at the water-air interface, decreasing the surface tension of the solution itself. c) Classification of surfactant depending on the nature of the polar head: anionic (SDS), cationic (CTAB), non-ionic (block copolymers) and zwitterionic (DOPC).

It consists in a long hydrophobic hydrocarbon (or halogenated) tail, bound to a hydrophilic head group. This peculiar molecular organization is known as amphiphilic structure, and its hydrophilic-lipophilic balance (HLB) can be used as a practice way to quantify this character. The HLB value range between 1 (highly hydrophobic) to 40 (highly hydrophilic). However, not all surfactants may display this structure: bile salts and cholesterol possess a facial conformation where various hydrophilic groups are bound on the hydrophobic body.[1] Depending on the head groups nature, the surfactant may be divided in anionic, cationic, zwitterionic and non-ionic (Figure 1.1c).



Despite this difference, all surfactants undergo self-assembly in solution. The driving force of this phenomenon is mostly represented by the hydrophobic effect, which acts to minimize the interface between the hydrocarbon tails and the surrounding polar solvent. The aggregation occurs at a specific concentration, the critical micellar concentration (CMC), giving aggregates called micelles. Upon reaching CMC, a clear change in the physical properties (i.e. adsorption, surface tension, conductivity, turbidity) takes place, and any further increase of surfactant concentration would just increase the number of micelles in solution. Indeed, the micellization can occur in an apolar solvent as well, giving micelles where the polar heads are buried inside the aggregates to avoid any contact with the apolar bulk.

Micelles are the simplest self-assembled structure that soft matter can build. However, the complexity of the structures can escalate at higher concentrations and more topologically or morphologically complex aggregates may become favored. The interplay and the balance between weak interactions and geometric factors drive the propensity to form different phases and structures in solution.[2]

In the 70s, a parameter to predict the possible geometry of the aggregates was theorized by Ninham and Israelachvili.[3] This first conceptual parameter, the critical packing parameter ( $P$ ), correlates geometric factor of the surfactant molecules, such as the volume and the length of tail ( $V_{tail}$  and  $l_{tail}$ , respectively) and the cross-section area of the head group ( $a_{head}$ ), as reported in eq. 1.1.

$$P = \frac{V_{tail}}{a_{head} \cdot l_{tail}} \quad \text{Eq. 1.1}$$

Moreover,  $P$  is correlated to the curvature of the interface ( $H$ ): for  $P < 1$ ,  $H$  is positive; for  $P > 1$ ,  $H$  is then negative. Finally, when  $P = 1$ ,  $H$  is equal to zero. In general, the plethora of self-assembled nanostructures observed by colloidal scientists can be rationalized as a function of these simple geometrical considerations.

## 1.2. Liquid Crystalline Phases

### 1.2.1. Bulk phases

Surfactants may self-assemble originating various architectures which are dependent on the surfactant's shape.[2] These mesophases are characterized by long-range orientation typical of

solid crystals and by a mobility related to liquids as well. Given these features, they are called liquid crystalline phases (LC) and can be divided in two categories:[4] **thermotropic** LC display a phase behavior temperature-dependent, while **lyotropic** LC present a phase transition due to a change in terms of surfactant concentration. In both cases, while the hydrophobic effect still remains the driving force for the self-assembly process, the final architecture of the aggregate will depend on the molecular shape and the mutual interactions between the building blocks.

The polymorphism of lyotropic LC is of great interest, since the architectures can influence deeply the properties of the system. An overview on the most common and important structure is reported in Fig. 1.2. Starting from micelles, discrete cubic, hexagonal, bicontinuous cubic, lamellar and their type II (water-in-oil) LC phases can be obtained depending on the surfactant concentration, temperature, salt concentration or addition of additives.

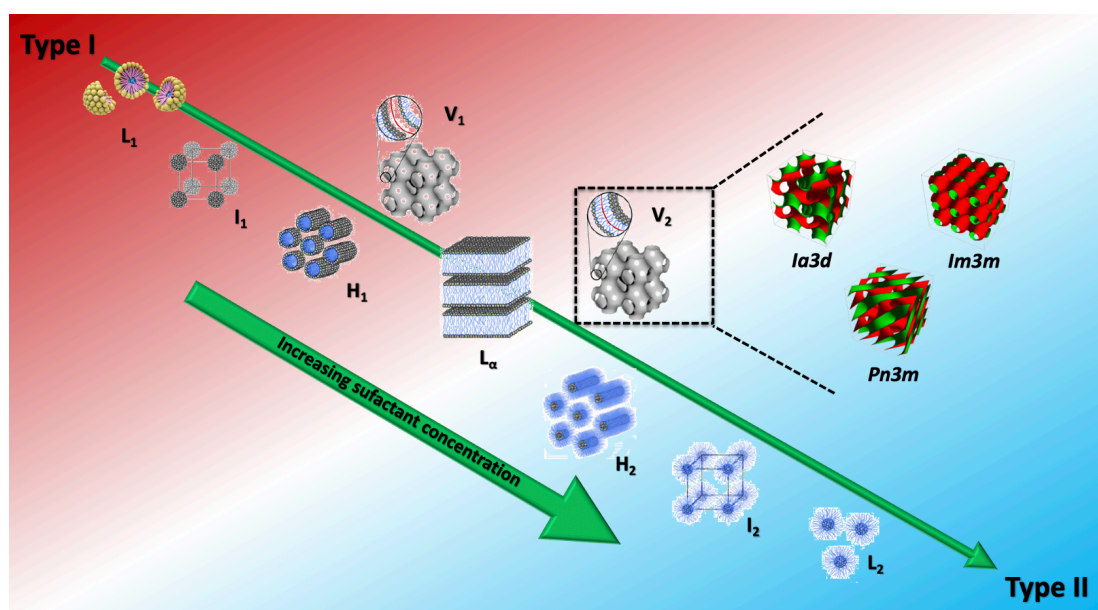


**Figure 1.2.** Architectures for lyotropic LC surfactants in water. The type I and type II correspond to oil-in-water and water-in-oil emulsions, respectively. Modified with permission from **Paper VII**.

### 1.2.1.1. Lamellar phase

The lamellar phase (L) consists of planar bilayers stacked in a 1-dimensional lattice separated by water layers, as shown in Fig. 1.3.

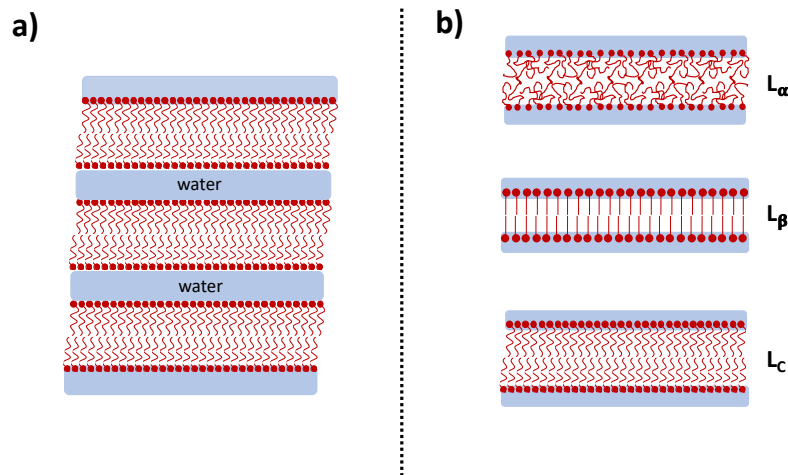


**Figure 1.3.** a) Schematic representation of a lamellar phase. b) Different arrangements of the surfactant's tail give birth to various lamellar phases:  $L_{\alpha}$ ,  $L_{\beta}$  and  $L_C$ .

These phases are optically anisotropic and birefringent. When observed in an optical microscope, they can be recognized since lamellar phases show a mosaic-like pattern.[2] Depending on the mobility of the carbon chain in the lattice, it is possible to describe three type of lamellar phases (Fig. 1.3b):

- ◆  $L_{\alpha}$ . The tails are molten and fluid. The  $L_{\alpha}$  is more fluid compared to the other lamellar phases;
- ◆  $L_{\beta}$ . The tails are arranged in a parallel manner between each other and the corresponding phase looks more like a gel;
- ◆  $L_C$ . It is the most ordered of the three lamellar phases, since the chains of the surfactant molecules are frozen into specific lattice site.

Cell membrane architecture is reminiscent of lamellar structure. Vesicles, lamellar dispersions in water, have been studied and investigated extensively due to this reason.

### 1.2.1.2. Hexagonal phase

The Hexagonal LC phase can be obtained for surfactants with a truncated or inverted truncated cone shape. It is formed by a dense packing of cylindrical micelles, arranged on a 2-dimensional hexagonal lattice. The oil-in-water (direct or Type I) and water-in-oil (inverse or Type II) phases are denoted as  $H_I$  and  $H_{II}$ , respectively. In the latter case, the water molecules flow in the cylindrical channel of the inverse phase and the remaining space is occupied by the hydrophobic tails. Under a polarized light, hexagonal phases exhibit birefringence and their common optical patterns are mosaic- or fan-like.

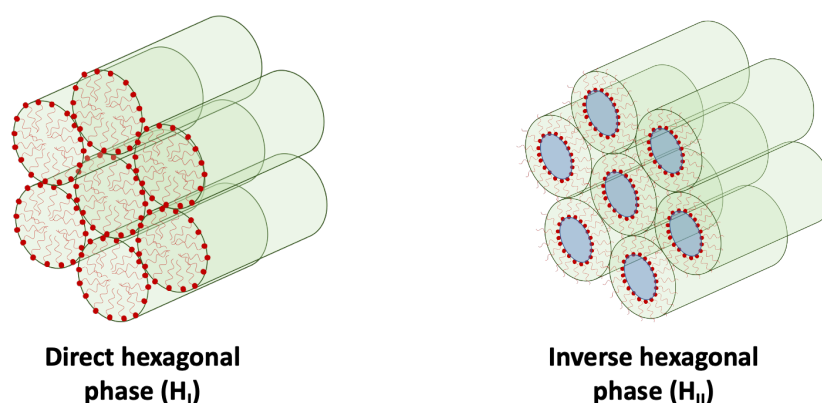


**Figure 1.4.** Direct and inverse hexagonal phase schematic representation.

These mesostructures should be considered as a packing of monolayer surfaces or bilayer architectures consisting of a hexagonal honeycomb.[2,5]

Hexagonal structures occur *in vivo* in the endoplasmic reticulum of the retinal pigment epithelium[6] and of the plasma membrane of bladder epithelium[7].

### 1.2.1.3. Bicontinuous cubic phases

The cubic phases present a 3-dimensional lattice arrangement and can be ascribed to two subclasses, (i) the discrete micellar (I) and (ii) the bicontinuous (V). In the former, micelles are packed on a cubic lattice, face-centered or body-centered, whereas cubic bicontinuous phases have a curved triply period non-intersecting bilayer folded on an infinite periodic minimal surface (IPMS). This conformation lead to the formation of two interpenetrated and disjointed continuous water networks. The average curvature of these architectures is equal to zero.

To date, only three cubic bicontinuous phases have been identified so far: the primitive  $Im3m$ , the double diamond  $Pn3m$  and the gyroid  $Ia3d$  (Fig. 1.5)

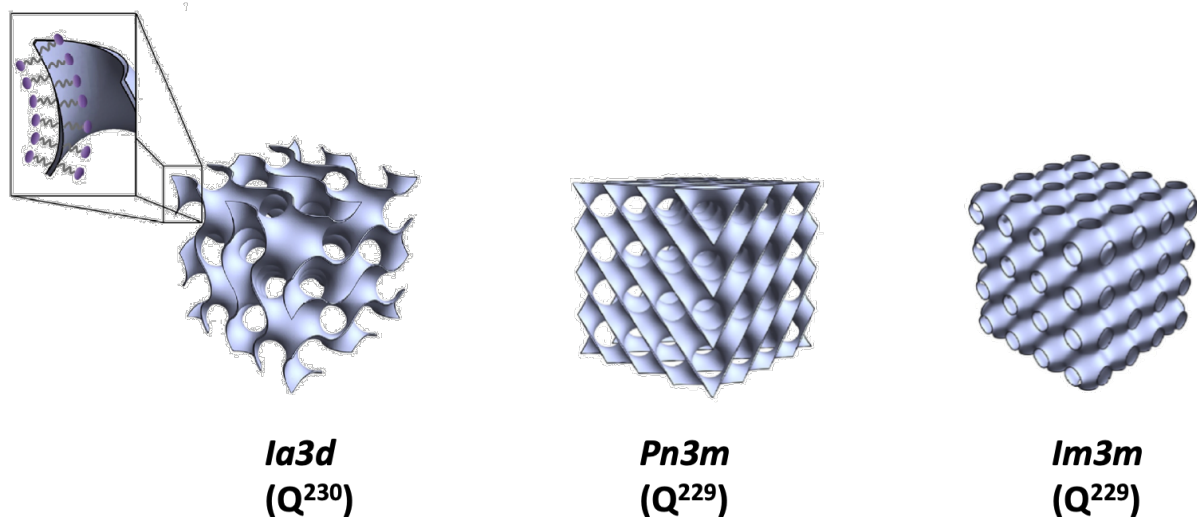


**Figure 1.5.** Representation of the inverse bicontinuous cubic phases *Ia3d*, *Pn3m* and *Im3m*. Reproduced with permission from reference [8].

The lipid bilayer is centered on the IMPS with the hydrophilic heads pointing outwards, while the water molecules fill the maze system on each side of the surface. The bicontinuous cubic phases are extremely viscous and optically isotropic, thus no evident texture is visible through polarized light microscopy. The lack of shear planes with the bicontinuous structure induces the high viscosity.

Bicontinuous cubic phases can occur *in vivo* in ribosomal inner membranes and they have been observed in cells under stress or affected by pathological conditions.[5,9]

### 1.2.4 Sponge Phase

The less known sponge phase ( $L_3$ ) is constituted by a 3-dimensional bilayer surrounded by two different water channels, as previously mentioned for the bicontinuous cubic structures. The main difference between these two phases is that the sponge phase is less ordered and can be considered a melt bicontinuous phase.

The interface of  $L_3$  is highly flexible and by heating it the long-range order of the network is broken down so that the interface is no longer arranged on a lattice. Sponge phases are characterized by flow birefringence, giving anisotropic optical textures, and they are isotropic under rest conditions.

### 1.2.1.5. Mesh phases

The mesh mesophases are intermediate to lamellar and bicontinuous phases. The main feature of these phases is the smectic stack of punctured bilayers. The arrangement of punctures within each bilayer gives a 3-dimensional lattice, similar to discrete micellar and bicontinuous mesophases.

To date, two polymorphs are known, the rhombohedral (R, space group  $R3m$ ), which contains a hexagonally close-packed array of punctures, and the body-centered tetragonal (T, space group  $I422$ ), characterized by a square array of punctures. Both R and T are optically anisotropic and are characterized by two cell parameters: the in-plane  $\alpha$ , describing the spaces between punctures, and the smectic  $c$  between bilayers.[2] It is very difficult to estimate for a relative location of mesh phases in a phase diagram, due to the extreme variability of their shape parameters.

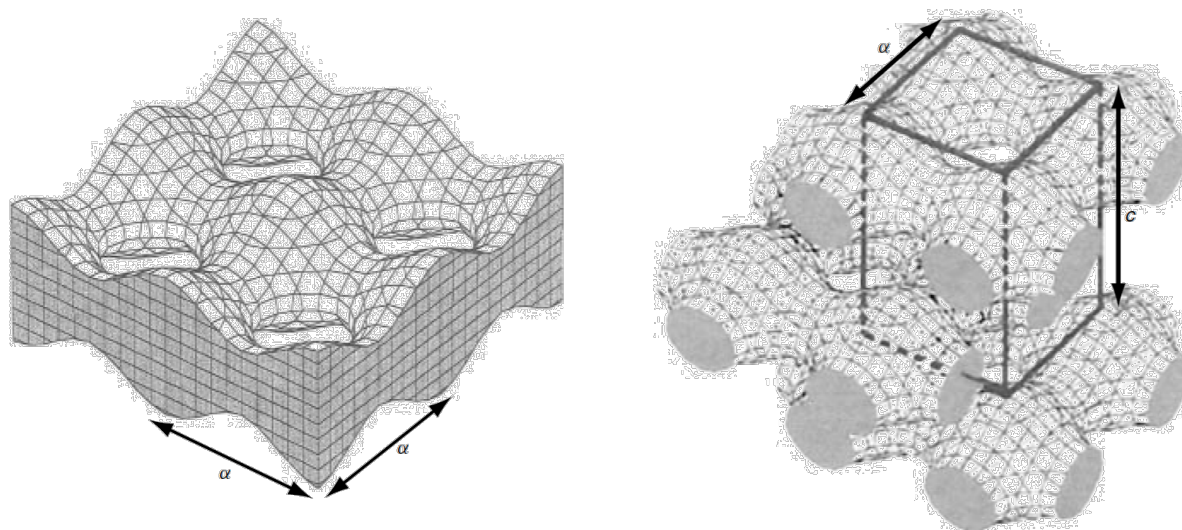


**Figure 1.6.** On the left, view of a single monolayer in a tetragonal (T) mesh mesophase. On the right, bilayers stacked in a staggered arrangement characterized by the two lattice parameters,  $\alpha$  and  $c$ . Reproduced with permission from reference [2].

## 1.3. Dispersions of liquid crystalline bulk phases

One peculiarity of liquid crystalline bulk phases is that they can be fragmented through an energy input in sub-micron particles, hence forming liquid crystalline nanoparticles (LCNPs) in excess of water. These dispersions are diluted, non-viscous aqueous materials with internal nanostructure.[10]

The LCNPs preparation method is based on a high-energy emulsification procedure, such as ultrasonication, high-pressure homogenization or high-speed shearing and requires a stabilizing agent, as it will be described later. These protocols can belong to the top-down or bottom-up classes. The former requires a high-energy apparatus, such as a homogenizer, to break the pre-formed bulk phase in smaller aggregates. In principle, it allows for the encapsulation of hydrophilic molecules (e.g. oligonucleotides, peptides and proteins). On the other hand, the bottom-up approach contemplates the dilution of the surfactant in an aqueous solution containing the stabilizer, followed by homogenization of the mixture. Spicer and collaborators suggested a novel procedure to produce dispersions of bicontinuous cubic phases based on bottom-up approach. An hydrotrope, an amphiphile incapable of displaying phase behavior by itself, is included in the formulation, thus providing a salting-in effect on the building blocks otherwise insoluble in water.[8,9]

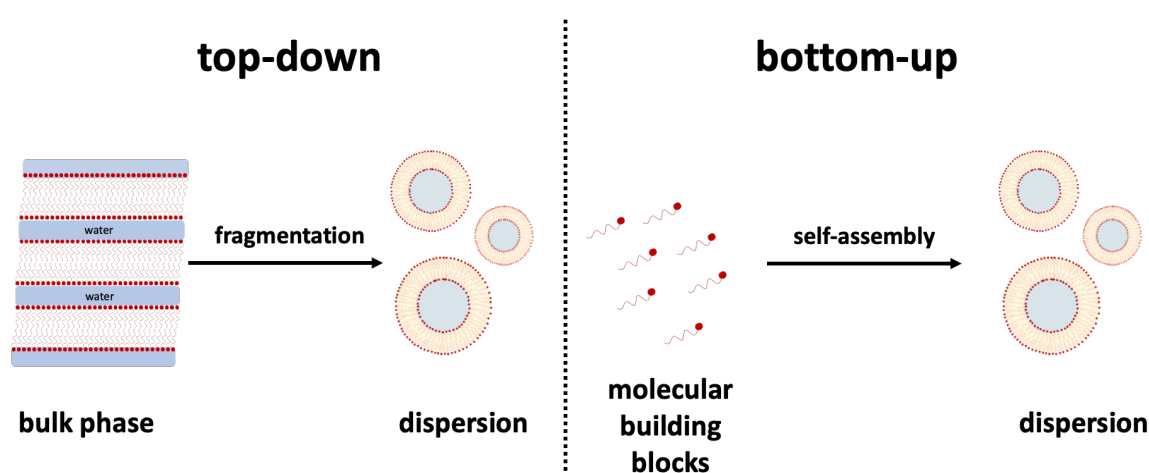


**Figure 1.7.** Top-down and bottom-up preparation methods for dispersions of liquid crystalline phases.

### 1.3.1. Vesicles

The simplest LCNPs are indeed vesicles, dispersion of a lamellar phase. They consist in a spherical bilayer that separates an aqueous core from the bulk water. Depending on the degree of lamellarity (the number of spherically concentric bilayers), their architecture can be defined as unilamellar (one bilayer), multilamellar (two or more) or multivesicular, as shown in Fig. 1.8. The most studied vesicular structures are liposomes, vesicles formed by phospholipids. They were identified and characterized for the first time by Bangham in the 60s through electron microscopy studies.[11] Liposomes are widely used as model reference for cell

membranes investigation, given their simple but representative architecture that resembles the fluid mosaic of living cells.

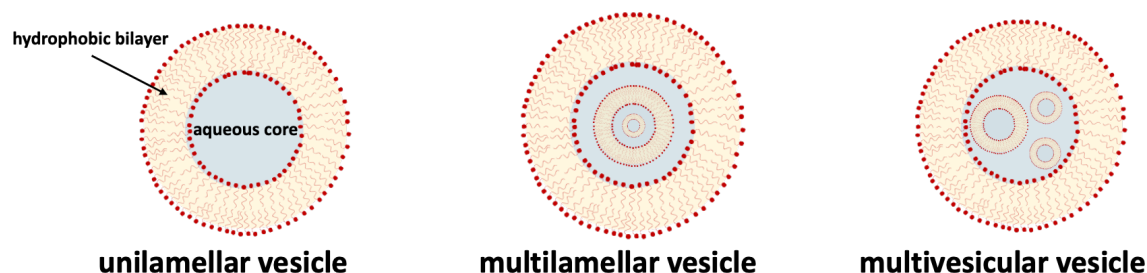


Figure 1.8. Vesicular structures in water.

### 1.3.2. Hexosomes and cubosomes

The aqueous dispersions of the inverse hexagonal and bicontinuous cubic phases, hexosomes and cubosomes respectively, can be obtained similarly to vesicles from bottom-up or top-down approaches. Within this kind of nanoparticles, the surfactant organization and the dynamic properties of the bulk phase is retained.[12] Larsson's group was the first to investigate on the morphology of these aggregates by means of cryo-TEM.[13]

Cubosomes were observed for the first time during triglycerides ingestion by Patton and Carey in 1979: the bicontinuous cubic phase was stabilized by a micellar solution of bile salts.[14]

### 1.3.3. Stability of LCNPs

Vesicles, hexosomes and cubosomes show kinetic stability, since they need an energy input to be formed in excess of water.

Dispersing a lamellar phase in water to obtain vesicles is an easy task: indeed, the ability of the lamellae to bend into a closed structure that avoids the contact between the hydrophobic domain and the bulk water permits to break easily the bulk phase. On the other hand, the dispersions of inverse hexagonal and bicontinuous cubic phases are more difficult given the boundary conditions imposed on the fragmented crystals.[10] Therefore, these aggregates possess a limited colloidal stability in aqueous dispersion.

An addition surfactant is required to facilitate the dispersion of these phases, and it acts as a stabilizer. The stabilizing agent may be inclined to interact strongly with the bilayer so that it could influence the structure of the LCNPs, as demonstrated by Landh in 1994.[15]

Polymers which present poly(ethylene oxide) (PEO) moieties, such as poloxamers, are chosen as stabilizers for cubosomes and hexosomes.[8,10] In this manner, a hydrophilic corona



surrounds the LCNPs, providing steric stabilization and, hence, preventing flocculation. For an exhaustive classification and effect of the stabilizing agents on cubosomes and hexosomes features, see Chapter 3.

## 1.4. Monoolein, a versatile building block

Various surfactants can be adopted to prepare LCNPs, but lipids are appointed as the most common. Among them, monoolein and phytantriol represent the most used lipids to prepare lipid liquid crystalline nanoparticles (LLCNPs). The molecular formulae are reported in Fig. 1.9.

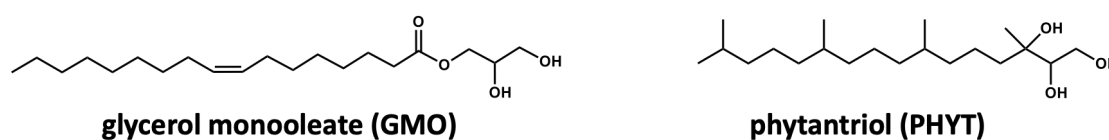


**Figure 1.9.** Molecular structures of 2,3-dihydroxypropyl-(Z)-octadec-9-enoate or glycerol monooleate (GMO) and 3,7,11,15-tetramethylhexadecane-1,2,3-triol or phytantriol (PHYT).

From a molecular point of view, glycerol monooleate or monoolein (GMO) is a monoglyceride of oleic acid. The head group is circumscribed to the glycerol unit, while the oleic acid residue acts as a tail. GMO is a non-toxic, clear amber or pale-yellow waxy paste at room temperature. GMO has been widely used as emulsifying agent and food additive since 1950.

The other building block, Phytantriol (PHYT) is an aliphatic alcohol and a colorless viscous liquid at room temperature with a sweetish odor.

Given its amphiphilic nature, GMO can self-assemble in aqueous solution and the hydrophobic effect leads to a rich polymorphism. The history of GMO/W phase diagrams is quite long, since the first study was constructed by Lutton in 1956,[16] thanks to empirical observations from polarizing optical microscopy and sample consistency. However, the different bicontinuous cubic phase were identified not before the investigations from Larsson[17,18] and Lonlgey and McIntosh[19] through NMR and scattering techniques in 1979 and 1983, respectively.

Hyde and coworkers reported the first (nearly) complete GMO/W diagram in 1984.[13] The phase transitions were carried out in the range 20 – 110 °C and up to 40 % wt as content of water. In the following decades, several contributions were made, especially in expanding the temperature interval and highlighting the phase boundaries.

Qiu and Caffrey extended the temperature range until  $-15\text{ }^{\circ}\text{C}$  and the water content up to 50 % wt and their phase diagram is shown in Fig. 1.10.

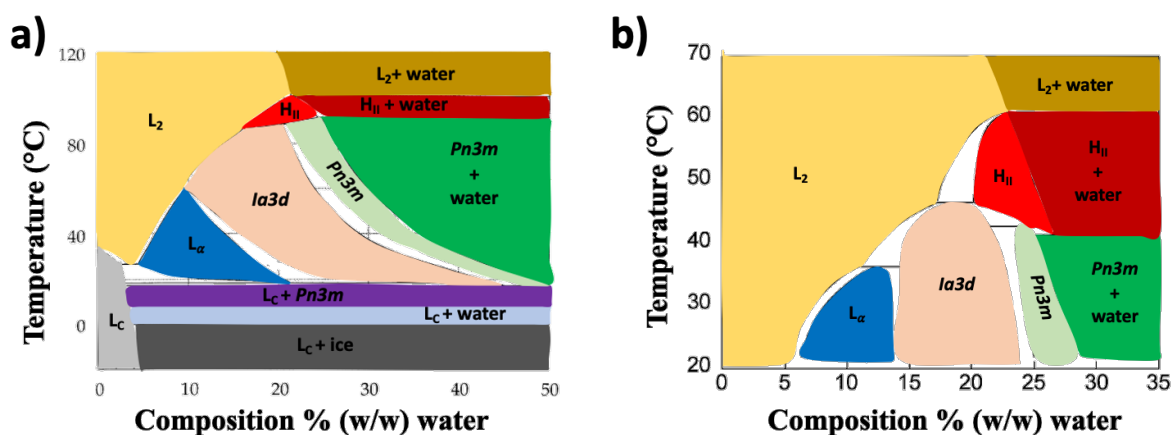


**Figure 1.10.** Phase diagrams for (a) GMO/water obtained by Qiu and Caffrey in 2000 and (b) PHYT/W investigated by Barauskas and collaborators in 2003. Modified with permission from references [20] and [21].

Having a close look, the phase diagram for the system GMO/W shows the presence of a lamellar crystalline region coexisting with various polymorphs, in the lower part of the diagram (low temperatures and low water content). By increasing the temperature but keeping fixed the amount of water, the  $L_c$  phase melts into a fluid isotropic phase, an inverse micellar ( $L_2$ ). An  $L_\alpha$  phase takes place further increasing the water content, while the increase of temperature generates again the  $L_2$ .

Bicontinuous cubic phase are present at higher water contents in the form of  $Ia3d$  and  $Pn3m$ . Increasing the temperature leads to an inverse hexagonal phase and to an inverse micellar phase at the end.

The interest on LLCNPs is based on a peculiar feature of monoglyceride/water systems. Above a certain percentage of solvent, water and a structured phase can coexist separately (liquid crystals + water excess region), indicating the maximum solubilization capacity of that phase for the solvent. Moreover,  $Pn3m$  can solubilize more water than  $H_{II}$  and  $L_2$  phases (40 %, 25 % and 20 % respectively).[22]

Regarding the system PHYT/W, at room temperature,[23] the phase sequence with increasing water content is reversed micellar, lamellar ( $L_\alpha$ ), cubic  $Ia3d$  and cubic  $Pn3m$ . The  $L_2$  phase occupies the high-temperature section of the diagram at all the hydration levels. In addition, an inverse hexagonal phase appears in the temperature range  $44 - 60\text{ }^{\circ}\text{C}$ .

Indeed, both GMO and PHYT can form several LC phases and their corresponding dispersions in water, as can be observed in their phase diagrams. However, since GMO was used as molecular building block in this thesis investigations, LLCNPs' PHYT features will be discussed only in comparison to GMO in the following paragraphs.

## **1.5. GMO-based LLCNPs as nanomedicine platforms**

The physico-chemical properties of GMO find applications in several fields, ranging from pharmaceuticals, food industry, personal care and agriculture. Moreover, its peculiar phase behavior makes GMO a versatile material since it can be included in various formulations.

Indeed, its biocompatibility and biocompatibility attracted great attention in the pharmaceutical field, since it can be employed as emulsifier, solubilizer and, especially, as building block for drug delivery platforms. Nanomedicine is defined as the application of materials in the nanoscale as tools to deliver drugs, antioxidants and imaging probes. The use of nanomaterials is less invasive in comparison with other therapies, and it allows to increase the selectivity and the effectiveness of the therapy. As GMO is an amphiphile and it is able to deliver both hydrophobic and hydrophilic bio-actives, allowing to cover a large plethora of therapies and diagnostic purposes.

### **1.5.1. Drug Delivery: an overview**

Drug design is a flourishing field aiming to develop new pharmaceutically-active compounds, and to improve subsequently the quality of therapy. The administration of the so-called “free drugs” (molecular dispersions of the drug) has often an optimum concentration range: below this value they are ineffective and above it they induce a toxic effect. Nevertheless, the rapid clearance from the blood circulation leads to drug concentration below the efficient therapeutic range in a short time. This drawback brings to a poor pharmacokinetic and an inappropriate biodistribution *in vivo*.<sup>[24]</sup> Furthermore, the lack of specificity entails an indiscriminate volume distribution of the drug with undesired accumulation in healthy tissues.

Some therapeutical agents, such as doxorubicin, have shown good performance *in vitro* as free drugs but, when administrated *in vivo*, they have highlighted cytotoxic effects or low clinical performances. Moreover, the low solubility in water of most therapeutics hinders their applicability.

To date, an efficient way to overcome most of these obstacles is represented by the encapsulation of the drug in colloidal systems that can act as nanocarriers. The biodistribution of the drug will be determined by that of the vector, since the different sizes regulate the biodistribution.

A wide variety of materials have been suggested as drug carriers, using both soft and hard components. Indeed, biocompatibility and biodegradability are mandatory requirements to meet the clinical criteria and to ensure a valid therapeutical effect. Depending on the nanoparticles' matrix, the drug release may occur *via* different diffusion process or by its degradation in the cell environment.[5,8,9] The former is ruled by various parameters, such as the geometry of the carrier, its porosity and the tortuosity of the matrix pores.[25]

Micelles of small surfactant molecules were the first systems to be adopted as pharmaceutical platforms. Given the lower CMCs and their lower dissociation rate, micelles based on polymers substituted them as drug vectors, especially block copolymers (i.e. poly(caprolactone), poly(aspartate), poly(lactate), poly(phosphate), etc.).[5] Polymers are able to form even a bilayer, in a manner similar to phospholipids for liposomes. These so-called polymerosomes can encapsulate both hydrophilic and hydrophobic drugs in the aqueous core and in the lipophilic bilayer, respectively.

Indeed, lipid-based nanocarriers represent the most suitable choice in terms of biocompatibility for nanomedicine applications. Among them, lamellar liquid crystalline dispersions (e.g. liposomes, niosomes, ethosomes and bilosomes) are the prominent ones, since some liposomal formulations have been already successfully marketed and more are still involved in pre-clinical and clinical trials.[26] However, liposomes exhibit several drawbacks that can affect significantly the therapeutic effect. First, given the small hydrophobic portion, the loading of lipophilic drug is quite reduced in comparison with the non-lamellar counterparts (as it will be discussed shortly).[9] The colloidal stability of these vesicular structures is reduced, and the storage conditions may affect the stability of the drug itself.[27] Several strategies can be employed to enhance the biological and physico-chemical performance of the vesicles. One method is based on using biological materials, such as cell membranes, that can be reconstituted in a physiological environment and hence be applied as personal medicines.[28–30] Chapter 5 will focus on this topic.

Given these limitations related to vesicles, the non-lamellar dispersions of LC phases, hexosomes and cubosomes, have been studied as alternative to liposomes. Indeed, their high mechanical rigidity, the structural stability, the large interfacial surface area per unit of volume and the higher hydrophobic volume are their most attractive features.[8,9,25] Nevertheless,

hexosomes and cubosomes require a stabilizing agent, to ensure their steric stabilization as well as to prevent the rapid clearance from the bloodstream by plasma proteins.[8] Flexible non-ionic block co-polymers such as poloxamers, poly(ethylene oxide) (PEO) poly(propylene oxide) (PPO) poly(ethylene oxide) (PEO), can be used for this purpose. The effect of block copolymers on the stabilization of cubosomes and hexosomes will be discussed in Chapter 3. Another kind of lipid-based drug delivery system is represented by solid lipid nanoparticles (SLNPs). The core is composed by solid lipids, usually glycerides, surrounded by an emulsifier shell that stabilized the particle from aggregation. Given the hydrophobic nature of the core, SLNPs can mainly encapsulate hydrophobic drugs.

Recently, another kind of non-lamellar aggregate have gained more attention as drug carrier: the sponge phase can be fragmented in nanoparticles similarly to their inverse hexagonal and bicontinuous cubic cousins. The nanoparticles, sometimes referred to as spongosomes, present larger water channels than cubosomes, given their more disorder structure, and thereby are able to encapsulate bigger macromolecules, such as enzymes.[31,32]

## 1.5.2 Bioimaging: an overview

Molecular imaging exploits specific molecular probes and contrast agents to visualize, characterize and measure the biological process at molecular and cellular levels *in vitro* or *in vivo*. [33,34] As a free drug dispersion presents many drawbacks, a free probe formulate lacks too of the specificity required to image a target tissue. Therefore, the probes can be encapsulated or specifically bound to the surface of carriers, such as LLCNPs.[35,36]

Various imaging techniques can be adopted, depending on the physical phenomenon or the target tissue. A short classification is reported in Table 1.1.

**Table 1.1.** Brief overview on different imaging approaches, their physical principle and the imaging probe adopted.

Technique	Acronym	Physical principle	Imaging probe
Magnetic Resonance Imaging	MRI	magnetic relaxation of nuclei	complexes of paramagnetic nuclei (e.g. Mn <sup>2+</sup> and Gd <sup>3+</sup> )
Positron Emission Tomography	PET	emission of positron	radiotracers (e.g. <sup>99</sup> Tc, <sup>123</sup> I and <sup>111</sup> In)
Computed Tomography	CT	absorption of X-rays	electron dense elements (e.g. I)

<u>U</u> ltrasound Imaging	<b>US</b>	reflection of sound waves	gas-filled microbubbles
<u>O</u> ptical <u>I</u> maging	<b>OI</b>	fluorescence or phosphorescence	fluorophores (e.g. rhodamines, cyanines, squarines, etc.)

Among these techniques, Fluorescence Optical Imaging (**FOI**) represent a non-ionizing and non-invasive approach that has acquired great importance in early diagnostics. These perks make FOI a suitable clinical diagnostic technique, since the patient can be exposed to repeated treatments without any drawbacks. The fluorophores absorb the incoming light and they re-emit it as a lower energy radiation (higher wavelength). The instrumentation needed for this approach is relatively cheap in comparison with other more sophisticated techniques. FOI is sensitive, versatile and easy to use. The main issue is represented by its poor penetration capacity, caused by attenuation of photon propagation in living tissues. Moreover, tissue autofluorescence yields a poor signal-to-noise ratio. Indeed, these are not trivial problems and they can be overcome by using emitters in the near infrared (NIR). The so-called biological window (650 – 950 nm) allows deeper penetration and minimization of the background.[35,37] UV-Vis emitters are suitable for *in vitro* investigations, whereas NIR emitters can be adopted for *in vivo* imaging.

Mainly, bioimaging is based on three strategies mainly:

- ◆ use of strong emitters that are internalized by cells and make them fluorescent;
- ◆ use of ligands or antibodies that can interact with specific domain or site on the cell to make fluorescence occur.
- ◆ use of probes and nanomaterials with sensing capabilities.

The strategies can be combined in order to increase and improve the signal or to highlight simultaneously different cellular phenomena.

### 1.5.3 Theranostics and targeting

Cancer represents the first cause of death worldwide. The term cancer is referred to a wide collection of genetic diseases and it involves an out-of-control proliferation and a minor specialization in comparison with normal cells.[38] Depending on the cell line considered and the quality of the tumor cells (e.g. solid or liquid), different type of cancer may arise. Given this heterogeneity, one treatment is not suitable and both pharmaceutical (to reduce symptoms)

and surgical (to eradicate) might be applied. Indeed, bioimaging and drug delivery can come in aid. Imaging the malign area is useful to ponder the therapeutical and surgical approach.

Since the high demand of multi-functional platforms, bioimaging and drug delivery can be integrated to obtain a theranostic carrier, instead of administrating the drug and the probe separately.[39,40] This new approach permits to evaluate simultaneously in a non-invasive manner the circulating time and the biodistribution *in vivo* of the carriers in real time.

Vesicles, and more recently cubosomes and hexosomes, have been proposed as theranostic platforms.[8] The integration of drug delivery with bioimaging within this LLCNPs can be achieved through various strategies. First, depending on their physico-chemical nature, the drug and the imaging probes can be co-encapsulated in the carriers, even though loading issues can occur.[41] Another possibility is represented by a surface functionalization of the carrier with the imaging probe, while the drug is encapsulated to ensure its biological activity.[42,43] As a side effect, the functionalization of the surface with fluorophores may affect the electron density of the fluorophore, thus shifting its emission. Finally, both the drug and the probe can be bound to the carrier's surface, however this modification could alter the therapeutical property of the drug.

The use of nanocarriers should promote an enhancement in terms of drug or probe concentration in the target tissue. Especially for cancer therapy, the drug should be localized in the tumor environment. In order to develop "smart" carriers and to avoid strong side effects, the nanoparticles can be targeted. The term targeting implies a selective interaction or recognition, based on geometrical, binding or dimensional considerations.[44] Two main targeting strategies can be adopted.[45]

The first one is represented by **passive targeting**. As described aforehand, the size of the carriers is quite large compared to the drug encapsulated and, depending on the LLCNPs considered, the size range is between 50 – 300 nm. The human body is designed to remove from the bloodstream what is considered non-self. Few guidelines related to the size of these materials are known. The lower threshold required to avoid a rapid clearance from kidney glomerula is 5 – 6 nm. The upper size boundary is hard to specify, and it is determined by the Reticulo Endothelial System (**RES**), which is a part of the immune system. It includes phagocytic cells such as monocytes and macrophages, localized in the spleen, lymph nodes and Kupffer cells in the liver. Taking into account these considerations, the passive targeting is based on the so-called Enhanced and Permeability Retention (**EPR**) effect.[46] The altered angiogenesis of a tumor mass leads to non-mature, tortuous and fenestrated blood vessels. Focusing on the latter, these defenestrations in the range 380 – 780 nm (depending on the

type)[38,39] promote accumulation of materials in the tumor tissues, leading to an increased retention time of nutrients in that size range. Therefore, nanoparticles can exploit the EPR effect to increase their localization in the target site, avoiding or reducing side effects. The size of the carrier plays then a crucial role in the therapy. Most of drug delivery platforms are designed on these principles.

Since the altered angiogenesis can vary with tumor type and status, the EPR effect is not feasible in all cases. An alternative path is represented by active targeting, which is based on a selective molecular recognition among a ligand (the targeting agent) on the surface of the nanoparticle and a receptor (the target) on cell membrane to induce receptor-mediated uptake of the carriers. Indeed, in order to enhance the efficacy of the therapy, the targeted receptors should be overexpressed on the target site with respect to other cells. Designing targeting agents is a rich field of research and several parameters should be taken into considerations. The functionalization of the nanoparticle should be thought in a way to preserve the natural conformation of the targeting agent (fundamental for its interaction with the receptor) and to achieve a sufficient coverage of its surface. The moiety used to anchor the targeting agent plays a crucial role: for cubosomes and hexosomes, the targeting agents is commonly bound to the stabilizers PEO end, since the functionalization of the lipid may affect its self-assembly features. Antibodies, peptides, aptamers and small molecules have been suggested for active targeting strategies.[8,9]

### 1.6. Administration routes

The route of administration is defined as the path by which a drug or an imaging probe is taken into the body for therapeutical or diagnosis purposes. Focusing specifically to drugs in this context, a drug must be administered where it should produce the therapeutic effect.

The route chosen affects directly the drug bioavailability, determining thereby the onset and the duration of the pharmacological effect. Indeed, the administration route is influenced by various factors, which include state and age of the patient, nature of the drug, first-pass metabolism, convenience of application.

Depending on these parameters, the administration routes can be divided into local (or topical) and systemic. The former is the simplest mode of administration, since the formulation containing the drug is applied where the desired action is required (e.g. application of a cream for burns on the damaged skin). On the other hand, the systemic administration of a drug or a



formulation is a more complex route since the enteral (*via* the gastrointestinal system) or the parenteral (bypassing the gastrointestinal system) mode can be adopted.

The enteral route involves drug adsorption via the gastrointestinal tract and includes oral, sublingual and rectal administration, whereas the parenteral route bypasses the gastrointestinal system and it exploits injection (e.g. intravenous, intramuscular, subcutaneous), inhalation or transdermal delivery. Indeed, each route presents advantages and drawbacks depending on the nature of the drug and the biodistribution necessary to achieve the therapeutical effect.

Up to date, LLCNPs formulations exploit both local[26] and systemic administration routes,[8,9] mostly oral, intravenous and dermal/transdermal delivery of drugs and imaging probes.

### **1.6.1. Oral administration**

The oral administration of drugs represents a non-invasive and easy route. Indeed, the age of the patient can hinder the therapy since parameters such as the taste and the smell of the formulation, non-relevant in other administrations, are indeed crucial.

The complex digestive mechanism of the gastrointestinal tract is designed to absorb as many nutrients as possible from our diet. Materials administered orally experience a harsh acidic environment in the stomach (pH 2 – 3) and it contains a large plethora of enzymes, e.g. lipases and proteases.[47] The chyme, partially digested material, is then passed to the first segment of the small intestine (duodenum) where the pancreatic enzymes and the bile salts are released from the common bile duct. The pH rises to 5 – 6 in the duodenum and close to neutrality in the mid-to-distal jejunum. The digestive processes are coordinated to sequentially break down complex nutrients into their building blocks and then absorb selectively these nutritional elements in an organized fashion.

Many efforts have focused on by-passing these harsh environments by encapsulating the drug in carriers. Indeed, the design of the formulation needs to take into account the effect of the lipase. Lipid-based nanoparticles are suitable for this task, given the natural biodegradability of the lipids.

The group of Boyd studied extensively the application of non-lamellar LLCNPs (especially cubosomes) for oral administration.[48,49] PHYT-based cubosomes showed good delivering properties for intestine targeting,[50,51] while GMO-based bicontinuous cubic dispersions are more labile due to lipase actions and thereby are efficient for stomach targeting.[52]

## 1.6.2. Intravenous administration

Among all the injectable routes of administration, the intravenous (IV) drug infusion or injection provides the most efficient and rapid effect, given the minor limitations in term of administration volume.[53]

After the injection, nanosized objects interact with physiological fluids (e.g. blood or extracellular matrices). The biological environment contains several kinds of protein-like macromolecules which can be adsorbed on the surface of the nanoparticles, thus leading to the formation of the so-called protein corona. Some of these proteins bind on the NPs' surface irreversibly and affect subsequently their biodistribution, immune system activation, cellular recognition and final fate.

The protein corona composition is strongly related to the physico-chemical properties of the nanoparticles, such as size, geometry, charge of the interface and, especially, surface features.[46,54] This fact underlines the necessity of investigating on and understanding the surface of nanoparticles by means of QCM-D and Ellipsometry (these techniques will be discussed in Chapter 2).

The hydrophilicity of the surface is considered to play a key role into the protein corona formation. It has been shown that the formation of the protein corona is partially inhibited when liposomes are coated with PEG. However, some recent studies have shown that this stealth effect is not straightforwardly related to the presence of PEG but it is conferred by specific proteins adsorbed on the PEGylated surface.[46] Another strategy to reduce the corona formation is represented by the introduction of zwitterionic moieties to make the materials almost neutral.[55]

The formation of the protein corona can be even exploited to form an active targeting on the surface. Both silica and lipid nanoparticles were able to adsorb on their surface apolipoprotein B[56] and apolipoprotein E[57], respectively, controlling the delivery of the carriers to their corresponding receptors on cell surfaces.

The nanoparticle travels in the bloodstream until it reaches though passive (EPR effect, in the case of tumors) or active targeting the target cell. The plasma (or cell) membrane is the first barrier for nanoparticles internalization. Indeed, different kind of NPs cross the cell membrane via different internalization pathways and each one is regulated by the physico-chemical feature of the carrier. It has been shown that LLCNPs are internalized through fluid-phase

pinocytosis:[46] the cell membrane will invaginate taking the fluid surrounding the NPs and will create a vesicle which transports them within the cell. After this mechanism, the fate of the nanoparticle is to be encapsulated within endosomes and then finally transferred to the lysosomes. Indeed, factors such as surface charge and shape can affect the events into the cells and the carrier might be able to reach the nucleus (common in gene therapy).[58–60]

To summarize, the formation of the protein corona and the internalization of the carrier represent two challenges to overcome for intravenous administration of LLCNPs. The two phenomena are close related, since the proteins adsorbed at the interface can hinder strongly the uptake.

### 1.6.3 Dermal/transdermal administration

Application of a formulation on the skin represents a non-invasive and safe route of drug administration.[26] The skin is a wide organ with the role to coat, defend and thermoregulate the body of many organism. Its peculiar structure allows us to prevent invasion of pathogens and to regulate the water content. Fig. 1.13 shows the various layers that it comprehends.

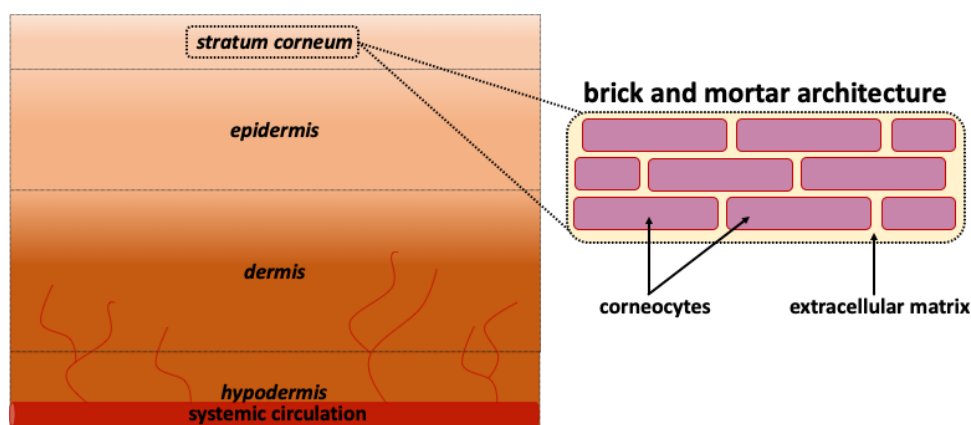


**Figure 1.13.** Graphical representation of the different skin *strata* and, on the right, focus on the *stratum corneum* brick and mortar architecture.

The stratum corneum (SC) is the outermost layer and it is formed by corneocytes (protein-enriched dead cells) and lipid sheets.[61] Closer examination of the SC barriers reveals a brick and mortar structure as described by Elias,[62] where the bricks represent non-living corneocyte cells rich in cross-linked keratin and the intracellular mortar is a mixture of lipids organized in lamellar arrays. This architecture resembles a gel-state characterized by a low mobility of the lipid alkyl chains.

Underneath this layer is the viable epidermis (EP), which measures 50 to 100  $\mu\text{m}$  and is avascular. Deeper is the dermis (DE), which is 1 – 3 mm thick and contains fibroblasts dispersed in an extracellular matrix rich in collagen which gives elasticity and mechanical resistance to the skin.

As the protein corona hinders the application of a drug carrier in intravenous administration, SC represents a challenging barrier in the administration of drugs. The alternation of hydrophilic and hydrophobic layers in the SC restricts strongly the diffusion of molecules through it, drugs included.[26]

Indeed, various approaches can be adopted to enhance the penetration of a drug into the skin layers. One way is represented by the use of formulations based on chemical permeation enhancers, e.g. lipids, which disrupt the highly ordered bilayers structures of the intracellular lipids found in SC.[63,64]

By overcoming the first line of defence, the repartition coefficient[65] of the drug decides its destiny: it can explicate its therapeutical effect in the layer of the skin (dermal release) or reach the capillaries and go into the systemic way (transdermal release). In the latter case, the fate of the nanoparticles is related to the considerations already discussed for the IV administration.

Different types of vesicles were tested effectively *in vitro* and *in vivo*. Their names suggest the type of components:

- ◆ niosomes: non-ionic surfactants-based;[66,67]
- ◆ ethosomes: phospholipids vesicles formulated with high ethanol content;[68,69]
- ◆ bilosomes: vesicles formed by cholesterol and bile salts;[70]
- ◆ transfersomes: highly deformable vesicles made with edge activators, molecule that can confer elasticity to lipid bilayers.[26,71]

On the other hand, non-lamellar liquid crystalline nanoparticles have been studied in the last decade as an alternative platform to vesicles for dermal/transdermal release. Even though few examples have been reported so far, hexosomes and cubosomes are able to deliver antimicrobial peptides,[72] drugs[73] and photosensitizers.[41]

## **1.7. Vesicles, hexosomes and cubosomes: a comparative highlight**

As described in the paragraph 4, some lipids or lipid mixture can form thermodynamically stable lyotropic liquid crystalline structures in excess of water. Vesicles, hexosomes and cubosomes can be obtained via bottom-up and top-down approaches as dispersions of the corresponding LC phase, since their inner structure is maintained during the preparation. Indeed, they are less viscous than their corresponding bulk phases, thereby their application as drug carriers for several administration routes is achievable.

Vesicles have limitations such as the colloidal stability and the limited hydrophobic volume fraction, which restricts the loading of apolar drugs and imaging probes. On the other hand, hexosomes and cubosomes show a larger hydrophobic portion per unit of volume compared to vesicles, but they require a steric stabilizer in order to avoid flocculation.

It is clear that all these carriers display drawbacks at different extents: the cytotoxicity of the components and their stability can restrict their applicability in the nanomedicine field. However, in the last decade, several studies were reported in order to improve the feature of the LLCNPs.

Vesicular structures are well-known since the 1960s and have been deeply characterized. Several types of vesicles were designed with the aim to improve the therapeutical properties. Liposomes, bilosomes, niosomes and ethosomes found application mostly in local administration, given the presence of permeation enhancers.[26]

The group of Cevc investigated profoundly on the technological features of various vesicular formulations for both dermal and transdermal release.[74–78] By using edge activators, e.g. sodium cholate, they developed new deformable and elastic carriers, the so-called transfersomes,[27] which showed excellent performances in passing through the SC.[71,77]

The knowledge on the physico-chemical features of lamellar dispersions as increased exponentially in the last decades as well as their biological effects on the cell environment.[76,79]

In order to enhance their colloidal stability in water, several hydrophilic additives were added. Fadda and collaborators introduced a new liposomal formulation by replacing an aliquot of the water phase (ca. 10 %) with glycerol, a harmless and accepted co-solvent for topical administration.[26,67]

Another issue is represented by the effect of the biological environment on the vesicles structure, as well for other carriers. Biomaterials derived cell membranes could be used as

components to prepare the carriers:[60,80] deriving from natural lipid bilayers and proteins, the biocompatibility results enhanced as well as their stability, given that the biomaterial will be in its native physiological environment. Some examples have been reported in literature, showing how vesicles such as exosomes can be used efficiently in the drug delivery and imaging fields.[29,60] Haney *et al.* engineered exosomes derived from macrophages and loaded with catalase, a potent antioxidant, for the treatment of Parkinson's disease.[29] Milk exosomes exhibited cross-species tolerance with no adverse immune and inflammatory response and they were applied as carrier for oral administration.[30]

Leaving the scene of vesicular structures, hexosomes' and cubosomes' achievements as nanomedicine platforms can be discussed. After their discovery four decades ago,[10,19] hexosomes and cubosomes have been studied in order to unveil their physico-chemical features. The groups of Baglioni,[81] Monduzzi,[12,82] Glatter[83–85] and Larsson[17–19] investigated extensively on their topology, local structure and morphology through AFM, NMR, SAXS and cryo-TEM techniques. In the last ten years, several papers were devoted to describing strategies to tune their bio-chemical features.

GMO and PHYT are the most used building blocks to prepare LLCNPs and their features have been characterized under both the physico-chemical and biological point of view.[8] GMO-based formulations are more biocompatible over a wide range of cell lines when compared to PHYT-based ones when the intravenous administration is desired.[8,9] On the other hand, the latter are more suitable for oral delivery in the small intestine since they are not degraded by lipases in the gastric environment.[50]

To date, other lipids and mixtures are able to self-assemble into cubosomes and hexosomes in excess of water. Yagmur and collaborators used citrem (a mixture of citric acid monoglycerides and diglycerides) and soy phosphatidylcholine at different ratios to produce bicontinuous cubic and inverse hexagonal dispersion in water, attractive for the development of more hemocompatibility drug carriers.[86]

Hexosomes for possible target delivery in the GI tract were prepared also by using diglycerol mono-isostearate as building block, showing good pH responsive release of ketoprofen.[87]

Moreover, omega-3 polyunsaturated fatty acids were used as building blocks in order to formulate hexosomes with beneficial health effects in various disorder and for the delivery of functional foods.[88,89]

It should be noted that several parameters such as temperature, pH, ionic strength, additives and impurities in the lipid sample can influence the self-assembly properties of these building blocks, thus inducing the formation of different phases.

Bioimaging applied hexosomes and cubosomes as tools, especially in the last decade, mainly for FOI and MRI. The functionalization of the stabilizer (mostly poloxamers such as Pluronic F127 and F108) permits to obtain fluorescently labelled nanoparticles, suitable for *in vitro* and *in vivo* investigations. Murgia and coworkers studied extensively both cubosomes and hexosomes functionalized with rhodamine[42,43] and dansyl[90] derivatives for fluorescence optical imaging *in vitro* and formulated them as theranostic platforms for cancer therapy.

Regarding MRI applications, Muir *et al.* incorporated a nitroxide lipid into the matrix of the LLCNPs, displaying a great enhancement of relaxivity when a Pn3m space group encapsulate the MRI probe, in comparison with the inverse hexagonal phase dispersion which is formed at high nitroxide loadings.[91] Moreover, both GMO- and PHYT-based LLCNPs were loaded with different nitroxide lipids in order to screen the effect of the structure and the lipid used on the application.[92] Few years later, Tran *et al.* developed dual-modal NIR-MRI cubosomes and hexosomes to evaluate the biodistribution of the aggregates *in vivo*.[93]

Multifunctional LLCNPs can be formulated including hard-based NPs in the lipid matrix: the group of Berti studied the inclusion of SPIONs[94] and hydrophobic Fe<sub>3</sub>O<sub>4</sub> nanoparticles[95] in lipid mesophases to prepare the so-called magnetocubosomes.

The functionalization of non-lamellar LLCNPs to obtain a fluorescently labelling of the surface is an active field. The first proof of concept of click chemistry (reaction between an alkyne and azide) applied on cubosomes was published by Boyd and collaborators: PHYT-based cubosomes were prepared using an azidocaproylphosphaethanolamine and Pluronic F108 as stabilizer and functionalized with a sulfo-DBCO-cyanine5.[96]

Given the increasing resistance of bacteria to antibiotics, antimicrobial peptides (AMPs) delivery is a new emerging application for LLCNPs, both in topical and systemic administrations. Boge *et al.* prepared GMO-based bicontinuous cubic dispersions containing the peptides AP114, DPK-060 and LL-37 showing how the encapsulation influenced the antimicrobial features of the AMPs.[97] In another paper, the same group studied the topical application of LL-37-loaded cubosomes, prepared with different methods, against *E. coli* and *S. aureus*, highlighting that the cubic structure preserved the AMP activity even in the presence of a proteolytic enzyme.[72] Within the same topic, Gontsarik *et al.* investigated on the pH-dependent properties of a nanocarrier made by GMO, oleic acid and the human cathelicidin AMP LL-37.[98] Their papers showed *via* electrophoretic mobility and SAXS measurements that the  $pK_a$  of oleic acid is strongly dependent on the carrier composition, providing more knowledge on the effect of pH on LLCNPs.

The state of art of non-lamellar LLCNPs highlights mostly two main issues that can be addressed. First, the components of the nanoparticles can induce hemolysis, the rupture of red blood cells *via* interaction with their lipid membranes. GMO was found to possess a hemolytic effect *in vitro* by Barauskas and coworkers.[99] GMO-based cubosomes hemolytic properties were evaluated *in vivo* by Biffi *et al.*, showing that below 60 µg/mL of GMO the formulation can be considered administrable in mices.[100]

Moreover, the stabilizer can influence the structure of the aggregates, leading to undesired phases that impact the delivering features. Murgia and Bazylińska formulated polymer-free GMO-cubosomes for photodynamic therapy using phospholipids as stabilizer and propylene glycol as hydrotrope.[41]

## 1.8. Objectives of the PhD thesis

Lipid self-assembly has been exploited to produce biocompatible and biodegradable drug carriers with different architectures. Vesicles, hexosomes and cubosomes are the main characters of this thesis and their bulk, surface and biological properties have been investigated. Indeed, after having highlighted the main features in the field of nanomedicine and LLCNPs, some questions may arise from this discussion:

- ◆ How can we enhance GMO-based LLCNPs' hemo- and bio-compatibility?
- ◆ By changing the stabilizer moiety, can the physico-chemical and biological features of the NPs be tuned?
- ◆ How a novel stabilizer can impact the surface (and thereby the biological) properties of cubosomes?
- ◆ Can cell-derived vesicles be useful in bio-imaging?
- ◆ Can bio-surfactants, e.g. bile salts, affect the permeation features of LLCNPs for local administration of drugs?

This PhD thesis try to shed some light on the physico-chemical and biological phenomena behind these questions, in order to provide questions to these topics.

In the following chapters the tunability of these LLCNPs depending on the administration route will be discussed, highlighting the strong connection among bulk, surface and biological properties.



First, Chapter 2 will introduce the experimental techniques adopted in the project development. Then the chapters devoted to the discussion of the experimental results are organized in such manner: an introduction on the specific topic is given and a brief discussion of the experimental data is presented. At the end of each chapters, the papers related to the topic are added as appendices.

Chapter 3 (**Papers I – III**) will focus on the role of different stabilizers (modified poloxamer, hemicellulose and a novel polyphosphoester) and how they can influence the physico-chemical and biological properties of GMO-based cubosomes formulated for systemic administration.

Chapter 4 (**Papers IV – V**) will investigate on the role of permeation enhancers and edge activators in liquid and gel formulations of LLCNPs for topical administration of antioxidants.

Chapter 5 (**Papers VI**) will evaluate the applicability of red blood cell-derived nanovesicles as bio-imaging tool *in vitro*.

A conclusive chapter will compare the results obtained to draw conclusions and answer the questions herein presented.

Finally, the papers published will be presented in the Annex section as well as **Paper VII**, a review on non-lamellar LLCNPs for bio-imaging applications.

## 1.9. References

- [1] M.C. Di Gregorio, L. Travaglini, A. Del Giudice, J. Cautela, N.V. Pavel, L. Galantini, Bile Salts: Natural Surfactants and Precursors of a Broad Family of Complex Amphiphiles, *Langmuir*. 35 (2019) 6803–6821. <https://doi.org/10.1021/acs.langmuir.8b02657>.
- [2] S. Biggs, *Handbook of Applied Surface and Colloid Chemistry*. (Ed K. Holmberg), Aust. J. Chem. (2002). [https://doi.org/10.1071/chv55n3\\_br](https://doi.org/10.1071/chv55n3_br).
- [3] J.N. Israelachvili, D.J. Mitchell, B.W. Ninham, Theory of self-assembly of hydrocarbon amphiphiles into micelles and bilayers, *J. Chem. Soc. Faraday Trans. 2 Mol. Chem. Phys.* (1976). <https://doi.org/10.1039/F29767201525>.
- [4] J. Israelachvili, *Intermolecular and Surface Forces*, 2011. <https://doi.org/10.1016/C2009-0-21560-1>.
- [5] J.Y.T. Chong, X. Mulet, B.J. Boyd, C.J. Drummond, *Steric Stabilizers for Cubic Phase Lyotropic Liquid Crystal Nanodispersions (Cubosomes)*, 1st ed., Elsevier Inc., 2015. <https://doi.org/10.1016/bs.adplan.2014.11.001>.
- [6] M.A. Yorke, D.H. Dickson, Lamellar to tubular conformational changes in the endoplasmic reticulum of the retinal pigment epithelium of the newt, *Notophthalmus viridescens*, *Cell Tissue Res.* 241 (1985) 629–637. <https://doi.org/10.1007/BF00214585>.
- [7] R.M. Hicks, ISOLATION OF THE PLASMA MEMBRANE OF THE LUMINAL EPITHELIUM, HEXAGONAL SURFACE OF RAT BLADDER AND THE OCCURRENCE OF A LATTICE OF SUBUNITS STAINED BOTH IN NEGATIVELY WHOLE MOUNTS AND IN SECTIONED, (1970).
- [8] S. Murgia, S. Biffi, R. Mezzenga, Recent advances of non-lamellar lyotropic liquid crystalline nanoparticles in nanomedicine, *Curr. Opin. Colloid Interface Sci.* 48 (2020) 28–39. <https://doi.org/10.1016/j.cocis.2020.03.006>.
- [9] H.M.G. Barriga, M.N. Holme, M.M. Stevens, Cubosomes: The Next Generation of Smart Lipid Nanoparticles?, *Angew. Chemie - Int. Ed.* 58 (2019) 2958–2978. <https://doi.org/10.1002/anie.201804067>.
- [10] J. Gustafsson, H. Ljusberg-Wahren, M. Almgren, K. Larsson, Submicron particles of reversed lipid phases in water stabilized by a nonionic amphiphilic polymer, *Langmuir*. 13 (1997) 6964–6971. <https://doi.org/10.1021/la970566+>.
- [11] A.D. Bangham, R.W. Horne, Negative staining of phospholipids and their structural modification by surface-active agents as observed in the electron microscope, *J. Mol. Biol.* 8 (1964) 660–668. [https://doi.org/10.1016/S0022-2836\(64\)80115-7](https://doi.org/10.1016/S0022-2836(64)80115-7).
- [12] M. Monduzzi, H. Ljusberg-Wahren, K. Larsson, A <sup>13</sup>C NMR study of aqueous dispersions of reversed lipid phases, *Langmuir*. 16 (2000) 7355–7358. <https://doi.org/10.1021/la0000872>.
- [13] S.T. Hyde, S. Andersson, B. Ericsson, K. Larsson, A cubic structure consisting of a lipid bilayer forming an infinite periodic minimum surface of the gyroid type in the glycerolmonooleat-water system, *Zeitschrift Fur Krist. - New Cryst. Struct.* (1984). <https://doi.org/10.1524/zkri.1984.168.1-4.213>.
- [14] J.S. Patton, M.C. Carey, Xline ffF ; f + 0000 ; triglyceride, (1849).
- [15] T. Landh, Phase behavior in the system pine oil monoglycerides-ploxamer 407-water at 20°C, *J. Phys.*

- Chem. (1994). <https://doi.org/10.1021/j100085a028>.
- [16] E.S. Lutton, Phase behavior of aqueous systems of monoglycerides, *J. Am. Oil Chem. Soc.* 42 (1965) 1068–1070. <https://doi.org/10.1007/BF02636909>.
- [17] G. Lindblom, K. Larsson, L. Johansson, K. Fontell, S. Forsén, The Cubic Phase of Monoglyceride-Water Systems. Arguments for a Structure Based upon Lamellar Bilayer Units, *J. Am. Chem. Soc.* 101 (1979) 5465–5470. <https://doi.org/10.1021/ja00513a002>.
- [18] K. Larsson, Two cubic phases in monoolein-water system, *Nature*. (1983). <https://doi.org/10.1038/304664c0>.
- [19] W. Longley, T.J. McIntosh, A bicontinuous tetrahedral structure in a liquid-crystalline lipid, *Nature*. 303 (1983) 612–614. <https://doi.org/10.1038/303612a0>.
- [20] H. Qiu, M. Caffrey, The phase diagram of the monoolein/water system: Metastability and equilibrium aspects, *Biomaterials*. 21 (2000) 223–234. [https://doi.org/10.1016/S0142-9612\(99\)00126-X](https://doi.org/10.1016/S0142-9612(99)00126-X).
- [21] J. Barauskas, T. Landh, Phase behavior of the phytantriol/water system, *Langmuir*. (2003). <https://doi.org/10.1021/la0350812>.
- [22] C. V. Kulkarni, W. Wachter, G. Iglesias-Salto, S. Engelskirchen, S. Ahualli, Monoolein: A magic lipid?, *Phys. Chem. Chem. Phys.* 13 (2011) 3004–3021. <https://doi.org/10.1039/c0cp01539c>.
- [23] J. Barauskas, T. Landh, Phase behavior of the phytantriol/water system, *Langmuir*. 19 (2003) 9562–9565. <https://doi.org/10.1021/la0350812>.
- [24] L. Mei, Z. Zhang, L. Zhao, L. Huang, X.L. Yang, J. Tang, S.S. Feng, Pharmaceutical nanotechnology for oral delivery of anticancer drugs, *Adv. Drug Deliv. Rev.* 65 (2013) 880–890. <https://doi.org/10.1016/j.addr.2012.11.005>.
- [25] S. Aleandri, R. Mezzenga, The physics of lipidic mesophase delivery systems, *Phys. Today*. 73 (2020) 38–44. <https://doi.org/10.1063/PT.3.4522>.
- [26] F. Lai, C. Caddeo, M.L. Manca, M. Manconi, C. Sinico, A.M. Fadda, What’s new in the field of phospholipid vesicular nanocarriers for skin drug delivery, *Int. J. Pharm.* 583 (2020). <https://doi.org/10.1016/j.ijpharm.2020.119398>.
- [27] G. Cevc, Transfersomes, liposomes and other lipid suspensions on the skin: Permeation enhancement, vesicle penetration, and transdermal drug delivery, *Crit. Rev. Ther. Drug Carrier Syst.* (1996). <https://doi.org/10.1615/CritRevTherDrugCarrierSyst.v13.i3-4.30>.
- [28] H. Zhang, Erythrocytes in nanomedicine: An optimal blend of natural and synthetic materials, *Biomater. Sci.* 4 (2016) 1024–1031. <https://doi.org/10.1039/c6bm00072j>.
- [29] M.J. Haney, N.L. Klyachko, Y. Zhao, R. Gupta, E.G. Plotnikova, Z. He, T. Patel, A. Piroyan, M. Sokolsky, A. V. Kabanov, E. V. Batrakova, Exosomes as drug delivery vehicles for Parkinson’s disease therapy, *J. Control. Release*. 207 (2015) 18–30. <https://doi.org/10.1016/j.jconrel.2015.03.033>.
- [30] R. Munagala, F. Aqil, J. Jeyabalan, R.C. Gupta, Bovine milk-derived exosomes for drug delivery, *Cancer Lett.* 371 (2016) 48–61. <https://doi.org/10.1016/j.canlet.2015.10.020>.
- [31] M. Valldeperas, A.P. Dabkowska, G.K. Pálsson, S. Rogers, N. Mahmoudi, A. Carnerup, J. Barauskas, T. Nylander, Interfacial properties of lipid sponge-like nanoparticles and the role of stabilizer on particle structure and surface interactions, *Soft Matter*. 15 (2019) 2178–2189. <https://doi.org/10.1039/c8sm02634c>.

- [32] J. Gilbert, M. Valdeperas, S.K. Dhayal, J. Barauskas, C. Dicko, T. Nylander, Immobilisation of  $\beta$ -galactosidase within a lipid sponge phase: Structure, stability and kinetics characterisation, *Nanoscale*. (2019). <https://doi.org/10.1039/c9nr06675f>.
- [33] S. Keereweer, J.D.F. Kerrebijn, P.B.A.A. Van Driel, B. Xie, E.L. Kaijzel, T.J.A. Snoeks, I. Que, M. Hutteman, J.R. Van Der Vorst, J.S.D. Mieog, A.L. Vahrmeijer, C.J.H. Van De Velde, R.J. Baatenburg De Jong, C.W.G.M. Löwik, Optical image-guided surgery - Where do we stand?, *Mol. Imaging Biol.* 13 (2011) 199–207. <https://doi.org/10.1007/s11307-010-0373-2>.
- [34] C. Wang, Z. Wang, T. Zhao, Y. Li, G. Huang, B.D. Sumer, J. Gao, Optical molecular imaging for tumor detection and image-guided surgery, *Biomaterials*. 157 (2018) 62–75. <https://doi.org/10.1016/j.biomaterials.2017.12.002>.
- [35] E.A. Owens, M. Henary, G. El Fakhri, H.S. Choi, Tissue-Specific Near-Infrared Fluorescence Imaging, *Acc. Chem. Res.* 49 (2016) 1731–1740. <https://doi.org/10.1021/acs.accounts.6b00239>.
- [36] H.S. Peng, D.T. Chiu, Soft fluorescent nanomaterials for biological and biomedical imaging, *Chem. Soc. Rev.* 44 (2015) 4699–4722. <https://doi.org/10.1039/c4cs00294f>.
- [37] R. Weissleder, M.J. Pittet, Imaging in the era of molecular oncology, *Nature*. (2008). <https://doi.org/10.1038/nature06917>.
- [38] National Institute of Cancer, Common Terminology Criteria for Adverse Events (CTCAE), 2010. <https://doi.org/10.1080/00140139.2010.489653>.
- [39] T. Lammers, S. Aime, W.E. Hennink, G. Storm, F. Kiessling, Theranostic nanomedicine, *Acc. Chem. Res.* (2011). <https://doi.org/10.1021/ar200019c>.
- [40] L.Y. Rizzo, B. Theek, G. Storm, F. Kiessling, T. Lammers, Recent progress in nanomedicine: Therapeutic, diagnostic and theranostic applications, *Curr. Opin. Biotechnol.* (2013). <https://doi.org/10.1016/j.copbio.2013.02.020>.
- [41] U. Bazylińska, J. Kulbacka, J. Schmidt, Y. Talmon, S. Murgia, Polymer-free cubosomes for simultaneous bioimaging and photodynamic action of photosensitizers in melanoma skin cancer cells, *J. Colloid Interface Sci.* 522 (2018) 163–173. <https://doi.org/10.1016/j.jcis.2018.03.063>.
- [42] V. Meli, C. Caltagirone, A.M. Falchi, S.T. Hyde, V. Lippolis, M. Monduzzi, M. Obiols-Rabasa, A. Rosa, J. Schmidt, Y. Talmon, S. Murgia, Docetaxel-Loaded Fluorescent Liquid-Crystalline Nanoparticles for Cancer Theranostics, *Langmuir*. 31 (2015) 9566–9575. <https://doi.org/10.1021/acs.langmuir.5b02101>.
- [43] V. Meli, C. Caltagirone, C. Sinico, F. Lai, A.M. Falchi, M. Monduzzi, M. Obiols-Rabasa, G. Picci, A. Rosa, J. Schmidt, Y. Talmon, S. Murgia, Theranostic hexosomes for cancer treatments: an in vitro study, *New J. Chem.* 41 (2017) 1558–1565. <https://doi.org/10.1039/c6nj03232j>.
- [44] K. Loomis, K. McNeeley, R. V. Bellamkonda, Nanoparticles with targeting, triggered release, and imaging functionality for cancer applications, *Soft Matter*. (2011). <https://doi.org/10.1039/c0sm00534g>.
- [45] N. Bertrand, J. Wu, X. Xu, N. Kamaly, O.C. Farokhzad, Cancer nanotechnology: The impact of passive and active targeting in the era of modern cancer biology, *Adv. Drug Deliv. Rev.* (2014). <https://doi.org/10.1016/j.addr.2013.11.009>.
- [46] V. Francia, K. Yang, S. Deville, C. Reker-Smit, I. Nelissen, A. Salvati, Corona Composition Can Affect the Mechanisms Cells Use to Internalize Nanoparticles, *ACS Nano*. (2019).

- <https://doi.org/10.1021/acsnano.9b03824>.
- [47] K. Krieser, J. Emanuelli, R.M. Daudt, S. Bilatto, J.B. Willig, S.S. Guterres, A.R. Pohlmann, A. Buffon, D.S. Correa, I.C. Külkamp-Guerreiro, Taste-masked nanoparticles containing Saquinavir for pediatric oral administration, *Mater. Sci. Eng. C*. 117 (2020). <https://doi.org/10.1016/j.msec.2020.111315>.
- [48] B.J. Boyd, C.A.S. Bergström, Z. Vinarov, M. Kuentz, J. Brouwers, P. Augustijns, M. Brandl, A. Bernkop-Schnürch, N. Shrestha, V. Prémat, A. Müllertz, A. Bauer-Brandl, V. Jannin, Successful oral delivery of poorly water-soluble drugs both depends on the intraluminal behavior of drugs and of appropriate advanced drug delivery systems, *Eur. J. Pharm. Sci.* 137 (2019) 104967. <https://doi.org/10.1016/j.ejps.2019.104967>.
- [49] T.H. Nguyen, T. Hanley, C.J.H. Porter, B.J. Boyd, Nanostructured liquid crystalline particles provide long duration sustained-release effect for a poorly water soluble drug after oral administration, *J. Control. Release*. 153 (2011) 180–186. <https://doi.org/10.1016/j.jconrel.2011.03.033>.
- [50] C.J.H. Porter, A.M. Kaukonen, A. Taillardat-Bertschinger, B.J. Boyd, J.M. O'Connor, G.A. Edwards, W.N. Charman, Use of in Vitro Lipid Digestion Data to Explain the in Vivo Performance of Triglyceride-Based Oral Lipid Formulations of Poorly Water-Soluble Drugs: Studies with Halofantrine, *J. Pharm. Sci.* 93 (2004) 1110–1121. <https://doi.org/10.1002/jps.20039>.
- [51] L.H. Nielsen, T. Rades, B. Boyd, A. Boisen, Microcontainers as an oral delivery system for spray dried cubosomes containing ovalbumin, *Eur. J. Pharm. Biopharm.* 118 (2017) 13–20. <https://doi.org/10.1016/j.ejpb.2016.12.008>.
- [52] R. Negrini, R. Mezzenga, PH-responsive lyotropic liquid crystals for controlled drug delivery, *Langmuir*. 27 (2011) 5296–5303. <https://doi.org/10.1021/la200591u>.
- [53] J. Wong, A. Brugger, A. Khare, M. Chaubal, P. Papadopoulos, B. Rabinow, J. Kipp, J. Ning, Suspensions for intravenous (IV) injection: A review of development, preclinical and clinical aspects, *Adv. Drug Deliv. Rev.* 60 (2008) 939–954. <https://doi.org/10.1016/j.addr.2007.11.008>.
- [54] A. Lesniak, A. Salvati, M.J. Santos-Martinez, M.W. Radomski, K.A. Dawson, C. Åberg, Nanoparticle adhesion to the cell membrane and its effect on nanoparticle uptake efficiency, *J. Am. Chem. Soc.* (2013). <https://doi.org/10.1021/ja309812z>.
- [55] D.G. L., P. N., M.-L. E., Controlling the acute hemodynamic effects associated with IV administration of particulate drug dispersions in dogs, *Drug Dev. Res.* (1996).
- [56] D.E. Owens, N.A. Peppas, Opsonization, biodistribution, and pharmacokinetics of polymeric nanoparticles, *Int. J. Pharm.* 307 (2006) 93–102. <https://doi.org/10.1016/j.ijpharm.2005.10.010>.
- [57] D.F. Driscoll, F. Etzler, T.A. Barber, J. Nehne, W. Niemann, B.R. Bistran, Physicochemical assessments of parenteral lipid emulsions: Light obscuration versus laser diffraction, *Int. J. Pharm.* 219 (2001) 21–37. [https://doi.org/10.1016/S0378-5173\(01\)00626-3](https://doi.org/10.1016/S0378-5173(01)00626-3).
- [58] H. Yin, K.J. Kauffman, D.G. Anderson, Delivery technologies for genome editing, *Nat. Rev. Drug Discov.* (2017). <https://doi.org/10.1038/nrd.2016.280>.
- [59] N. Nayerossadat, P. Ali, T. Maedeh, Viral and nonviral delivery systems for gene delivery, *Adv. Biomed. Res.* (2012). <https://doi.org/10.4103/2277-9175.98152>.
- [60] S.M. Patil, S.S. Sawant, N.K. Kunda, Exosomes as drug delivery systems: A brief overview and progress update, *Eur. J. Pharm. Biopharm.* 154 (2020) 259–269.

- <https://doi.org/10.1016/j.ejpb.2020.07.026>.
- [61] S.M. Pyo, H.I. Maibach, Skin Metabolism: Relevance of Skin Enzymes for Rational Drug Design, *Skin Pharmacol. Physiol.* 32 (2019) 283–293. <https://doi.org/10.1159/000501732>.
- [62] P.M. Elias, Structure and function of the stratum corneum extracellular matrix, *J. Invest. Dermatol.* 132 (2012) 2131–2133. <https://doi.org/10.1038/jid.2012.246>.
- [63] M.R. Prausnitz, R. Langer, Transdermal drug delivery, *Nat. Biotechnol.* 26 (2008) 1261–1268. <https://doi.org/10.1038/nbt.1504>.
- [64] Q.D. Pham, S. Björklund, J. Engblom, D. Topgaard, E. Sparr, Chemical penetration enhancers in stratum corneum - Relation between molecular effects and barrier function, *J. Control. Release.* 232 (2016) 175–187. <https://doi.org/10.1016/j.jconrel.2016.04.030>.
- [65] A. Wolde-Kidan, Q.D. Pham, A. Schlaich, P. Loche, E. Sparr, R.R. Netz, E. Schneck, Influence of polar co-solutes and salt on the hydration of lipid membranes, *Phys. Chem. Chem. Phys.* 21 (2019) 16989–17000. <https://doi.org/10.1039/c9cp01953g>.
- [66] S.R.M. Moghddam, A. Ahad, M. Aqil, S.S. Imam, Y. Sultana, Formulation and optimization of niosomes for topical diacerein delivery using 3-factor, 3-level Box-Behnken design for the management of psoriasis, *Mater. Sci. Eng. C.* 69 (2016) 789–797. <https://doi.org/10.1016/j.msec.2016.07.043>.
- [67] M.L. Manca, M. Manconi, A. Nacher, C. Carbone, D. Valenti, A.M. MacCioni, C. Sinico, A.M. Fadda, Development of novel diolein-niosomes for cutaneous delivery of tretinoin: Influence of formulation and in vitro assessment, *Int. J. Pharm.* 477 (2014) 176–186. <https://doi.org/10.1016/j.ijpharm.2014.10.031>.
- [68] G. Sharma, H. Goyal, K. Thakur, K. Raza, O.P. Katare, Novel elastic membrane vesicles (EMVs) and ethosomes-mediated effective topical delivery of aceclofenac: a new therapeutic approach for pain and inflammation, *Drug Deliv.* 23 (2016) 3135–3145. <https://doi.org/10.3109/10717544.2016.1155244>.
- [69] A. Mistry, P. Ravikumar, Development and evaluation of azelaic acid based ethosomes for topical delivery for the treatment of acne, *Indian J. Pharm. Educ. Res.* 50 (2016) S232–S243. <https://doi.org/10.5530/ijper.50.3.34>.
- [70] C. Faustino, C. Serafim, P. Rijo, C.P. Reis, Bile acids and bile acid derivatives: use in drug delivery systems and as therapeutic agents, *Expert Opin. Drug Deliv.* 13 (2016) 1133–1148. <https://doi.org/10.1080/17425247.2016.1178233>.
- [71] G.M. El Zaafarany, G.A.S. Awad, S.M. Holayel, N.D. Mortada, Role of edge activators and surface charge in developing ultradeformable vesicles with enhanced skin delivery, *Int. J. Pharm.* 397 (2010) 164–172. <https://doi.org/10.1016/j.ijpharm.2010.06.034>.
- [72] L. Boge, K. Hallstenson, L. Ringstad, J. Johansson, T. Andersson, M. Davoudi, P.T. Larsson, M. Mahlapuu, J. Håkansson, M. Andersson, Cubosomes for topical delivery of the antimicrobial peptide LL-37, *Eur. J. Pharm. Biopharm.* 134 (2019) 60–67. <https://doi.org/10.1016/j.ejpb.2018.11.009>.
- [73] V.K. Rapalli, T. Waghule, N. Hans, A. Mahmood, S. Gorantla, S.K. Dubey, G. Singhvi, Insights of lyotropic liquid crystals in topical drug delivery for targeting various skin disorders, *J. Mol. Liq.* 315 (2020). <https://doi.org/10.1016/j.molliq.2020.113771>.
- [74] G. Cevc, U. Vierl, Nanotechnology and the transdermal route. A state of the art review and critical appraisal, *J. Control. Release.* (2010). <https://doi.org/10.1016/j.jconrel.2009.10.016>.

- [75] G. Cevc, Lipid vesicles and other colloids as drug carriers on the skin, *Adv. Drug Deliv. Rev.* (2004). <https://doi.org/10.1016/j.addr.2003.10.028>.
- [76] G. Blume, G. Cevc, Liposomes for the sustained drug release in vivo, *BBA - Biomembr.* (1990). [https://doi.org/10.1016/0005-2736\(90\)90440-Y](https://doi.org/10.1016/0005-2736(90)90440-Y).
- [77] G. Cevc, G. Blume, New, highly efficient formulation of diclofenac for the topical, transdermal administration in ultradeformable drug carriers, *Transfersomes, Biochim. Biophys. Acta - Biomembr.* (2001). [https://doi.org/10.1016/S0005-2736\(01\)00369-8](https://doi.org/10.1016/S0005-2736(01)00369-8).
- [78] G. Cevc, Chapter 9 Material transport across permeability barriers by means of lipid vesicles, in: *Handb. Biol. Phys.*, 1995. [https://doi.org/10.1016/S1383-8121\(06\)80026-6](https://doi.org/10.1016/S1383-8121(06)80026-6).
- [79] M. Schlich, C. Sinico, D. Valenti, A. Gulati, M.D. Joshi, V. Meli, S. Murgia, T. Xanthos, Towards long-acting adrenaline for cardiopulmonary resuscitation: Production and characterization of a liposomal formulation, *Int. J. Pharm.* 557 (2019) 105–111. <https://doi.org/10.1016/j.ijpharm.2018.12.044>.
- [80] J. Yan, J. Yu, C. Wang, Z. Gu, Red Blood Cells for Drug Delivery, *Small Methods*. 1 (2017) 1700270. <https://doi.org/10.1002/smtd.201700270>.
- [81] C. Neto, G. Aloisi, P. Baglioni, K. Larsson, Imaging soft matter with the atomic force microscope: Cubosomes and hexosomes, *J. Phys. Chem. B.* (1999). <https://doi.org/10.1021/jp984551b>.
- [82] P. Pitzalis, M. Monduzzi, N. Krog, H. Larsson, H. Ljusberg-Wahren, T. Nylander, Characterization of the liquid-crystalline phases in the glycerol monooleate/diglycerol monooleate/water system, *Langmuir*. 16 (2000) 6358–6365. <https://doi.org/10.1021/la0002031>.
- [83] F. Muller, A. Salonen, O. Glatter, Phase behavior of Phytantriol/water bicontinuous cubic Pn3m cubosomes stabilized by Laponite disc-like particles, *J. Colloid Interface Sci.* 342 (2010) 392–398. <https://doi.org/10.1016/j.jcis.2009.10.054>.
- [84] A. Yaghmur, O. Glatter, Characterization and potential applications of nanostructured aqueous dispersions, *Adv. Colloid Interface Sci.* (2009). <https://doi.org/10.1016/j.cis.2008.07.007>.
- [85] O. Glatter, *Scattering methods and their application in colloid and interface science*, 2018. <https://doi.org/10.1016/c2016-0-04640-5>.
- [86] R. Prajapati, S.W. Larsen, A. Yaghmur, Citrem-phosphatidylcholine nano-self-assemblies: Solubilization of bupivacaine and its role in triggering a colloidal transition from vesicles to cubosomes and hexosomes, *Phys. Chem. Chem. Phys.* (2019). <https://doi.org/10.1039/c9cp01878f>.
- [87] J.R. Magana, M. Homs, J. Esquena, I. Freilich, E. Kesselman, D. Danino, C. Rodríguez-Abreu, C. Solans, Formulating stable hexosome dispersions with a technical grade diglycerol-based surfactant, *J. Colloid Interface Sci.* 550 (2019) 73–80. <https://doi.org/10.1016/j.jcis.2019.04.084>.
- [88] X. Shao, G. Bor, S. Al-Hosayni, S. Salentinig, A. Yaghmur, Structural characterization of self-assemblies of new omega-3 lipids: docosahexaenoic acid and docosapentaenoic acid monoglycerides, *Phys. Chem. Chem. Phys.* 20 (2018) 23928–23941. <https://doi.org/10.1039/C8CP04256J>.
- [89] A. Yaghmur, S. Al-Hosayni, H. Amenitsch, S. Salentinig, Structural Investigation of Bulk and Dispersed Inverse Lyotropic Hexagonal Liquid Crystalline Phases of Eicosapentaenoic Acid Monoglyceride, *Langmuir*. 33 (2017) 14045–14057. <https://doi.org/10.1021/acs.langmuir.7b03078>.
- [90] S. Murgia, S. Bonacchi, A.M. Falchi, S. Lampis, V. Lippolis, V. Meli, M. Monduzzi, L. Prodi, J. Schmidt, Y. Talmon, C. Caltagirone, Drug-loaded fluorescent cubosomes: Versatile nanoparticles for

- potential theranostic applications, *Langmuir*. (2013). <https://doi.org/10.1021/la401047a>.
- [91] B.W. Muir, D.P. Acharya, D.F. Kennedy, X. Mulet, R.A. Evans, S.M. Pereira, K.L. Wark, B.J. Boyd, T.H. Nguyen, T.M. Hinton, L.J. Waddington, N. Kirby, D.K. Wright, H.X. Wang, G.F. Egan, B.A. Moffat, Metal-free and MRI visible theranostic lyotropic liquid crystal nitroxide-based nanoparticles, *Biomaterials*. (2012). <https://doi.org/10.1016/j.biomaterials.2011.12.018>.
- [92] N. Bye, O.E. Hutt, T.M. Hinton, D.P. Acharya, L.J. Waddington, B.A. Moffat, D.K. Wright, H.X. Wang, X. Mulet, B.W. Muir, Nitroxide-loaded hexosomes provide MRI contrast in vivo, *Langmuir*. 30 (2014) 8898–8906. <https://doi.org/10.1021/la5007296>.
- [93] N. Tran, N. Bye, B.A. Moffat, D.K. Wright, A. Cuddihy, T.M. Hinton, A.M. Hawley, N.P. Reynolds, L.J. Waddington, X. Mulet, A.M. Turnley, M.C. Morganti-Kossmann, B.W. Muir, Dual-modality NIRF-MRI cubosomes and hexosomes: High throughput formulation and in vivo biodistribution, *Mater. Sci. Eng. C*. 71 (2017) 584–593. <https://doi.org/10.1016/j.msec.2016.10.028>.
- [94] M. Mendoza, C. Montis, L. Caselli, M. Wolf, P. Baglioni, D. Berti, On the thermotropic and magnetotropic phase behavior of lipid liquid crystals containing magnetic nanoparticles, *Nanoscale*. 10 (2018) 3480–3488. <https://doi.org/10.1039/c7nr08478a>.
- [95] C. Montis, B. Castroflorio, M. Mendoza, A. Salvatore, D. Berti, P. Baglioni, Magnetocubosomes for the delivery and controlled release of therapeutics, *J. Colloid Interface Sci.* 449 (2015) 317–326. <https://doi.org/10.1016/j.jcis.2014.11.056>.
- [96] N. Alcaraz, Q. Liu, E. Hanssen, A. Johnston, B.J. Boyd, Clickable Cubosomes for Antibody-Free Drug Targeting and Imaging Applications, *Bioconjug. Chem.* 29 (2018) 149–157. <https://doi.org/10.1021/acs.bioconjchem.7b00659>.
- [97] L. Boge, A. Umerska, N. Matougui, H. Bysell, L. Ringstad, M. Davoudi, J. Eriksson, K. Edwards, M. Andersson, Cubosomes post-loaded with antimicrobial peptides: Characterization, bactericidal effect and proteolytic stability, *Int. J. Pharm.* 526 (2017) 400–412. <https://doi.org/10.1016/j.ijpharm.2017.04.082>.
- [98] M. Gontsarik, A. Yaghmur, S. Salentinig, Dispersed Liquid Crystals as pH-adjustable Antimicrobial Peptide Nanocarriers, *J. Colloid Interface Sci.* (2020). <https://doi.org/10.1016/j.jcis.2020.09.081>.
- [99] J. Barauskas, C. Cervin, M. Jankunec, M. Špandyreva, K. Ribokaite, F. Tiberg, M. Johnsson, Interactions of lipid-based liquid crystalline nanoparticles with model and cell membranes, *Int. J. Pharm.* (2010). <https://doi.org/10.1016/j.ijpharm.2010.03.016>.
- [100] S. Biffi, L. Andolfi, C. Caltagirone, C. Garrovo, A.M. Falchi, V. Lippolis, A. Lorenzon, P. Macor, V. Meli, M. Monduzzi, M. Obiols-Rabasa, L. Petrizza, L. Prodi, A. Rosa, J. Schmidt, Y. Talmon, S. Murgia, Cubosomes for in vivo fluorescence lifetime imaging, *Nanotechnology*. 28 (2017). <https://doi.org/10.1088/1361-6528/28/5/055102>.

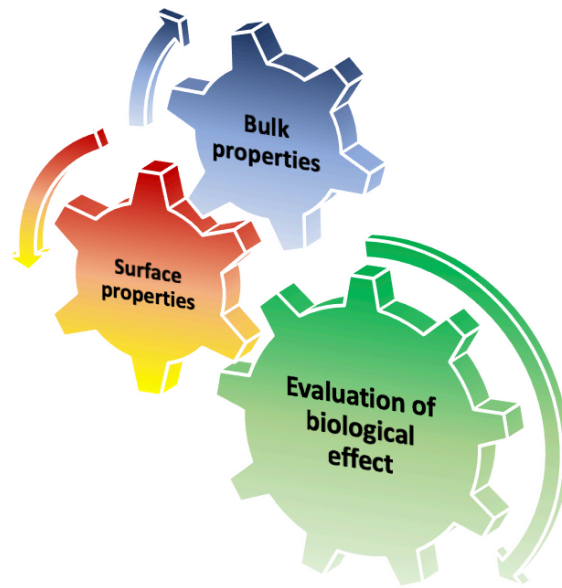






# 2

## Experimental characterization of LLCNPs



### Chapter 2 – Table of contents

- 2.1. Bulk Techniques
  - 2.1.1. Scattering Techniques
    - 2.1.1.1. Light Scattering
    - 2.1.1.2. Electrophoretic Light Scattering
    - 2.1.1.3. Small angle X-ray scattering
    - 2.1.1.4. Small angle neutron scattering
  - 2.1.2. Microscopy Techniques
    - 2.1.2.1. Fluorescence microscopy
    - 2.1.2.2. Electron Microscopy: cryo-TEM
- 2.2. Surface Techniques
  - 2.2.1. QCM-D
  - 2.2.2. Ellipsometry
    - 2.2.2.1. Null Ellipsometry
    - 2.2.2.2. Spectroscopic Ellipsometry
- 2.3. Bioassays
  - 2.3.1. In vitro
  - 2.3.2. In vivo
- 2.4. Techniques used in the papers
- 2.5. References

---

In this section, several techniques of characterization of LLCNPs will be discussed. Different approaches can be employed to investigate on LLCNPs features, depending on the aim and the application of these formulations.

Mainly, the characterization techniques for NPs in nanomedicine can be divided in three categories:

- ◆ **Bulk techniques**, that aim to assess the bulk properties of the aggregates such as size, morphology, structure and colloidal stability;
- ◆ **Surface techniques**, which investigate on the surface of the particles suggesting how they could interact with other kind of surfaces;
- ◆ **Bioassays *in vitro* and *in vivo***, evaluating the biological impact of the NPs on cells, tissues and model animals.

The physico-chemical characterization (bulk + surface) requires the employment of several techniques. The most common used in investigating on LLCNPs are scattering and microscopy

methods. Spectroscopies such as nuclear magnetic resonance (NMR), UV-Vis, Fluorescence, Raman, Fourier transform infrared (FT-IR) can improve the knowledge of the local structure or the orientation of specific molecules in the lipid bilayer.

The figures obtained by bulk and surface characterization can give a hint on the possible biological impact of the aggregates *in vitro* or *in vivo*. Indeed, the correlation between all these complementary techniques is crucial to develop the most efficient formulation for drug delivery or imaging purposes.

## 2.1. Bulk Techniques

### 2.1.1. Scattering Techniques

Scattering techniques represent the major tool to investigate on NPs' structure, size, charge and molecular dynamics. They have been widely used in literature to characterize several systems such as polymers, liquid crystalline phases and hard matter-based, both as bulk phased or colloidal dispersions.[1,2]

The scattering phenomenon is caused by fluctuations in the medium. Usually these fluctuations are associated with variations in the density of scattering materials within the medium, i.e. a colloidal particle scatters light when it has a different refractive index from the liquid it is dispersed in.

Basically, three different scattering experiments can be employed, each one giving different information. Measuring the angle-dependence of the average scattered intensity (**static light experiments**) yields structural information. In dilute systems, size, shape and mass of the individual particles and the arrangement of the material within them can be unveiled, while in a concentrated system, information about the average spatial arrangement of the particles in the sample can be obtained. If the absolute magnitude of the scattered intensity is reported, the experiment can also provide information on the mass or molecular weight of the scattering objects. In a second set-up (**dynamic light experiments**), the dynamics of the sample are related to the analysis of time-dependence of fluctuations in the scattered radiation. In this way, the experiment tells us how particles are moving in Brownian motion and how their configuration fluctuates with time.

All scattering techniques share the main physical principle: an incident light beam (visible light, X-rays or neutrons) collides on the sample or scattering medium. Part of the beam is transmitted unaffected; part is absorbed, and the remaining is scattered by the sample. The wavelength of the radiation should be selected in order to minimize the absorption from the sample. Fig. 2.1 shows the basic principle of a scattering experiment.

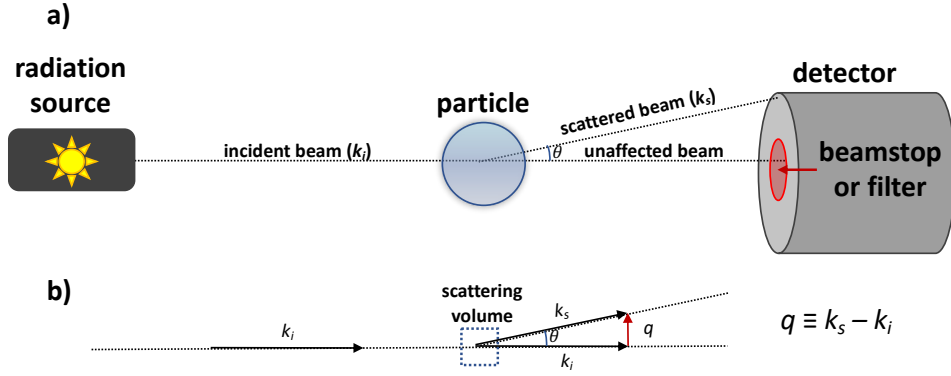


**Figure 2.1.** a) Set-up of a scattering experiment. b) Physical consideration regarding the scattering vector,  $q$ .

The scattering intensity is detected by a vector at a chosen scattering angle,  $\theta$ , which is the angle between the wave vector of the incident beam,  $\vec{k}_i$ , and that of the scattered beam,  $\vec{k}_s$ . The modulus of the scattering vector,  $q$ , can be obtained from equation 2.1:

$$q = |\vec{q}| = \frac{4\pi \sin\left(\frac{\theta}{2}\right)}{\lambda} \quad \text{Eq. 2.1}$$

where  $\lambda$  is the wavelength of the incident beam and, depending on its magnitude, different length scales within the sample can be studied.

In order to investigate on the desired length scale, there should be a contrast variation between the medium and the sample. This contrast originates from the difference in density of the scattering particles in the medium. As the radiation influences its interaction with the sample, the contrast term differs from one scattering experiment to another. While light scattering is related to variations in dielectric properties (or refractive index), X-rays and neutrons scatterings are associated with electrons and nuclei, respectively. Indeed, each type of radiation has its own advantages as a probe of soft matter.

### 2.1.1.1. Light Scattering

In a light scattering experiment, the radiation source is a monochromatic plane-polarized laser beam ( $\lambda$  is equal to 632.8 nm in the instrument used for the measurements of this thesis).

When the light passes through the sample, it interacts with the electrons of the atoms in the medium and it induces oscillating dipoles, that acts as a supply for the scattered light. Particles in solutions undergo Brownian motions. As their local concentration fluctuates in

time, the scattered light fluctuates as well. The study of these intensity fluctuations over time is the aim of a dynamic light scattering (DLS) experiment.[3] The technique is also called photon correlation spectroscopy (PCS) or quasi-elastic light scattering (QELS), but in this thesis we the acronym DLS will be used.

In DLS, the normalized time correlation function of the scattered intensity is defined as:

$$g^{(2)}(q, t) \equiv \frac{\langle I(q,0)I(q,t) \rangle}{\langle I(q) \rangle^2} \quad \text{Eq. 2.2}$$

where  $I(q,0)$  and  $I(q,t)$  are the scattered intensity at time 0 and after a delayed time  $t$ , respectively.

Light scattering can be analyzed on the basis of diffraction from point scatterers when the particles in the sample are much smaller than the wavelength ( $d \ll \lambda/20$ ), as defined by the Rayleigh scattering. Depending on the ratio between the sample size and the wavelength, other models such as Rayleigh-Debye-Gans ( $d \gg \lambda/20$ ) and Mie scattering can be used.

The main output of DLS is the value of translational diffusion coefficient of the particles,  $D$ , is defined as:

$$D = \lim_{q \rightarrow 0} \left( \frac{\Gamma}{q^2} \right) \quad \text{Eq. 2.3}$$

where  $\Gamma = \frac{1}{\tau}$  is the relaxation rate.

Then diffusion coefficient at the infinite dilute concentration,  $D_0$ , can be determined by studying how  $D$  varies depending on the concentration of the particles in the sample. After its determination, the Stock-Einstein equation can be used to calculate the hydrodynamic diameter of the particle, defined as the diameter of a hard sphere that diffuse with the same diffusion coefficient of the particle in solution:

$$D_h = \frac{kT}{3\pi\eta_0 D_0} \quad \text{Eq. 2.4}$$

The following parameters are used in the Stock-Einstein equation:  $k$  is the Boltzmann constant ( $1.38064852 \times 10^{-23} \text{ m}^2 \text{ kg s}^{-2} \text{ K}^{-1}$ ),  $\eta_0$  is the viscosity of the medium at the absolute temperature  $T$ . If the dilute regime could affect the self-assembly properties of the system, the apparent



diffusion coefficient  $D$  could be used instead of  $D_0$ , giving an apparent hydrodynamic diameter, influenced by both hydrodynamic and inter-particles interactions.

Indeed, the hydrodynamic diameter does not represent the real diameter of the particle given the approximation of the hard-sphere model. Moreover, water molecules and ions strongly bound to the surface of the particles contribute to the hydrodynamic size of the particle since they affect the fluctuation of the dipoles in solution and they are considered as a part of the particle itself.

### 2.1.1.2. Electrophoretic Light Scattering

Electrophoretic Light Scattering (ELS) measurements provide information about the zeta (or  $\zeta$ ) potential of the formulation to investigate on the colloidal stability.

The colloidal stability of an aggregate is commonly related to the Derjaguin-Landau and Verwey-Overbeek (DLVO) theory. The balance of the electrostatic repulsions and the dispersion attractive forces is the main principle of this theory. The total potential of the system ( $V_T$ ) of two identical spheres in vacuum is given by:

$$V_T = V_{Attraction} + V_{Repulsion} + V_{Sterical} \quad \text{Eq. 2.5}$$

where  $V_{sterical}$  is the sterical potential, crucial in the case of polymers adsorbed at the interface. The main contribution to the attractive forces is represented by London forces (dispersion forces) and its expression can be obtained from equation 2.6:

$$V_{Attraction} = -\frac{aA}{(12H)} \quad \text{Eq. 2.6}$$

where  $a$  is the particle radius,  $A$  the Hamaker constant and  $H$  the interparticle distance. The repulsive term,  $V_{repulsion}$ , can be formulated through two different equations:

$$V_{Repulsion,1} = \Psi = \Psi_0 \cdot e^{(-\kappa H)} \quad \text{Eq. 2.7}$$

$$V_{Repulsion,2} = \Psi = \Psi_0 \cdot \frac{a}{r} \cdot e^{[-\kappa(r-a)]} \quad \text{Eq. 2.8}$$

where  $\Psi_0$  is the surface potential,  $1/\kappa$  is the Debye length,  $a$  the particle radius and  $(r-a)$  the distance from the charged surface.

The ionic environment in proximity to a charged surface can be described using the double layer model. Fig. 2.2 reports a scheme for a particle dispersed in a medium.

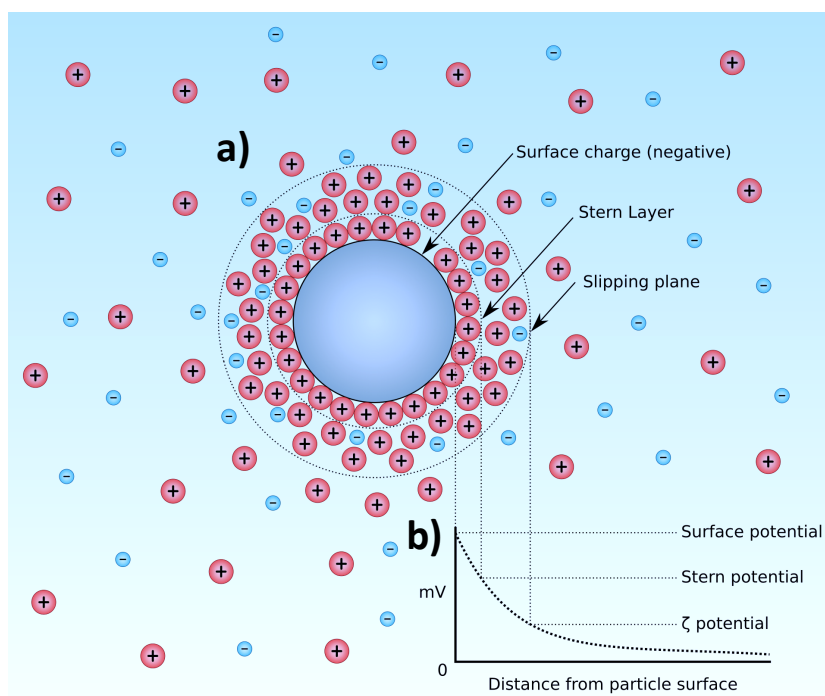


**Figure 2.2.** a) Graphical representation of the electric double layer surrounding a particle in solution. b) Trend of the potential calculated on the surface of the particle as a function of the distance from the particle surface.

The charged surface of the particle affects the ion distribution in the interfacial region. This phenomenon leads to an increased concentration of counter ions close to the surface to the particle, thus to an electrical double layer.

The liquid layer surrounding the object in solution has two regions. The first one, the Stern layer, present ions strongly bound to the surface of the particle, whereas the Guy-Chapman layer is an outer and diffuse region where the ions are less firmly bound. Within the latter layer, a notional boundary in which the ions and the particles form a stable entity can be identified, called hydrodynamic shear or slipping plane. The potential measured at the slipping plane is known as  $\zeta$  (zeta) potential. Its magnitude gives an indication on the stability of the colloidal system in study. Fig. 2.3 summarizes the stability range of a nanoparticle in relation to its  $\zeta$  potential.

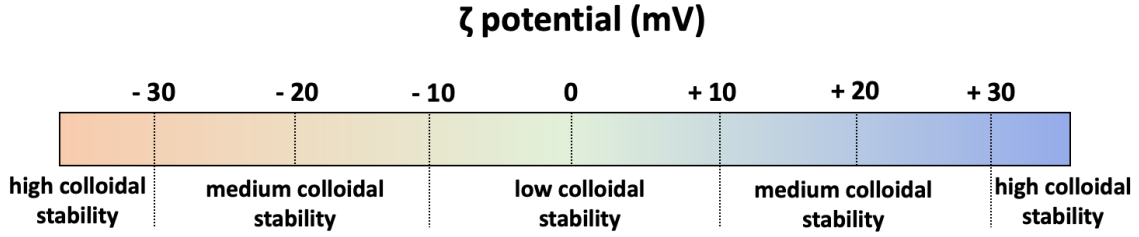


**Figure 2.3.** Empirical stability range related to  $\zeta$  potential measurements on a colloidal dispersion.

High values of  $\zeta$  potentials imply that the nanoparticles will repel each other, hence they will not flocculate. On the other hand, low figures of this parameter entail the instability of the system.

Zeta potential can be obtained indirectly by performing Electrophoretic Mobility (**EM**) measurements.

Charged particles are attracted towards the electrode of opposite charge, but viscous forces tend to oppose to this movement. When equilibrium between these two opposite forces is reached, the particle will move with constant velocity, the Electrophoretic Mobility, given by the Henry equation:

$$\mu_E = \frac{[\varepsilon \cdot \zeta \cdot f(\kappa a)]}{1.5 \cdot \eta} \quad \text{Eq. 2.9}$$

where  $\varepsilon$  and  $\eta$  are the dielectric constant and the viscosity of the medium, respectively,  $\zeta$  is the zeta potential, and  $f(\kappa a)$  the Henry's function.

The shape of the double layer for curved surfaces can be described in terms of the dimensionless term  $\kappa a$ , the ratio between the radius of curvature and the double layer thickness. When a spherical particle can be treated as a point charged in an unperturbed electric field, but the particle is large enough for Stokes' law to apply,  $\kappa a$  is small and  $f(\kappa a) = 1$ , called Huckel's approximation.

The  $\zeta$  potential measurements shown in this thesis are obtained from the Smoluchowski's approximation, implying that the double layer is flat,  $\kappa a$  is large and  $f(\kappa a) = 1.5$ .

### 2.1.1.3. Small Angle X-ray Scattering

Small angle X-ray scattering (SAXS) represents the most powerful tool to investigate on the local ordering and structure of colloidal systems in the length scale 1 – 300 nm.[1] The angle is typically less than 5°, in contrast with wide angle X-ray scattering where it is larger than this value.

The source of the analytical radiation is an X-rays lamp: electrons are generated on the cathode (usually a W filament) and then they are accelerated towards the anode (the metal target). When reaching certain critical energies, an electron on the K-shell of the anode is excited, causing another electron from the outer shell to jump filling the void. This phenomenon leads to a high intensity radiation (X-rays) with a defined wavelength related to the metal target. Indeed, the Cu-K $\alpha$  is the most common wavelength adopted in SAXS experiments.

In the last decades, the synchrotron radiation has been exploited as a source in SAXS experiments. The high intensity X-rays produced by a synchrotron provide mainly two chief benefits over lab-based instruments. The high intensity allows to perform measurements at a greater sample-to-detector distance, hence giving access to a wider range of length scales than a lab instrument. Indeed, the measurements using a synchrotron source are faster given the higher intensity, allowing structural investigation *in situ* and the study of kinetic processes, such as ordering and alignment in liquid crystalline materials or microstructural changes.

For the development and the design of the experiments herein reported, a conventional Cu-K $\alpha$  source was used.

If the objects under investigation have a highly ordered and periodic arrangement, sharp and defined peaks are observed due to constructive interferences between the radiation and the electron cloud of the samples.

As the Bragg condition (eq 2.10) is fulfilled, these peaks (known as Bragg peaks) appear in the pattern:

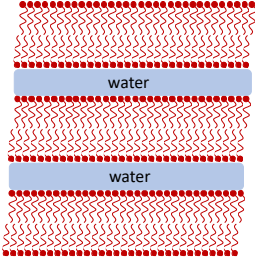
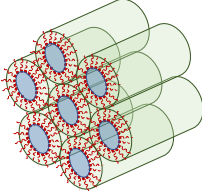
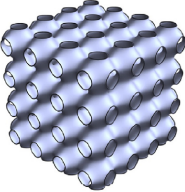
$$n\lambda = 2d \sin\left(\frac{\theta}{2}\right) \quad \text{Eq. 2.10}$$

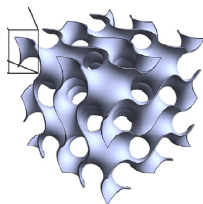
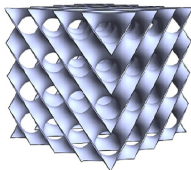
where  $n$  is an integer,  $\lambda$  the radiation wavelength,  $d$  the distance between the crystalline planes identified by Miller indices and  $\theta$  the scattering angle.

Lipids self-assembly can be studied by means of SAXS and SANS since Bragg peaks related to long-range order are detected.

The ratios between the peaks positions in the q scale determines the LLC structure. In Table 2.1, the most common structures are reported.

**Table 2.1.** Summary of the most common LLC phases for lipid-based formulations. The equations allow to calculate the lattice parameters of the elementary cell, given the Miller's indices ( $hkl$ ). The representations of the inverse bicontinuous cubic phases are taken from reference [4].

LLC phase	Lattice dimension	Lattice parameter ( $a$ ) and water channel radius ( $r_w$ )	Miller's indices ( $hkl$ )
<u>Lamellar</u> ( $L_\alpha$ ) 	1D ( $k, l = 0$ )	$a = h \cdot d$	100
			200
			300
			400
			500
			600
<u>Inverse Hexagonal</u> ( $H_{II}$ ) 	2D ( $l = 0$ )	$a = \frac{2}{\sqrt{3}} \cdot d \cdot \sqrt{h^2 + k^2 + hk}$ $r_w = a \sqrt{(1 - \phi)} \cdot \left(\frac{\sqrt{3}}{2}\right)^{\frac{1}{2}}$	100
			110
			200
			210
			220
			300
<u>Inverse Bicontinuous</u> <u>Cubic</u> $Im3m$ (primitive, $Q^{223}$ ) 	3D	$a = d \cdot \sqrt{h^2 + k^2 + l^2}$ $r_w = a \cdot \left(\frac{A_0}{-2\pi\chi}\right)^{\frac{1}{2}} - l$	$Im3m$
			110
			200
			211
			220
			310
			222
			$Ia3d$

<i>Ia3d</i> (gyroid, $Q^{230}$ )	211
	220
	321
	400
	420
	332
<i>Pn3m</i> (double-diamond, $Q^{224}$ )	<i>Pn3m</i>
	110
	111
	200
	211
	220
	221

The parameter  $\phi$  is called volume fraction or lipid fraction and can be obtained from:

$$\phi = \left( \frac{\frac{w_{lip}}{\rho_{lip}}}{\frac{w_{lip}}{\rho_{lip}} + \frac{w_{solv}}{\rho_{solv}}} \right) \quad \text{Eq. 2.11}$$

where  $w_{lip}$ ,  $\rho_{lip}$ ,  $w_{solv}$  and  $\rho_{solv}$  are the weight and the density of the lipid and the solvent, respectively.

The water channel radius formula for the bicontinuous cubic phases exhibit the Euler-Poincaré characteristic,  $\chi$ , and the ratio of the minimal surfaces in a unit cell,  $A_0$ , which differ among the cubic mesophases (Table 2.2)

**Table 2.2.** Values of the Euler-Poincaré characteristic and the ratio of the minimal surfaces for the cubic phases *Pn3m*, *Im3m* and *Ia3d*.

Cubic Phase	Minimal Surface	$\chi$	$A_0$
<i>Pn3m</i>	D	-2	1.919
<i>Im3m</i>	P	-4	2.345
<i>Ia3d</i>	G	-8	3.091

#### 2.1.1.4. Small Angle Neutron Scattering

During a small ange neutron scattering (SANS) measurement, the neutron beam interacts with the nuclei of the atoms in the sample. SANS is an isotope-sensitive technique, since the scattering contrast is given by the neutrons and the protons that form the nuclei.

The neutron scattering length,  $b$ , describes the scattering from each nucleus and, as mentioned above, it can be quite different when comparing isotopes. The averaged scattering length density of a material (SLD) can be calculated from eq. 2.12 using the neutron scattering length from each element in the material.

$$\rho = \sum_i \frac{b_i}{V} \quad \text{Eq. 2.12}$$

where  $b_i$  represents the coherent scattering length of each nuclei  $i$  in a given volume  $V$ .

The scattering intensity is correlated with the SLD, therefore variations in the SLD of the sample and the surrounding media yields scattering intensity changes. This figure underlines the potency of SANS: by replacing  $H^1$  with  $H^2$ , the technique allows to obtain different structural information. This contrast variation represents the most common approach to create or vary the contrast of the sample or in parts of it.

### 2.1.2. Microscopy techniques

The microscopy techniques provide *in situ*, non-destructive and non-invasive measurements.

#### 2.1.2.1. Fluorescence microscopy

It is an optical imaging technique which allows for the excitation of fluorophores. The emitted photons are detected by a camera or a photomultiplier tube, creating an intensity dependent grey scale image.[5]

Fluorescence microscopy is a highly sensitive and reliable method to investigate on dynamic processes in cells, or cell membranes. Several microscopies fluorescence-based exist allowing for a wide range of image resolution and extracted information. Conventional techniques such as confocal or epifluorescence microscopy can resolve structures to a maximum of 200 nm, whereas super-resolution methods can distinguish down to 20 nm. Indeed, the latter techniques are characterized by some drawbacks, i.e. slow image acquisition or the occurrence of phototoxicity.

### 2.1.2.2. Electron microscopy: Cryo-TEM

The image resolution in a microscopy experiment is limited by the wavelength of the light in use. Therefore, to provide real-space images of three-dimensional objects at the nanoscale, electrons should be employed. Electron microscopy provides structural information with resolution in the nanoscale and is thus applied to image soft matter. There are two main classes of electron microscopy: scanning electron microscopy (**SEM**) and transmission electron microscopy (**TEM**). SEM images the exterior of an object, scanning across it and knocking secondary electrons out of its surface. Indeed, SEM can be considered a surface technique as well, since it can provide a rough estimation on the superficial roughness of the sample.

TEM is a well-known technique for imaging solid material at atomic resolutions. The main information acquired by a TEM measurement is the morphology of the sample, while structural information can be obtained using a high-resolution set-up.

Similar to an optical microscope, the radiation (high energy electrons) are focused on electromagnetic lenses, and it collides on an electron-transparent sample. The image acquired is then projected on a fluorescent screen or a CCD camera.

Both TEM and SEM are restricted to “dry” materials, since the high vacuum in the microscope is a requirement to maintain the electron beam focused.

Cryogenic TEM (**cryo-TEM**), a microscopy variant of TEM in which the sample is vitrified prior to the measurements, represents a powerful tool to investigate on both the structure and the morphology of soft matter-based systems.

Chemical treatments such fixation, dehydration or resin embedding may cause artifacts. Cryo-TEM avoids these procedures and it employs vitrification as preparation method. James Dubochet developed this method[6–8] for freezing water-based samples so rapidly that the water forms a disordered glass state, rather than crystalline ice.

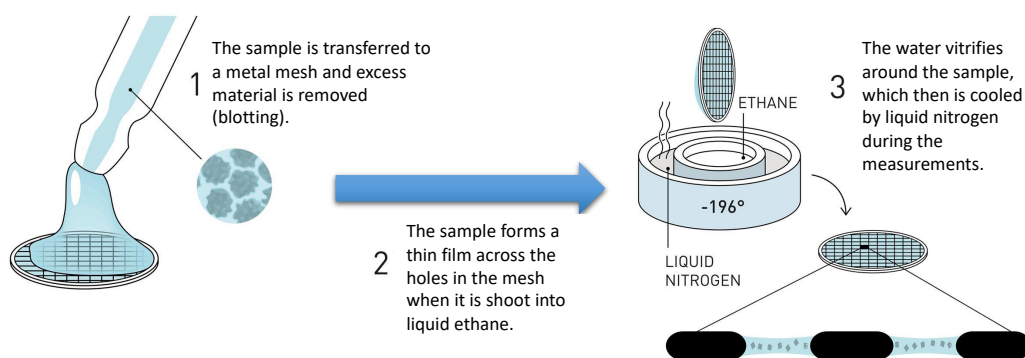




**Figure 2.4.** Vitrification method proposed by James Dubochet. Copyright from JOHAN JARNESTAD/THE ROYAL SWEDISH ACADEMY OF SCIENCES.

During the vitrification process, the sample is deposited on a grid, immersed quickly into liquid ethane ( $-190\text{ }^{\circ}\text{C}$ ) and then stored into liquid nitrogen prior to any measurements. The fast cooling rate does not permit to the water molecules in the sample to crystallize into ice, but only to vitrify. Otherwise, ice crystals would strongly diffract the microscope's electron beam, obscuring any information about the supramolecular aggregates. The relative humidity and the temperature of the deposition of the samples can be accurately controlled in a preparation chamber.

Despite cryo-TEM is adopted to study the morphology, the size and size distribution of the aggregates, fast Fourier transforms of cryo-TEM images can be used to determine precisely the interplanar distances and angles between crystallographic planes, giving structural information as in SAXS measurements.

## 2.2. Surface Techniques

Unveiling how NPs interacts with cells requires knowledge of their surface properties. These features can be investigated via interaction with model or complex surfaces characterized by hydrophilic, hydrophobic or amphiphilic properties.

### 2.2.1. QCM-D

Quartz crystal microbalance with dissipation (**QCM-D**) gives information about the interfacial wet mass adsorbed on a surface, its viscoelastic properties and the kinetics of adsorption. In a typical experiment, an alternating voltage is applied at a specific frequency to make a quartz crystal oscillate at its resonance frequency.[10,11] When a molecule is bound or adsorbed to the crystal surface, a decrease in the resonance frequency ( $\Delta f$ ) is detected.

As some conformational variations occur at the interface without changing the adsorbed amount (same  $\Delta f$ ), the energy loss in the system when the voltage is switched off can be detected. Therefore, QCM can be coupled with a dissipation ( $\Delta D$ ) unit that measures this energy loss. When the shift in dissipation is low ( $< 1 - 1.5\text{ ppm}$ ), the film adsorbed on the crystal is rigid and the adsorbed mass is linearly correlated to the shift in frequency. This phenomenon is summed up in the Sauerbrey Model (equation 2.17):[12]

$$\Delta m = -\frac{C}{n} \cdot \Delta f \quad \text{Eq. 2.19}$$

where  $C$  is a proportionality constant (for a 5 MHz crystal it is equal to  $-17.7 \text{ ng s cm}^{-2}$ ) and  $n$  is the overtone number.

When the dissipations exceed 1 – 1.5 ppm, the Sauerbrey equation is not valid and the Voigt viscoelastic model can be exploited. The analysis of the QCM data with this model take into account a frequency-dependence of the QCM response and hence additional energy dissipations are induced.

The contribution of coupled water and the solvent used into the adsorbed film is added to produce a complex shear modulus ( $G$ ) according to:

$$G = G' + iG'' = \mu_f + i2\pi f\eta_f = \mu_f(1 + i2\pi f\tau_f) \quad \text{Eq. 2.20}$$

where  $\mu_f$  is the elastic shear modulus,  $\eta_f$  the shear viscosity,  $f$  the oscillation frequency,  $\alpha\nu\delta$   $\tau_f$  the characteristic relaxation time of the film.

The frequency and dissipation variations are then correlated to the viscoelastic properties of the film as

$$\Delta f = \frac{\text{Im}(\beta)}{2\pi t_q \rho_q} \quad \text{Eq. 2.21}$$

and

$$\Delta D = -\frac{\text{Re}(\beta)}{\pi f t_q \rho_q} \quad \text{Eq. 2.22}$$

where  $t_q$  and  $\rho_q$  are the thickness and density of the quartz crystal, respectively;  $\beta$  relies on the thickness ( $t$ ) and the density ( $\rho$ ) of the film and on the bulk-liquid density ( $0.997 \text{ g cm}^{-3}$ ) and viscosity ( $0.9 \text{ mPa s}$ ).

### 2.2.2. Ellipsometry

Ellipsometry (EP) is a non-destructive technique based on the analysis of polarization changes caused by reflection of light and it allows detailed optical and microstructural characterization of surfaces, thin films, and multilayers.[13,14] As photons are used as radiation probe, a

vacuum ambient is not needed. Therefore, the technique can be used directly at a solid-liquid interface.

The basic quantity measured is the complex reflectance ratio, defined as:

$$\rho = \frac{R_p}{R_s} \quad \text{Eq. 2.23}$$

where  $R_p$  and  $R_s$  are the reflection coefficients for the polarized light parallel (p) and perpendicular (s) to the plane of incidence, respectively. Usually,  $\rho$  is written in complex polar form:

$$\rho = \tan\psi \cdot e^{(i\Delta)} \quad \text{Eq. 2.24}$$

where  $i = \sqrt{-1}$ . The two parameters  $\psi$  and  $\Delta$  represent the ellipsometric angles and they are experimentally determined during an EP experiment.

The measurement is performed using an ellipsometer, a system capable of determining the complex reflection ratio  $\rho$ .

The components are arranged in an optical path so that the light emerging from the polarization generator is reflected at the sample surface and then it enters into the polarization state detector. Ellipsometer systems can be classified in null (or compensating) and photometric (or non-compensating) ellipsometers.

### 2.2.2.1. Null Ellipsometry

In a null ellipsometry experiment, the polarization changes due to the reflection at the sample surface is compensated by the optical components in the instrument to achieve extinction at the detector. The compensation is obtained by adjusting their azimuths, phase retardation or other parameters. The readings of these terms at “null condition” constitute the experimental data, which in most configurations have simple relations to  $\psi$  or  $\Delta$ .

The classical null ellipsometer type is the so-called polarizer-compensator-sample-analyzer (PCSA) system. The light source is often a HeNe laser (633 nm) or a mercury lamp coupled with a filter to transmit the intense emission line at 546 nm. In the latter case a collimating lens system is included in the optical path. The collimated beam is made linearly polarized. Then the beam passes through a compensator, a quarter-wave plate that induces a phase shift in the beam. After being reflected at the sample’s surface and hence causing an additional phase shift,

the light passes through the analyzer. Finally, a detector measures the transmitted intensity through the whole system.

The main operation in this system is to adjust the optical components so that the light is extinguished at the detector. This task can be achieved only if the light is linearly polarized before the analyzer. The polarizer-compensator combination generates an elliptically polarized light, and the reflection from the sample must compensate for the phase difference between the components of the beam to generate linearly polarized light. The following relations are then valid for the beam after its path through the system:

$$\psi = 180^\circ - A' \quad \text{Eq. 2.25}$$

$$\Delta = 2P' - 90^\circ \quad \text{Eq. 2.26}$$

In modern instrument design, the polarizer and the analyzer are computer controlled with stepping motors and an automatic search algorithm is used to find the intensity minimum. The compensator is a monochromatic device; hence a null EP-meter is not suited for spectroscopic measurements but only for single-wavelength measurements. On the other hand, null EP relies on robustness, simplicity of use and high precision as advantages.

### 2.2.2.2. Spectroscopic Ellipsometry

In a photometric EP instrument, the state of polarization before reflection is normally predetermined and after reflection it is measured by analyzing the intensity variation recorded by the detector as a function of azimuth, retardation of one of several parameters of the optical components in the optical path.[15] Usually, the measured quantities in a photometric ellipsometer are  $\tan \psi$  and  $\cos \Delta$ .

The rotating-analyzer-ellipsometer (RAE) is the basic spectroscopic ellipsometer system. It requires a computer for its basic operations. In the RAE configuration, the radiation is emitted by a white light source, such as a Xe lamp (typical wavelength of 190 – 1000 nm). The monochromatic light is polarized with a polarizer and reflected at the sample surface. After reflection, the light is elliptically polarized and hence it cannot be extinguished with a polarizer. The state of polarization of the reflected beam is measured by using a rotating analyzer located between the sample and the detector. Only the component of the polarization ellipse of the reflected wave parallel to the transmission axis of the analyzer passes, but the whole

polarization ellipse is traced as the analyzer is rotating. If the analyzer prism rotates at a constant speed, the output signal is ideally sinusoidal with the minimum and the maximum corresponding to the minor and major axis, respectively, of the polarization ellipse. The signal,  $I$ , versus the time  $t$  can be expressed as:

$$I = I_0[1 + \hat{\alpha}\cos 2A(t) + \hat{\beta}\sin 2A(t)] \quad \text{Eq. 2.27}$$

where  $I_0$  is the average intensity,  $\hat{\alpha}$  and  $\hat{\beta}$  are the normalized Fourier coefficients of the signal and  $A(t)$  is the angular position of the rotating analyzer. The ellipsometric angles  $\Delta$  and  $\psi$  (and thereby the complex reflectance ratio,  $\rho$ ) can be determined from  $\hat{\alpha}$  and  $\hat{\beta}$ , if the polarization of the incident beam is known. The relations can be written as:

$$\tan \psi = \tan P \sqrt{\frac{1+\hat{\alpha}}{1-\hat{\alpha}}} \quad \text{Eq. 2.28}$$

$$\cos \Delta = \frac{\hat{\beta}}{\sqrt{1-\hat{\alpha}^2}} \quad \text{Eq. 2.29}$$

The polarization of the incident beam is controlled by a polarizer with azimuth  $P$ . The polarizer can be followed by an optional compensator, not common for spectroscopic EP since it is a chromatic device.

The polarizer can be fixed at  $P = 45^\circ$  to ensure equal intensity in the directions of the sample. A complete automatic RAE system requires an electronic detection device capable of monitoring the output signal and a computer overhead to control the light wavelength and the azimuths of the two polarizers.

### 2.3. Bioassays and biological characterization

Given that LLCNPs found application mostly in the nanomedicine and pharmaceutical field, a biological characterization of these aggregates is mandatory in order to evaluate their efficacy as drug carriers. Indeed, the phenomena observed in an *in vitro* or *in vivo* test need to be correlated with the results of the physico-chemical characterization (bulk and surface). Several papers have shown that NPs' size, zeta potential, polydispersity and, of course, components

can induce a cytotoxic effect in/on the cell environment.[16–18] Depending on the biological sample (cell/tissue or model animal), these studies can be divided into *in vitro* and *in vivo*.

### 2.3.1. *In vitro* studies

*In vitro* experiments provide an initial cost-effective assessment of the toxicity and efficacy of a nanomaterial-based therapeutic and inform the design of animal studies. Moreover, they also enable the elucidation of biochemical mechanism, under controlled conditions not achievable by *in vivo* tests. Indeed, the fewer variables and amplified reactions of these assays generally make their results more interpretable than their complementary *in vivo* experiments.

Several parameters can be observed, depending on the application of the formulations.

- ◆ **Biocompatibility**. One measure of NPs' biocompatibility is their effect on adherent cell lines. Cell viability is assessed by employing methods based on different phenomena, such as the loss of membrane integrity (tripan-blue test), loss of metabolic activity (MTT test), loss of monolayer adherence or monitor progression through the cell cycle (DNA staining techniques and Flow Cytometry).
- ◆ **Hemolysis**. The NPs administrated in the systemic circulation will interact with the blood components. The building block of the formulation may induce a cytotoxic effect on red blood cells (RBCs), provoking the hemoglobin release. This phenomenon called hemolysis can lead to life-threatening conditions such as hemolytic anemia, jaundice and renal failure.
- ◆ **Complement activation**. The complement system consists of more than 30 proteins. Some are present as soluble in the blood or as membrane-associated proteins. Its activation leads to the so-called complement activation pathways (alternative, classical and lectin as shown in Fig. 2.6), a sequential cascade of enzymatic reactions resulting in the formation of the anaphylatoxins C3a and C5a. All the pathways converge at the formation of the protein C3, the most abundant found in the blood, and afterwards the formation of its activation products. These cytotoxins are responsible of a large plethora of physiological responses from chemoattraction to apoptosis. Indeed, NPs' surface chemistry plays a huge role in activating the complement: recent papers have shown that the hydrophilicity of the surface is the key element.[16,19]

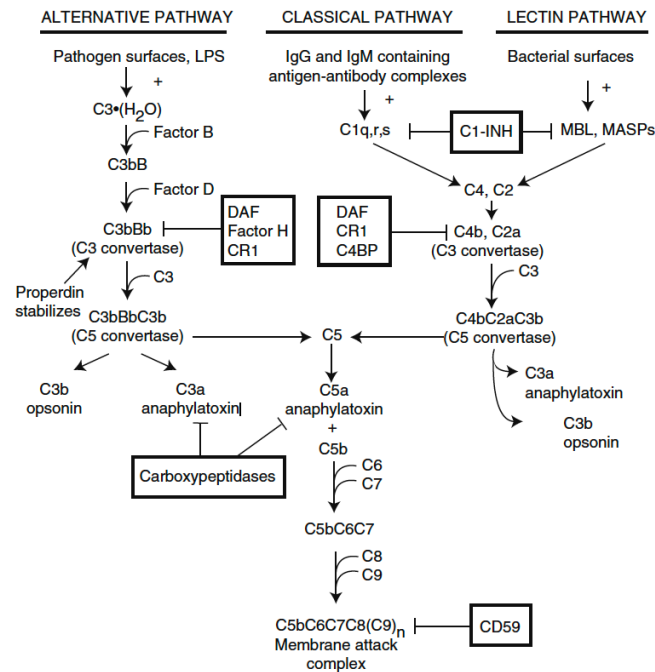


**Figure 2.5.** The three different pathways of complement system activation: alternative, classical and lectin. Reproduced with permission from reference [20].

- ◆ **Permeation and penetration tests.** The applicability of a formulation for topical administration can be evaluated by permeation test on skin or a model membrane. These experiments can provide information about the amount of drug permeated through the different layers of the skin and how the contact time of the formulation on the skin can influence its applications. The penetration and permeation tests are usually performed in diffusion cells, such as vertical Franz cells. The skin (or a synthetic membrane) is put between a donor and a receptor compartment. The formulation is deposited on the side of the skin exposed in the donor compartment whereas the receptor units is filled with a biological fluid or a physiological solution (i.e. normal saline or PBS buffer pH 7.4). Withdrawals at selective times allow to determine quantitatively the amount of drug penetrated through the skin. The skin layers can be separated at the end of the experiment in order to evaluate the amount of drug accumulated in the stratum corneum, epidermis or dermis.

### 2.3.2. *In vivo* studies

Although *in vitro* models can give an initial estimate of a formulation toxicity, the complex biological interplay found *in vivo* cannot be matched. The information gained from bulk,

surface and *in vitro* characterizations of a formulation allow to describe a model, that still need to be corroborated in real physiological conditions. Therefore, *in vivo* experiments can provide the full insight on the effect of LLCNPs after administration. The biodistribution (mostly through imaging) and the toxicity, the main two parameters, are characterize in animal models. The FDA offers guidelines for *in vivo* studies:[21,22] historically, the effects of a formulation have been evaluated on organs and the immune system. However, in the last decades, hematology, clinical chemistry, gross pathology and histology are recommended.

## 2.4. Techniques employed in the papers

Throughout my PhD, I had the possibility to work on several techniques to investigate on LLCNPs features. The following techniques have been employed in each study:

### Chapter 3: *Effect of stabilizers on cubosomes for systemic administration*

**Paper I:** DLS, ELS, SAXS, cryo-TEM, MTT test, *in vitro* cell viability;

**Paper II:** DLS, ELS, SAXS, cryo-TEM, AFM;

**Paper III:** DLS, ELS, cryo-TEM, MTT test, confocal microscopy, *in vitro* hemolysis, *in vitro* complement activation.

### Chapter 4: *Topical administration of LLCNPs*

**Paper IV:** DLS, ELS, SAXS, *in vitro* permeation tests;

**Paper V:** DLS, ELS, SAXS, cryo-TEM, *in vitro* permeation tests.

### Chapter 5: *Bio-inspired vesicles for imaging applications*

**Paper VI:** DLS, ELS, stability test, cryo-TEM, fluorescence microscopy.



## 2.5. References

- [1] O. Glatter, R. May, Small-angle techniques, in: *Int. Tables Crystallogr.*, 2006. <https://doi.org/10.1107/97809553602060000581>.
- [2] L. Cipelletti, V. Trappe, D.J. Pine, Scattering techniques, in: *Fluids, Colloids Soft Mater. An Introd. to Soft Matter Phys.*, 2018. <https://doi.org/10.1002/9781119220510.ch8>.
- [3] R. Pecora, Dynamic light scattering measurement of nanometer particles in liquids, *J. Nanoparticle Res.* (2000). <https://doi.org/10.1023/A:1010067107182>.
- [4] S. Murgia, S. Biffi, R. Mezzenga, Recent advances of non-lamellar lyotropic liquid crystalline nanoparticles in nanomedicine, *Curr. Opin. Colloid Interface Sci.* 48 (2020) 28–39. <https://doi.org/10.1016/j.cocis.2020.03.006>.
- [5] A. Diaspro, P. Bianchini, F. Cella Zanacchi, L. Lanzaò, G. Vicidomini, M. Oneto, L. Pesce, I. Cainero, Fluorescence microscopy, in: *Springer Handbooks*, 2019. [https://doi.org/10.1007/978-3-030-00069-1\\_21](https://doi.org/10.1007/978-3-030-00069-1_21).
- [6] M. Adrian, J. Dubochet, J. Lepault, A.W. McDowell, Cryo-electron microscopy of viruses, *Nature.* (1984). <https://doi.org/10.1038/308032a0>.
- [7] J. Dubochet, J. Lepault, CRYO-ELECTRON MICROSCOPY OF VITRIFIED WATER, *Le J. Phys. Colloq.* (1984). <https://doi.org/10.1051/jphyscol:1984709>.
- [8] E. Knappek, J. Dubochet, Beam damage to organic material is considerably reduced in cryo-electron microscopy, *J. Mol. Biol.* (1980). [https://doi.org/10.1016/0022-2836\(80\)90382-4](https://doi.org/10.1016/0022-2836(80)90382-4).
- [9] S.S. Bair, Rheology, in: *Handb. Lubr. Tribol. Vol. II Theory Des. Second Ed.*, 2012. <https://doi.org/10.1201/b12265>.
- [10] B. Zhang, Q. Wang, Quartz Crystal Microbalance with Dissipation, in: *Nanotechnol. Res. Methods Foods Bioprod.*, 2012. <https://doi.org/10.1002/9781118229347.ch10>.
- [11] Q. Chen, S. Xu, Q. Liu, J. Masliyah, Z. Xu, QCM-D study of nanoparticle interactions, *Adv. Colloid Interface Sci.* (2016). <https://doi.org/10.1016/j.cis.2015.10.004>.
- [12] C.K. O’Sullivan, G.G. Guilbault, Commercial quartz crystal microbalances - Theory and applications, *Biosens. Bioelectron.* (1999). [https://doi.org/10.1016/S0956-5663\(99\)00040-8](https://doi.org/10.1016/S0956-5663(99)00040-8).
- [13] H.G. Tompkins, E.A. Irene, *Handbook of Ellipsometry*, 2005. <https://doi.org/10.1515/arh-2005-0022>.
- [14] H. Fujiwara, Ellipsometry, in: *Handb. Opt. Metrol. Princ. Appl. Second Ed.*, 2015. <https://doi.org/10.4011/shikizai1937.79.217>.
- [15] R. Pascu, M. Dinescu, Spectroscopic ellipsometry, *Rom. Reports Phys.* (2012). [https://doi.org/10.1007/978-981-10-6156-1\\_100](https://doi.org/10.1007/978-981-10-6156-1_100).
- [16] V. Francia, K. Yang, S. Deville, C. Reker-Smit, I. Nelissen, A. Salvati, Corona Composition Can Affect the Mechanisms Cells Use to Internalize Nanoparticles, *ACS Nano.* (2019). <https://doi.org/10.1021/acsnano.9b03824>.
- [17] A. Lesniak, A. Salvati, M.J. Santos-Martinez, M.W. Radomski, K.A. Dawson, C. Åberg, Nanoparticle adhesion to the cell membrane and its effect on nanoparticle uptake efficiency, *J. Am. Chem. Soc.* (2013). <https://doi.org/10.1021/ja309812z>.
- [18] S. Biffi, R. Voltan, E. Rampazzo, L. Prodi, G. Zauli, P. Secchiero, Applications of nanoparticles in

## Chapter 2 – Experimental characterization of LLCNPs

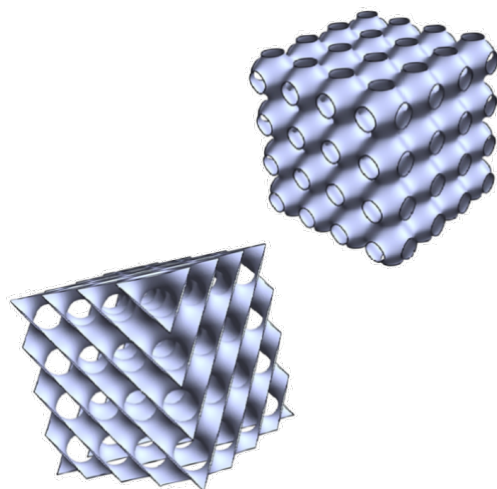
- cancer medicine and beyond: Optical and multimodal in vivo imaging, tissue targeting and drug delivery, *Expert Opin. Drug Deliv.* 12 (2015) 1837–1849.  
<https://doi.org/10.1517/17425247.2015.1071791>.
- [19] M. Fornasier, S. Biffi, B. Bortot, P. Macor, A. Manhart, F.R. Wurm, S. Murgia, Cubosomes stabilized by a polyphosphoester-analog of Pluronic F127 with reduced cytotoxicity, *J. Colloid Interface Sci.* (2020). <https://doi.org/10.1016/j.jcis.2020.07.038>.
- [20] J.V. Sarma, P.A. Ward, The complement system, *Cell Tissue Res.* (2011).  
<https://doi.org/10.1007/s00441-010-1034-0>.
- [21] FDA, Guidance for industry. Drug interaction studies study design, data analysis, implications for dosing, and labeling recommendations, *Guid. Doc.* (2012).
- [22] CDER/FDA, Guidance for Industry, Waiver of in vivo bioavailability and bioequivalence studies for immediate release solid oral dosage forms based on a biopharmaceutics classification system, *Cent. Drug Eval. Res.* (2015).





# 3

## **The effect of stabilizers in cubosomes for systemic administrations**

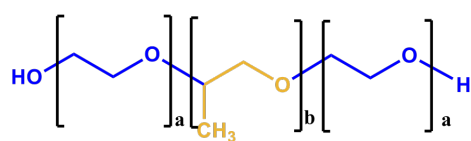


---

### Chapter 3 – Table of contents

- 3.1. Cubosomes functionalized with a photosensitizer for PDT applications
  - 3.2. Hemicellulose as stabilizer for bicontinuous cubic phase dispersions
  - 3.3. Stabilization of cubosomes by a polyphosphoester analog of Pluronic F127
  - 3.4. Surface characterization of PPE-stabilized cubosomes
  - 3.5. Conclusions and future perspectives
  - 3.6. References
- 

To increase the kinetical stability of cubosomes formulations, an amphiphilic stabilizer that adsorbs at the interface is required: it lowers the interfacial free energy between the inverse phase and the bulk water. In this way, the presence of the stabilizer avoids flocculation of the colloidal particles. Several studies report different kind of stabilizer, using bile salts,[1] phospholipids,[2] and protein.[3] However, triblock copolymers such as poloxamers have been historically the first[4] to be adopted to stabilize these non-lamellar aggregates in water. They are formed by poly(ethylene oxide) (PEO) arms (hydrophilic) and an inner poly(propylene oxide) (PPO) body (hydrophobic), as shown in Fig 3.1.



**Pluronic F127: a = 100 and b = 65**

**Pluronic F108: a = 132 and b = 50**

**Figure 3.1.** General molecular structure of poloxamers.

The PEO corona surrounds the nanoparticles providing steric stabilization, whereas the hydrophobic PPO moiety interacts with the lipid bilayer, partially anchoring to it. This kind of non-ionic polymer is widely studied as an emulsifier and as drug carrier.[5,6] The PEO ends can be modified in order to functionalize the poloxamers with fluorescent units or targeting agents. Murgia and Caltagirone investigated the functionalization of both Pluronic F108 and F127 by bounding folic acid and fluorophores, formulating cubosomes and hexosomes suitable for theranostic applications.[7–10] In **Paper I**, a photosensitizer is bound to the PPO units of Pluronic F108 used as a stabilizer to formulate cubosomes suitable for both photodynamic therapy (PDT) and cancer therapy.[11]

The PPO moiety may interact strongly with the lipid bilayer, inducing a phase transition. Indeed, this feature is quite common in GMO-based cubosomes stabilized with Pluronics, which presents both the  $Pn3m$  (the native structure of GMO at the concentration of usage) and  $Im3m$  inverse bicontinuous cubic structures when the dispersion is investigated by means of SAXS. Nakano and collaborators highlighted this phenomenon when the concentration of the poloxamer Pluronic F127 have saturated the cubosomes' surface.[12] This phase transition may impact the diffusion of the drug,[13] thus affecting the efficacy of the treatment. Moreover, one less appealing character of the poloxamers family is that they are not biodegradable *in vivo*[14,15] and they may exert a (low) cytotoxic effect.[16,17] For this reason, **Paper II** and **Paper III**[18] investigated on the effect of two biodegradable stabilizers (hemicellulose and a synthetic polyphosphoester, respectively) for cubosomes suitable for systemic administration.

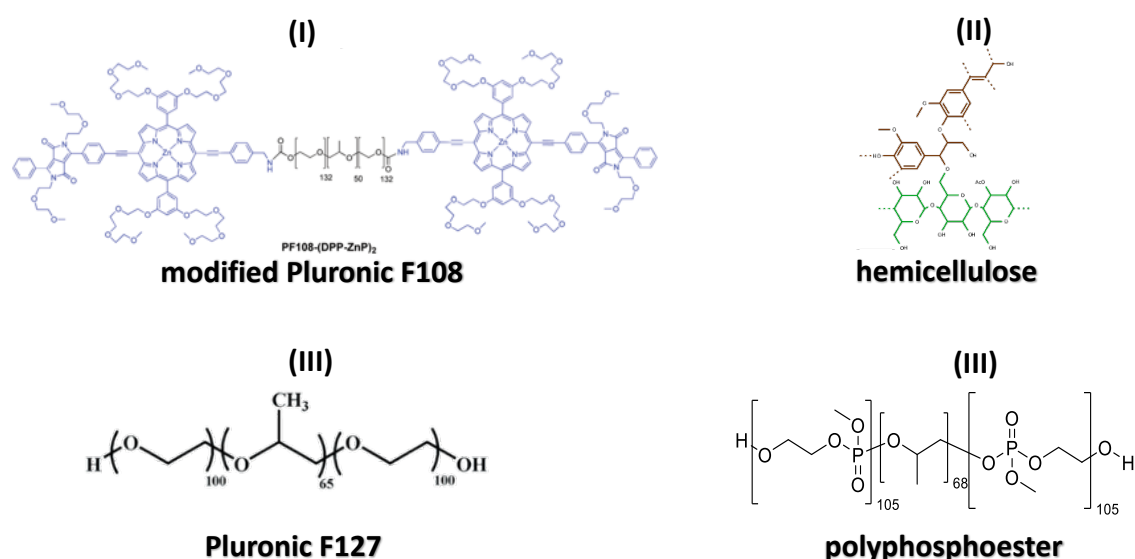


**Figure 3.2.** Molecular structure of the polymeric stabilizers used in the investigations. The Roman numbers symbolize the number of the paper which they were studied in.

### 3.1. Modification of poloxamer Pluronic F108 for application in PDT

PDT has been approved by the US Food and Drug Administration as a systemic therapeutical procedure, given its minimal invasiveness which can be combined with other antitumor treatments.[19] It requires few components to achieve the therapeutical effect: a photosensitizer (PS) molecule, light, oxygen and a target. Briefly, the PS is injected into the bloodstream and it reaches the target; light irradiation (600 – 800 nm) is then applied and the PS absorbs the radiation. After an intersystem crossing process,[19] the SP reaches an excited triple state, transferring its energy to molecular oxygen  $O_2$  and thereby producing highly cytotoxic  $^1O_2$  or radical oxygen species upon interaction with other molecules.[20] The treatment induces direct tumor cell death, microvascular damage and an inflammatory reaction which can lead to the development of systemic immunity.

Tetrapyrrolic macrocycle is the most reported moiety as PS, due to its high absorption peak, no dark toxicity and relatively rapid clearance from healthy tissues.[11,21,22] Therefore, to simultaneously formulate cubosomes with both imaging and therapeutic properties, the antineoplastic drug docetaxel (DTX) was encapsulated within GMO-based cubosomes. In a previous study, the encapsulation of DTX within the cubosomes lipid palisade increased its cytotoxicity by one order of magnitude respect to molecular dispersions of the drug.[8,9] The PS DPP-Zn-NH<sub>2</sub> was covalently linked to Pluronic F108, as shown in the reaction scheme below (Fig. 3.3).

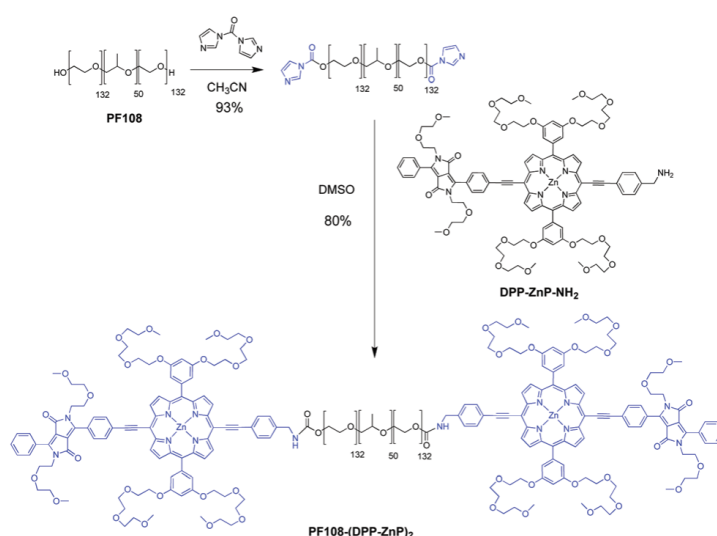


**Figure 3.3.** Functionalization steps of Pluronic F108 with the PS DPP-Zn-NH<sub>2</sub> to give the product PF108-(DPP-ZnP)<sub>2</sub>. Reproduced with permission from **Paper I**. [11]



The cubosomes formulation was obtained by mixing GMO with 40 % of PF108-(DPP-ZnP)<sub>2</sub> and 60 % of classical Pluronic F108. The physico-chemical characterization highlighted the formation of quite monodispersed cubosomes, exhibiting a biphasic *Pn3m* and *Im3m* structure, common feature of poloxamer-stabilized LLCNPs. The functionalization of the Pluronic moiety did not affect significantly the apparent hydrodynamic diameter (159 nm) and the  $\zeta$  potential (ca. – 22 mV) in comparison with a formulation stabilized by Pluronic F108 alone. The encapsulation of DTX within the lipid bilayer of the bicontinuous cubic phase was high (99.5 %), giving 1.1 mM as drug content.

Cytotoxic studies (MTT test) were then conducted on HeLa cells of the formulations loaded with and without DTX. Depending on the dilution ratio, the formulation loaded with DTX became toxic, whereas the PS did not result cytotoxic (Fig. 3.4a).

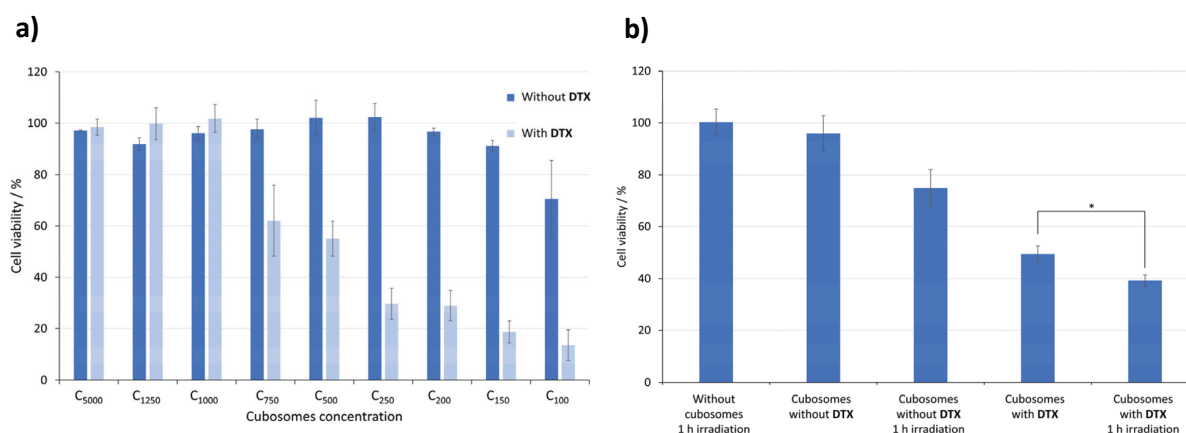


**Figure 3.4.** Effect of the formulations on the cell viability (a) and phototoxicity experiments with a light dose of 130 J cm<sup>-2</sup>. Reproduced with permission from **Paper I.**[11]

On the same cell line, phototoxicity studies induced by monophotonic excitation were performed (Fig. 3.4b). The cubosomes formulation stabilized with PF108-(DPP-ZnP)<sub>2</sub> without the drug did not exerted a cytotoxic effect on HeLa cells. However, upon irradiation, the phototoxicity reached 20 % even though the same light dose in absence of cubosomes did not affect the cell viability. The formulation containing DTX caused an decreased the cell viability to 50 % and upon irradiation the phototoxicity increased at 60 %.

These figures highlighted a possible synergistic effect of PS on DTX activity and the potential of these multifunctional platforms in combined chemo- and photodynamic therapy.

## 3.2. Hemicellulose as stabilizer for bicontinuous cubic phase dispersions

Polysaccharides are molecules of great interest as potential stabilizer for LLCNPs, given their stability of a broad range of temperatures and pH. Various studies reported GMO-based cubosomes stabilized by modified-polysaccharides to increase their hydrophobic character.[23,24] Whereas the stabilization of the inverse bicontinuous cubic structure was achieved successfully, a more careful examination of the available resources should be taken into account. Among the plant and wood products, hemicelluloses (HemCs) are heteropolysaccharides and they differ between each other in term the molecular weight and structure. The type of plant which they are extracted from and the extraction method itself influence deeply the nature of this polysaccharides. Usually, HemC is associated within the wood matrix to lignin, a highly hydrophobic aromatic polyphenol that provides mechanical resistance to cell walls. HemCs displayed excellent emulsifying properties in various applications.[25–27] Lignin plays a crucial role in the stabilization of oil-in-water emulsion, given its hydrophobicity.[26]

Therefore, the investigations of **Paper II** focused on the application of galactoglucomannans (GGM), the most abundant HemC in spruce and pine, stabilizer for GMO-based cubosomes. GGM exhibit a linear (1→4)-linked  $\beta$ -D-mannopyranosyl backbone partially substituted with (1→4)- linked  $\beta$ -D-glucopyranosyl units and  $\alpha$ -galactopyranosyl side groups that are (1→6)-linked to the backbone.[28]

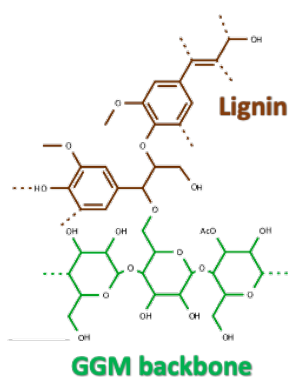


**Figure 3.5.** Hemicellulose structure.

Two type of softwood HemCs were used: (i) one isolated from thermomechanical pulp (TMP) extraction, presenting a low content of lignin, and (ii) a sample originated from a sodium-based sulphite liquor (SSL) extraction with high lignin concentration.

In this case, a top-down approach was used in combination with the thin layer evaporation method to produce the lipid dispersions. The GMO range content and the HemCs concentration were 1 – 3 wt % and 3 mg /mL, respectively, but stable cubosomes were obtained only for 1 wt %.

Table 3.1 contains the physico-chemical characterization of these formulation stabilized by SSL- and TMP-HemCs.

**Table 3.1.** DLS and EM characterization of the cubosome formulations stabilized by TMP and SSL hemicelluloses and the values of  $\zeta$  potential and pH of the HemCs dispersions alone in water.

Sample	$D_H$ [nm]	PdI	Derived count rate	$\zeta$ potential [mV]	pH
TMP-NPs	151 ± 1	0.21 ± 0.02	940 ± 3	-38	6.4
SSL-NPs	152.2 ± 0.9	0.19 ± 0.01	2032 ± 20	-49	6.5
TMP	-	-	-	-18	5.0
SSL	-	-	-	-33	4.6

Since the charge of hemicelluloses is dependent on the extraction method, TMP and SSL HemCs' dispersions alone (without the lipid) displayed different negative charges, even though GGMs are neutral polysaccharides. This finding can be explained by the presence of hydrolyzable acids on the GGM backbone.[29]

The formulations exhibited a higher (in absolute values)  $\zeta$  potential than the one reported for GMO-based cubosomes stabilized by non-ionic poloxamers (commonly between -20 and -30 mV). The negative charge at the interface of cubosomes have been quite debated in literature. This phenomenon can be explained by an adsorption of hydroxides ions at the lipid/water interface, inducing a polarized layer that surrounds the NP. The negative  $\zeta$  potential of systems composed of non-ionic surfactants was found in other lipid and polymeric formulations.[18,30] Both TMP- and SSL-based formulations showed polydispersity index and apparent hydrodynamic sizes in accordance with cubosomes stabilized with poloxamers. By comparing the derived count rates measured, the SSL-cubosomes possess almost twice as high as the value of the TMP-NPs, indicating a higher number of particles in solution.

The structure of these aggregates, reported in Fig. 3.6, exhibited a typical  $Pn3m$  SAXS pattern. It is reasonable to assume that both GGMs interact with the GMO bilayer, without affecting its native structure in water at this concentration.

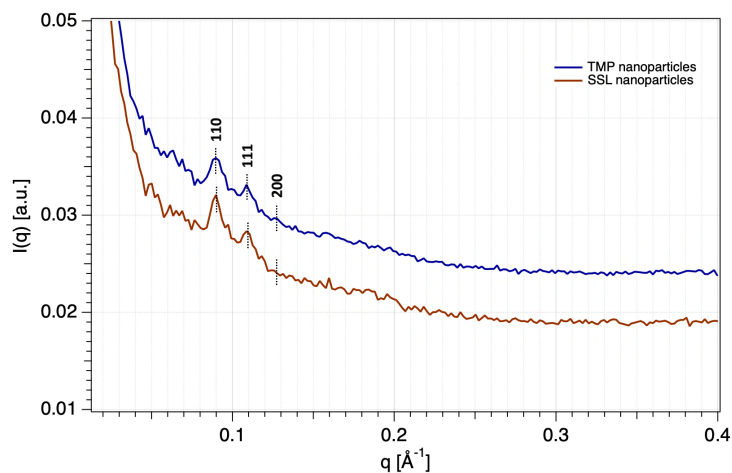


**Figure 3.6.** SAXS pattern of the formulations stabilized by the two GGMs displaying the typical  $Pn3m$  Bragg peaks (Miller's indices are reported above each crystalline plane that scattered the radiation).

The lattice parameters of the  $Pn3m$  phase calculated using the positions of the Bragg peaks are  $99.6 \pm 0.8$  and  $98.7 \pm 0.4$  for TMP- and SSL-NPs, respectively. These values are in accordance with the lattice parameters of GMO-based cubosomes stabilized with different poloxamers, such as Pluronic F108 and F127.

The morphology of the particles was then evaluated by means of cryo-TEM, showing some differences between the two GGM-stabilized samples.

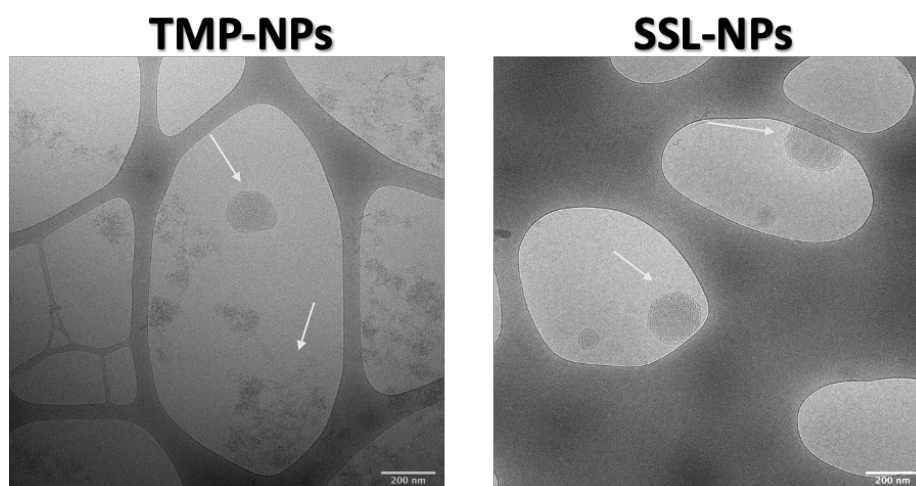


**Figure 3.7.** Cryo-images of the two samples in study. The scale bar is 200 nm for both images.

Both samples present the morphology typical for bicontinuous cubic phases, but in the case of TMP-NPs, a large number of fractal-like structures (common features of softwood hemicellulose) was observed.[29] This feature can be attributed to the excess of hemicellulose that is not incorporated in the sample.

The interaction of the particles with a hydrophobized silica surface was studied *via* AFM: it appears that the cubosomes spread on the surface and take a flat conformation, highlighting the hydrophobic nature of the surface of these aggregates.

The stability of both formulations in water was evaluated using DLS, showing no significant changes in the hydrodynamic diameters and polydispersity index for 42 days.

Given the possible application of this aggregates as nanomedicine for systemic administration, the stability of the nanoparticles was studied in phosphate buffered saline (PBS) at pH 7.4 to emulate the physiological isotonic condition *in vivo*. The salt concentration induces an increase in terms of size of both formulations: the SSL-NPs stabilized around 250 nm, whereas the TMP-stabilized aggregates reached ca. 700 nm. Indeed, the  $\zeta$  potential of both formulations was affected by the PBS buffer, given that TMP-NPs displayed almost neutral charge and SSL-NPs ca.  $-8$  mV.

These data suggest that **(i)** hemicelluloses can be used as stabilizers to produce LLCNPs and **(ii)** SSL-extract, given the higher lignin content, can efficiently stabilized the inverse bicontinuous cubic structure, even in isotonic conditions.

### 3.3. Stabilization of cubosomes by a polyphosphoester analog of Pluronic F127

As explained in Chapter 1, the use of safe and biocompatible building blocks is a mandatory requirement to translate the application of a formulation from *in vitro* to clinical trials. polyphosphoesters (PPEs) may represent a possible solution in order to substitute the commonly used Pluronics, which are not biodegradable and activate the complement system in the blood, causing cardiopulmonary distress in sensitive patients.[31]

PPEs are based on phosphoric acid derivatives, given the high stable C–O–P bond and degradable on demand through specific enzymes.[32,33]

In this regard, a novel PPE analog of Pluronic F127 was adopted as stabilizer in formulating cubosome dispersions with reduced cytotoxicity (**Paper III**).[18] The polymer was synthesized by organocatalyzed ring-opening polymerization, as reported in Fig. 3.8.

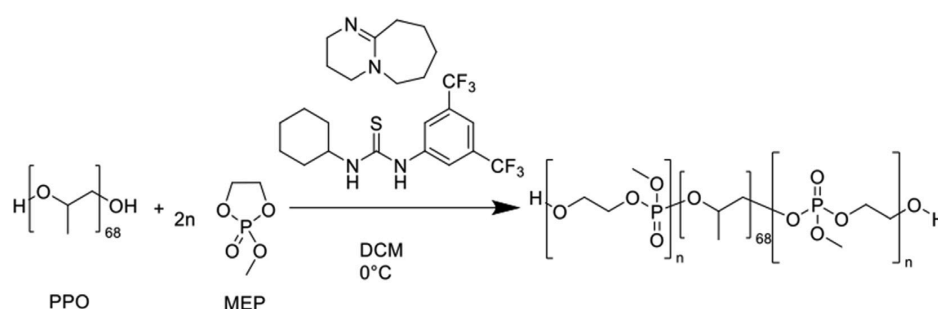


**Figure 3.8.** Reaction of organocatalyzed ring-opening polymerization between methyl ethylene phosphate (MEP) and poly(propylene oxide)<sub>68</sub> (PPO) to obtain the PPE used in **Paper III**. [18]

First, the GMO-based formulations were prepared increasing the PPE concentration from 0.3 to 1.2 wt % and keeping constant the GMO content (3.3 wt %). The physico-chemical features of the carriers were evaluated by DLS, EM, cryo-TEM and SAXS.

By increasing the PPE content, the apparent hydrodynamic diameter decreased, whereas the zeta potentials of the formulation were highly negative (ca. – 47 mV for all concentrations investigated). Interestingly, the SAXS patterns of the formulations (Fig. 3.9) showed a pattern related to the *Pn3m* inverse bicontinuous cubic phase.

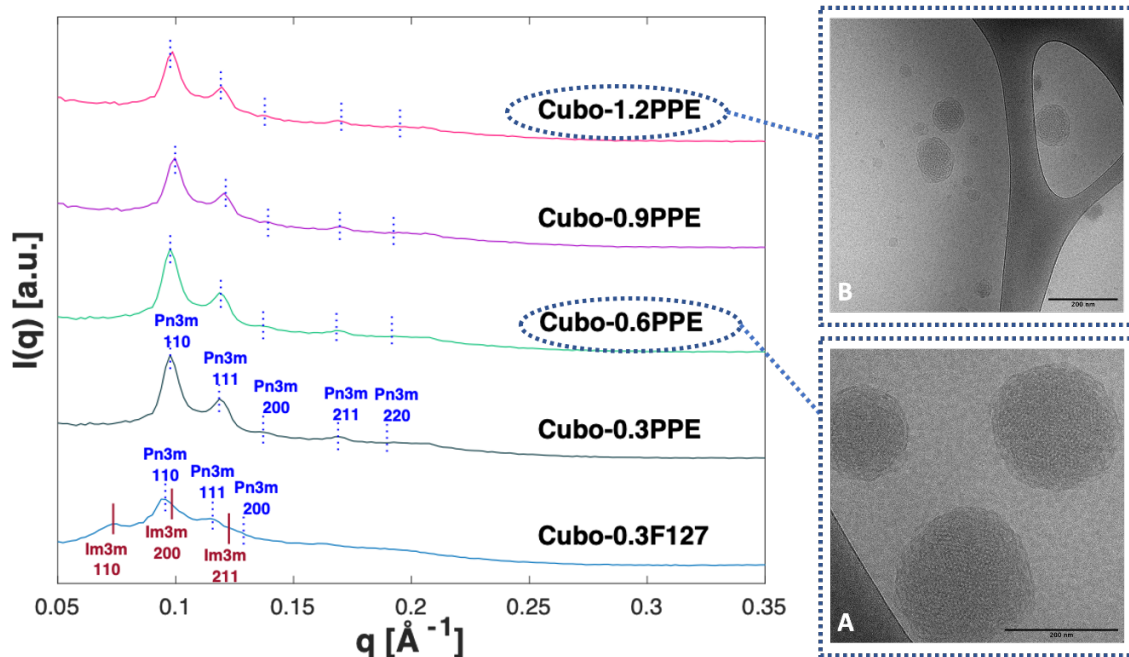


**Figure 3.9.** SAXS patterns of the cubosomes formulated with PPE as stabilizer in the range concentration 0.3 – 1.2 wt % and cryo-TEM images related to the 0.6 and 1.2 wt % of PPE into the formulations. Modified with permission from **Paper III**. [18]

This finding strongly suggests that the hydrophobic unit of the PPE interacts differently than the poloxamers with the GMO lipid bilayer, since the *Im3m* phase, typical features of GMO-dispersions stabilized by Pluronic, was not observed. The lattice parameters and the water channel radii slightly decreased by increasing the concentration of the PPE.

The morphology of the aggregates consisted in spherical nanoparticles exhibiting a dense inner matrix characterized by a honeycomb structure, as reported in other papers. [16,17] In the case of the sample Cubo-1.2PPE, small interlamellar attachments, intermediates in the transition from lamellar to reverse bicontinuous cubic structures, can be observed. Indeed, the concentration of PPE may induce the formation of these architecture and, reasonably, higher PPE content can provoke a phase transition to unilamellar vesicles, as shown in cubosomes formulated with Pluronic F127.

Investigations on the pH evidenced that the PPE-based formulations are slightly acid in comparison with Cubo-0.3F127, decreasing from 6.50 (PPE 0.3 wt %) to 6.27 (PPE 1.2 wt %) while increasing the PPE content. Moreover, pH halved upon one-month aging in the case of all PPE-stabilized cubosomes (final pH = 3.4), whereas the one stabilized with Pluronic F127 remained constant within the considered time frame. This figure is not surprising, given that PPE degradation in water produces phosphates that can decrease the pH of the dispersion. [14]

The formulation presenting 0.6 wt % of the novel stabilizer appeared to be the most stable. Its stability was investigated following variations in the apparent hydrodynamic diameters, PDI and zeta potentials of the dispersion in water over 5 months. These parameters did not change significantly, highlighting the high colloidal stability of the formulation.

In order to study the behavior of the aggregates in different pH, the sample Cubo-0.6PPE was diluted in two different buffers: (i) PBS (100 mM) at pH 7.4 to emulate the physiological isotonic environment and (ii) citrate buffer (100 mM) pH 3.4 to recreate the acidic character observed in the formulation upon aging. The *Pn3m* phase of the sample at pH 6.4 was preserved in physiological conditions (pH 7.4), without any significant changes to the lattice parameters or the water channel radius. However, a biphasic system with both *Im3m* and *Pn3m* inverse bicontinuous cubic phases was obtained: this result was not fully understood, but it could be ascribed to the more complex interactions between the PPE and the GMO bilayer. The hydrodynamic size of Cubo-0.6PPE did not change significantly at both pHs, while the  $\zeta$  potentials dropped given the shielding effect of the ions in the buffer. Table 3.2 summarizes these findings related to the pH environment.

**Table 3.2.** DLS, EM and SAXS measurements of the formulation Cubo-0.6PPE at different pHs from Paper III.[18]

pH	$D_H$ [nm]	PdI	$\zeta$ potential [mV]	a [Å]	$r_w$ [Å]
3.4	159.2 ± 1.9	0.11 ± 0.01	− 6.1 ± 0.6	<i>Pn3m</i> 92.0 ± 0.4	<i>Pn3m</i> 19.0 ± 0.2
				<i>Im3m</i> 120.3 ± 0.6	<i>Im3m</i> 19.7 ± 0.2
6.4	160.0 ± 1.0	0.09 ± 0.01	− 47.0 ± 1.0	<i>Pn3m</i> 91.2 ± 0.6	<i>Pn3m</i> 18.6 ± 0.1
7.4	164.8 ± 1.2	0.10 ± 0.01	− 10.2 ± 0.8	<i>Pn3m</i> 91.5 ± 0.4	<i>Pn3m</i> 18.8 ± 0.1

The sample of cubosomes formulated with Pluronic F127 as stabilizer was tested as well in the different pHs, but its physico-chemical parameters (structure, size, PdI) did not change significantly.

Moreover, the temperature-dependent behavior of the PPE formulation was investigated in the range 25 – 50 °C (and then back to 25 °C). The *Pn3m* phase was retained up to 45 °C, temperature at which the peaks related to an inverse hexagonal phase started to appear. At 50 °C the phase transition was completed, and the *Pn3m* structure was reformed by cooling down the sample to 25 °C, showing the reversibility of the process.

Given the application of cubosomes as drug carriers, quercetin, a natural antioxidant, was encapsulated in both F127 and PPE cubosomes. The encapsulation of the antioxidant did not



alter the physico-chemical properties of both the carriers and no significant differences were observed in terms of encapsulation efficiency and drug content.

Finally, the biological activity of the PPE-stabilized cubosomes was evaluated *in vitro* on adherent cell lines. In comparison with Pluronic F127-stabilized aggregates, the experiments on HEK-293 and HUVEC proved the higher biocompatibility of the PPE cubosomes at different GMO concentration range (10, 25, 50, 75 and 100  $\mu\text{g}/\text{mL}$ ) and incubation times (24, 48 and 72 h). Indeed, hemolysis represents an issue for GMO-based cubosomes, as reported in other studies,[34,35] therefore hemolysis test were performed in the same GMO concentration range as for HEK-293 and HUVEC. In our case, the PPE stabilized formulation ensured excellent hemocompatibility over the whole range of GMO concentrations, whereas F127-stabilized aggregates induced a significant hemolytic effect above 50  $\mu\text{g}/\text{mL}$  (Fig. 3.10).

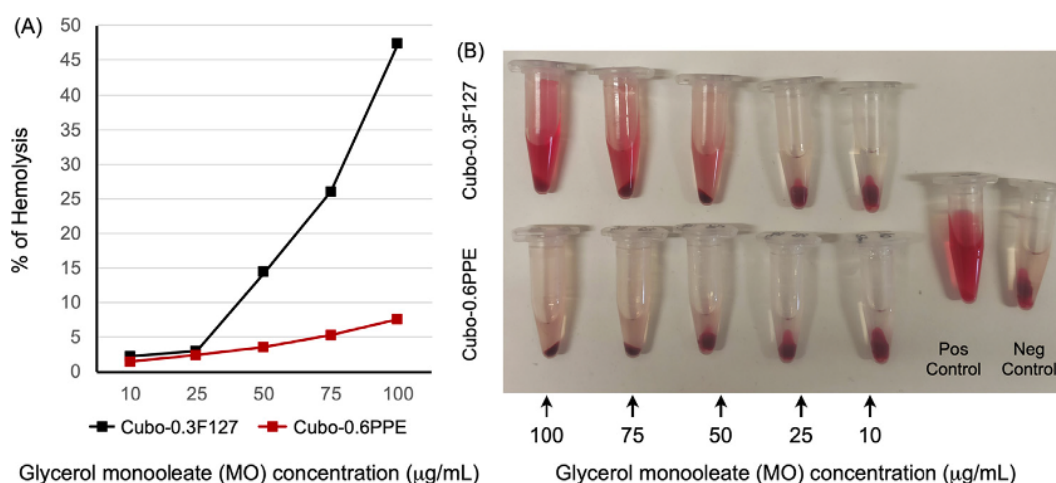


**Figure 3.10.** In vitro hemolysis tests performed with the samples Cubo-0.3F127 and Cubo-0.6PPE. Reproduced with permission from **Paper III**. [18]

The capacity of the two formulations to trigger the complement system was investigated as well. Cubo-0.3F127 was induced a triggering effect on the complement: this finding could be related to the alternative pathway of the complement system, through the binding and subsequent activation of the component C3.[36] On the other hand, Cubo-0.6PPE did not interact with the C3 component of the complement system, avoiding the typical nucleophilic attack of C3.

Indeed, the reduced capacity of activating the complement system guarantees an increased stability in serum and a lower elimination rate by phagocytes. Therefore, PPE resulted as an efficient and biocompatible stabilizer to formulate cubic LLCNPs for systemic administration, improving their colloidal and biological features.

### 3.3. Surface characterization of PPE-stabilized cubosomes

As shown in the previous paragraph, cubosomes stabilized with the novel PPE display excellent colloidal and biological features. However, the bulk and the biological characterization are not enough in order to fully understand the mechanism underlying cell internalization and the nature of the interactions with the cell membrane.

Surface techniques, such as QCM-D and EP can shed some light onto the surface properties of these novel carriers. For this reason, the surface properties of the PPE-stabilized cubosomes from **Paper III** were investigated on both hydrophilic and hydrophobic surfaces. This study is currently undergoing, therefore a brief overview on the preliminary QCM-D data will be presented.

The formulation Cubo-0.6PPE was diluted 1:500 in water, in order to obtain concentrations of the components similar to the *in vitro* experiments. The QCM-D experiments were performed in a E4 system from Q-Sense (Gothenburg, Sweden) using SiO<sub>2</sub>-coated quartz crystals sensors with a fundamental frequency of 4.95 Hz (QSX303, QSense). The hydrophobization of the crystals was achieved by gas-phase silanization, using dimethyloctylchlorosilane (Fluka) and following a procedure reported in literature.[37] The frequency trend and dissipation shifts were followed over the acquisition time until stabilization of both signals.

No adsorption of the aggregates was observed on hydrophilic silica surfaces, since no  $\Delta F$  and  $\Delta D$  were obtained (data not shown). It appears that cubosomes flow in the QCM cell without interacting with the surface, and this finding could be explained by an electrostatic repulsion between the surface and the particles. Indeed, the silica surface displays a low negative charge in water due to the dissociation of silanol groups[38] and given the high negative charge of the PPE-cubosomes, this results in an electrostatic repulsion which hinders the adsorption.

On the other hand, the experiment on hydrophobic surface highlighted an interaction between the PPE-cubosomes particles and the surface (Fig. 3.11).

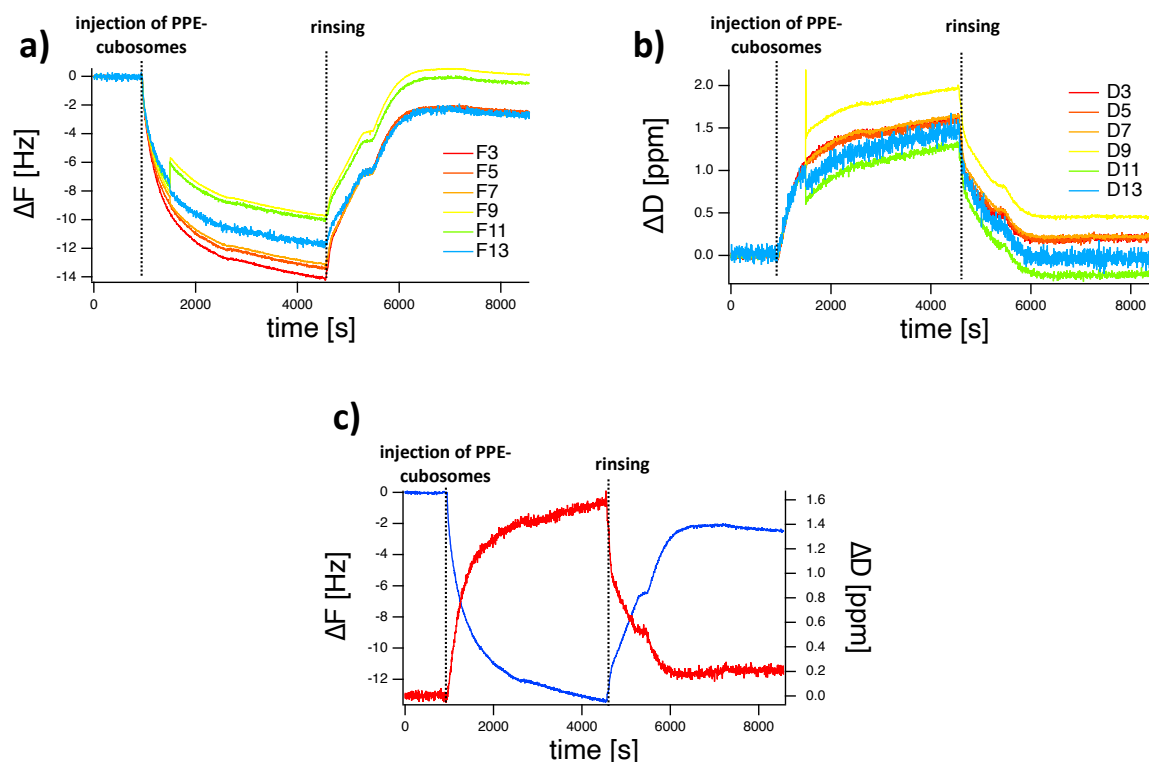


**Figure 3.11.** QCM-D experiment on hydrophobic surface with the formulation Cubo-0.6PPE. a) Frequency shift, b) Dissipation shift and c) Overtones F5 and D5 trends.

As it can be observed,  $\Delta F$  decreases to ca.  $-12$  Hz (fifth harmonic) upon addition of the sample, with some differences between the different overtones. This observation indicates that there is a clear adsorption of the particles on the surface. The rinsing with water can be divided in two steps. First, the loosely bound nanoparticles are removed from the surface, as shown by a small plateau of the  $\Delta F$  around 5600 s. After ca. 5 minutes, the competitive water-NPs interactions induce the removal of most of the material from the surfaces. The system does not go back to the initial state, since the  $\Delta F$  plateaus at ca.  $-3$  Hz. The presence of material adsorbed onto the surface highlights that PPE-cubosomes exhibit hydrophobic domains which can play a role into the interaction with surfaces. Moreover,  $\Delta D$  reaches ca. 1.6 ppm and 0.2 ppm upon addition of cubosomes and after rinsing, respectively. Initially, the adsorbed layer appears to be slightly viscoelastic, given the  $\Delta D > 1$  ppm, whereas the rinsing makes it go back to a more rigid film at the surface. Although the system clearly shows some viscoelastic properties, the Sauerbrey equation was applied to evaluate the adsorbed amount on this hydrophobic surface, giving  $49.6$   $\text{ng cm}^{-2}$  and  $10.6$   $\text{ng cm}^{-2}$  before and after rinsing, respectively. The overtone F5 was fitted using the Sauerbrey model (QSense Dfind software), giving a thickness of the layer adsorbed of 2.4 nm (before rinsing) and this value could be related to the presence of a monolayer. Similar

finding was obtained by Vandoolaeghe and coworkers via Ellipsometry measurements on GMO-based cubosomes stabilized by Pluronic F127 in water on hydrophobized silica surfaces.[39]

This preliminary information gives just a hint on the surface properties of the PPE-stabilized cubosomes. Indeed, more investigations using different models should be conducted in order to evaluate the adsorbed amount and thickness of the adsorbed layer. Moreover, taking into account the pH-dependent behavior of the PPE-stabilized, we are currently investigating on how the pH can impact the adsorption of the particles, in order to correlate the bulk and surface characterization in comparison with the poloxamer stabilized cubosomes.

## 3.4. Conclusions and future perspectives

The role of the stabilizing agent is crucial in formulating nanoparticles for systemic administration. The stabilizer covers the surface of the carrier, altering the surface properties. Indeed, this “new” surface will interact with several blood components (e.g. the complement system) and the cell surface, inducing a different biological response.

The functionalization of Pluronic PPE arms ensure to give new functionalities, making the carrier suitable for different therapeutical approaches, as shown in **Paper I**. Indeed, poloxamers are not biodegradable *in vivo*, therefore there is a strong need to choose biocompatible and biodegradable components of LLCNPs. **Paper II** and **Paper III** investigated on the applicability of hemicellulose and a novel polyphosphoester as stabilizers for cubosomes. Two different hemicellulose extracts (**Paper II**) were able to stabilize the Pn3m cubic structure of GMO in water, without inducing the formation of new phases that may impact the diffusion of a drug. SSL- NPs showed high stability both over time and in a physiological buffer, highlighting their possible applicability as drug carriers. *In vitro* experiments on adherent or in suspension cells are needed to assess their biological performance.

PPE (**Paper III**) showed excellent performances in stabilizing GMO-based cubosomes, without affecting the lipid self-assembly behavior in water. Moreover, the correlation of the bulk and biological data with the surface characterization enable to have a full picture on the carrier properties, especially to predict and model the possible *in vivo* response.

The PPE-stabilized cubosomes displayed an excellent bio- and hemocompatibility, two main requirements for formulations suitable for systemic administration. The interesting surface behavior may help to interpretate the phenomena occurring at the cell-NP interface.

Further investigations are indeed needed to assess the biological and biochemical effect of PPE-cubosomes on living cells and *in vivo* on model animal.

### 3.5. References

- [1] P. Pitzalis, M. Monduzzi, N. Krog, H. Larsson, H. Ljusberg-Wahren, T. Nylander, Characterization of the liquid-crystalline phases in the glycerol monooleate/diglycerol monooleate/water system, *Langmuir*. 16 (2000) 6358–6365. <https://doi.org/10.1021/la0002031>.
- [2] U. Bazylińska, J. Kulbacka, J. Schmidt, Y. Talmon, S. Murgia, Polymer-free cubosomes for simultaneous bioimaging and photodynamic action of photosensitizers in melanoma skin cancer cells, *J. Colloid Interface Sci.* 522 (2018) 163–173. <https://doi.org/10.1016/j.jcis.2018.03.063>.
- [3] J. Zhai, L. Waddington, T.J. Wooster, M.I. Aguilar, B.J. Boyd, Revisiting  $\beta$ -casein as a stabilizer for lipid liquid crystalline nanostructured particles, *Langmuir*. 27 (2011) 14757–14766. <https://doi.org/10.1021/la203061f>.
- [4] J. Gustafsson, H. Ljusberg-Wahren, M. Almgren, K. Larsson, Submicron particles of reversed lipid phases in water stabilized by a nonionic amphiphilic polymer, *Langmuir*. 13 (1997) 6964–6971. <https://doi.org/10.1021/la970566+>.
- [5] E. Tasca, P. Andreozzi, A. Del Giudice, L. Galantini, K. Schillén, A. Maria Giuliani, M. de los A. Ramirez, S.E. Moya, M. Giustini, Poloxamer/sodium cholate co-formulation for micellar encapsulation of doxorubicin with high efficiency for intracellular delivery: An in-vitro bioavailability study, *J. Colloid Interface Sci.* (2020). <https://doi.org/10.1016/j.jcis.2020.06.096>.
- [6] E. Tasca, A. Del Giudice, L. Galantini, K. Schillén, A.M. Giuliani, M. Giustini, A fluorescence study of the loading and time stability of doxorubicin in sodium cholate/PEO-PPO-PEO triblock copolymer mixed micelles, *J. Colloid Interface Sci.* 540 (2019) 593–601. <https://doi.org/10.1016/j.jcis.2019.01.075>.
- [7] C. Caltagirone, M. Arca, A.M. Falchi, V. Lippolis, V. Meli, M. Monduzzi, T. Nylander, A. Rosa, J. Schmidt, Y. Talmon, S. Murgia, Solvatochromic fluorescent BODIPY derivative as imaging agent in camptothecin loaded hexosomes for possible theranostic applications, *RSC Adv.* 5 (2015) 23443–23449. <https://doi.org/10.1039/c5ra01025j>.
- [8] V. Meli, C. Caltagirone, C. Sinico, F. Lai, A.M. Falchi, M. Monduzzi, M. Obiols-Rabasa, G. Picci, A. Rosa, J. Schmidt, Y. Talmon, S. Murgia, Theranostic hexosomes for cancer treatments: an in vitro study, *New J. Chem.* 41 (2017) 1558–1565. <https://doi.org/10.1039/c6nj03232j>.
- [9] V. Meli, C. Caltagirone, A.M. Falchi, S.T. Hyde, V. Lippolis, M. Monduzzi, M. Obiols-Rabasa, A. Rosa, J. Schmidt, Y. Talmon, S. Murgia, Docetaxel-Loaded Fluorescent Liquid-Crystalline Nanoparticles for Cancer Theranostics, *Langmuir*. 31 (2015) 9566–9575. <https://doi.org/10.1021/acs.langmuir.5b02101>.
- [10] S. Murgia, S. Bonacchi, A.M. Falchi, S. Lampis, V. Lippolis, V. Meli, M. Monduzzi, L. Prodi, J. Schmidt, Y. Talmon, C. Caltagirone, Drug-loaded fluorescent cubosomes: Versatile nanoparticles for potential theranostic applications, *Langmuir*. (2013). <https://doi.org/10.1021/la401047a>.
- [11] S. Jenni, G. Picci, M. Fornasier, M. Mamusa, J. Schmidt, Y. Talmon, A. Sour, V. Heitz, S. Murgia, C. Caltagirone, Multifunctional cubic liquid crystalline nanoparticles for chemo- And photodynamic synergistic cancer therapy, *Photochem. Photobiol. Sci.* (2020). <https://doi.org/10.1039/c9pp00449a>.
- [12] M. Nakano, A. Sugita, H. Matsuoka, T. Handa, Small-angle X-ray scattering and  $^{13}\text{C}$  NMR investigation on the internal structure of “cubosomes,” *Langmuir*. 17 (2001) 3917–3922.

- <https://doi.org/10.1021/la010224a>.
- [13] S. Aleandri, R. Mezzenga, The physics of lipidic mesophase delivery systems, *Phys. Today*. 73 (2020) 38–44. <https://doi.org/10.1063/PT.3.4522>.
- [14] K.N. Bauer, H.T. Tee, M.M. Velencoso, F.R. Wurm, Main-chain poly(phosphoester)s: History, syntheses, degradation, bio-and flame-retardant applications, *Prog. Polym. Sci.* 73 (2017) 61–122. <https://doi.org/10.1016/j.progpolymsci.2017.05.004>.
- [15] S. Schöttler, G. Becker, S. Winzen, T. Steinbach, K. Mohr, K. Landfester, V. Mailänder, F.R. Wurm, Protein adsorption is required for stealth effect of poly(ethylene glycol)- and poly(phosphoester)-coated nanocarriers, *Nat. Nanotechnol.* 11 (2016) 372–377. <https://doi.org/10.1038/nnano.2015.330>.
- [16] S. Murgia, S. Biffi, R. Mezzenga, Recent advances of non-lamellar lyotropic liquid crystalline nanoparticles in nanomedicine, *Curr. Opin. Colloid Interface Sci.* 48 (2020) 28–39. <https://doi.org/10.1016/j.cocis.2020.03.006>.
- [17] H.M.G. Barriga, M.N. Holme, M.M. Stevens, Cubosomes: The Next Generation of Smart Lipid Nanoparticles?, *Angew. Chemie - Int. Ed.* 58 (2019) 2958–2978. <https://doi.org/10.1002/anie.201804067>.
- [18] M. Fornasier, S. Biffi, B. Bortot, P. Macor, A. Manhart, F.R. Wurm, S. Murgia, Cubosomes stabilized by a polyphosphoester-analog of Pluronic F127 with reduced cytotoxicity, *J. Colloid Interface Sci.* (2020). <https://doi.org/10.1016/j.jcis.2020.07.038>.
- [19] J. Golab, P. Agostinis, K. Berg, K.A. Cengel, T.H. Foster, A.W. Girotti, S.O. Gollnick, S.M. Hahn, M.R. Hamblin, A. Juzeniene, D. Kessel, M. Korbelik, J. Moan, P. Mroz, D. Nowis, J. Piette, B.C. Wilson, Photodynamic Therapy of Cancer: An Update, *Ca-a Cancer J. Clin.* (2011).
- [20] S. Foote, *Mechanisms* 4, 162 (1968) 963–970.
- [21] J. Schmitt, V. Heitz, A. Sour, F. Bolze, H. Ftouni, J.F. Nicoud, L. Flamigni, B. Ventura, Diketopyrrolopyrrole-porphyrin conjugates with high two-photon absorption and singlet oxygen generation for two-photon photodynamic therapy, *Angew. Chemie - Int. Ed.* (2015). <https://doi.org/10.1002/anie.201407537>.
- [22] S. Jenni, F. Bolze, C.S. Bonnet, A. Pallier, A. Sour, É. Tóth, B. Ventura, V. Heitz, Synthesis and In Vitro Studies of a Gd(DOTA)–Porphyrin Conjugate for Combined MRI and Photodynamic Treatment, *Inorg. Chem.* (2020). <https://doi.org/10.1021/acs.inorgchem.0c02189>.
- [23] M. Uyama, M. Nakano, J. Yamashita, T. Hana, Useful modified cellulose polymers as new emulsifiers of cubosomes, *Langmuir.* (2009). <https://doi.org/10.1021/la900386q>.
- [24] P.T. Spicer, W.B. Small, M.L. Lynch, J.L. Burns, Dry powder precursors of cubic liquid crystalline nanoparticles (cubosomes), *J. Nanoparticle Res.* (2002). <https://doi.org/10.1023/A:1021184216308>.
- [25] K.S. Mikkonen, C. Xu, C. Berton-Carabin, K. Schroën, Spruce galactoglucomannans in rapeseed oil-in-water emulsions: Efficient stabilization performance and structural partitioning, *Food Hydrocoll.* (2016). <https://doi.org/10.1016/j.foodhyd.2015.08.009>.
- [26] M.H. Lahtinen, F. Valoppi, V. Juntti, S. Heikkinen, P.O. Kilpeläinen, N.H. Maina, K.S. Mikkonen, Lignin-Rich PHWE Hemicellulose Extracts Responsible for Extended Emulsion Stabilization, *Front. Chem.* (2019). <https://doi.org/10.3389/fchem.2019.00871>.
- [27] Z. Zhang, R. Zhang, L. Zou, D.J. McClements, Protein encapsulation in alginate hydrogel beads: Effect

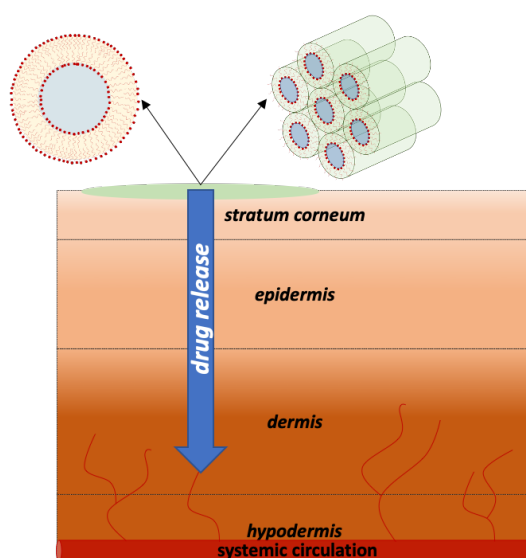
- of pH on microgel stability, protein retention and protein release, *Food Hydrocoll.* 58 (2016) 308–315. <https://doi.org/10.1016/j.foodhyd.2016.03.015>.
- [28] S. Willför, R. Sjöholm, C. Laine, M. Roslund, J. Hemming, B. Holmbom, Characterisation of water-soluble galactoglucomannans from Norway spruce wood and thermomechanical pulp, *Carbohydr. Polym.* (2003). [https://doi.org/10.1016/S0144-8617\(02\)00288-6](https://doi.org/10.1016/S0144-8617(02)00288-6).
- [29] M. Bhattarai, F. Valoppi, S.P. Hirvonen, S. Hietala, P. Kilpeläinen, V. Aseyev, K.S. Mikkonen, Time-dependent self-association of spruce galactoglucomannans depends on pH and mechanical shearing, *Food Hydrocoll.* (2020). <https://doi.org/10.1016/j.foodhyd.2019.105607>.
- [30] T.H. Nguyen, T. Hanley, C.J.H. Porter, B.J. Boyd, Nanostructured liquid crystalline particles provide long duration sustained-release effect for a poorly water soluble drug after oral administration, *J. Control. Release.* 153 (2011) 180–186. <https://doi.org/10.1016/j.jconrel.2011.03.033>.
- [31] I.D.M. Azmi, P.P. Wibroe, L.P. Wu, A.I. Kazem, H. Amenitsch, S.M. Moghimi, A. Yaghmur, A structurally diverse library of safe-by-design citrem-phospholipid lamellar and non-lamellar liquid crystalline nano-assemblies, *J. Control. Release.* (2016). <https://doi.org/10.1016/j.jconrel.2016.08.011>.
- [32] Y.C. Wang, L.Y. Tang, T.M. Sun, C.H. Li, M.H. Xiong, J. Wang, Self-assembled micelles of biodegradable triblock copolymers based on poly(ethyl ethylene phosphate) and poly( $\epsilon$ -caprolactone) as drug carriers, *Biomacromolecules.* 9 (2008) 388–395. <https://doi.org/10.1021/bm700732g>.
- [33] D.F. Xiang, A.N. Bigley, Z. Ren, H. Xue, K.G. Hull, D. Romo, F.M. Raushel, Interrogation of the Substrate Profile and Catalytic Properties of the Phosphotriesterase from *Sphingobium* sp. Strain TCM1: An Enzyme Capable of Hydrolyzing Organophosphate Flame Retardants and Plasticizers, *Biochemistry.* 54 (2015) 7539–7549. <https://doi.org/10.1021/acs.biochem.5b01144>.
- [34] S. Biffi, L. Andolfi, C. Caltagirone, C. Garrovo, A.M. Falchi, V. Lippolis, A. Lorenzon, P. Macor, V. Meli, M. Monduzzi, M. Obiols-Rabasa, L. Petrizza, L. Prodi, A. Rosa, J. Schmidt, Y. Talmon, S. Murgia, Cubosomes for in vivo fluorescence lifetime imaging, *Nanotechnology.* 28 (2017). <https://doi.org/10.1088/1361-6528/28/5/055102>.
- [35] J. Barauskas, C. Cervin, M. Jankunec, M. Špandyreva, K. Ribokaite, F. Tiberg, M. Johnsson, Interactions of lipid-based liquid crystalline nanoparticles with model and cell membranes, *Int. J. Pharm.* (2010). <https://doi.org/10.1016/j.ijpharm.2010.03.016>.
- [36] K. Yu, B.F.L. Lai, J.H. Foley, M.J. Krisinger, E.M. Conway, J.N. Kizhakkedathu, Modulation of complement activation and amplification on nanoparticle surfaces by glycopolymer conformation and chemistry, *ACS Nano.* (2014). <https://doi.org/10.1021/nn504186b>.
- [37] F. Wan, T. Nylander, C. Foged, M. Yang, S.G. Baldursdottir, H.M. Nielsen, Qualitative and quantitative analysis of the biophysical interaction of inhaled nanoparticles with pulmonary surfactant by using quartz crystal microbalance with dissipation monitoring, *J. Colloid Interface Sci.* 545 (2019) 162–171. <https://doi.org/10.1016/j.jcis.2019.02.088>.
- [38] S.H. Behrens, D.G. Grier, The charge of glass and silica surfaces, *J. Chem. Phys.* (2001). <https://doi.org/10.1063/1.1404988>.
- [39] P. Vandoolaeghe, F. Tiberg, T. Nylander, Interfacial behavior of cubic liquid crystalline nanoparticles at hydrophilic and hydrophobic surfaces, *Langmuir.* 22 (2006) 9169–9174. <https://doi.org/10.1021/la061224j>.







## Topical administration of LLCNPs



### Chapter 4 – Table of contents

- 4.1. Effect of LCh on the penetration properties
  - 4.2. BSs as edge activators in LLCNPs
  - 4.3. Conclusions and Future Perspectives
  - 4.4. References
- 

The application of formulations on the skin is a feasible way to administrate drugs or compounds with antioxidant activity. As described in **Chapter 1**, the *stratum corneum* is a passive barrier which offers a protective layer against the external environment. Targeting its composition and architecture, chemical permeation enhancers have been exploited in order to improve the permeability of drug carriers.[1–3] Ideally these materials should meet several criteria, such as pharmacologically inertia and atoxicity, while being non-irritating, non-allergenic, and inexpensiveness.[3] The enhancer should not lead to the loss of body fluids, electrolytes and endogenous materials and, more importantly, the interactions with the skin should be reversible allowing SC to regain its architecture.

Various permeation enhancers have been tested in the last decades, especially based on fatty acid and their esters. The saturation of the alkyl chain is an interesting parameter that can tune the permeability: some studies showed that unsaturated lipid chains can impact in a beneficial way the penetration properties of flurbiprofen emulsions in comparison with saturated chains.[4] Oleic acid was found to be the most efficient permeation enhancer among the unsaturated fatty acids in permitting the transdermal release of diclofenac.[2,4]

Glycerides are effective permeation enhancers. The saturation of the lipid chain has an effect on the penetration properties as well as for simple fatty acids. In a recent MD study from Gupta and collaborators, GMO was found to be partitioned completely from the solvent layer to the skin lipid layer.[5]

Edge activators are another type of components that can be added in formulations for topical administration. They are bilayer softeners, conferring elasticity and deformability features to bilayer structures.[1] This phenomenon has been widely exploited in transferosomes.[6,7] The penetration mechanism has not been fully understood. Some studies explain that this incredible deformability allow transferosomes to squeeze and overcome the SC by taking advantage of the space between the corneocytes. Indeed, the separation between these kind of cells ( 3 – 4 nm) is quite small in comparison with the lipid bilayer thickness ( 5 – 6 nm, depending on the

lipid), therefore many researchers have been recently highlighting that all these types of carriers actually break up due to the interaction with the skin lipids and then fluidify the SC as molecular identities.[1]

Among the various edge activators, bile salts (BSs) represent an interesting category. Chemically speaking, they are organic anions with a steroid nucleus formed by enzymatic conversion of cholesterol.[8]

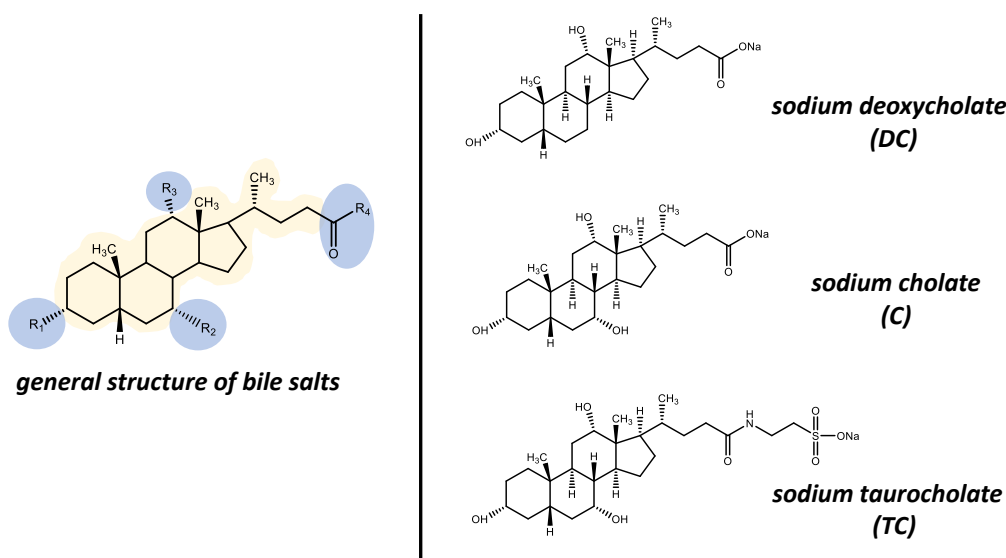


**Figure 4.1.** General moiety of BSs and some examples of the bile salts used in Paper VI and VII. The hydrophilic domains are colored in light blue, whereas the hydrophobic backbone in yellow.

BSs play a crucial role in hepatobiliary and intestinal homeostasis. Under physiological conditions, they can solubilize lipophilic molecules in the intestine to enable their uptake from the lumen.

Their protonation changes them to their acidic form (bile acids). The salt form is prevalent at a physiological pH, due to a  $pK_a$  of 1 and 4 – 5 for glycine- and taurine-conjugated BSs, respectively.[9,10]

Non-lamellar LLCNPs have recently found application as drug carriers for topical administration. These carriers exhibit high hydration and easy distribution in comparison with emulsions, given the similarity with the stratum corneum structure.[11] The cubic phase have been found to possess strong bio-adhesive properties and it forms a cubosomal depot by interacting with the SC lipids.[12] Moreover, the water contained in the LLC's water channels

#### Chapter 4 – Topical administration of LLCNPs

acts as reservoir and it provides hydration to the tissue.[11] Cubosomes were applied as photosensitizer carriers for applications in photodynamic therapy.[13,14]

Inverse hexagonal phase carriers were applied limitedly as topical nanomedicine. Cohen-Avrahami and coworkers prepared hexosomal gel with GMO and trycaprylin for the transdermal delivery of sodium diclofenac and studied the penetration properties on porcine skin in the presence of a peptide permeation enhancer, obtaining good concentration of the drug across the skin.[15,16]

Up to date, hexosomes were not applied as carriers for topical administration. In this Chapter, the investigations on the formulations designed for topical administrations of antioxidants will be discussed.

**Paper IV** focused on the role of lauroylcholine (LCh) as permeation enhancer to formulate a liquid- and a gel-like carriers for topical administration of an inhibitor of human tyrosinase, whereas **Papers V** discussed the effect of BSs as edge activators within GMO-based formulations to deliver natural antioxidants through the skin.

## 4.1. Effect of LCh on the penetration properties

The synergic effect of two permeation enhancer have been exploited in **Paper IV**.<sup>[17]</sup> GMO and LCh were used to prepare liquid- and gel-like vesicular carriers for the topical administration of 3-hydroxycoumarin (3-HC). 3-HC has been proven as an effective inhibitor of tyrosinase from mushrooms, therefore its inhibitory activity was tested *in vitro* on recombinant human tyrosinase (RHT). Indeed, tyrosinase is a key enzyme in the biosynthesis of melanin in animals, as it is involved in the melanogenesis. Defects in tyrosinase activity could lead to skin disorders, such as age spots and hyperpigmentation.<sup>[17]</sup>

In a mixture of RHT, L-DOPA and MBTH (3-methyl-2-benzothiazolinone hydrazone), the presence of 3HC (0.05 mM) was able to strongly inhibit the transformation of L-DOPA into dopaquinone, one reaction occurring into melanogenesis.

Following a previous study,<sup>[18,19]</sup> LCh was added to GMO dispersions to follow the evolution of the system from dilute unilamellar vesicle dispersion to a vesicular lipid gel (in the range of 4 – 14 wt % of the dispersed phase, DP). The structural and rheological features of these formulations were evaluated, suggesting the possible application as drug carriers for topical administration.

Therefore, the DP range was extended in our study, reaching up to 22 wt %. Using a bottom-up approach, the formulations were prepared, and 3-HC was dispersed in the molten monoolein. Table 1 summarizes the composition of the samples in study.

**Table 4.1.** Composition of the samples investigated in **Paper IV**. The compositions are given as wt %.

sample	GMO	LCh	W	3HC	macroscopic appearance
DP8	7.0	0.6	92.4	-	viscous liquid
DP8 + 3-HC	7.0	0.6	92.3	0.1	viscous liquid
DP16	14.5	1.5	84.0	-	viscous gel
DP16 + 3-HC	14.5	1.5	83.9	0.1	viscous gel
DP20	18.2	1.8	80.0	-	very viscous gel
DP20 + 3-HC	18.3	1.8	79.3	0.6	very viscous gel
DP22	20.0	2.0	78.0	-	hard gel
DP22 + 3-HC	19.9	2.0	77.3	0.8	hard gel

The structure of the samples was evaluated by SAXS, showing two fundamental aspects: (i) the increasing DP induces a transition from unilamellar to oligolamellar vesicles and (ii) the presence of 3-HC enhances the lamellarity of the system (Fig. 4.2).

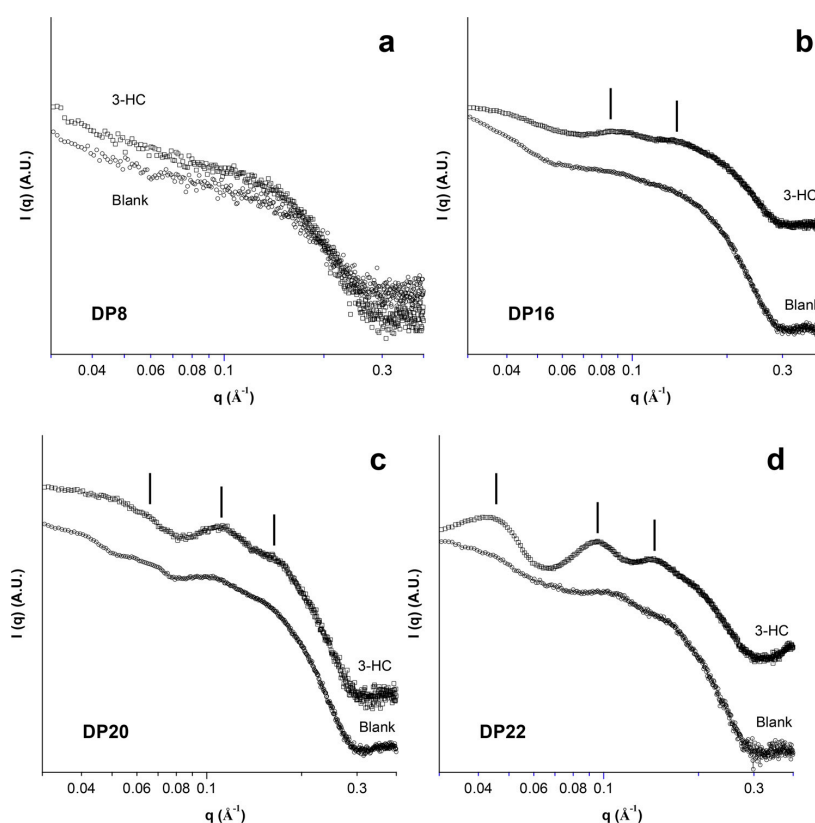


**Figure 4.2.** SAXS diffractograms of the GMO/LCh systems. The term “blank” refers to the formulations without 3HC. Reproduced with permission from **Paper IV**.<sup>[17]</sup>

The increase in the lamellarity of vesicular systems typically occurs upon raising the DP content above the critical effective volume fraction, as a convenient way to arrange the additional interface area.

DP8 and DP16 were chosen as candidates for *in vitro* penetration tests on new-born pig skin, in order to compare the delivery properties of the liquid- and gel-like formulations at two different contact time with the skin (8 h and 2 h). LCh-based vesicles (DP 4 wt %) were already tested highlighting the role of the lipid as permeation enhancer.<sup>[19]</sup>

In our case, Fig. 4.2a shows that both formulations possess good skin permeation properties after being in contact with the skin for 8 h, as highlighted by the high cumulative content of 3HC in the receptor compartment. Moreover, the sample DP16 displays a superior ability to accumulate the drug in the SC, given the higher amount of lipids able to disturb the dense network of keratin and lipids of the outermost layer.



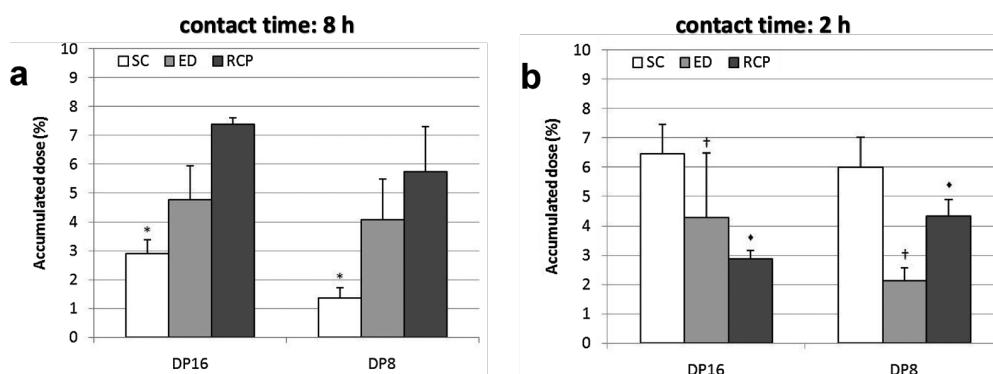


**Figure 4.3.** Accumulated doses of 3HC delivered in the skin layers (stratum corneum = SC, epidermis = E, dermis = D) and in the receptor compartment (RCP) by the formulations DP16 and DP8. Reproduced with permission from **Paper IV**. [17]

With the aim of reducing the amount of systemic administrated 3-HC, while increasing the local accumulation, the formulations were removed after 2 h from the skin surface in a second subset of experiments. The tuning of contact time resulted primarily in an accumulation of 3HC in the first skin layer, with SC being the richest, and a lower amount of drug was able to reach the receptor compartment. The transdermal release of the liquid formulation appeared to be less time-dependent than the gel-like sample, as the former still allowed a high 3-HC delivery in the receptor's medium.

The cytotoxicity of DP8 (either empty or loaded with 3-HC) was evaluated in B16F19 cell cultures, clearly evidencing that neither the vesicles alone nor those containing the drug exerted a cytotoxic affect at the concentration investigated.

Indeed, the tunable features of GMO/LCh dispersions could be directly translated to clinical settings and home treatment, as the patient may be easily instructed to remove the medication after a given time to optimize the skin accumulation, thus minimizing the systemic adsorption and the side effects.

## 4.2. BSs as edge activators in LLCNPs

The phase behavior of lipids in the presence of BSs have been studied widely in order to investigate of the digestion of glycerides. Their phases have been determined by means of SAXS and NMR studies.

To date, only one paper was devoted to investigating on the role of BSs in both Dimodan U/J (a mixture of monoacyl-glycerides, monoolein and monolinolein as main components) and PHYT-based non-lamellar LLCNPs, showing that a phase transition from inverse bicontinuous

cubic to lamellar phase dispersion occurs when sodium cholate and deoxycholate mixtures are used as dispersant. Nevertheless, the applicability of GMO/BSs systems has not been studied for topical administration so far.

**Paper V** is focused on effect of three BSs (cholate, deoxycholate and taurocholate) on the phase behavior of GMO-based LCCNPs in order to prepare carriers suitable to deliver catechin, a potent natural antioxidant, through the skin layers.

First, the presence of BSs in a cubosome formulation stabilized by Pluronic F108 affected the packing parameter of GMO, thus influencing the interfacial curvature of the system. SAXS experiments showed that a bicontinuous cubic-to-unilamellar phase transition occur in the dispersed system for all the BSs in study. Moreover, DLS studies highlighted a shrinking in terms of apparent hydrodynamic diameter for the formulations, as shown in Fig. 4.4.

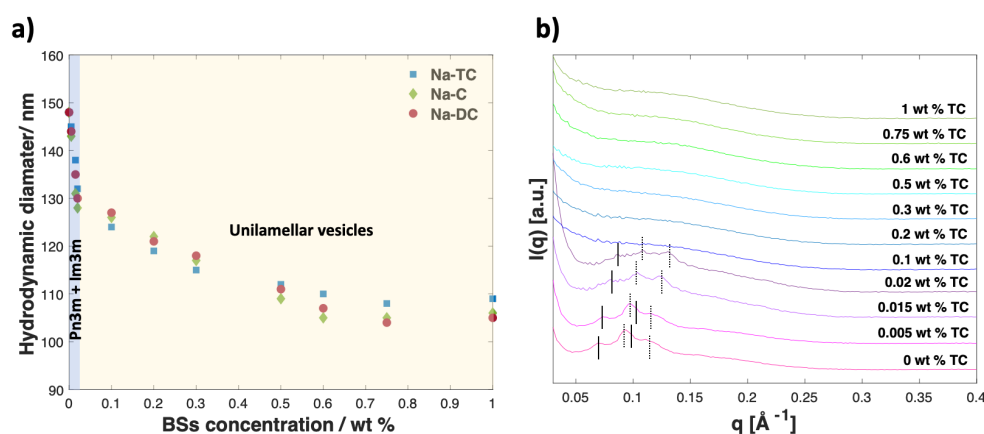


**Figure 4.4.** DLS (a) and SAXS (b) investigations on the effect of TC on GMO-based dispersions in water. In (b) the dashed lines and the filled lines correspond to the Bragg peaks of a  $Pn3m$  and  $Im3m$  phase, respectively.

Among the three BSs, sodium taurocholate gave the most stable formulations: no phase separation was observed up to one month for the composition GMO/PF108/TC/W = 3.0/0.2/0.3/0.3/96.2 (wt%).

Oleic acid (OA) is usually added to GMO/W systems to obtain hexosomes, the dispersion of the inverse hexagonal phase. Moreover, OA is a well-known permeation enhancer used in several emulsions for topical administration.[20,21]

Therefore, OA was added to the most stable composition in order to change the curvature of the lipid bilayer. Unilamellar vesicles or hexosomes were formed in a range composition equal to 0.1 – 0.6 wt % of OA content, as shown by the cryo-TEM measurements reported in Fig.

4.5. This phenomenon was highlighted by SAXS measurements as well, showing that hexosomes are formed above 0.4 wt % of OA content.

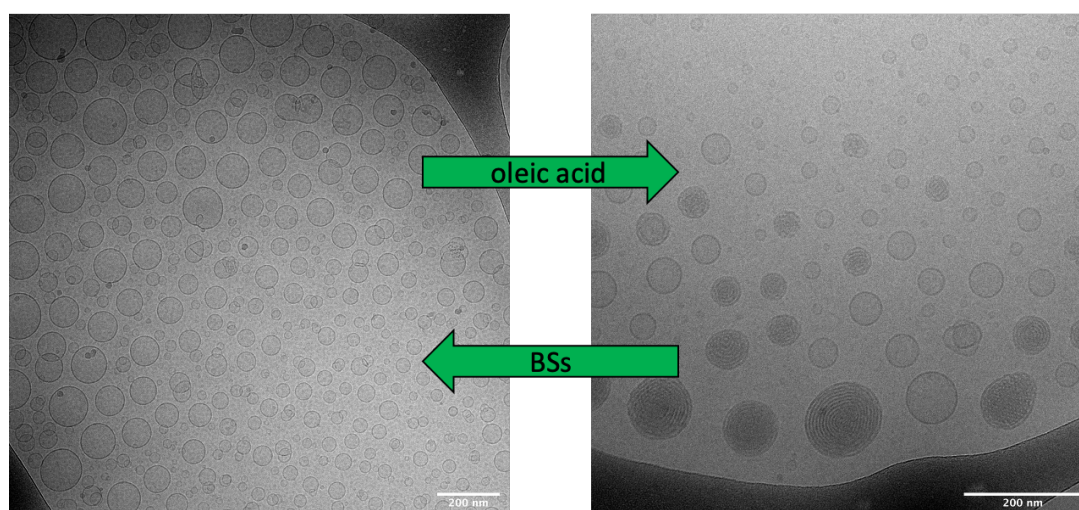


**Figure 4.5.** Cryo-TEM micrographs of the samples with composition (a) GMO/OA/TC/PF108/W = 3.0/0.2/0.3/0.3/96.2 (wt%) and (b) GMO/OA/TC/PF108/W = 3.0/0.5/0.3/0.3/95.9 (wt%).

Catechin was then encapsulated in the formulation GMO/OA/PF108/TC/W = 3.0/0.5/0.3/0.3/95.9. The investigations *via* SAXS, DLS and Electrophoretic Light Scattering showed that the physico-chemical properties (size,  $\zeta$  potential, structure and lattice parameter) of the system did not change due to the encapsulation of the antioxidant. The encapsulation efficiency of catechin was evaluated by means of UV-Vis spectroscopy ( $99.9 \pm 0.1$ ).

The ability of the formulation to overcome the SC was evaluated *in vitro*, using again vertical Franz cells. The penetration properties of the TC-doped hexosomes formulation containing catechin were evaluated in comparison with two more samples loaded with the same antioxidant: a vesicular formulation made by GMO and LCh (Ves) and hexosomes (Hex), both not containing BSs. The composition and the physico-chemical parameters of the systems are reported in Table 4.2.

**Table 4.2.** Overview on the formulations Hex and Ves (not containing BSs) used for the *in vitro* penetration tests.

Formulation	Composition (wt %)	$D_h$ (nm)	PdI	$\zeta$ (mV)	EE %
Hex + Cat	GMO/OA/PF108/W =	$160 \pm 2$	$0.13 \pm$	$-29 \pm 1$	$99.5 \pm 0.2$
	3.0/0.5/0.3/96.2		0.01		

Ves + Cat	GMO/LCh/W = 3.3/0.3/96.4	80 ± 3	0.24 ± 0.01	+42 ± 2	97.4 ± 1.2
-----------	-----------------------------	--------	----------------	---------	------------

As reported in Fig. 4.5, the accumulated concentration of catechin in was enhanced in the presence of TC within the carrier: the edge activator improved the accumulation of the antioxidant in all the skin layers and favoring the transdermal release as well.

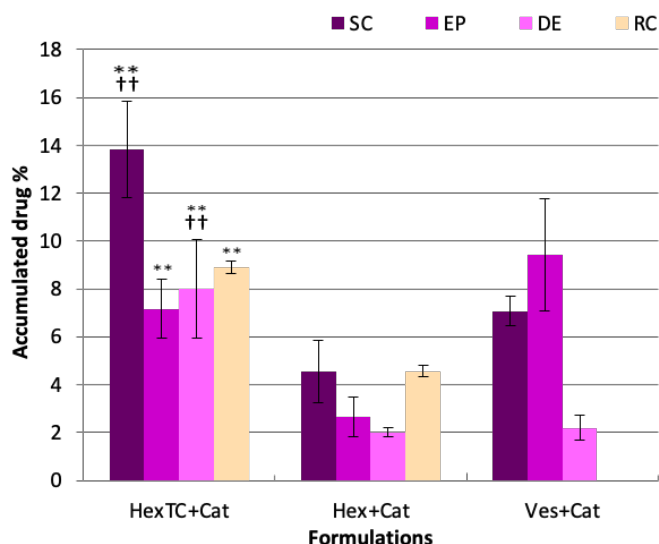


**Figure 4.6.** Cumulative amount of catechin retained into and permeated through the skin layers after 8 h treatment with TC-loaded hexosomes, HexTC + Cat, hexosomes without TC, Hex + Cat and a GMO-vesicle formulation, Ves + Cat. SC, stratum corneum; Ep, epidermis; D, dermis; and RC, receptor compartment

Finally, an *in vitro* DDPH test showed that the antioxidant activity of catechin was preserved within the different LLCNPs, highlighting that the encapsulation did not affect the antioxidant properties.

### 4.3. Conclusions and future perspectives

The addition of permeation enhancers and edge activators can tune both the physico-chemical and penetration properties of GMO-based LLCNPs. Subsequently, the modification of the critical packing parameter of GMO (due to the presence of other amphiphiles) allows the formation of several architectures that can be adopted as drug carriers. Both liquid and gel-like formulations applied on the skin permit to avoid the harsh gastrointestinal environment that can affect the drug delivery and the stability of the carriers.

LCh has been already used as additive in GMO-formulations, showing good performances in delivering drugs in the first layers of the skin, without systemic absorption. Indeed, the amount of dispersed lipids in the carrier and the contact time with the skin can be tuned in order to achieve the dermal or transdermal release of the bio-active compounds, as shown in **Paper IV**. **Paper V** represents the first proof of concept of BSs-loaded hexosomes for topical administration of antioxidants. The inverse hexagonal phase architectures enable to load a higher content of drugs, given the higher hydrophobic volume per nanoparticle. The presence of sodium taurocholate, an edge activator, improved the penetration properties of the hexosomal formulation, in comparison with formulations not containing BSs. **Paper V** validates BSs as enhancers of the penetration properties of LLCNPs. The addition of sodium taurocholate improved the dermal release of various antioxidants, given the ability of the edge activators to disturb the brick and mortar matrix of the SC. For pH-sensitive drugs or antioxidants used in cancer therapy as adjuvant, the amount of BSs and of the permeation enhancers could be tuned in order to evaluate the improved systemic absorption. The diffusion through the lipid matrix is found to be different in bicontinuous cubic, hexagonal or lamellar phases.[22] Therefore, the impact of different architectures on the skin release should be considered in future studies.

## 4.4. References

- [1] F. Lai, C. Caddeo, M.L. Manca, M. Manconi, C. Sinico, A.M. Fadda, What's new in the field of phospholipid vesicular nanocarriers for skin drug delivery, *Int. J. Pharm.* 583 (2020). <https://doi.org/10.1016/j.ijpharm.2020.119398>.
- [2] G. Cevc, G. Blume, New, highly efficient formulation of diclofenac for the topical, transdermal administration in ultradeformable drug carriers, *Transfersomes, Biochim. Biophys. Acta - Biomembr.* (2001). [https://doi.org/10.1016/S0005-2736\(01\)00369-8](https://doi.org/10.1016/S0005-2736(01)00369-8).
- [3] M.R. Prausnitz, R. Langer, Transdermal drug delivery, *Nat. Biotechnol.* 26 (2008) 1261–1268. <https://doi.org/10.1038/nbt.1504>.
- [4] V.R. Sinha, M. Pal Kaur, Permeation enhancers for transdermal drug delivery, *Drug Dev. Ind. Pharm.* 26 (2000) 1131–1140. <https://doi.org/10.1081/DDC-100100984>.
- [5] R. Gupta, B.S. Dwadasi, B. Rai, S. Mitragotri, Effect of Chemical Permeation Enhancers on Skin Permeability: In silico screening using Molecular Dynamics simulations, *Sci. Rep.* 9 (2019) 1–11. <https://doi.org/10.1038/s41598-018-37900-0>.
- [6] G. Cevc, U. Vierl, Nanotechnology and the transdermal route. A state of the art review and critical appraisal, *J. Control. Release.* (2010). <https://doi.org/10.1016/j.jconrel.2009.10.016>.
- [7] G. Cevc, Transfersomes, liposomes and other lipid suspensions on the skin: Permeation enhancement, vesicle penetration, and transdermal drug delivery, *Crit. Rev. Ther. Drug Carrier Syst.* (1996). <https://doi.org/10.1615/CritRevTherDrugCarrierSyst.v13.i3-4.30>.
- [8] L.M. de Buy Wenniger, T. Pusch, U. Beuers, *Bile Salts*, 2nd ed., Elsevier Inc., 2013. <https://doi.org/10.1016/B978-0-12-378630-2.00031-1>.
- [9] C. Faustino, C. Serafim, P. Rijo, C.P. Reis, Bile acids and bile acid derivatives: use in drug delivery systems and as therapeutic agents, *Expert Opin. Drug Deliv.* 13 (2016) 1133–1148. <https://doi.org/10.1080/17425247.2016.1178233>.
- [10] E. Moghimipour, A. Ameri, S. Handali, Absorption-Enhancing Effects of Bile Salts, *Molecules.* 20 (2015) 14451–14473. <https://doi.org/10.3390/molecules200814451>.
- [11] V.K. Rapalli, T. Waghule, N. Hans, A. Mahmood, S. Gorantla, S.K. Dubey, G. Singhvi, Insights of lyotropic liquid crystals in topical drug delivery for targeting various skin disorders, *J. Mol. Liq.* 315 (2020). <https://doi.org/10.1016/j.molliq.2020.113771>.
- [12] N.R. Rarokar, S.D. Saoji, N.A. Raut, J.B. Taksande, P.B. Khedekar, V.S. Dave, Nanostructured Cubosomes in a Thermoresponsive Depot System: An Alternative Approach for the Controlled Delivery of Docetaxel, *AAPS PharmSciTech.* 17 (2016) 436–445. <https://doi.org/10.1208/s12249-015-0369-y>.
- [13] S. Jenni, G. Picci, M. Fornasier, M. Mamusa, J. Schmidt, Y. Talmon, A. Sour, V. Heitz, S. Murgia, C. Caltagirone, Multifunctional cubic liquid crystalline nanoparticles for chemo- And photodynamic synergistic cancer therapy, *Photochem. Photobiol. Sci.* (2020). <https://doi.org/10.1039/c9pp00449a>.
- [14] U. Bazylińska, J. Kulbacka, J. Schmidt, Y. Talmon, S. Murgia, Polymer-free cubosomes for simultaneous bioimaging and photodynamic action of photosensitizers in melanoma skin cancer cells, *J. Colloid Interface Sci.* 522 (2018) 163–173. <https://doi.org/10.1016/j.jcis.2018.03.063>.
- [15] M. Cohen-Avrahami, D. Libster, A. Aserin, N. Garti, Penetratin-induced transdermal delivery from H II

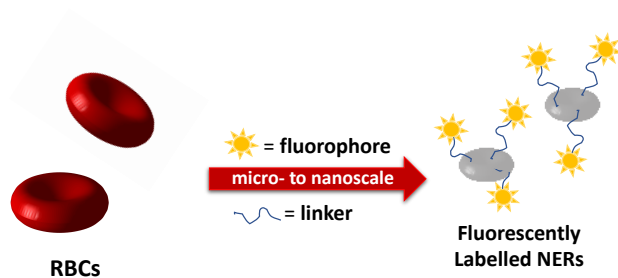
- mesophases of sodium diclofenac, *J. Control. Release.* 159 (2012) 419–428.  
<https://doi.org/10.1016/j.jconrel.2012.01.025>.
- [16] M. Cohen-Avrahami, A. Aserin, N. Garti, HII mesophase and peptide cell-penetrating enhancers for improved transdermal delivery of sodium diclofenac, *Colloids Surfaces B Biointerfaces.* 77 (2010) 131–138. <https://doi.org/10.1016/j.colsurfb.2010.01.013>.
- [17] M. Schlich, M. Fornasier, M. Nieddu, C. Sinico, S. Murgia, A. Rescigno, 3-Hydroxycoumarin Loaded Vesicles for Recombinant Human Tyrosinase Inhibition in Topical Applications, *Colloids Surfaces B Biointerfaces.* 171 (2018) 675–681. <https://doi.org/10.1016/j.colsurfb.2018.08.008>.
- [18] R. Angelico, M. Carboni, S. Lampis, J. Schmidt, Y. Talmon, M. Monduzzi, S. Murgia, Physicochemical and rheological properties of a novel monoolein-based vesicle gel, *Soft Matter.* 9 (2013) 921–928. <https://doi.org/10.1039/c2sm27215f>.
- [19] M. Carboni, A.M. Falchi, S. Lampis, C. Sinico, M.L. Manca, J. Schmidt, Y. Talmon, S. Murgia, M. Monduzzi, Physicochemical, Cytotoxic, and Dermal Release Features of a Novel Cationic Liposome Nanocarrier, *Adv. Healthc. Mater.* (2013). <https://doi.org/10.1002/adhm.201200302>.
- [20] G.M.M. El Maghraby, A.C. Williams, B.W. Barry, Interactions of surfactants (edge activators) and skin penetration enhancers with liposomes, *Int. J. Pharm.* 276 (2004) 143–161. <https://doi.org/10.1016/j.ijpharm.2004.02.024>.
- [21] R. Kumar, A. Sirvi, S. Kaur, S.K. Samal, S. Roy, A.T. Sangamwar, Polymeric micelles based on amphiphilic oleic acid modified carboxymethyl chitosan for oral drug delivery of bcs class iv compound: Intestinal permeability and pharmacokinetic evaluation, *Eur. J. Pharm. Sci.* 153 (2020) 105466. <https://doi.org/10.1016/j.ejps.2020.105466>.
- [22] S. Aleandri, R. Mezzenga, The physics of lipidic mesophase delivery systems, *Phys. Today.* 73 (2020) 38–44. <https://doi.org/10.1063/PT.3.4522>.





# 5

## Cell-inspired nanovectors for imaging applications



### Chapter 5 – Cell-inspired nanovectors for imaging applications

5.1. NERs stability and functionalization routes

5.2. Conclusions and future perspectives

5.3. References

---

Colloidal scientists, pharmacists and chemists have been emulating nature and mimicking its architectures in order to prepare biocompatible carriers. Vesicles' structure represents an example given the similarities with living cells: for this reason, they were largely designed and developed in order to deliver drugs and imaging probes. Indeed, drawbacks such as low long-term stability and biocompatibility hinder their applications as nanomedicines.[1]

In the last two decades, a new approach have emerged: living cells and cellular structures can be exploited to formulate new nanocarriers.[2–4] Indeed, these materials display an enhanced biocompatibility *in vivo*[4] and they, in principle, should not trigger an immunological response. The concept of exploiting cell-inspired carriers goes back to the early 2000s: exosomes, vesicles deputed to the extra-cellular communication, were isolated from different matrices[3,5] and passively loaded with drugs.[5]

Red blood cells (RBCs)-inspired carriers can be prepared in hypotonic condition (osmolarity less than the value in the physiological environment, called isotonic): the hemoglobin content is then removed, and the cell membranes can reassemble in the microscale upon addition of an isotonic buffer, giving the so-called ghosts. They present high biocompatibility since they are made with the same components of RBCs.[4,6] However, they suffer from a significant drawback: their micrometric size induces fast clearance from the blood stream due to the activation of the RES.[4,7–9]

A significant attempt to improve the applicability of RBC-based vesicles was performed by Lejeune in 1994:[7] the size of the ghost was reduced through a protocol based on ultracentrifugation steps, obtaining a bluish solution. These dispersions are called nanoerythroosomes (NERs). They have been studied recently as drug carriers,[10–12] whereas their application in the imaging field has been limitedly characterized.

In fluorescent optical imaging field, the functionalization of the surface of the carrier with a fluorescent probe represent one strategy. Indeed, various functionalization route have been studied and proposed for an efficient labelling of the nanoparticles, but concerns regarding the

safety of the reactants used for the synthesis have been underlined.[13] Moreover, some compounds may display an amphiphilic behavior that could affect the integrity of the membrane. In this regard, click chemistry has proven to be a powerful tool in order to achieve a safe and efficient labelling.[14] It exploits a reaction among an azide and an alkyne, usually catalyzed by copper species, to obtain a stable covalent 1,2,3-triazole ring conjugate.

Such azide-alkyne cycloaddition found a rich variety of applications, especially in cell membrane functionalization.[15,16] Since the residue of Cu species in the reaction environment could affect the cell functionality or protein folding process,[15] a Cu-free click chemistry route called strain-promoted azide-alkyne cycloaddition (SpAAC) possess superior perks such as biocompatibility, stability, specificity and bio-orthogonality.[14,17–19]

With the aim to formulate a new imaging tool, the surface of the NERs aggregates was functionalized with two fluorophores evaluating their physico-chemical features (**Paper VI**).

## 5.1. NERs stability and functionalization routes

NERs were obtained from a total bovine blood sample, according to a protocol reported by Kuo *et al.* that was slightly improved.[20,21] It consists of several centrifugation and washing steps in order to separate the RBCs from the serum and the other blood components. The RBCs are then lysed in a hypotonic solution and the pellet (the disrupted cell membranes) is purified from the hemoglobin. Ultrasonication of the pellet in PBS pH 7.4 yields a bluish dispersion of NERs, characterized by an average hydrodynamic diameter of 100 nm and a high negative zeta potential of ca. – 30 mV. This figure can be explained by an ion adsorption at the NP-solution interface.

Both water and PBS pH 7.4 can be used to formulate NERs,[7,20] but the latter was found to be the best dispersant, given the higher stability of the particles (Figure 5.1). The apparent hydrodynamic diameter and the polydispersity index appeared to be stable in PBS, whereas aggregation processes were highlighted in water.

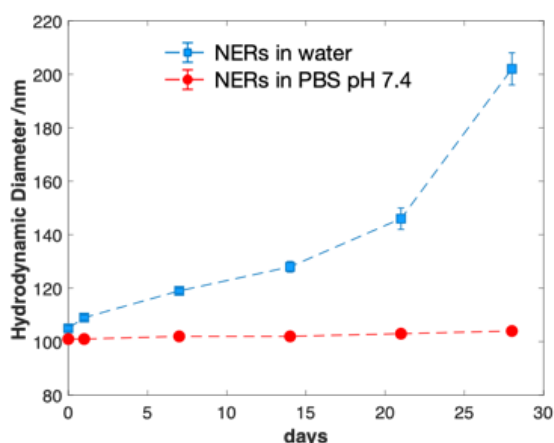


**Figure 5.1.** Investigation on NERs stability in water and PBS pH 7.4. Reproduced with permission from **Paper VI**. [21]

Moreover, the stability in PBS was checked for 5 months: in this timeframe, the formulation was found to be stable without any significant variations of the hydrodynamic radius and the PdI.

The morphology of the aggregate was studied in hypertonic conditions by Raghavan,[20] highlighting that it is reminiscent of that exhibited by RBCs, displaying the same biconcave structure. In physiological (isotonic) conditions (**Paper VI**), NERs showed a round-shape

vesicular morphology coexisting with some membranes not reassembled into vesicles (Fig. 5.2).



**Figure 5.2.** Cryo-TEM image of the NERs dispersion in isotonic condition. Black arrowheads point at pieces of membrane not reassembled, while the white arrows at unilamellar vesicles. Reproduced with permission from **Paper VI**. [21]

This finding can be explained by a membrane flipping process during the reconstituting process, a common phenomenon during membrane reconstruction after shearing. Moreover, the sonication applied during the preparation could solubilized some membrane proteins materials that aggregates in solution with their lipid surroundings, [22] originating the structures observed in the cryo-TEM image.

Assuming the retention of membrane structures that display free  $-NH_2$ , [7] NERs surface was decorated with two fluorophores following the scheme reported in Fig. 5.3.

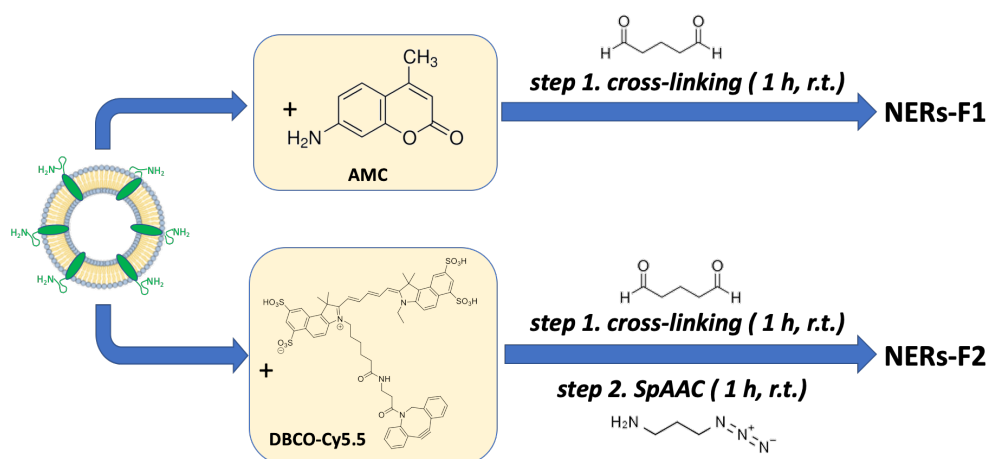


**Figure 5.3.** Functionalization scheme of the NERs dispersion to obtain the fluorescently labelled NERs-F1 and NERs-F2.

The cross-linking with glutaraldehyde permitted to bound on NERs surface (i) 7-ammino-3-methylcoumarin, a UV-Vis emitter, and (ii) a DBCO-Cy5.5, a NIR-emitter (exploiting also SpAAC in the latter case) to give NERs-F1 and NERs-F2, respectively.

Both reactions were found to be quite robust and reproducible, yielding concentration of the dyes suitable for imaging purposes.

The functionalization influenced mostly the  $\zeta$  potential of the formulations (Table 5.1), given the reduction of charged groups in the electric double layer related to the cross-linking reaction.

**Table 5.1.** Physico-chemical characterization of the formulations NERs, NERs-F1 and NERs-F2.

Formulation	$D_h$ [nm]	PdI	$\zeta$ -potential [mV]
NERs	101 ± 1	0.12 ± 0.01	-31.2 ± 1.1
NERs-F1	120 ± 4	0.20 ± 0.01	-23.2 ± 2.1
NERs-F2	127 ± 4	0.18 ± 0.02	-24.0 ± 2.3

The emission properties of the formulations were evaluated by means of fluorescence spectroscopy: in comparison with the free fluorophores, both dyes exhibited a red shift of the emission maxima, probably indicating that they are experiencing a more polar environment. Moreover, the labelled formulations showed a strong emission signal after dilution up to 1:500 in PBS pH 7.4.

Finally, NERs-F2, formulation for possible *in vivo* investigation, was studied using single-molecule fluorescence microscopy, being able to discern individual particles in the microscopy images. By analyzing this data, the average number of DBCO-Cy5.5 bound to the surface was estimated to be 1.5.

These appealing features highlight the importance of NERs formulation in both fields of imaging and drug delivery, especially when a personalized nano-tool is required in order to reduce the immunological response.

## 5.2. Conclusions and future perspectives

The use of cell-derived materials to produce drug and imaging probe carriers represent an appealing approach in the nanomedicine field. Indeed, the biocompatibility results enhanced, and the organism should recognize the nanovectors as autologous, being derived from bio-structures already present in the same organism. Reactions such as SpAAC and cross-linking permit to modify the surface of the carriers in an accessible and easy way, as shown in the data of **Paper VI**.

RBCs can be easily separated from the blood. Moreover, they are anucleate and contain mostly hemoglobin, therefore the preparation methods do not require several purification steps. Indeed, as NERs can be produced from RBCs, we could assume that other kind of cells, such as leukocytes or even cancer cells could provide the material to formulate biocompatible nanocarriers. For instance, Fang *et al.* used the membrane of B16F10 mouse melanoma and MDA-MB-435 human melanoma to coat polymeric NPs for applications in anticancer vaccination and drug delivery.[23]

In order to increase the selectivity of the treatment, targeting agents could be coupled on NERs surface. One example is represented by exendin-4, a ligand for GLP-1R expressed mainly in islets  $\beta$ -cells. In this way, a non-toxic and selective imaging tool of pancreatic  $\beta$ -cells could be provided.

## 5.3. References

- [1] S. Murgia, S. Biffi, R. Mezzenga, Recent advances of non-lamellar lyotropic liquid crystalline nanoparticles in nanomedicine, *Curr. Opin. Colloid Interface Sci.* 48 (2020) 28–39. <https://doi.org/10.1016/j.cocis.2020.03.006>.
- [2] M.J. Haney, N.L. Klyachko, Y. Zhao, R. Gupta, E.G. Plotnikova, Z. He, T. Patel, A. Piroyan, M. Sokolsky, A. V. Kabanov, E. V. Batrakova, Exosomes as drug delivery vehicles for Parkinson’s disease therapy, *J. Control. Release.* 207 (2015) 18–30. <https://doi.org/10.1016/j.jconrel.2015.03.033>.
- [3] S.M. Patil, S.S. Sawant, N.K. Kunda, Exosomes as drug delivery systems: A brief overview and progress update, *Eur. J. Pharm. Biopharm.* 154 (2020) 259–269. <https://doi.org/10.1016/j.ejpb.2020.07.026>.
- [4] J. Yan, J. Yu, C. Wang, Z. Gu, Red Blood Cells for Drug Delivery, *Small Methods.* 1 (2017) 1700270. <https://doi.org/10.1002/smtd.201700270>.
- [5] R. Munagala, F. Aqil, J. Jeyabalan, R.C. Gupta, Bovine milk-derived exosomes for drug delivery, *Cancer Lett.* 371 (2016) 48–61. <https://doi.org/10.1016/j.canlet.2015.10.020>.
- [6] Y.W. Wu, H. Goubran, J. Seghatchian, T. Burnouf, Smart blood cell and microvesicle-based Trojan horse drug delivery: Merging expertise in blood transfusion and biomedical engineering in the field of nanomedicine, *Transfus. Apher. Sci.* 54 (2016). <https://doi.org/10.1016/j.transci.2016.04.013>.
- [7] A. Lejeune, M. Moorjani, C. Gicquaud, J. Lacroix, P. Poyet, C.R. Gaudreault, Nanoerythroosome, a new derivative of erythrocyte ghost: Preparation and antineoplastic potential as drug carrier for daunorubicin, *Anticancer Res.* 14 (1994) 915–919.
- [8] A. Lejeune, P. Poyet, R. C.-Gaudreault, C. Gicquaud, Nanoerythroosomes, a new derivative of erythrocyte ghost: III. Is phagocytosis involved in the mechanism of action?, *Anticancer Res.* 17 (1997) 3599–3603.
- [9] J. Désilets, A. Lejeune, J. Mercer, C. Gicquaud, Nanoerythroosomes, a new derivative of erythrocyte ghost: IV. Fate of reinjected nanoerythroosomes, *Anticancer Res.* (2001).
- [10] K.A. Nangare, S.D. Powar, S.A. Payghan, Nanoerythroosomes : Engineered, 2016 (2016) 223–233.
- [11] X. Han, S. Shen, Q. Fan, G. Chen, E. Archibong, G. Dotti, Z. Liu, Z. Gu, C. Wang, Red blood cell-derived nanoerythroosome for antigen delivery with enhanced cancer immunotherapy, *Sci. Adv.* 5 (2019) 1–10. <https://doi.org/10.1126/sciadv.aaw6870>.
- [12] C. Gutiérrez Millán, D.G. Bravo, J.M. Lanao, New erythrocyte-related delivery systems for biomedical applications, *J. Drug Deliv. Sci. Technol.* 42 (2017) 38–48. <https://doi.org/10.1016/j.jddst.2017.03.019>.
- [13] S. Chandrudu, P. Simerska, I. Toth, Chemical methods for peptide and protein production, *Molecules.* 18 (2013) 4373–4388. <https://doi.org/10.3390/molecules18044373>.
- [14] Y. Takayama, K. Kusamori, M. Nishikawa, Click chemistry as a tool for cell engineering and drug delivery, *Molecules.* 24 (2019). <https://doi.org/10.3390/molecules24010172>.
- [15] V. Hong, N.F. Steinmetz, M. Manchester, M.G. Finn, Labeling live cells by copper-catalyzed alkyne-azide click chemistry, *Bioconjug. Chem.* 21 (2010) 1912–1916. <https://doi.org/10.1021/bc100272z>.
- [16] W. Tang, M.L. Becker, “click” reactions: A versatile toolbox for the synthesis of peptide-conjugates, *Chem. Soc. Rev.* 43 (2014) 7013–7039. <https://doi.org/10.1039/c4cs00139g>.



- [17] N. Alcaraz, Q. Liu, E. Hanssen, A. Johnston, B.J. Boyd, Clickable Cubosomes for Antibody-Free Drug Targeting and Imaging Applications, *Bioconjug. Chem.* 29 (2018) 149–157. <https://doi.org/10.1021/acs.bioconjchem.7b00659>.
- [18] J.C. Jewett, C.R. Bertozzi, Cu-free click cycloaddition reactions in chemical biology, *Chem. Soc. Rev.* 39 (2010) 1272–1279. <https://doi.org/10.1039/b901970g>.
- [19] S. Azides, Copper- free Click Chemistry ( DBCO reagents ), (n.d.).
- [20] Y.C. Kuo, H.C. Wu, D. Hoang, W.E. Bentley, W.D. D’Souza, S.R. Raghavan, Colloidal Properties of Nanoerythrocytes Derived from Bovine Red Blood Cells, *Langmuir*. 32 (2016) 171–179. <https://doi.org/10.1021/acs.langmuir.5b03014>.
- [21] M. Fornasier, A. Porcheddu, A. Casu, S.R. Raghavan, P. Jönsson, K. Schillén, S. Murgia, Surface-modified nanoerythrocytes for potential optical imaging diagnostics, *J. Colloid Interface Sci.* (2021). <https://doi.org/10.1016/j.jcis.2020.08.032>.
- [22] R. Deák, J. Mihály, I.C. Szigyártó, T. Beke-Somfai, L. Turiák, L. Drahos, A. Wacha, A. Bóta, Z. Varga, Nanoerythrocytes tailoring: Lipid induced protein scaffolding in ghost membrane derived vesicles, *Mater. Sci. Eng. C*. 109 (2020) 110428. <https://doi.org/10.1016/j.msec.2019.110428>.
- [23] R.H. Fang, C.M.J. Hu, B.T. Luk, W. Gao, J.A. Copp, Y. Tai, D.E. O’Connor, L. Zhang, Cancer cell membrane-coated nanoparticles for anticancer vaccination and drug delivery, *Nano Lett.* 14 (2014) 2181–2188. <https://doi.org/10.1021/nl500618u>.



## Concluding remarks

Lipids present a rich phase behavior that can be exploited in order to formulate liquid crystalline dispersions. These systems have found application especially as selective and performant drug and probe carriers in the nanomedicine field. Both lamellar and non-lamellar liquid crystalline dispersions have been widely investigated, providing new theranostical approaches. The biocompatibility and the stabilization of these aggregates are main issues in the colloidal chemistry community. These aspects could hinder the applicability of cubosomes, hexosomes and vesicles as nanomedicine platforms. Unveiling the phenomena happening *in vitro* requires indeed a multi-technique approach based on bulk, surface and biological investigations. Moreover, the translation of these investigations to *in vivo* studies possess several pre-requirements, such as the biocompatibility of the formulation.

My PhD thesis gave an idea on some strategies that can be employed in order to enhance the physico-chemical and biological performances of LLCNPs: **(i)** the use of biocompatible stabilizers to formulate cubosomes suitable for systemic administrations, **(ii)** the addition of edge activators to hexosomes for topical administration and **(iii)** the formulation of cell-derived and fluorescently labelled carriers for application in bioimaging. All these approaches share the application of bio-surfactants (PPE, BSs, RBCs membranes) as key components.

Hemicellulose can be adopted as stabilizer for cubosomes, showing how the lignin content play a significant role in the stabilization of the inverse bicontinuous cubic dispersion.

A novel PPE, a biodegradable and biocompatible polymer, was able to stabilize efficiently the lipid-water interface in GMO-based cubosomes. The excellent colloidal stability and the biological features yield a suitable drug carrier. Indeed, hexosomes could be formulated (upon addition of oleic acid) in the same manner, giving more biocompatible inverse hexagonal phase dispersions. The formulations based on PPE as stabilizer should represent a valid alternative to poloxamer-stabilizer carriers for systemic administrations.

Another kind of bio-surfactants, BSs, provided an enhancement of the penetration properties of hexosomes on skin to deliver an antioxidant in the deeper skin *strata*. This investigation represents a first example of BSs-doped non-lamellar LLCNPs for topical administration. The penetration properties could be further improved by formulating cubosomes and hexosomes with a higher amount of edge activators and additives that counterbalance the effect of BSs on the curvature of the interface.

Indeed, carriers suitable for transdermal drug delivery could be formulated with both BSs and PPE: the first component should provide the penetration properties, whereas the stabilizer would confer the required biocompatibility of the NPs when they reach the bloodstream.

Finally, the concept of using cell-derived drug and probe carrier can ensure the highest-degree of biocompatibility. The cells can be harvested from the same patient to whom they will be injected in, creating a new approach in the field of personalized medicine. RBCs-inspired carriers, the nanoerythrocytes, can be efficiently decorated using different functionalization routes, such as cross-linking and SpAAC. The latter can provide bio-orthogonality and biocompatibility of 1,3,5-triazol rings, which emulate biological structures. The excellent emission properties of the NERs formulations fluorescently labelled with the FOI probes AMC and DBCO-Cy5.5 highlight the possible application of NERs in FOI. Moreover, their surface could be decorated with targeting agents, providing a selective delivery of the imaging probe into the target cell.

This thesis demonstrated that starting from simple physico-chemical and biological considerations, the performances of LLCNPs can be improved in order to tackle the challenges found in systemic and topical administrations of bio-active compounds.





# Annex

## **Disclosure**

**The published and submitted papers are reproduced in agreement with the policies of Elsevier and RCS.**

**For more information, see the following links:**

**<https://www.elsevier.com/about/policies/copyright>**

**<https://www.rsc.org/journals-books-databases/journal-authors-reviewers/licences-copyright-permissions/#reuse-permission-requests>**



# Paper I

*“Multifunctional cubic liquid crystalline nanoparticles for chemo- and photodynamic synergistic cancer therapy”*

S. Jenni, G. Picci, **M. Fornasier**, M. Mamusa, J. Schmidt, Y. Talmon, A. Sour, V. Heitz, S. Murgia, C. Caltagirone;

Photochemical & Photobiological Sciences, 2020, 19, 674-680.

**DOI: 10.1039/c9pp00449a**

Copyright © from RCS 2020



Cite this: DOI: 10.1039/c9pp00449a

## Multifunctional cubic liquid crystalline nanoparticles for chemo- and photodynamic synergistic cancer therapy†

Sébastien Jenni,<sup>‡a</sup> Giacomo Picci,<sup>‡b</sup> Marco Fornasier,<sup>b</sup> Marianna Mamusa,<sup>id c</sup> Judith Schmidt,<sup>d</sup> Yesshayahu Talmon,<sup>d</sup> Angélique Sour,<sup>a</sup> Valérie Heitz,<sup>id \*a</sup> Sergio Murgia<sup>id \*b</sup> and Claudia Caltagirone<sup>id \*b</sup>

With the aim of engineering multifunctional nanoparticles useful for cancer therapy, a diketopyrrolopyrrole-porphyrin based photosensitizer was here conjugated to a block copolymer (Pluronic F108), and used to stabilize in water lipidic cubic liquid crystalline nanoparticles (cubosomes), also loaded with the antineoplastic agent docetaxel. The physicochemical characterization by SAXS, DLS, and cryo-TEM demonstrated that the formulation consisted of cubosomes, about 150 nm in size, possessing a bicontinuous cubic structure (space group  $Pn3m$ ). The cellular imaging experiments proved that these nanoparticles localized in lysosomes and mitochondria, while cytotoxicity tests evidenced a slight but significant synergistic effect which, after irradiation, increased the toxicity induced by docetaxel alone, allowing further reduction of cell viability.

Received 16th November 2019,

Accepted 7th April 2020

DOI: 10.1039/c9pp00449a

rsc.li/pps

### 1. Introduction

Bicontinuous cubic liquid crystalline nanoparticles, universally known as cubosomes, represent a very peculiar class of soft matter-based materials that are different from their lamellar counterpart, liposomes. In cubosomes, the three-dimensional arrangement of the lipid bilayer is folded in space on an infinite periodic minimal surface of cubic symmetry and separates two interwoven water channels,<sup>1,2</sup> resembling that of bicontinuous cubic bulk phases.<sup>3,4</sup> In addition, since the lipid matrix completely fills the inner portion of the nanoparticles, compared to single-bilayer liposomes, cubosomes offer a larger (up to three times) hydrophobic volume, at the same time exposing to water only 60% of their surface with respect to that of liposomes.<sup>5</sup> Such characteristics made cubosomes extremely

interesting for pharmaceutical applications as drug delivery vehicles.<sup>6,7</sup> Therefore, cubosomes have been largely explored in nanomedicine, and numerous articles have been published discussing their potential for the topical,<sup>8–10</sup> enteral,<sup>11–14</sup> or parenteral<sup>15–21</sup> administration of drugs. Particularly, cubosomes can be designed to simultaneously transport imaging agents and therapeutic agents, so they can be effectively used in theranostic nanomedicine.<sup>22–24</sup> Although numerous investigations demonstrated that cubosomes may be somewhat cytotoxic, and some types of cubosome formulations were also shown to induce hemolysis,<sup>25,26</sup> they can be formulated and administered at a non-toxic concentration still useful for medical purposes. By contrast, only a few *in vivo* experiments have been performed so far, and much more are needed to fully understand the relevance of this kind of nanoparticle in medical applications.<sup>10,27–30</sup>

Among many therapeutic procedures approved by the US FDA, Photodynamic Therapy (PDT) has been proven as an interesting and emerging tool for cancer treatment, since its first application. PDT is a minimally invasive approach that can be safely combined with other antitumor treatments, such as chemotherapy, radiotherapy, and surgery.<sup>31</sup> It requires a photosensitizer (PS) molecule, light and oxygen. After injection of the PS into the bloodstream and its accumulation into the target tissues, light irradiation (600–800 nm) is applied. After absorption of light and intersystem crossing, the PS in the excited triplet state can transfer its energy to molecular oxygen O<sub>2</sub> (Type II process), giving highly cytotoxic <sup>1</sup>O<sub>2</sub> or it can react

<sup>a</sup>Laboratoire de Synthèse des Assemblages Moléculaires Multifonctionnels, Institut de Chimie de Strasbourg, CNRS/UMR 7177, Université de Strasbourg, 4, rue Blaise Pascal, 67000 Strasbourg, France. E-mail: v.heitz@unistra.fr

<sup>b</sup>Department of Chemical and Geological Sciences and CSGI, University of Cagliari, s.s. 554 bivio Sestu, 09042 Monserrato (CA), Italy. E-mail: ccaltagirone@unica.it, murgias@unica.it

<sup>c</sup>CSGI, Department of Chemistry Ugo Schiff, University of Florence, 50019 Sesto Fiorentino (FI), Italy

<sup>d</sup>Department of Chemical Engineering, Technion – Israel Institute of Technology, Haifa 3200003, Israel

† Electronic supplementary information (ESI) available: SAXS diffractogram. See DOI: 10.1039/c9pp00449a

‡ These authors contributed equally to this work.

with the surrounding biomolecules by electron or proton transfer (Type I process) leading to radical species that further react with oxygen to generate Radical Oxygen Species (ROSS).<sup>32</sup> The effects of the treatment are first the direct tumor cell death, microvascular damage, and later an inflammatory reaction that can lead to the development of systemic immunity.<sup>33</sup> The most reported structure of a PS is the tetrapyrrolic macrocycle due to its high absorption peak in the optical window of tissue, no dark toxicity, ability to generate singlet oxygen and relatively rapid clearance from healthy tissues.<sup>34–37</sup> Recent papers showed how a two-photon photosensitizer for PDT connected to one or two GdDOTA-based complexes could be used as a theranostic tool in PDT and MRI, giving low dark toxicity and promising results on HeLa cells.<sup>38,39</sup>

Enhancing the accumulation of the PS in the target tumor cells is one of the most important aims in PDT. The use of nanoparticles, soft or hard matter based, represents a strategy to achieve this goal; many examples of tumortropic active- and passive-targeted lipid-based and polymeric nanoparticles have been reported in the last few decades, showing how the high loading efficiency and the flexibility of the nanoparticles can improve the biodistribution, the blood circulation time of the photosensitizer, and the efficacy of PDT.<sup>40–42</sup>

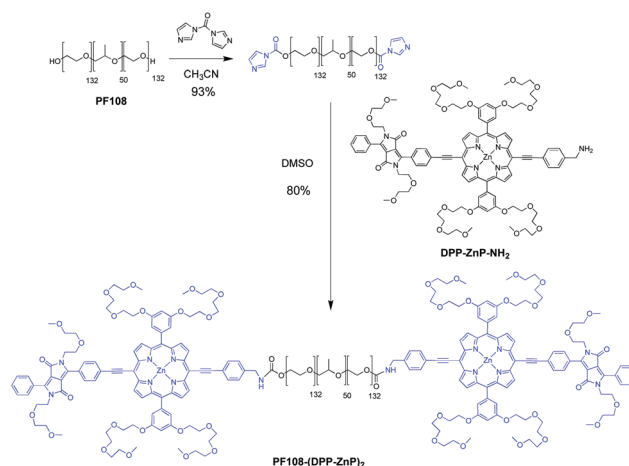
Cubosomes were recently proven useful in PDT. Indeed, polymer-free cubosomes proposed for topical applications were loaded with a photosensitizer, and used for bioimaging PDT of skin malignant melanoma cells. With respect to the free photosensitizer, a superior cytotoxic effect was detected when the latter was encapsulated within the cubosomes.<sup>9</sup> Here, a multifunctional fluorescent cubosome formulation was engineered for cancer PDT and chemotherapy after parental administration. Particularly, a newly synthesized fluorescent PS was conjugated to the block copolymer used to stabilize the nanoparticles in water, while docetaxel, an anti-neoplastic drug, was encapsulated in the nanoparticles.

It is notable that grafting imaging therapeutic molecules to the cubosome surface instead of encapsulating them between the lipid bilayer could be an effective strategy to avoid the phase transition of the inner phase, taking into account that lipid self-assembly processes are delicately poised, and can be easily altered by inserting molecules within the lipid palisade.

## 2. Results and discussion

### 2.1. Synthesis of the copolymer–photosensitizer conjugate

To simultaneously provide cubosomes with both imaging and therapeutic properties, docetaxel (DTX) was loaded within the lipid bilayer, while the PS **DPP-ZnP-NH<sub>2</sub>**<sup>38</sup> was covalently linked to the block copolymer **PF108** typically used to stabilize cubosomes in water. The diketopyrrolopyrrole-Zn(II)porphyrin conjugate **DPP-ZnP** was chosen as the PS based on our previous studies that revealed its fluorescence properties (quantum yield of 0.15 in DMSO), its good capacity to generate singlet oxygen (quantum yield of 0.54 in DMSO) and its ability to be an effective PS for PDT.<sup>37,43</sup>



Scheme 1 Synthetic scheme of **PF108-(DPP-ZnP)<sub>2</sub>**.

After activation of **PF108** with carbonyldiimidazole, an addition–elimination reaction with **DPP-ZnP-NH<sub>2</sub>** was performed in  $\text{CH}_3\text{CN}$  to obtain the conjugate **PF108-(DPP-ZnP)<sub>2</sub>** (Scheme 1).

### 2.2. Physicochemical and spectroscopic characterization of the cubosome formulation

Cubosomes loaded with **DTX** in the lipid bilayer were prepared, as reported in Section 3.3, using monoolein as the molecular building block and stabilizing the dispersion in water with 40% **PF108-(DPP-ZnP)<sub>2</sub>** and 60% classical **PF108**. The concentrations of **DTX** and PS in such a formulation were 1.1 mM with an EE% of 99.5% and 188  $\mu\text{M}$ , respectively. The 40/60 ratio between the conjugated and non-conjugated Pluronic was used to allow proper stabilization of the nanoparticles in water. Indeed, when 100% of the newly synthesized stabilizer was used, the formulation promptly phase separates.

The cubosome morphology was evaluated by cryo-TEM (Fig. 1). The nanoscopic inspection of the formulation disclosed the presence of polydisperse cubic and round shaped nanoparticles characterized by the dense inner lipid matrix usually shown by cubosomes. Analysis of the cryo-TEM picture

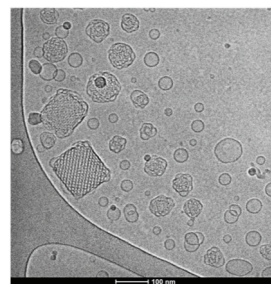


Fig. 1 Cryo-TEM image of the cubosome formulation stabilized 40% of **PF108-(DPP-ZnP)<sub>2</sub>** and 60% of **PF108**. The dark areas on the left side are part of the support film.

in Fig. 1 also revealed the presence of unilamellar vesicles, as frequently observed in cubosome formulations.

According to DLS, the cubosome average hydrodynamic diameter, polydispersity index, and  $\zeta$ -potential were found to be 159 nm, 0.20, and  $-21.9$  mV, respectively. These values are well within the range typically found for this kind of formulation.<sup>44–46</sup>

The inner bicontinuous cubic structure of the nanoparticles was definitely proved by SAXS. Particularly, the SAXS diffractogram reported in Fig. S1 (ESI)<sup>†</sup> is characterized by the superimposition of two patterns given by two different cubic bicontinuous liquid crystalline phases, one belonging to the  $Pn3m$  space group and the other to the  $Im3m$  space group. The coexistence of these two phases has already been reported in the literature. It is worth recalling here that, according to the monoolein/water binary phase diagram, at room temperature, an excess of monoolein in water gives only the  $Pn3m$  phase, and the presence of the  $Im3m$  phase in this system can be ascribed to the interaction of the block copolymer with the lipid bilayer. In a seminal work, Nakano demonstrated that the  $Im3m$  phase grows at the expense of the  $Pn3m$  phase as the Pluronic content (PF127 in that case) is increased.<sup>47</sup> On the basis of that observation, he suggested that the  $Im3m$  nanostructure originated from the incorporation of the surfactant in the bilayer. From the Bragg peaks detected in SAXS experiments on our nanoparticles, the calculated lattice parameters were  $136.8 \pm 0.2$  and  $100.1 \pm 0.2$  Å, respectively, for the  $Im3m$  and  $Pn3m$  phases, while the calculated radii of the water channels (see Section 3.5) were  $24.8 \pm 0.1$  and  $22.8 \pm 0.1$  Å.

These values are in good agreement with those typically found in similar systems, evidencing that the tiny amount of DTX added, and the conjugation of the PS to PF108 (rather than encapsulating it in the nanoparticles) did not modify the original cubosome nanostructure.

The absorption of an aqueous suspension of PF108-(DPP-ZnP)<sub>2</sub> stabilized cubosomes without DTX showed two bands with low resolution due to light scattering from the turbid suspension (ESI, Fig. S2<sup>†</sup>). They were ascribable to the Soret band at 456 nm and a Q band at 663 nm of the DPP-ZnP unit. The emission spectra recorded at room temperature (ESI Fig. S3<sup>†</sup>) showed an unstructured large emission band at 666 nm with a shoulder at 695 nm. Both absorption and emission features are in line with those reported for DPP-ZnP.<sup>43</sup>

### 2.3. Cellular imaging and cytotoxic activity

The PS DPP-ZnP-NH<sub>2</sub> conjugated to PF108 in the cubosome formulation is fluorescent, thus allowing cell localization studies. The cells were incubated with the cubosome formulation at a concentration of  $C_{500}$  (the original formulation was diluted 500 times) for 4 h. One hour before the acquisition of the images, Hoechst 33258, Mitotracker green or LysoTracker blue was also added (Fig. 2 and Fig. S4<sup>†</sup>).

A colocalisation between LysoTracker blue and cubosome fluorescence in lysosomes was observed. This lysosomal localization was also observed by other groups for this type of surfactant.<sup>48</sup> Quite surprisingly, a colocalization between the fluo-

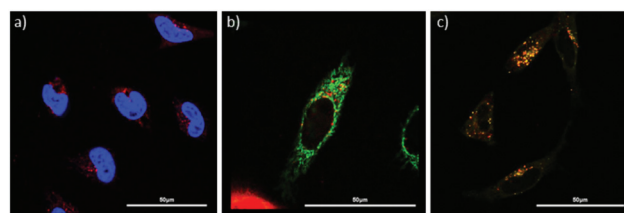


**Fig. 2** Confocal fluorescence images of HeLa cells after 4 h incubation with the cubosome formulation ( $C_{500}$ ) detected by its red fluorescence ( $\lambda_{\text{ex}}$ : 488 nm,  $\lambda_{\text{em}}$ : 700–800 nm); the cells are costained with (a) Hoechst 33258 ( $\lambda_{\text{ex}}$ : 405 nm,  $\lambda_{\text{em}}$ : 425–500 nm), (b) Mitotracker green ( $\lambda_{\text{ex}}$ : 488 nm,  $\lambda_{\text{em}}$ : 500–600 nm), and (c) LysoTracker blue ( $\lambda_{\text{ex}}$ : 405 nm,  $\lambda_{\text{em}}$ : 425–500 nm). Scale bar: 50  $\mu\text{m}$ .

rescence of the mitotracker and the cubosomes was also detected, suggesting mitochondria as an extra targeting site. Remarkably, localization studies performed with PF85 (having a structure analogous to PF108 linked to a fluorophore (tetramethylrhodamine)) also showed mitochondria localization.<sup>49</sup>

DTX is an antineoplastic drug, which causes cell death by acting on the microtubular network, preventing cell division.<sup>50</sup> It had been already demonstrated that dispersing DTX in a cubosome formulation increases its cytotoxicity by about one order of magnitude with respect to the molecularly dispersed drug.<sup>5</sup> As PDT does not induce anticancer resistance, and could be useful in killing localized resistant cells, a cubosome formulation was engineered, carrying both DTX and a PS, with the aim of providing a synergistic toxic effect in cancer cell killing.<sup>51</sup>

Cytotoxicity studies were performed on HeLa cells, 4 h after incubation of the cubosome formulation loaded or not with DTX. The cubosome concentrations were between  $C_{5000}$  and  $C_{50}$ , corresponding to a concentration of DPP-ZnP-NH<sub>2</sub> between 0.04  $\mu\text{M}$  and 3.8  $\mu\text{M}$ , and of DTX between 0.21  $\mu\text{M}$  and 21  $\mu\text{M}$ . The cell viability was evaluated with an MTT test and the results are presented in Fig. 3.

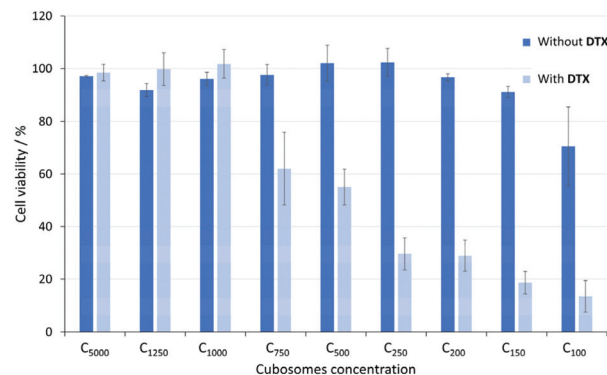


**Fig. 3** Cytotoxicity induced in HeLa cells by the cubosome formulation with PF108-(DPP-ZnP)<sub>2</sub> and with or without DTX, after 4 h incubation. The index numbers correspond to the dilution factor of the original formulation.

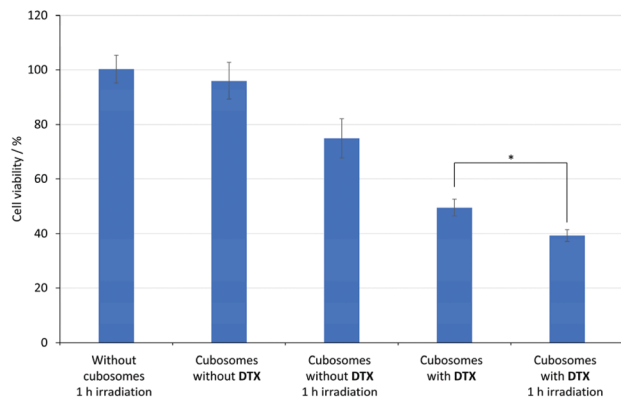


**Fig. 4** Phototoxicity on HeLa cells incubated for 4 h with a cubosome formulation with **PF108-(DPP-ZnP)<sub>2</sub>** and with or without **DTX**, after 1 h irradiation at 660 nm at 36 mW cm<sup>-2</sup>. Cell viability was evaluated 24 h after the irradiation. \*: Statistically significant difference ( $p < 0.05$ ) via the *t* test.

The cubosome stabilized with **PF108-(DPP-ZnP)<sub>2</sub>** and incorporated with **DTX** became toxic for a concentration of  $C_{750}$  and  $IC_{50}$  was estimated between  $C_{750}$  and  $C_{500}$ . It is interesting to note that cubosomes without **DTX** are not toxic at these concentrations suggesting that toxicity derived from the drug and not from the PS. This finding is in good agreement with the results previously obtained. A toxicity of 30% for a **DTX** concentration of 0.8  $\mu$ M after 4 h incubation in HeLa cells was reported.<sup>5</sup> In the present study, the cubosomes induced 40% of cell death at a concentration of **DTX** of 1.4  $\mu$ M.

The studies of phototoxicity induced by monophotonic excitation were performed on HeLa cells after incubation with a dispersion of cubosome formulation stabilized with **PF108-(DPP-ZnP)<sub>2</sub>**, with or without **DTX**. The cells were incubated at  $C_{750}$ , corresponding to a concentration of 0.25  $\mu$ M for the PS and 1.4  $\mu$ M for **DTX**, for 4 h. The cells were then irradiated at 660 nm for 1 h with a fluence rate of 36 mW cm<sup>-2</sup>. Cell viability was evaluated 24 h after the irradiation by the MTT test (Fig. 4).

According to the results obtained from this experiment, the cubosome formulation stabilized with **PF108-(DPP-ZnP)<sub>2</sub>** without **DTX** did not induce any toxic effect, while irradiation of the same formulation with a high light dose of 130 J cm<sup>-2</sup> caused phototoxicity at around 20%. It should be noticed that such a light dose did not induce cell death. When the cubosomes were loaded with **DTX**, the toxicity increased, reaching about 50%, while the irradiation of cubosomes incorporating **DTX** caused a further slight increase of the toxicity up to 60%, showing some additive effect between the photosensitizer and **DTX** in cell killing.

## 3. Experimental

### 3.1. Materials

Monoolein (MO, 1-monooleoylglycerol, RYLO MG 19 PHARMA, glycerol monooleate, 98.1 wt%) was kindly provided by

Danisco A/S, DK-7200, Grinsted, Denmark. Pluronic F108 (PF108, PEO132-PPO50-PEO132) was purchased from Sigma Aldrich, and docetaxel (**DTX**) from TCI Europe. Distilled water was used to prepare the sample and for the dilution, after passing through a Milli-Q water-purification system (Millipore).

All the materials were used without further purification. Compound **DPP-ZnP-NH<sub>2</sub>** and the CDI-Activated Pluronic F108 (F108-CDI) were prepared according to the literature.<sup>23,38</sup>

### 3.2. Synthesis of the conjugate **PF108-(DPP-ZnP)<sub>2</sub>**

To a solution of Pluronic F108-CDI (0.16 g, 0.011 mmol) in dry acetonitrile (10 mL), **DPP-ZnP-NH<sub>2</sub>** (40 mg, 0.022 mmol) was added and the mixture was kept stirring under a nitrogen atmosphere in the dark for 24 h. Then, the solution was concentrated and recrystallized in diethyl ether. The product was dried under reduced pressure and collected as a green powder. Yield: 80% <sup>1</sup>H NMR (500 MHz, DMSO-*d*<sub>6</sub>, 298 K):  $\delta_{\text{H}}$  1.05 (d,  $J = 6$  Hz, 3H  $\times$  50, -CH<sub>3</sub> of PPO), 2.65–2.75 (m, 2H  $\times$  2 protons adjacent to the terminal amine), 2.96 (q,  $J = 6$  Hz, 2H  $\times$  2 protons adjacent to the amide bond), 3.185–3.646 (m, peg chain), 3.47–3.54 (m, 3H  $\times$  50, 4H  $\times$  264, -CH<sub>2</sub>-CH(CH<sub>3</sub>)-O- of PPO and -CH<sub>2</sub>-CH<sub>2</sub>-O- of PEO), 7.00 (ar-H), 7.04 (ar-H), 7.35 (ar-H), 7.63 (ar-H), 8.26 (ar-H), 8.93 (d, pyr), 9.75 (d, pyr), 12.09 (-NH).

### 3.3. Cubosome preparation

Cubosomes were prepared by melting MO at 37 °C and then adding the appropriate amount of an aqueous solution of the stabilizers (**PF108/PF108-(DPP-ZnP)<sub>2</sub>**, molar ratio 60/40). Finally, the mixture was homogenized using a UP100H ultrasonic processor developed by Hiescher (cycle 0.9, amplitude 90%) for 5, 3, and 2 min cycles. Cubosomes loaded with **DTX** were obtained by dispersing the drug in the melted MO with the help of an ultrasonic bath before adding the Pluronic solution. The cubosome formulation used for the cellular studies was usually 2 mL with approximately 96.4 wt% water, 3.3 wt% MO, and 0.3 wt% of the Pluronic mixture.

### 3.4. Dialysis and encapsulation efficiency

The cubosome dispersion loaded with the drug was purified from the non-encapsulated **DTX** by dialysis as follows: 2 mL of cubosome dispersion were loaded into a dialysis tubing cellulose membrane (14 kDa MW cutoff, purchased by Sigma-Aldrich) and dialyzed against 2 L of water for 2 h at room temperature, replacing the water after 1 h. The encapsulation efficiency (EE%) of **DTX** was determined by UV-Vis spectroscopy after the disruption of cubosomes with ethanol reading the absorption of **DTX** at 283 nm in a Thermo Nicolet Evolution 300 UV-Vis Spectrophotometer. EE% was calculated using the following equation:<sup>52</sup>  $EE\% = (\text{weight of the drug in nanoparticles}) / (\text{weight of the feeding drug}) \times 100\%$ .

### 3.5. Small-angle X-ray scattering (SAXS)

SAXS patterns were recorded using an S3-MICRO SWAXS camera system (HECUS, X-ray Systems, Graz, Austria). The Cu

$K_{\alpha}$  wavelength (1.542 Å) was provided using a GeniX-X-ray generator (50 kV and 1 mA). A 1D-PSD-50 M system (HECUS, X-ray Systems, Graz, Austria) containing 1024 channels (54.0 μm) was used for the detection of scattered X-rays in the small angle region. The working  $q$  range was  $0.003 \leq q \leq 0.6$  (Å<sup>-1</sup>), where  $q = 4\pi\sin(\theta)\lambda^{-1}$  is the scattering vector. Thin-walled (2 mm) glass capillaries were filled with the cubosome dispersions. The SAXS patterns were recorded for 2 h. The camera volume was kept under vacuum during the measurements to minimize scattering from air. Silver behenate (CH<sub>3</sub>-(CH<sub>2</sub>)<sub>20</sub>-COOAg, a  $d$  spacing value of 58.38 Å) was used as the standard to calibrate the angular scale of the measured intensity.

The lattice parameter,  $a$ , for the bicontinuous cubic phases was calculated using the relation

$$a = d(h^2 + k^2 + l^2)^{1/2} \quad (1)$$

where  $d = 2\pi/q$  and  $h$ ,  $k$ , and  $l$  are the Miller indices. The water channel radii ( $r_w$ ) of the cubic phases were calculated using the equation

$$r_w = [(A_0 / -2\pi\chi)^{1/2}a] - L_{MO} \quad (2)$$

where  $L_{MO}$  is the length of the monoolein hydrophobic chain (17 Å), while  $A_0$  and  $\chi$  are, respectively, the surface area and the Euler characteristic of the IPMS geometries ( $Pn3m$ ,  $A_0 = 1.919$ ,  $\chi = -2$ ;  $Im3m$ ,  $A_0 = 2.345$ ,  $\chi = -4$ ). The length for the MO used in this study was originally calculated in the binary MO/water system.<sup>53</sup> Herein, it is assumed that this value does not vary significantly due to the presence of the Pluronic mixture at the interface.

### 3.6. Dynamic light scattering (DLS)

Each sample was diluted to 1:50 in Milli-Q water prior to any measurements. The intensity-weighted size distributions based on the apparent mean hydrodynamic diameter ( $D_h$ ) and polydispersity indexes (PdI) of cubosome formulations were determined by DLS. To this aim, a Nano Series Zetasizer from Malvern Instruments (Worcestershire, U. K.) at an angle of 173° in optically homogeneous square polystyrene cells was used. The measurements were performed at 25 °C and obtained as an average of three runs with at least 10 measurements.

The  $\zeta$ -potential of the nanoparticles was measured using the micro-electrophoretic method with the Malvern Zetasizer Nano ZS apparatus. Each value was obtained as an average of three subsequent runs of the instrument at 25 °C, with at least 20 measurements.

### 3.7. Spectroscopic measurements

The cubosome stock dispersion was diluted 100 times with distilled water. UV-vis spectra were recorded on a UVIKON XL spectrophotometer. Emission spectra were obtained using a spectrofluorometer FluoroMax from Horiba-Jobin Yvon.

### 3.8. Cell culture and MTT cell viability test

HeLa cells were cultured at 37 °C in DMEM complete culture medium containing phenol red with 5% CO<sub>2</sub>. They were

seeded and maintained in a 25 mL Falcon culture flask or multi well LabTek (Lab-Tek® II) culture flasks. Cell viability was assessed in pentaplicate by adding a solution of 3-(4,5-dimethyl-2-thiazolyl)-2,5-diphenyl-2H-tetrazolium bromide (50 μL of a 5 mg mL<sup>-1</sup> solution in DMEM by well). After an incubation period of 45 minutes, the media were removed and replaced by DMSO (150 μL). The absorbance was measured using a Safas Xenius spectrofluorimeter 96 well plate reader at 550 nm.

### 3.9. Dark cytotoxicity

HeLa cells were seeded in 96 well culture plates. After one day, the cells were incubated with different concentrations of cubosomes with or without DTX ( $C_{5000}$ - $C_{100}$  refers to the concentration obtained from the original formulation with the index number representing the dilution factor). After 4 h incubation, the cell viability was assessed using the MTT test described in Section 3.7.

### 3.10. Phototoxicity tests

One-photon phototoxicity tests were performed as described in the literature using homemade apparatus<sup>39,43</sup> with a 800 mA high power LED Deep Red (640–660 nm) (FutureEden™) adapted for Corning® 96 well special optic plates. HeLa cells were seeded in these plates for 24 h and incubated with cubosome solutions ( $C_{750}$ ) with or without DTX for 4 h. The medium was replaced by new DMEM free of cubosomes and the plates were irradiated for 1 h at a light power of 36 mW cm<sup>-2</sup>. The LED power was measured with a Thorlabs PM100D powermeter. The cell viability was then assessed 24 h after irradiation using the MTT test previously described.

## 4. Conclusions

With the aim of engineering a multifunctional cubosome formulation useful for imaging and therapeutic applications, a fluorescent PS, DPP-ZnP-NH<sub>2</sub>, was conjugated to the block copolymer PF108, used to stabilize the nanoparticles against phase separation. In addition, docetaxel, an antineoplastic drug, was loaded within the lipid bilayer to induce higher cell death, exploiting possible synergistic toxic effects. The physico-chemical characterization demonstrated that a stable cubosome formulation was obtained by using a mixture of the newly synthesized PF108-(DPP-ZnP)<sub>2</sub> and the commercial PF108 in a 40/60 ratio. Interestingly, after incubation with HeLa cells, the imaging experiments indicated localization of the fluorescence in lysosomes and mitochondria, while a slight but significant synergistic effect on increasing cytotoxicity was observed when docetaxel containing cubosomes incubated with HeLa cells were also irradiated to induce the monophotonic excitation of the photosensitizer.

On the whole, these results suggest that the proposed fluorescent formulation possesses some potential in combined chemo- and photodynamic therapy of cancer.

## Conflicts of interest

There are no conflicts to declare.

## Acknowledgements

The icFRC (<http://www.icfrc.fr>), LabEx CSC, are gratefully acknowledged for their support. The Ministry of Education and Research and the University of Strasbourg are acknowledged for a Ph.D. fellowship to S. J.

S. M. and C. C. thank Fondazione Banco di Sardegna and Regione Autonoma della Sardegna (Progetti Biennali d'Ateneo FdS/RAS Annualità 2016, CUP F72F16003060002). C. C. and G. P. acknowledge the financial support from MIUR (PRIN 2017 project 2017EKCS35). The cryo-TEM work was performed at the Technion Center for Electron Microscopy of Soft Matter, supported by the Technion Russell Berrie Nanotechnology Institute (RBNI).

C. C. and G. P. thank MIUR for PRIN 2017 (project 2017EKCS35).

## Notes and references

- H. M. G. Barriga, M. N. Holme and M. M. Stevens, *Angew. Chem., Int. Ed.*, 2019, **58**, 2958–2978.
- X. Mulet, B. J. Boyd and C. J. Drummond, *J. Colloid Interface Sci.*, 2013, **393**, 1–20.
- K. Larsson, *Nature*, 1983, **304**, 664.
- S. Murgia, S. Lampis, P. Zucca, E. Sanjust and M. Monduzzi, *J. Am. Chem. Soc.*, 2010, **132**, 16176–16184.
- V. Meli, C. Caltagirone, A. M. Falchi, S. T. Hyde, V. Lippolis, M. Monduzzi, M. Obiols-Rabasa, A. Rosa, J. Schmidt, Y. Talmon and S. Murgia, *Langmuir*, 2015, **31**, 9566–9575.
- I. D. Azmi, S. M. Moghimi and A. Yaghmur, *Ther. Delivery*, 2015, **6**, 1347–1364.
- Z. Karami and M. Hamidi, *Drug Discovery Today*, 2016, **21**, 789–801.
- L. Boge, K. Hallstenson, L. Ringstad, J. Johansson, T. Andersson, M. Davoudi, P. T. Larsson, M. Mahlapuu, J. Håkansson and M. Andersson, *Eur. J. Pharm. Biopharm.*, 2019, **134**, 60–67.
- U. Bazylińska, J. Kulbacka, J. Schmidt, Y. Talmon and S. Murgia, *J. Colloid Interface Sci.*, 2018, **522**, 163–173.
- S. Salah, A. A. Mahmoud and A. O. Kamel, *Drug Delivery*, 2017, **24**, 846–856.
- C. von Halling Laier, B. Gibson, M. van de Weert, B. J. Boyd, T. Rades, A. Boisen, S. Hook and L. H. Nielsen, *Int. J. Pharm.*, 2018, **550**, 35–44.
- Z. Liu, L. Luo, S. Zheng, Y. Niu, R. Bo, Y. Huang, J. Xing, Z. Li and D. Wang, *Int. J. Nanomed.*, 2016, **11**, 3571–3583.
- S. B. Rizwan, W. T. McBurney, K. Young, T. Hanley, B. J. Boyd, T. Rades and S. Hook, *J. Controlled Release*, 2013, **165**, 16–21.
- Y. S. R. Elnaggar, S. M. Etman, D. A. Abdelmonsif and O. Y. Abdallah, *Int. J. Nanomed.*, 2015, **10**, 5459–5473.
- M. Godlewska, A. Majkowska-Pilip, A. Stachurska, J. F. Biernat, D. Gawel and E. Nazaruk, *Electrochim. Acta*, 2019, **299**, 1–11.
- S. Akbar, A. Anwar, A. Ayish, J. M. Elliott and A. M. Squires, *Eur. J. Pharm. Sci.*, 2017, **101**, 31–42.
- E. Nazaruk, A. Majkowska-Pilip and R. Bilewicz, *ChemPlusChem*, 2017, **82**, 570–575.
- M. Szlezak, D. Nieciecka, A. Joniec, M. Pękała, E. Gorecka, M. Emo, M. J. Stébé, P. Krysiński and R. Bilewicz, *ACS Appl. Mater. Interfaces*, 2017, **9**, 2796–2805.
- J. Zhai, R. Suryadinata, B. Luan, N. Tran, T. M. Hinton, J. Ratcliffe, X. Hao and C. J. Drummond, *Faraday Discuss.*, 2016, **191**, 545–563.
- M. J. Kim and D. Y. Lee, *Macromol. Res.*, 2016, **24**, 197–204.
- S. Murgia, A. M. Falchi, V. Meli, K. Schillén, V. Lippolis, M. Monduzzi, A. Rosa, J. Schmidt, Y. Talmon, R. Bizzarri and C. Caltagirone, *Colloids Surf., B*, 2015, **129**, 87–94.
- S. Aleandri, D. Bandera, R. Mezzenga and E. M. Landau, *Langmuir*, 2015, **31**, 12770–12776.
- C. Caltagirone, A. M. Falchi, S. Lampis, V. Lippolis, V. Meli, M. Monduzzi, L. Prodi, J. Schmidt, M. Sgarzi, Y. Talmon, R. Bizzarri and S. Murgia, *Langmuir*, 2014, **30**, 6228–6236.
- S. Deshpande, E. Venugopal, S. Ramagiri, J. R. Bellare, G. Kumaraswamy and N. Singh, *ACS Appl. Mater. Interfaces*, 2014, **6**, 17126–17133.
- J. Barauskas, C. Cervin, M. Jankunec, M. Špandryeva, K. Ribokaitė, F. Tiberg and M. Johnsson, *Int. J. Pharm.*, 2010, **391**, 284–291.
- J. C. Bode, J. Kuntsche, S. S. Funari and H. Bunjes, *Int. J. Pharm.*, 2013, **448**, 87–95.
- X. Shi, T. Peng, Y. Huang, L. Mei, Y. Gu, J. Huang, K. Han, G. Li, C. Hu, X. Pan and C. Wu, *Pharm. Dev. Technol.*, 2017, **22**, 322–329.
- N. Tran, N. Bye, B. A. Moffat, D. K. Wright, A. Cuddihy, T. M. Hinton, A. M. Hawley, N. P. Reynolds, L. J. Waddington, X. Mulet, A. M. Turnley, M. C. Morganti-Kossmann and B. W. Muir, *Mater. Sci. Eng., C*, 2017, **71**, 584–593.
- S. Biffi, C. Garrovo, P. Macor, C. Tripodo, S. Zorzet, E. Secco, F. Tedesco and V. Lorusso, *Mol. Imaging*, 2008, **7**, 272–282.
- C. Nilsson, B. Barrios-Lopez, A. Kallinen, P. Laurinmäki, S. J. Butcher, M. Raki, J. Weisell, K. Bergström, S. W. Larsen, J. Østergaard, C. Larsen, A. Urtti, A. J. Airaksinen and A. Yaghmur, *Biomaterials*, 2013, **34**, 8491–8503.
- P. Agostinis, K. Berg, K. A. Cengel, T. H. Foster, A. W. Girotti, S. O. Gollnick, S. M. Hahn, M. R. Hamblin, A. Juzeniene, D. Kessel, M. Korbelik, J. Moan, P. Mroz, D. Nowis, J. Piette, B. C. Wilson and G. Jakub, *CA. Cancer J. Clin.*, 2011, **61**, 250–281.
- C. S. Foote, *Science*, 1968, **162**, 963–970.
- J. S. Dysart and M. S. Patterson, *Phys. Med. Biol.*, 2005, **50**, 2597–2616.

- 34 R. R. Allison and C. H. Sibata, *Photodiagn. Photodyn. Ther.*, 2010, **7**, 61–75.
- 35 B. Chen, T. Roskams and P. A. M. de Witte, *Photochem. Photobiol.*, 2002, **76**, 509.
- 36 F. Bolze, S. Jenni, A. Sour and V. Heitz, *Chem. Commun.*, 2017, **53**, 12857–12877.
- 37 J. Schmitt, V. Heitz, A. Sour, F. Bolze, H. Ftouni, J. F. Nicoud, L. Flamigni and B. Ventura, *Angew. Chem., Int. Ed.*, 2015, **54**, 169–173.
- 38 J. Schmitt, V. Heitz, A. Sour, F. Bolze, P. Kessler, L. Flamigni, B. Ventura, C. S. Bonnet and É. Tóth, *Chem. – Eur. J.*, 2016, **22**, 2775–2786.
- 39 J. Schmitt, S. Jenni, A. Sour, V. Heitz, F. Bolze, A. Pallier, C. S. Bonnet, É. Tóth and B. Ventura, *Bioconjugate Chem.*, 2018, **29**, 3726–3738.
- 40 D. K. Chatterjee, L. S. Fong and Y. Zhang, *Adv. Drug Delivery Rev.*, 2008, **60**, 1627–1637.
- 41 H. Gong, Z. Dong, Y. Liu, S. Yin, L. Cheng, W. Xi, J. Xiang, K. Liu, Y. Li and Z. Liu, *Adv. Funct. Mater.*, 2014, **24**, 6492–6502.
- 42 S. S. Lucky, K. C. Soo and Y. Zhang, *Chem. Rev.*, 2015, **115**, 1990–2042.
- 43 S. Jenni, A. Sour, F. Bolze, B. Ventura and V. Heitz, *Org. Biomol. Chem.*, 2019, **17**, 6585–6594.
- 44 A. M. Falchi, A. Rosa, A. Atzeri, A. Incani, S. Lampis, V. Meli, C. Caltagirone and S. Murgia, *Toxicol. Res.*, 2015, **4**, 1025–1036.
- 45 E. Jabłonowska, E. Nazaruk, D. Matyszewska, C. Speziale, R. Mezzenga, E. M. Landau and R. Bilewicz, *Langmuir*, 2016, **32**, 9640–9648.
- 46 C. Montis, B. Castroflorio, M. Mendozza, A. Salvatore, D. Berti and P. Baglioni, *J. Colloid Interface Sci.*, 2015, **449**, 317–326.
- 47 M. Nakano, A. Sugita, H. Matsuoka and T. Handa, *Langmuir*, 2001, **17**, 3917–3922.
- 48 N. Rapoport, A. Marin, Y. Luo, G. D. Prestwich and M. Muniruzzaman, *J. Pharm. Sci.*, 2002, **91**, 157–170.
- 49 D. Y. Alakhova, N. Y. Rapoport, E. V. Batrakova, A. A. Timoshin, S. Li, D. Nicholls, V. Y. Alakhov and A. V. Kabanov, *J. Controlled Release*, 2010, **142**, 89–100.
- 50 P. Zhao and D. Astruc, *ChemMedChem*, 2012, **7**, 952–972.
- 51 M. Gary-Bobo, O. Hocine, D. Brevet, M. Maynadier, L. Raehm, S. Richeter, V. Charasson, B. Looock, A. Morère, P. Maillard, M. Garcia and J.-O. Durand, *Int. J. Pharm.*, 2012, **423**, 509–515.
- 52 Z. Liu, D. Liu, L. Wang, J. Zhang and N. Zhang, *Int. J. Mol. Sci.*, 2011, **12**, 1684–1696.
- 53 M. Briggs, J. Chung and H. Caffrey, *J. Phys. II*, 1996, **6**, 723–751.



## Electronic Supplementary Material (ESI)

### **Multifunctional cubic liquid crystalline nanoparticles for chemo- and photodynamic synergistic cancer therapy**

Sébastien Jenni,<sup>a</sup> Giacomo Picci,<sup>b</sup> Marco Fornasier,<sup>b</sup> Marianna Mamusa,<sup>c</sup> Judith Schmidt,<sup>d</sup>  
Yeshayahu Talmon,<sup>d</sup> Angélique Sour,<sup>a</sup> Valérie Heitz,<sup>\* a</sup> Sergio Murgia,<sup>\* b</sup> Claudia Caltagirone.<sup>\* b</sup>

<sup>a</sup>Laboratoire de Synthèse des Assemblages Moléculaires Multifonctionnels, Institut de Chimie de  
Strasbourg, CNRS/UMR 7177, Université de Strasbourg, 4, rue Blaise Pascal, 67000 Strasbourg, France.

<sup>b</sup>Department of Chemical and Geological Sciences and CSGI, University of Cagliari, s.s. 554 bivio Sestu,  
09042 Monserrato (CA), Italy.

<sup>c</sup>CSGI, Department of Chemistry Ugo Schiff, University of Florence, 50019 Sesto Fiorentino (FI), Italy.

<sup>d</sup>Department of Chemical Engineering, Technion – Israel Institute of Technology, Haifa 32000, Israel.

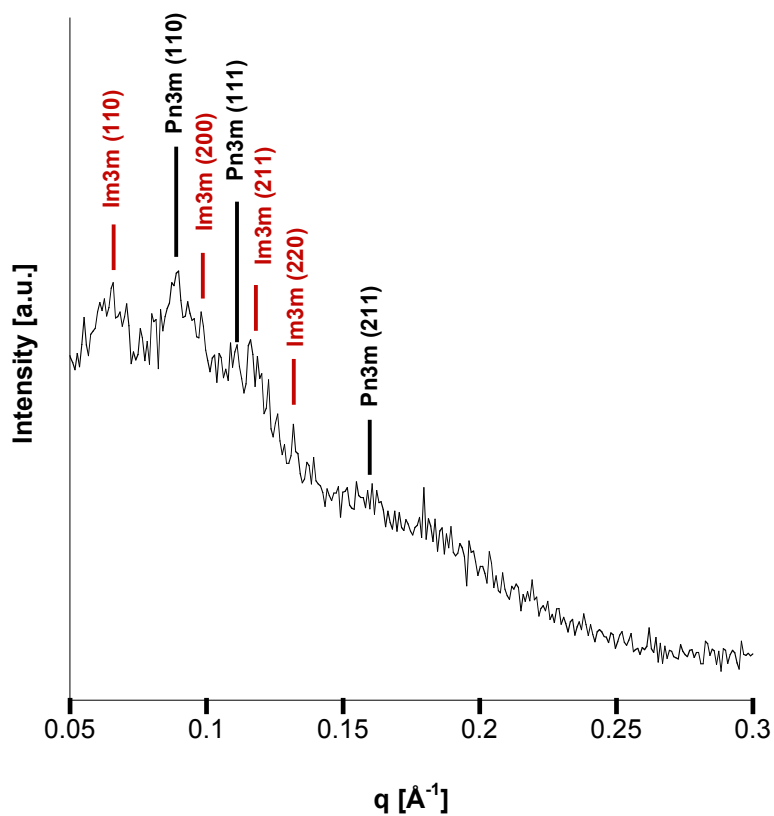
#### Table of content

Figure S1. SAXS diffractogram

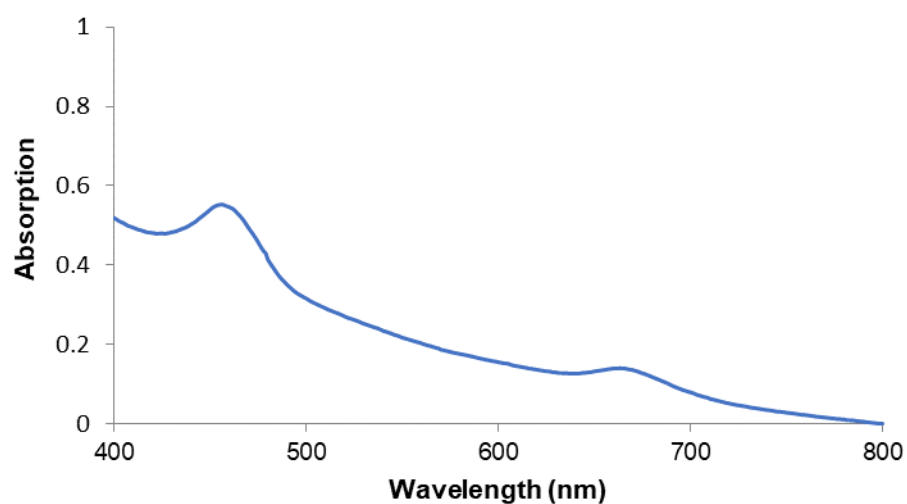
Figure S2. Absorption spectrum of an aqueous dispersion of cubosomes without  
DTX

Figure S3. Normalized emission spectrum of an aqueous dispersion of  
cubosomes without DTX

Figure S4. Fluorescence microscopy images of Hela cells after incubation with  
the cubosomes and organelle markers.



**Figure S1.** SAXS pattern of the cubosome formulation loaded with **DTX** and stabilized in water using a 60/40 mixture of **PF108** and **PF108-(DPP-ZnP)<sub>2</sub>**. The Miller indices for the Im3m and the Pn3m phases are shown on the top of the corresponding Bragg peak.



**Figure S2.** Absorption spectrum of an aqueous dispersion of cubosomes without **DTX**.

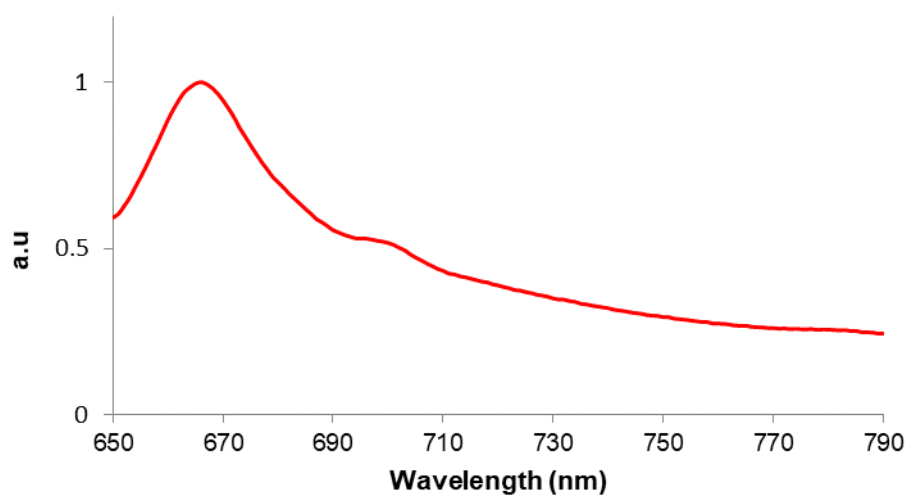


**Figure S3.** Normalized emission spectra of an aqueous dispersion of cubosomes without **DTX**,  $\lambda_{ex} = 480$  nm.

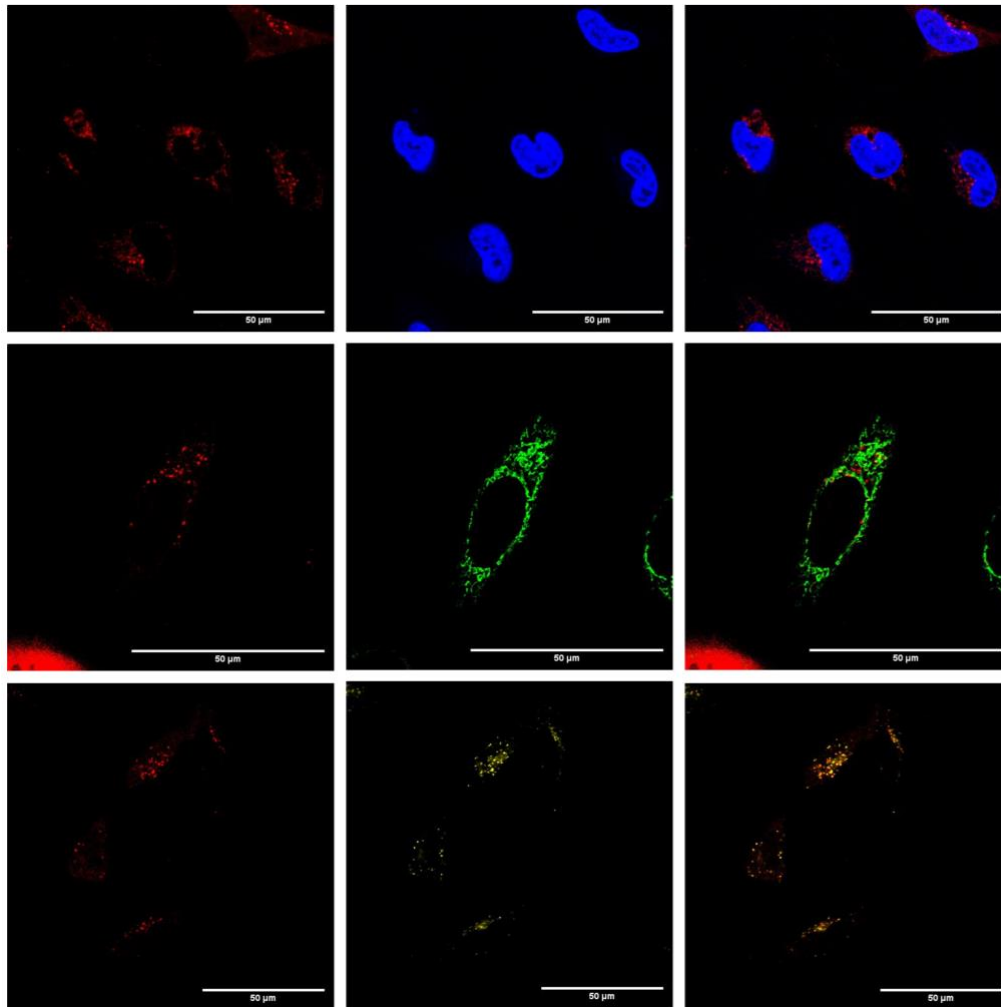


**Figure S4.** Confocal fluorescence images of HeLa cells incubated 4h with the cubosome formulation (C<sub>500</sub>) detected by its red fluorescence ( $\lambda_{\text{ex}}$ : 488 nm,  $\lambda_{\text{em}}$ : 700–800 nm) (left column) ; the cells are costained with Hoechst 33258 ( $\lambda_{\text{ex}}$ : 405 nm,  $\lambda_{\text{em}}$ : 425–500 nm) (top), Mitotracker green ( $\lambda_{\text{ex}}$ : 488 nm,  $\lambda_{\text{em}}$ : 500–600 nm) (middle), and (c) Lysotracker blue ( $\lambda_{\text{ex}}$ : 405 nm,  $\lambda_{\text{em}}$ : 425–500 nm) (bottom) ; the right row corresponds to the overlay. Scale bar: 50  $\mu\text{m}$ .

# Paper II

*“Bicontinuous cubic liquid crystalline phase nanoparticles stabilized by softwood hemicellulose”*

P. Naidjonoka\*, **M. Fornasier\***, D. Pålsson, Gregor Rudolph, Basel Al-Rudainy, S. Murgia, T. Nylander;

\*These authors equally contributed to the study.

Manuscript submitted to Colloids and Surfaces B, 2020.

# **Bicontinuous cubic liquid crystalline phase nanoparticles stabilized by softwood hemicellulose**

Polina Naidjonoka,<sup>a,§,\*</sup> Marco Fornasier,<sup>a,b,§,\*</sup> David Pålsson,<sup>a,§</sup> Gregor Rudolph<sup>c</sup>, Basel Al-Rudainy<sup>c</sup>, Sergio Murgia,<sup>b</sup> Tommy Nylander<sup>a,d,e</sup>

<sup>a</sup>*Division of Physical Chemistry, Department of Chemistry, Lund University, P.O. Box 124, Lund, SE-221 00, Sweden*

<sup>b</sup>*Department of Chemical and Geological Sciences, University of Cagliari, s.s 554 bivio Sestu, Monserrato I-09042, Italy*

<sup>c</sup>*Department of Chemical Engineering, Lund University, SE-221 00, Lund, Sweden.*

<sup>d</sup>*NanoLund, Lund University, Lund Sweden*

<sup>e</sup>*Lund Institute of Advanced Neutron and X-ray Science LINXS, Lund, Sweden.*

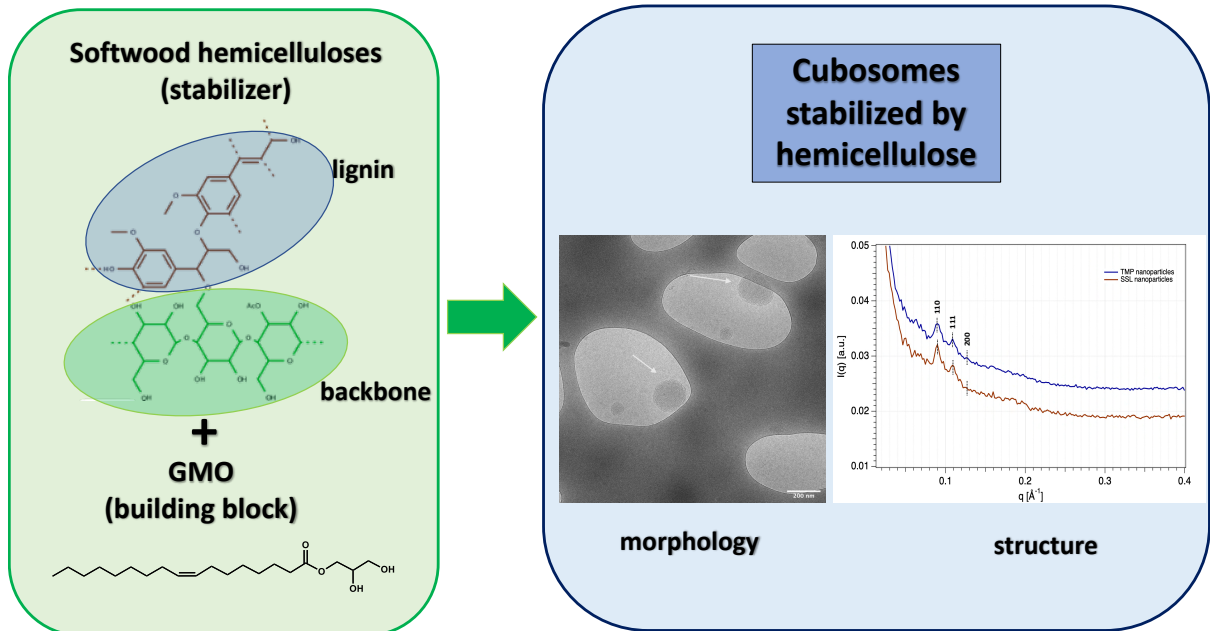
**§These authors equally contributed to this work.**

## **Corresponding Authors:**

Polina Naidjonoka (polina.naidjonoka@fkem1.lu.se)

Marco Fornasier (mfornasier@unica.it)

## Graphical Abstract



## **Abstract**

The colloidal stability of lipid based cubosomes, aqueous dispersion of inverse bicontinuous cubic phase, can be significantly increased by a stabilizer. The most commonly used are non-ionic tri-block copolymers, poloxamers, which adsorb at the lipid-water interface and hence sterically stabilize the dispersion. One of the challenges with these synthetic polymers is the effect on the internal structure of the cubosomes and the potential toxicity when these nanoparticles are applied as nanomedicine platforms. The natural polysaccharide, softwood hemicellulose, has been proved to be an excellent stabilizer for oil-in-water emulsions, partially due to the hydrophobic lignin which to some extent is associated to hemicellulose.

Herein, we reported for the first time cubosomes stabilized by two types of softwood hemicelluloses, where one is extracted through thermomechanical pulping (TMP, low lignin content) and the other from sodium-based sulfite liquor (SSL, high lignin content). The effect of the two hemicellulose samples on the colloidal stability and structure of GMO-based cubosomes have been investigated via DLS, SAXS, AFM and cryo-TEM. The data obtained suggest that both types of the hemicelluloses stabilize GMO based cubosomes in water without significantly affecting their size, morphology and inner structure. SSL-extracted hemicellulose yields the most stable cubosomes, likely due to the higher content of lignin in comparison to TMP-stabilized ones. In addition, the stability of these aggregates was tested under physiological conditions relevant to possible application as drug carriers.

## **Keywords**

cubosomes, stabilizer, hemicellulose, lignin



## Introduction

Non-lamellar Lipid Liquid Crystalline Nanoparticles (LLCNPs) have been widely studied in the last decades due to their intriguing structure and morphology. Examples of these kind of aggregates are cubosomes,<sup>1,2</sup> hexosomes<sup>2,3</sup> and the dispersion of sponge phase (spongosomes).<sup>4,5</sup>

Cubosomes are dispersions of an inverse bicontinuous cubic phase in which a curved non-intersecting bilayer forms two continuous and unconnected system water channels. The curved bilayer can be described by an infinite periodic minimal surface (IPMS), such as the primitive (Im3m), the gyroid (Ia3d) and the double-diamond (Pn3m). Monoolein (GMO) and phytantriol are among the most studied lipids that form cubic phase,<sup>1,6</sup> nevertheless other lipids can be adopted to formulate the particles.<sup>7,8</sup>

The preparation of the LLCNPs is based on a top-down, bottom-up or microfluidic approach. Lipid Liquid Crystalline (LLC) cubic bulk phase can be fragmented with e.g. homogenization involving high-energy input often with the help of an emulsifier. The most common bottom-up method yields the aggregates *via* dissolution of the lipid components in solvent and thereafter mixing of the lipid solution with an aqueous solution of additives to obtain the dispersion.

Colloidally stable cubosome dispersions require a stabilizing agent, such as tri-block copolymers, to a larger extent than their lamellar counterpart, liposomes. Here, poloxamers (poly(ethylene oxide)-poly(propylene oxide)-poly(ethylene oxide)), i.e. Pluronics F127 and F108, are the most common stabilizers, where the hydrophobic PPO moiety interacts with the lipid bilayer and the PEO units form a hydrophilic corona that prevents NPs from aggregating. The biocompatibility and biodegradability of the components of the formulations are crucial parameters for application of cubosomes in drug delivery and imaging.<sup>9-14</sup> Although the GMO-based carriers are less cytotoxic compared to those based on phytantriol,<sup>1,6</sup> the intrinsic cytotoxicity of the stabilizer could prevent the application of the system.<sup>15</sup> Therefore, stabilizing the cubic dispersion and at the same time providing a “safe” formulation can be challenging.

Recently, a polyphosphoester (PPE) tri-block copolymer, a structural analog of Pluronic F127, was shown to be able to stabilize GMO-based cubosomes.<sup>16</sup> Biocompatibility essay on Human umbilical vein endothelial cells (HUVEC) and blood cells showed that the PPE-stabilized NPs were less cytotoxic at the same concentration in comparison to the cubosomes stabilized with Pluronic F127. These new formulations were also shown to have less tendency to activate the complement system, which our body employs to remove anything foreign from the blood stream.

The cytotoxic effect can be reduced by mimicking natural molecular structures and thereby improving the efficacy of the therapy. For this reason, natural polysaccharides are of great interest as potential nanoparticle stabilizers. In addition, they can remain functional as stabilizers over a relatively broad range of temperatures and pH. However, lack of clear and structured amphiphilic character brings a variety of challenges to the table. Several studies have been published where monoolein cubosomes have been stabilized by different polysaccharides like starch and cellulose.<sup>17-19</sup> These polysaccharides were, however, modified by introducing hydrophobic groups in their structure. This is a promising alternative to commonly used

Pluronic F127 that is believed to have some unwanted physiological side effects when ingested or inhaled,<sup>19</sup> and also has shown to affect the internal structure of monoolein based cubosomes. Here we have explored the potential of hemicellulose that along with cellulose and lignin is one of the main polymer constituents of plant cell walls. Hemicelluloses are heteropolysaccharides that vary in structure and size depending on the plant type. Lignin, on the other hand, is a highly hydrophobic group of aromatic polyphenol compounds that are strongly associated with hemicelluloses and help to provide mechanical strength to the cell walls.<sup>20</sup> Hemicelluloses have been shown to have excellent emulsifying properties in several applications.<sup>21–26</sup>

The chemical composition of hemicellulose is dependent on the plant type and is often affected by the extraction method. A great variety of methods have been developed in order to obtain high purity extracts. However, one of the biggest challenges still remains the removal of lignin since it is covalently bound to hemicellulose sugar groups via glycosidic, ester or ether bonds.<sup>25</sup> Interestingly, when it comes to stabilizing oil in water emulsions, lignin plays an impartial role as it is believed to interact with the hydrophobic moiety of lipids and anchor hemicellulose chains on the interface. Hemicellulose in turn provides steric stabilization mechanism due to chains with high molecular weight.

The most abundant hemicellulose in spruce and pine is galactoglucomannan (GGM). It accounts for 25 – 35 % of dry wood mass.<sup>27,28</sup> Galactoglucomannans, often acetylated, have a linear (1→4)-linked  $\beta$ -D-mannopyranosyl (Man $p$ ) backbone partially substituted with (1→4)-linked  $\beta$ -D-glucopyranosyl (Glc $p$ ) units and  $\alpha$ -galactopyranosyl (Gal $p$ ) side groups that are (1→6)-linked to the backbone.<sup>29,30</sup>

In this study, we investigate the ability of two different softwood hemicellulose preparations to stabilize monoolein cubic nanoparticles. One is the TMP (thermomechanical pulping) hemicellulose, which has been isolated from thermomechanical pulp and contains a very low amount of lignin, whereas the SSL (spent-sulfite-liquor) preparation originates from a sodium-based sulphite liquor with high lignin concentration. The effect of these stabilizing agents on the physico-chemical properties of the lipid based cubosome was studied in order to identify their possible application as components to prepare future drug carriers.

## Experimental section

### Materials

The main component of the cubosomes, glycerol monooleate (MO, 1-monooleoylglycerol, RYLO MG 19 PHARMA, 98.1 wt% monoglycerides) was kindly provided by Danisco A/S (Denmark). Fresh distilled water purified using a Milli-Q® Water Purification system (MerckMillipore, Darmstadt, Germany) was used for preparing each sample and it was filtered with a 0.22 µm pore size hydrophilic filter prior to any use. Chloroform (99.8% purity) and phosphate buffered saline (PBS) tablets were purchased from Sigma-Aldrich (0.01 M phosphate buffer, 0.0027 M potassium chloride and 0.137 M sodium chloride).

The TMP hemicellulose sample was obtained from Stora Enso Kvarnsvedens bruk (Kvarnsveden, Sweden) and was purified by filtration and anti-solvent precipitation as described by Thuvander *et al.*<sup>31</sup> and Zasadowski *et al.*<sup>32</sup> The sample was characterized according to the National Renewable Energy Laboratory (NREL) procedure.<sup>33</sup> The SSL hemicellulose sample was provided by Domsjö Fabriker (Örnsköldsvik, Sweden) which was further ultrafiltrated and the components used in the study were precipitated with acetone. Details of the extraction procedure and analysis can be found at Al-Rudainy *et al.*<sup>34</sup> Table 1 shows a summary of the main components present in each of the samples.

**Table 1.** The chemical composition of the TMP and SSL hemicellulose extracts shown as weight percentage of total dry solids (TDS).

	Wt % of TDS	
	TMP	SSL
<b>Ash</b>	0	2.02
<b>Lignin</b>	1.26	7.3
<b>Carbohydrates</b>		
<b>Arabinose</b>	0	1.11
<b>Galactose</b>	10.4	18.7
<b>Glucose</b>	8.8	14.85
<b>Xylose</b>	4.7	7.05
<b>Mannose</b>	76	30.78
<b>Cellobiose</b>	n.d.	1.14
<b>Lactic acid</b>	n.d.	1.68
<b>Acetic acid</b>	n.d.	3.99
<b>Formic acid</b>	n.d.	1.63
<b>Levulinic acid</b>	n.d.	2.17
<b>Furfural</b>	n.d.	1.25
<b>Hydroxymethylfurfural</b>	n.d.	0.62

### Methods

#### Sample preparation

Cubosome formulations were prepared by first dissolving 10 mg of monoolein in 1 mL of chloroform in a vial. The chloroform was then evaporated under a gentle stream of nitrogen to yield a lipid film, which was left to dry under vacuum overnight at room temperature to remove any trace of chloroform. 1 mL of GGM aqueous solution with a concentration of 3 mg mL<sup>-1</sup> was then added to the vial with the monoolein film. The sample was vortexed for a few seconds and left to equilibrate at room temperature for one hour. After that, the mixture was placed in

an ice bath and sonicated with a tip sonicator (equipped with a controller Sonics Vibra Cells, both from Chemical Instruments AB, Sweden) for 15 min at 70% amplitude with 10 s pulses in 10 s intervals. The samples were characterized within 48 hours after preparation.

### **Dynamic Light Scattering (DLS) and Electrophoretic Mobility (EM)**

Dynamic light scattering experiments were performed on a Zetasizer Nano ZS (Malvern Instruments Ltd, Worshestershire, UK) at a set angle of 173° using the non-invasive backscatter technology. The instrument was equipped with a 4 mW He-Ne laser with a 632.8 nm wavelength and an Avalanche photodiode detection unit. The electrophoretic mobility measurements were performed using M3-PALS technology at 13°. The obtained correlation functions were analyzed using the cumulants method available in the Malvern software.

The cubosome formulations were diluted 500 times with either Milli-Q water or PBS buffer, placed in the Zetasizer measurement cell and equilibrated at 25°C for 2 minutes before starting the measurement.

### **Small Angle X-ray Scattering (SAXS)**

SAXS measurements were performed at the SAXSLab instrument (JJ-Xray, Denmark) available at Lund University. The instrument was equipped with a 30 W Cu X-RAY TUBE for GeniX 3D and a 2D 300 K Pilatus detector (Dectris). The X-ray wavelength was 1.54 Å<sup>-1</sup> and the sample-to-detector distance was 480 nm, yielding a q-range of 0.012 – 0.67 Å<sup>-1</sup>. The measurements were recorded at 25°C. The temperature was controlled using a Julabo T Controller CF41 from Julabo Labortechnik GmbH (Germany).

The magnitude of the scattering vector is defined by  $q = 4 \pi / (\lambda \cdot \sin\theta)$ , where the wavelength  $\lambda$  equals to 1.54 Å, Cu K $\alpha$  wavelength, and  $\theta$  is half of the scattering angle.

The repeat distance or  $d$  spacing was obtained using the following expression:

$$d = \frac{2\pi}{q} \quad (\text{eq. 1})$$

Then, the cubic phase lattice parameter ( $a$ ) is given by eq. 2:

$$a = d \cdot \sqrt{h^2 + k^2 + l^2} \quad (\text{eq. 2})$$

Here,  $h$ ,  $k$  and  $l$  are the Miller indexes that describe the crystalline planes into the liquid crystalline lattice. The lattice parameter was used to estimate the water channel radius ( $r_w$ ) of the bicontinuous cubic phase (eq. 3)<sup>35</sup>:

$$r_w = (a - l) \cdot \sqrt{\frac{A_0}{-2\pi\chi}} \quad (\text{eq. 3})$$

where  $\chi$  and  $A_0$  are the Euler characteristic and the surface area of the IPMS geometry (Pn3m,  $\chi = -2$ ,  $A_0 = 1.919$ ), respectively, and  $l$  is the MO hydrophobic chain length at 25 °C (17 Å).

The formulations in PBS buffer were prepared by diluting the aqueous stock of cubosome dispersion 10 times with the buffer.

### **Cryogenic-TEM (cryo-TEM)**

A 4  $\mu\text{L}$  drop of the formulations at the initial concentration was placed on a lacey carbon coated formvar grid (Ted Pella Inc, Redding, CA, USA). A thin film was then created by gently blotting the grid with a filter paper. After that the grid was prepared for imaging using an automatic plunge-freezer system (Leica Em GP, Leica Microsystems, Wetzlar, Germany). The environmental chamber was operated at 25  $^{\circ}\text{C}$  and 90% relative humidity to prevent evaporation from the sample. The specimen was vitrified by rapidly plunging the grid into liquid ethane ( $-183^{\circ}\text{C}$ ) and the samples were stored in liquid nitrogen ( $-196^{\circ}\text{C}$ ) and transferred into the microscope using a cryo transfer tomography holder (Fischione, Model 2550, E.A. Fischione Instruments, Inc., Corporate Circle Export, PA, USA). The grids were imaged with a Jeol JEM-2200FS transmission electron microscope (JEOL, Tokyo, Japan) equipped with a field-emission electron source, a cryo-pole piece in the objective lens and an in-column energy filter (omega filter). Zero-loss images were recorded with a bottom-mounted TemCam F416 digital camera (TVIPS-Tietz Video and Image Processing Systems GmbH, Gauting, Germany) using SerialEM under low-dose conditions at an acceleration voltage of 200 kV.

Gwyddion software was used to apply 2D Fourier transform filter to cryo-TEM micrographs and extract lattice parameter.

### **Atomic Force Microscopy (AFM)**

AFM was performed with a Park XE—100 (Park Systems Corp., Suwon, Korea) in a non-contact mode. Samples were probed in a liquid state under ambient conditions. A silicon cantilever with a 3 N/m spring constant and 75 kHz resonance frequency was used. The image analysis was done with the XEI software (Park Systems Corp., Suwon, Korea). A hydrophobized silicon wafer was covered with 90  $\mu\text{L}$  of SSL-NPs formulation and left to adsorb for 4 hours before rinsing with Milli-Q water. The wafer with liquid sample was then placed in the AFM liquid cell and Milli-Q water was added, after which the imaging was performed. The preparation was done in this way in order to avoid crossing air/water interface.

## **Results and Discussion**

### **Preparation of the NPs and their bulk characterization**

Formulations stabilized by softwood hemicellulose extracted with two different methods were prepared and characterized in a similar manner using ultrasonication. This approach has been found effective to reduce the size of the aggregates and inducing a good size distribution.<sup>1,6</sup>

After preparation, both formulations appeared homogeneous and milky, however the SSL-stabilized solution was less translucent than the TMP-stabilized sample. The DLS and  $\zeta$ -potential results, reported in Table 2, indicate that the formulations contain negatively charged, electrostatically stable particles of relatively low polydispersity.

**Table 2.** Apparent average hydrodynamic diameter ( $d_H$ ), polydispersity index (PdI), derived count rate,  $\zeta$ -potential and pH of pure TMP and SSL extract, as well as TMP-NPs and SSL-NPs determined at 25 °C.

Sample	$d_H \pm SD$ [nm]	PdI $\pm$ SD	Derived count rate $\pm$ SD	$\zeta$ -potential [mV]	pH
<b>TMP-NPs</b>	151 $\pm$ 1	0.21 $\pm$ 0.02	940 $\pm$ 3	-37.7	6.39
<b>SSL-NPs</b>	152.2 $\pm$ 0.9	0.19 $\pm$ 0.01	2032 $\pm$ 20	-49.5	6.52
<b>TMP</b>	-	-	-	-10 $\pm$ 1	6.44
<b>SSL</b>	-	-	-	-14.8 $\pm$ 0.2	6.58

The  $\zeta$ -potential of the TMP- and SSL- stabilized cubosomes was -37.7 and -49.5 mV, respectively. Negative charge of the nanoparticles could partially be explained by a negative  $\zeta$ -potential of their respective hemicellulose extracts (-18.3 and -32.7 mV for TMP and SSL, respectively). These values are lower than it was reported for GGM in literature.<sup>21,22</sup> However, the charge is highly dependent on the extraction method and the purity of the sample. Galactoglucomannans are neutral polysaccharides, the charge is believed to be caused by the presence of acidic groups.<sup>22</sup> The amount of acidic groups present in the TMP sample was not determined, however, the SSL extract contains at least 10% as shown in Table 1. Interestingly, the apparent negative charge is a common feature of the GMO-based dispersions: this phenomenon is not fully understood in literature, but it has been reported for other lipid formulations stabilized with non-ionic block-copolymers.<sup>16,36</sup> A possible reason could be related to an adsorption of hydroxide ions at the oil-water interface, resulting in a polarized outer layer surrounding the NPs and an apparent negative surface potential.<sup>37</sup>

Dispersions formulated with both GGMs exhibited the same size, around 150 nm in diameter, with relatively low polydispersity. Similar size and polydispersity have been previously reported in literature for cubosomes stabilized with different kinds of polymers.<sup>11,38</sup> The intensity of the scattering from the dispersion of the SSL-stabilized NPs is more than twice as high (2032  $\pm$  20) as from the TMP-NPs formulation (940  $\pm$  3), indicating a larger number of particles present in the solution. This finding correlates with the less translucent appearance of the former sample.

It has previously been shown that the presence of lignin in GGM strongly increases their capability in stabilizing oil in water emulsions.<sup>21,23–25</sup> Lignin consists of phenolic compounds that are usually associated or even covalently bound to hemicellulose sugar units via glycosidic, ester or ether bonds.<sup>25</sup> Due to their hydrophobic nature, phenolic residues interact with the hydrophobic part of the lipids and thus anchor bound hemicellulose chains that in turn provide steric stabilization of the oil/water interface. Consequently, a larger amount of nanoparticles in the sample could be stabilized by the SSL hemicellulose preparation, given its higher content of lignin. In addition, the SSL-NPs have a more negative  $\zeta$ -potential than the corresponding TMP-NPs. This could contribute to the electrostatic stabilization of the nanoparticles, although it has been suggested that emulsion stabilization with hemicellulose is mainly due to steric repulsion.<sup>39</sup>

SAXS was used to reveal internal NP structure. Figure 1 shows SAXS data TMP- and SSL-stabilized nanoparticles. Lyotropic GMO-based aqueous dispersions show a rich polymorphism depending on the water content.<sup>40</sup> In excess of water, monoolein is expected to form a Pn3m cubic phase. The presence of a stabilizer can affect monoolein self-assembly as reported by e.g. Nakano *et al.*<sup>41</sup> in cubosome dispersions stabilized by Pluronic F127. The interaction between the PPO lipophilic moiety of the stabilizer locally affects the organization of the lipid bilayer, giving two types bicontinuous cubic phases, Im3m and Pn3m, depending on the amount of added stabilizer. In the case of GGM-stabilized formulations, both of the SAXS curves have similar patterns with at least two clearly visible Bragg peaks, which corresponds to a Pn3m. This is highlighting that the GGM is covering the surface of the NPs without affecting the internal structure in water. This is in contrast to formulations stabilized with Pluronics. This finding represents a crucial point for a possible application of these aggregates as drug delivery systems. It has been shown that due to higher porosity, the diffusion coefficient of small hydrophilic molecules in Pn3m phase is larger than in Im3m phase.<sup>42</sup> On closer examination, lattice parameter and water channel radius could be determined from the scattering curves. As reported in Table 3, formulations contain particles with a lattice parameter characteristic to Pn3m phase cubosomes equal to 99.6 Å and 94.7 Å for TMP- and SSL-NPs, respectively.

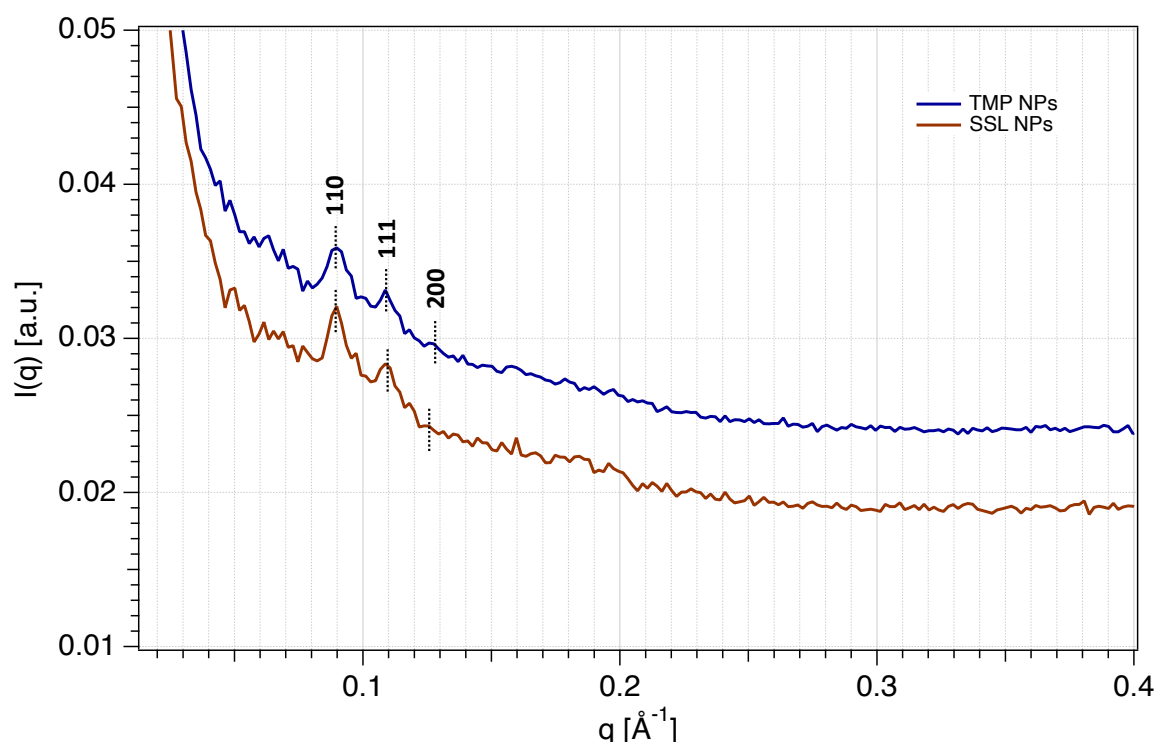


**Figure 1.** SAXS curves of the TMP (dark blue) and SSL (brown) nanoparticles. The scattering profile of the TMP was shifted upwards by a factor of 0.01 for clarity.

**Table 3.** Phase, lattice parameter ( $a$ ) and water channel radius ( $r_w$ ) of TMP-NPs and SSL-NPs as determined from SAXS curves seen in Figure 1. All SAXS measurements were performed at 25°C.

Sample	Phase	$a \pm \text{SD}$ [Å]	$r_w \pm \text{SD}$ [Å]
TMP-NPs	Pn3m	$99.6 \pm 0.8$	$21.9 \pm 0.3$

SSL-NPs	Pn3m	$98.7 \pm 0.4$	$21.6 \pm 0.1$
---------	------	----------------	----------------

These values of lattice parameters are in line with the ones already reported for Pluronic-stabilized cubosomes, with no significant difference between the two types of hemicellulose stabilizers.

In order to assess the morphology of the aggregates, the samples were imaged with cryo-TEM and the results of the two different formulations are shown in Figure 2 (TMP-NPs) and Figure 3 (SSL-NPs). In all of the micrographs, aggregates with a defined internal structure can be observed that agrees with the SAXS data showing the presence of a bicontinuous cubic phase dispersion.

As it can be seen from Figure 2, the TMP-NPs sample contains 200 – 250 nm large cubosomes, in addition to fractal-like aggregates. Different types of softwood hemicellulose have previously been shown to assemble into similar structures and therefore the aggregates observed in Figure 2 can be attributed to the excess hemicellulose that is not incorporated in the cubic nanoparticles.<sup>43,44</sup> Additionally, the TMP-stabilized sample contains a small amount of vesicles that are approximately 150 nm large (Figure 2B).

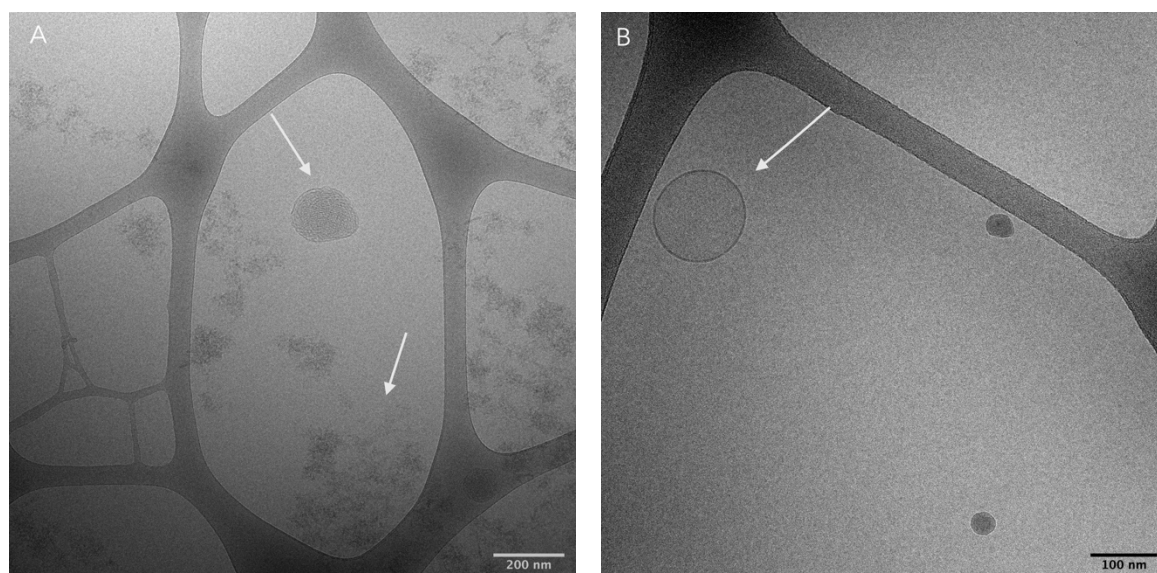


**Figure 2.** Cryo-TEM images of TMP-NPs at  $10\text{mg mL}^{-1}$  concentration incubated at  $25\text{ }^{\circ}\text{C}$  prior to blotting.

Figure 3 shows the cryo-TEM images of SSL-stabilized sample. This sample looks more homogenous without the presence of hemicellulose fractal structures. This indicates that most of the hemicellulose is associated with monoolein in the cubosomes. The cubosomes range in diameter from 50 – 200 nm that agrees well with the DLS results. Similar to the TMP-NPs, a low amount of vesicles is present in this sample as well (Figure 3B).

Since at this concentration, monoolein gives a Pn3m cubic phase with excess water, the presence of vesicles in the sample confirms that hemicellulose interacts with the monoolein lipid bilayer. This result is not surprising, since other studies have highlighted the effect that stabilizers can have on the morphology of cubosomes.<sup>36,38,45,46</sup> Here we note that in our study we observed a small or negligible fraction of vesicles.



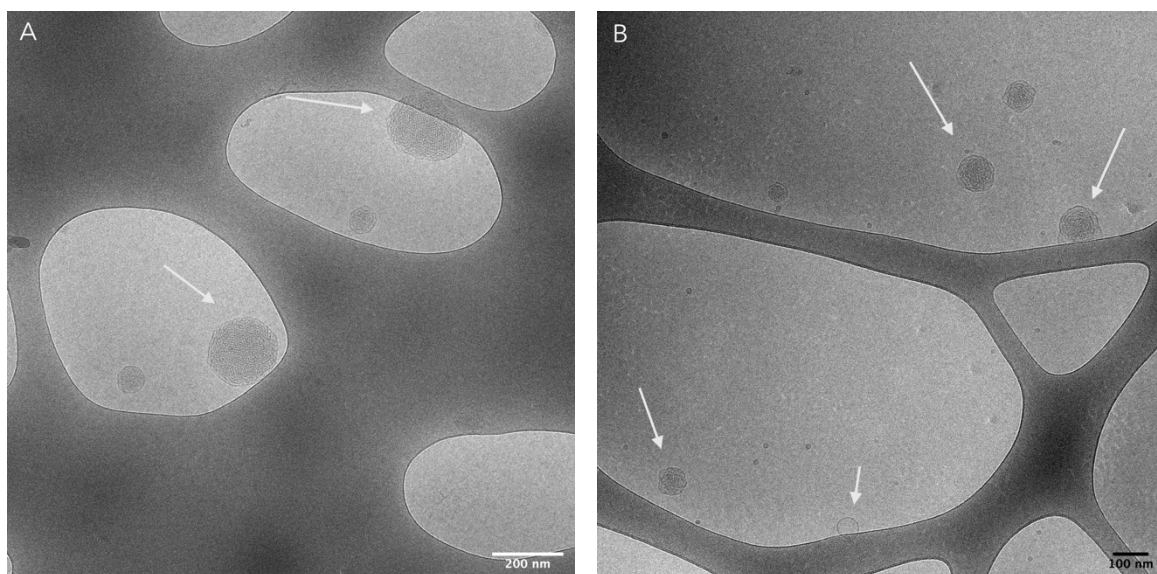


**Figure 3.** Cryo-TEM images of SSL-NPs at  $10\text{mg mL}^{-1}$  concentration incubated at  $25^\circ\text{C}$  prior to blotting.

In order to confirm internal structure of the nanoparticles, 2D Fourier transform filter was applied to the cryo-TEM images and lattice parameter was extracted. The Fourier transform filtered images of the cubosome internal structure can be seen in Figure 4. Obtained lattice parameters are  $89\text{ \AA}$  for TMP-NPs and  $110\text{ \AA}$  for SSL-NPs which agrees well with values extracted based on SAXS patterns.

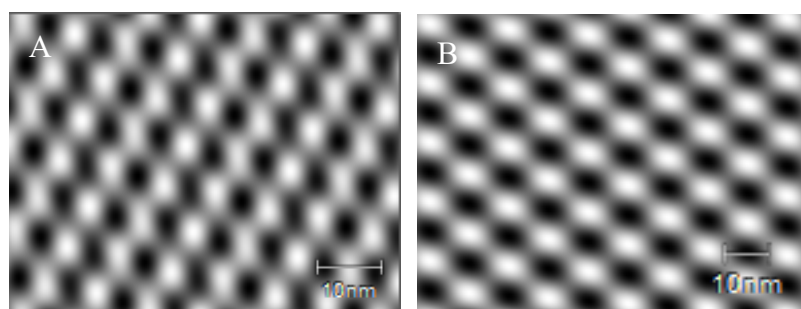


**Figure 4.** Fourier transform filtered images of cubosomes observed in cryo-TEM micrographs of TMP-NPs (A) and SSL-NPs (B).

### **Imaging of the nanoparticles on hydrophobic surface liquid AFM**

In addition to cryo-TEM, SSL-NPs were imaged with AFM on a hydrophobized silica surface in liquid mode. As it can be seen in Figure 5, the nanoparticles are generally  $30 - 60\text{ nm}$  in height and  $250 - 600\text{ nm}$  in diameter. The fact that the diameter is much larger than we have observed both with DLS and cryo-TEM, indicates that the cubosomes partly spread on the surface and adopt a flatter conformation.

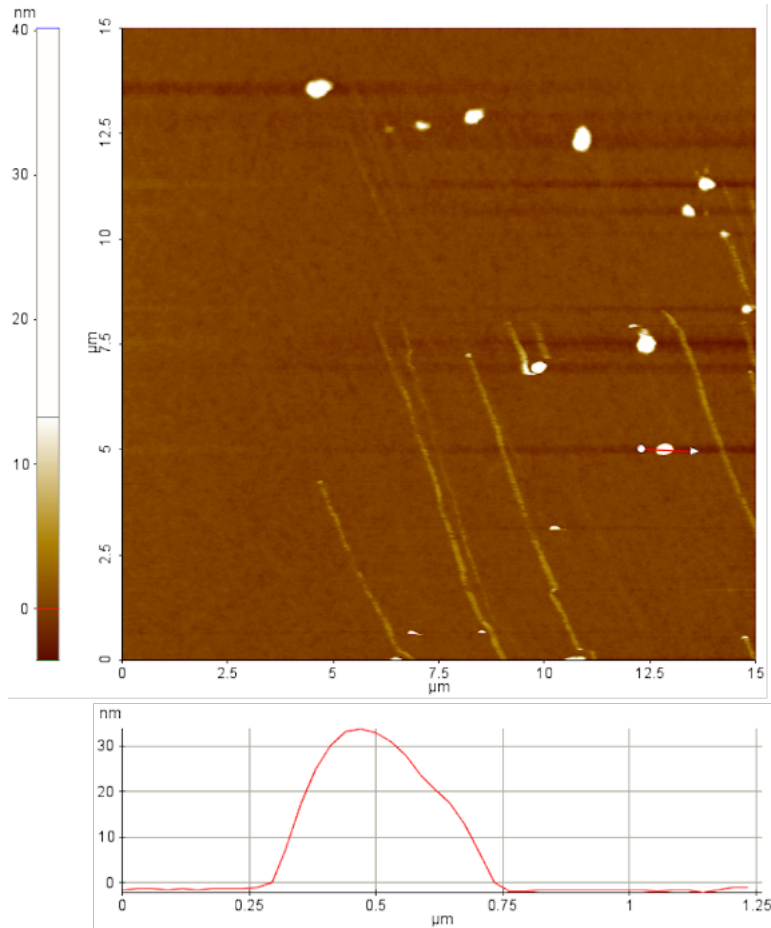


**Figure 5.** AFM images of SSL-NPs on hydrophobic silica in liquid obtained in tapping mode.

### Stability of the nanoparticles in water

The shelf-life presents a critical feature of a formulation, therefore understanding the colloidal stability over time is fundamental in applying these aggregates as drug carriers. The cubosomes dispersion stability over time has been investigated and the results are summarized in Figure 6. Both formulations are stable in terms of apparent hydrodynamic diameter and polydispersity index for at least 42 days at room temperature. These results show that both TMP and SSL extracts are stabilizing the lipid-water interface, preventing the system from flocculating.

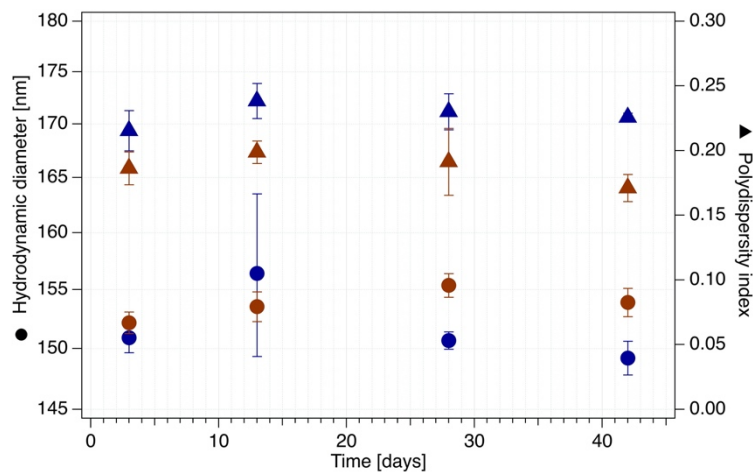


**Figure 6.** Hydrodynamic diameter (circles) and polydispersity (triangles) over time of TMP-NPs (dark blue) and SSL-NPs (brown).

### Effect of physiological environment

The application of cubosomes for drug delivery and other biomedical applications make their stability in a physiological environment a crucial requirement. Indeed, pH and salt concentration can affect lipid self-assembly in terms of size, charge and structure.<sup>47</sup> Taking these factors into account, 10 mM phosphate saline buffer (PBS) pH 7.4 has been used to mimic the physiological environment.

First, an aliquot of the formulations was diluted 500 times in PBS in order to follow the changes in the size and polydispersity of the nanoparticles under these conditions. The size of the nanoparticles of both formulations increases significantly (to 250 nm) at the start of the incubation but remains stable in case of SSL-NPs (Figure 7). However, the size of the TMP-NPs continues to increase for the next two hours until it reaches 400 nm. The polydispersity is relatively stable in SSL-stabilized sample over the whole investigated time span, while it increases from 0.15 to 0.25 during the first 3 hours in the TMP-stabilized formulation. These changes might indicate aggregation of particles due to screening effect caused by increasing the ionic strength with the added buffer.

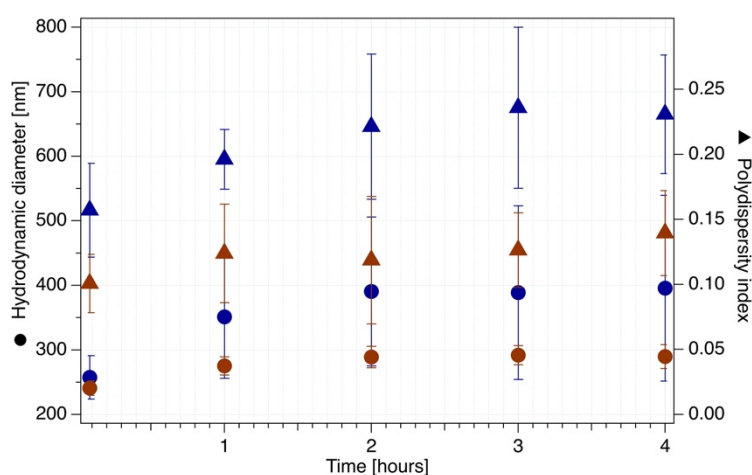


**Figure 7.** Hydrodynamic diameter (circles) and polydispersity (triangles) of TMP-NPs (dark blue) and SSL-NPs (brown) in PBS buffer over 4 h time period.

Indeed, the electrophoretic mobility measurements showed that the negative potential has decreased significantly explaining the reduction of the cubosome colloidal stability, which in particular for TMP-NPs causes aggregation (see Table 4).

**Table 4.**  $\zeta$ -potential of TMP-NPs, SSL-NPs, as well as TMP and SSL extracts in PBS buffer determined at 25 °C.

Sample	$\zeta$ -potential $\pm$ SD [mV]
TMP-NPs	-0.9 $\pm$ 0.4
SSL-NPs	-7.4 $\pm$ 0.9
TMP	-1 $\pm$ 2
SSL	-6 $\pm$ 2

The effect of PBS on the structure of the two GGMs stabilized cubosomes was evaluated through SAXS measurements. It has previously been reported that the change in ionic strength can trigger shift from one phase to another.<sup>48,49</sup>

Figure 8 shows the scattering curves of the TMP- and SSL-stabilized samples after dilution in PBS buffer 0.1 times.

The TMP-stabilized nanoparticles precipitated as soon as the buffer was added. The precipitation was observed with the SSL-stabilized sample as well, however to a lower extent and the sample still appeared milky after dilution. Indeed, the SAXS patterns confirm that the SSL-NPs retain Pn3m phase with no significant change in terms of lattice parameter and water channel radius after addition of the PBS buffer. The lattice parameter and water channel radius of the SSL-NPs in PBS buffer was  $93.1 \pm 0.4 \text{ \AA}$  and  $19.4 \pm 0.1 \text{ \AA}$ , respectively. On the other hand, the Bragg peaks completely disappear in case of the TMP-NPs indicating that the internal structure is at least partly lost. Similar tendency was observed with DLS: due to a much lower concentration, the aggregation of the TMP-NPs could not be monitored beyond a size of 400 nm.

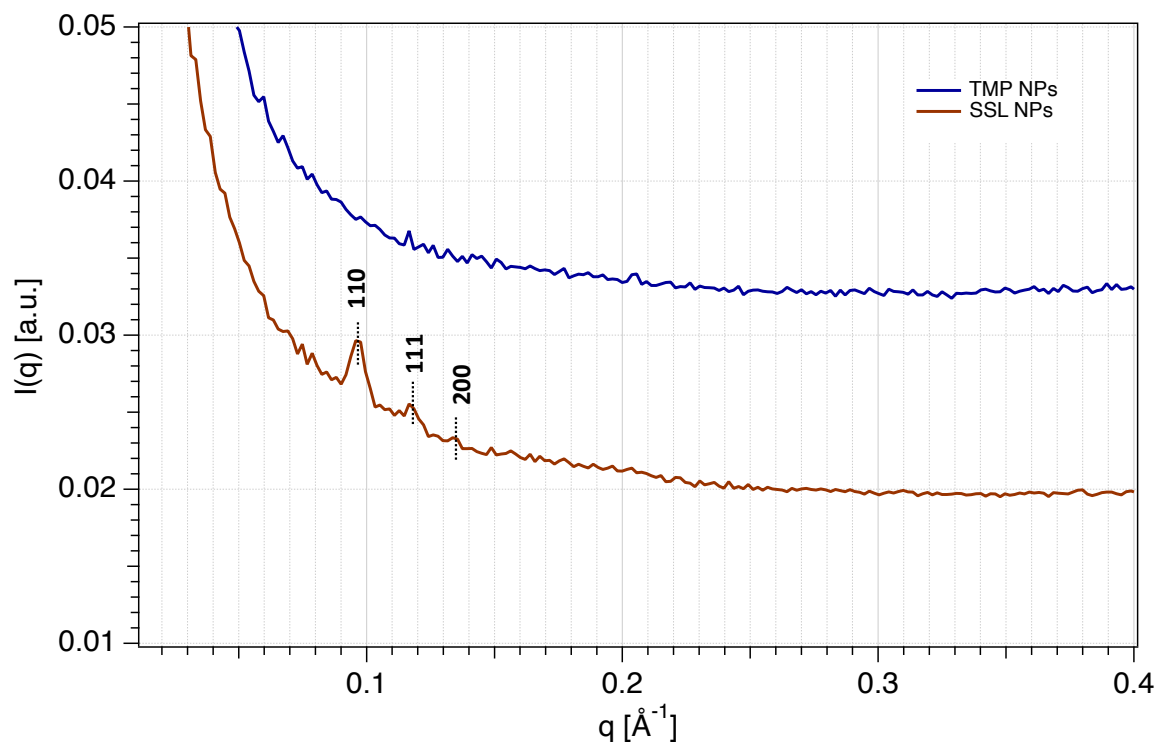


**Figure 8.** SAXS curves of the TMP (dark blue) and SSL (brown) nanoparticles in PBS buffer. The scattering curve of the TMP was shifted upwards by a factor of 0.01 for clarity.

The fact that the SSL-NPs formulation is more stable at an elevated ionic strength might be due to the higher  $\zeta$ -potential as presented in Table 2. Moreover, a larger amount of monoolein is dispersed in the SSL-NPs sample than in the TMP-NPs one.

## Conclusions

Softwood hemicellulose is an underutilized and abundant resource that can be used for a variety of applications thanks to its unique properties.<sup>23,26,50–52</sup> Its application as a stabilizer has already

been proven in previous studies for oil-in-water emulsions. Indeed, other hemicelluloses such as xylan have found application in several fields, given their promising biological features.<sup>53</sup> The ability of two softwood hemicellulose extracts, with different amounts of lignin, to stabilize monoolein-based cubosomes was investigated in this study. While both extracts were able to act as stabilizers, the higher lignin content in the SSL-extract facilitated stabilization of a larger fraction of the dispersed lipid phase. The presence of the hemicellulose extracts did not affect the self-assembly structure of monoolein in aqueous dispersions, giving a Pn3m bicontinuous cubic structure. Moreover, both formulations were stable over the period of at least 42 days with no significant changes in size or polydispersity.

Since the application of cubosomes is mostly related to nanomedicine applications, the stability of the formulations under physiological conditions was investigated. The results show that the physiological environment did not affect the structure for the SSL-stabilized cubosomes.

Indeed, the SSL-hemicellulose provided a better colloidal stability in comparison with the TMP-extract. This study shows that hemicellulose can be used as a natural substitute to Pluronics to stabilize lipid liquid crystalline nanoparticles. Further studies are needed to reveal the biological effect of these aggregates, hence *in vitro* investigations will be performed as a future perspective.

### Acknowledgements

The research in this work was financed by BIOFUNC research project (supported by the Swedish Foundation for Strategic Research RBP14-0046) and FORMAS. The National Center for High Resolution Electron Microscopy, Lund University, is gratefully acknowledged for providing experimental resources. We also thank Anna Carnerup for the support provided during the cryo-TEM measurements. The PhD scholarship of M.F. was funded by the program POR-FSE Sardegna 2014-2020.

### References

- (1) Barriga, H. M. G.; Holme, M. N.; Stevens, M. M. Cubosomes: The Next Generation of Smart Lipid Nanoparticles? *Angew. Chem. Int. Ed. Engl.* **2019**, *58* (10), 2958–2978. <https://doi.org/10.1002/anie.201804067>.
- (2) Neto, C.; Aloisi, G.; Baglioni, P.; Larsson, K. Imaging Soft Matter with the Atomic Force Microscope: Cubosomes and Hexosomes. *J. Phys. Chem. B* **1999**, *103* (19), 3896–3899. <https://doi.org/10.1021/jp984551b>.
- (3) Meli, V.; Caltagirone, C.; Sinico, C.; Lai, F.; Falchi, A. M.; Monduzzi, M.; Obiols-Rabasa, M.; Picci, G.; Rosa, A.; Schmidt, J.; Talmon, Y.; Murgia, S. Theranostic Hexosomes for Cancer Treatments: An *in Vitro* Study. *New Journal of Chemistry* **2017**, *41* (4), 1558–1565. <https://doi.org/10.1039/c6nj03232j>.
- (4) Chen, Y.; Angelova, A.; Angelov, B.; Drechsler, M.; M. Garamus, V.; Willumeit-Römer, R.; Zou, A. Sterically Stabilized Spongosomes for Multidrug Delivery of Anticancer Nanomedicines. *Journal of Materials Chemistry B* **2015**, *3* (39), 7734–7744. <https://doi.org/10.1039/C5TB01193K>.
- (5) Gilbert, J.; Valldeperas, M.; K. Dhayal, S.; Barauskas, J.; Dicko, C.; Nylander, T. Immobilisation of  $\beta$ -Galactosidase within a Lipid Sponge Phase: Structure, Stability and Kinetics Characterisation. *Nanoscale* **2019**, *11* (44), 21291–21301. <https://doi.org/10.1039/C9NR06675F>.

- (6) Murgia, S.; Biffi, S.; Mezzenga, R. Recent Advances of Non-Lamellar Lyotropic Liquid Crystalline Nanoparticles in Nanomedicine. *Current Opinion in Colloid & Interface Science* **2020**, *48*, 28–39. <https://doi.org/10.1016/j.cocis.2020.03.006>.
- (7) Magana, J. R.; Homs, M.; Esquena, J.; Freilich, I.; Kesselman, E.; Danino, D.; Rodríguez-Abreu, C.; Solans, C. Formulating Stable Hexosome Dispersions with a Technical Grade Diglycerol-Based Surfactant. *Journal of Colloid and Interface Science* **2019**, *550*, 73–80. <https://doi.org/10.1016/j.jcis.2019.04.084>.
- (8) Prajapati, R.; Salentinig, S.; Yaghmur, A. Temperature Triggering of Kinetically Trapped Self-Assemblies in Citrem-Phospholipid Nanoparticles. *Chemistry and Physics of Lipids* **2018**, *216*, 30–38. <https://doi.org/10.1016/j.chemphyslip.2018.09.003>.
- (9) Bazylińska, U.; Kulbacka, J.; Schmidt, J.; Talmon, Y.; Murgia, S. Polymer-Free Cubosomes for Simultaneous Bioimaging and Photodynamic Action of Photosensitizers in Melanoma Skin Cancer Cells. *Journal of Colloid and Interface Science* **2018**, *522*, 163–173. <https://doi.org/10.1016/j.jcis.2018.03.063>.
- (10) Biffi, S.; Andolfi, L.; Caltagirone, C.; Garrovo, C.; Falchi, A. M.; Lippolis, V.; Lorenzon, A.; Macor, P.; Meli, V.; Monduzzi, M.; Obiols-Rabasa, M.; Petrizza, L.; Prodi, L.; Rosa, A.; Schmidt, J.; Talmon, Y.; Murgia, S. Cubosomes Forin Vivofluorescence Lifetime Imaging. *Nanotechnology* **2016**, *28* (5), 055102. <https://doi.org/10.1088/1361-6528/28/5/055102>.
- (11) Murgia, S.; Falchi, A. M.; Meli, V.; Schillén, K.; Lippolis, V.; Monduzzi, M.; Rosa, A.; Schmidt, J.; Talmon, Y.; Bizzarri, R.; Caltagirone, C. Cubosome Formulations Stabilized by a Dansyl-Conjugated Block Copolymer for Possible Nanomedicine Applications. *Colloids and Surfaces B: Biointerfaces* **2015**, *129*, 87–94. <https://doi.org/10.1016/j.colsurfb.2015.03.025>.
- (12) Alcaraz, N.; Liu, Q.; Hanssen, E.; Johnston, A.; Boyd, B. J. Clickable Cubosomes for Antibody-Free Drug Targeting and Imaging Applications. *Bioconjugate Chem.* **2018**, *29* (1), 149–157. <https://doi.org/10.1021/acs.bioconjchem.7b00659>.
- (13) Boge, L.; Umerska, A.; Matougui, N.; Byssell, H.; Ringstad, L.; Davoudi, M.; Eriksson, J.; Edwards, K.; Andersson, M. Cubosomes Post-Loaded with Antimicrobial Peptides: Characterization, Bactericidal Effect and Proteolytic Stability. *International Journal of Pharmaceutics* **2017**, *526* (1), 400–412. <https://doi.org/10.1016/j.ijpharm.2017.04.082>.
- (14) Mendozza, M.; Montis, C.; Caselli, L.; Wolf, M.; Baglioni, P.; Berti, D. On the Thermotropic and Magnetotropic Phase Behavior of Lipid Liquid Crystals Containing Magnetic Nanoparticles. *Nanoscale* **2018**, *10* (7), 3480–3488. <https://doi.org/10.1039/C7NR08478A>.
- (15) Azmi, I. D. M.; Wibroe, P. P.; Wu, L.-P.; Kazem, A. I.; Amenitsch, H.; Moghimi, S. M.; Yaghmur, A. A Structurally Diverse Library of Safe-by-Design Citrem-Phospholipid Lamellar and Non-Lamellar Liquid Crystalline Nano-Assemblies. *J Control Release* **2016**, *239*, 1–9. <https://doi.org/10.1016/j.jconrel.2016.08.011>.
- (16) Fornasier, M.; Biffi, S.; Bortot, B.; Macor, P.; Manhart, A.; Wurm, F. R.; Murgia, S. Cubosomes Stabilized by a Polyphosphoester-Analog of Pluronic F127 with Reduced Cytotoxicity. *Journal of Colloid and Interface Science* **2020**, *580*, 286–297. <https://doi.org/10.1016/j.jcis.2020.07.038>.
- (17) Uyama, M.; Nakano, M.; Yamashita, J.; Handa, T. Useful Modified Cellulose Polymers as New Emulsifiers of Cubosomes. *Langmuir* **2009**, *25* (8), 4336–4338. <https://doi.org/10.1021/la900386q>.

- (18) Almgren, M.; Borné, J.; Feitosa, E.; Khan, A.; Lindman, B. Dispersed Lipid Liquid Crystalline Phases Stabilized by a Hydrophobically Modified Cellulose. *Langmuir* **2007**, *23* (5), 2768–2777. <https://doi.org/10.1021/la062482j>.
- (19) Spicer, P. T.; Small, W. B.; Small, W. B.; Lynch, M. L.; Burns, J. L. Dry Powder Precursors of Cubic Liquid Crystalline Nanoparticles (Cubosomes). *Journal of Nanoparticle Research* **2002**, *4* (4), 297–311. <https://doi.org/10.1023/A:1021184216308>.
- (20) Fengel, D.; Wegener, G. *Wood: Chemistry, Ultrastructure, Reactions*; Walter de Gruyter, 2011.
- (21) Mikkonen, K. S.; Xu, C.; Berton-Carabin, C.; Schroën, K. Spruce Galactoglucomannans in Rapeseed Oil-in-Water Emulsions: Efficient Stabilization Performance and Structural Partitioning. *Food Hydrocolloids* **2016**, *52*, 615–624. <https://doi.org/10.1016/j.foodhyd.2015.08.009>.
- (22) Bhattarai, M.; Valoppi, F.; Hirvonen, S.-P.; Hietala, S.; Kilpeläinen, P.; Aseyev, V.; Mikkonen, K. S. Time-Dependent Self-Association of Spruce Galactoglucomannans Depends on PH and Mechanical Shearing. *Food Hydrocolloids* **2020**, *102*, 105607. <https://doi.org/10.1016/j.foodhyd.2019.105607>.
- (23) Valoppi, F.; H. Lahtinen, M.; Bhattarai, M.; J. Kirjoranta, S.; K. Juntti, V.; J. Peltonen, L.; O. Kilpeläinen, P.; S. Mikkonen, K. Centrifugal Fractionation of Softwood Extracts Improves the Biorefinery Workflow and Yields Functional Emulsifiers. *Green Chemistry* **2019**, *21* (17), 4691–4705. <https://doi.org/10.1039/C9GC02007A>.
- (24) Lahtinen, M. H.; Valoppi, F.; Juntti, V.; Heikkinen, S.; Kilpeläinen, P. O.; Maina, N. H.; Mikkonen, K. S. Lignin-Rich PHWE Hemicellulose Extracts Responsible for Extended Emulsion Stabilization. *Front. Chem.* **2019**, *7*. <https://doi.org/10.3389/fchem.2019.00871>.
- (25) Lehtonen, M.; Merinen, M.; Kilpeläinen, P. O.; Xu, C.; Willför, S. M.; Mikkonen, K. S. Phenolic Residues in Spruce Galactoglucomannans Improve Stabilization of Oil-in-Water Emulsions. *Journal of Colloid and Interface Science* **2018**, *512*, 536–547. <https://doi.org/10.1016/j.jcis.2017.10.097>.
- (26) Mikkonen, K. S.; Kirjoranta, S.; Xu, C.; Hemming, J.; Pranovich, A.; Bhattarai, M.; Peltonen, L.; Kilpeläinen, P.; Maina, N.; Tenkanen, M.; Lehtonen, M.; Willför, S. Environmentally-Compatible Alkyd Paints Stabilized by Wood Hemicelluloses. *Industrial Crops and Products* **2019**, *133*, 212–220. <https://doi.org/10.1016/j.indcrop.2019.03.017>.
- (27) Lundqvist, J.; Teleman, A.; Junel, L.; Zacchi, G.; Dahlman, O.; Tjerneld, F.; Stålbrand, H. Isolation and Characterization of Galactoglucomannan from Spruce (*Picea Abies*). *Carbohydrate Polymers* **2002**, *48* (1), 29–39. [https://doi.org/10.1016/S0144-8617\(01\)00210-7](https://doi.org/10.1016/S0144-8617(01)00210-7).
- (28) Hannuksela, T.; Tenkanen, M.; Holmbom, B. Sorption of Dissolved Galactoglucomannans and Galactomannans to Bleached Kraft Pulp. *Cellulose* **2002**, *9* (3), 251–261. <https://doi.org/10.1023/A:1021178420580>.
- (29) Henrik Vibe Scheller; Peter Ulvskov. Hemicelluloses. *Annual Review of Plant Biology* **2010**, *61* (1), 263–289. <https://doi.org/10.1146/annurev-arplant-042809-112315>.
- (30) Willför, S.; Sjöholm, R.; Laine, C.; Roslund, M.; Hemming, J.; Holmbom, B. Characterisation of Water-Soluble Galactoglucomannans from Norway Spruce Wood and Thermomechanical Pulp. *Carbohydrate Polymers* **2003**, *52* (2), 175–187. [https://doi.org/10.1016/S0144-8617\(02\)00288-6](https://doi.org/10.1016/S0144-8617(02)00288-6).

- (31) Thuvander, J.; Jönsson, A.-S. Extraction of Galactoglucomannan from Thermomechanical Pulp Mill Process Water by Microfiltration and Ultrafiltration—Influence of Microfiltration Membrane Pore Size on Ultrafiltration Performance. *Chemical Engineering Research and Design* **2016**, *105*, 171–176. <https://doi.org/10.1016/j.cherd.2015.12.003>.
- (32) Zasadowski, D.; Yang, J.; Edlund, H.; Norgren, M. Antisolvent Precipitation of Water-Soluble Hemicelluloses from TMP Process Water. *Carbohydrate Polymers* **2014**, *113*, 411–419. <https://doi.org/10.1016/j.carbpol.2014.07.033>.
- (33) Biomass Compositional Analysis Laboratory Procedures | Bioenergy | NREL <https://www.nrel.gov/bioenergy/biomass-compositional-analysis.html> (accessed Oct 15, 2020).
- (34) Al-Rudainy, B.; Galbe, M.; Schagerlöf, H.; Wallberg, O. Antisolvent Precipitation of Hemicelluloses, Lignosulfonates and Their Complexes from Ultrafiltered Spent Sulfite Liquor (SSL). 2018.
- (35) Kulkarni, C. V.; Wachter, W.; Iglesias-Salto, G.; Engelskirchen, S.; Ahualli, S. Monoolein: A Magic Lipid? *Phys. Chem. Chem. Phys.* **2011**, *13* (8), 3004–3021. <https://doi.org/10.1039/C0CP01539C>.
- (36) Akhlaghi, S. P.; Ribeiro, I. R.; Boyd, B. J.; Loh, W. Impact of Preparation Method and Variables on the Internal Structure, Morphology, and Presence of Liposomes in Phytantriol-Pluronic® F127 Cubosomes. *Colloids Surf B Biointerfaces* **2016**, *145*, 845–853. <https://doi.org/10.1016/j.colsurfb.2016.05.091>.
- (37) Kim, J.-Y.; Song, M.-G.; Kim, J.-D. Zeta Potential of Nanobubbles Generated by Ultrasonication in Aqueous Alkyl Polyglycoside Solutions. *Journal of Colloid and Interface Science* **2000**, *223* (2), 285–291. <https://doi.org/10.1006/jcis.1999.6663>.
- (38) Fornasier, M.; Biffi, S.; Bortot, B.; Macor, P.; Manhart, A.; Wurm, F. R.; Murgia, S. Cubosomes Stabilized by a Polyphosphoester-Analog of Pluronic F127 with Reduced Cytotoxicity. *Journal of Colloid and Interface Science* **2020**, *580*, 286–297. <https://doi.org/10.1016/j.jcis.2020.07.038>.
- (39) S. Mikkonen, K.; Merger, D.; Kilpeläinen, P.; Murtomäki, L.; S. Schmidt, U.; Wilhelm, M. Determination of Physical Emulsion Stabilization Mechanisms of Wood Hemicelluloses via Rheological and Interfacial Characterization. *Soft Matter* **2016**, *12* (42), 8690–8700. <https://doi.org/10.1039/C6SM01557C>.
- (40) Qiu, H.; Caffrey, M. The Phase Diagram of the Monoolein/Water System: Metastability and Equilibrium Aspects. *Biomaterials* **2000**, *21* (3), 223–234. [https://doi.org/10.1016/S0142-9612\(99\)00126-X](https://doi.org/10.1016/S0142-9612(99)00126-X).
- (41) Nakano, M.; Sugita, A.; Matsuoka, H.; Handa, T. Small-Angle X-Ray Scattering and <sup>13</sup>C NMR Investigation on the Internal Structure of “Cubosomes.” *Langmuir* **2001**, *17* (13), 3917–3922. <https://doi.org/10.1021/la010224a>.
- (42) Aleandri, S.; Mezzenga, R. The Physics of Lipidic Mesophase Delivery Systems. *Physics Today* **2020**, *73*, 38–44. <https://doi.org/10.1063/PT.3.4522>.
- (43) Naidjonoka, P.; Arcos Hernandez, M.; K. Pålsson, G.; Heinrich, F.; Stålblbrand, H.; Nylander, T. On the Interaction of Softwood Hemicellulose with Cellulose Surfaces in Relation to Molecular Structure and Physicochemical Properties of Hemicellulose. *Soft Matter* **2020**. <https://doi.org/10.1039/D0SM00264J>.
- (44) Kishani, S.; Vilaplana, F.; Xu, W.; Xu, C.; Wågberg, L. Solubility of Softwood Hemicelluloses. *Biomacromolecules* **2018**, *19* (4), 1245–1255. <https://doi.org/10.1021/acs.biomac.8b00088>.



- (45) Murgia, S.; Bonacchi, S.; Falchi, A. M.; Lampis, S.; Lippolis, V.; Meli, V.; Monduzzi, M.; Prodi, L.; Schmidt, J.; Talmon, Y.; Caltagirone, C. Drug-Loaded Fluorescent Cubosomes: Versatile Nanoparticles for Potential Theranostic Applications. *Langmuir* **2013**, *29* (22), 6673–6679. <https://doi.org/10.1021/la401047a>.
- (46) Jenni, S.; Picci, G.; Fornasier, M.; Mamusa, M.; Schmidt, J.; Talmon, Y.; Sour, A.; Heitz, V.; Murgia, S.; Caltagirone, C. Multifunctional Cubic Liquid Crystalline Nanoparticles for Chemo- and Photodynamic Synergistic Cancer Therapy. *Photochemical & Photobiological Sciences* **2020**, *19* (5), 674–680. <https://doi.org/10.1039/C9PP00449A>.
- (47) Liu, Q.; Dong, Y.-D.; Hanley, T. L.; Boyd, B. J. Sensitivity of Nanostructure in Charged Cubosomes to Phase Changes Triggered by Ionic Species in Solution. *Langmuir* **2013**, *29* (46), 14265–14273. <https://doi.org/10.1021/la402426y>.
- (48) Muir, B. W.; Zhen, G.; Gunatillake, P.; Hartley, P. G. Salt Induced Lamellar to Bicontinuous Cubic Phase Transitions in Cationic Nanoparticles. *J. Phys. Chem. B* **2012**, *116* (11), 3551–3556. <https://doi.org/10.1021/jp300239g>.
- (49) Hartnett, T. E.; Ladewig, K.; O'Connor, A. J.; Hartley, P. G.; McLean, K. M. Size and Phase Control of Cubic Lyotropic Liquid Crystal Nanoparticles. *J. Phys. Chem. B* **2014**, *118* (26), 7430–7439. <https://doi.org/10.1021/jp502898a>.
- (50) Hartman, J.; Albertsson, A. C.; Lindblad, M. S.; Sjöberg, J. Oxygen Barrier Materials from Renewable Sources: Material Properties of Softwood Hemicellulose-Based Films. *Journal of Applied Polymer Science* **2006**, *100* (4), 2985–2991. <https://doi.org/10.1002/app.22958>.
- (51) Mikkonen, K. S.; Tenkanen, M.; Cooke, P.; Xu, C.; Rita, H.; Willför, S.; Holmbom, B.; Hicks, K. B.; Yadav, M. P. Mannans as Stabilizers of Oil-in-Water Beverage Emulsions. *LWT - Food Science and Technology* **2009**, *42* (4), 849–855. <https://doi.org/10.1016/j.lwt.2008.11.010>.
- (52) Willför, S.; Sundberg, K.; Tenkanen, M.; Holmbom, B. Spruce-Derived Mannans – A Potential Raw Material for Hydrocolloids and Novel Advanced Natural Materials. *Carbohydrate Polymers* **2008**, *72* (2), 197–210. <https://doi.org/10.1016/j.carbpol.2007.08.006>.
- (53) Li, X.; Shi, X.; Wang, M.; Du, Y. Xylan Chitosan Conjugate - A Potential Food Preservative. *Food Chemistry* **2011**, *126* (2), 520–525. <https://doi.org/10.1016/j.foodchem.2010.11.037>.



# Paper III

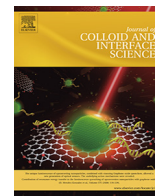
*“Cubosomes stabilized by a polyphosphoester-analog of Pluronic F127 with reduced cytotoxicity”*

**M. Fornasier**, S. Biffi, B. Bortot, P. Macor, A. Manhart, F. R. Wurm, S. Murgia;

Journal of Colloid and Interface Science, 2020, 580, 286-297.

**DOI: 10.1016/j.jcis.2020.07.038**

Copyright © from Elsevier 2020



## Cubosomes stabilized by a polyphosphoester-analog of Pluronic F127 with reduced cytotoxicity

Marco Fornasier<sup>a,b</sup>, Stefania Biffi<sup>c</sup>, Barbara Bortot<sup>c</sup>, Paolo Macor<sup>d</sup>, Angelika Manhart<sup>e</sup>, Frederik R. Wurm<sup>e,\*</sup>, Sergio Murgia<sup>a,b,\*</sup>

<sup>a</sup> Department of Chemical and Geological Sciences, University of Cagliari, s.s. 554 bivio Sestu, 09042 Monserrato, Cagliari, Italy

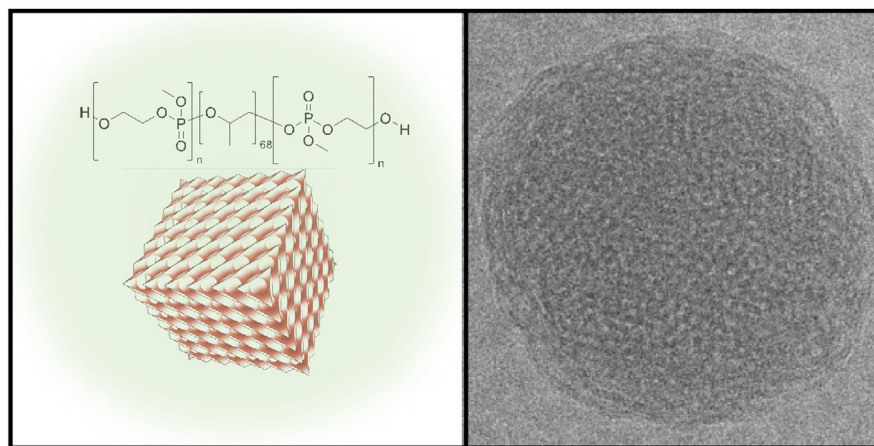
<sup>b</sup> CSGI, Consorzio Interuniversitario per lo Sviluppo dei Sistemi a Grande Interfase, via della Lastruccia 3, 50019 Sesto Fiorentino, Florence, Italy

<sup>c</sup> Institute for Maternal and Child Health, IRCCS Burlo Garofolo, Trieste, Italy

<sup>d</sup> Department of Life Sciences, University of Trieste, Italy

<sup>e</sup> Max Planck Institute for Polymer Research, Ackermannweg 10, 55128 Mainz, Germany

### GRAPHICAL ABSTRACT



### ARTICLE INFO

#### Article history:

Received 5 April 2020

Revised 2 July 2020

Accepted 7 July 2020

Available online 13 July 2020

#### Keywords:

Lipid nanoparticles

Nanomedicine

Hemolysis

Complement system

### ABSTRACT

Lytotropic liquid crystalline nanoparticles with bicontinuous cubic internal nanostructure, known as cubosomes, have been proposed as nanocarriers in various medical applications. However, as these nanoparticles show a certain degree of cytotoxicity, particularly against erythrocytes, their application in systemic administrations is limited to date. Intending to produce a more biocompatible formulation, we prepared cubosomes for the first time stabilized with a biodegradable polyphosphoester-analog of the commonly used Pluronic F127. The ABA-triblock copolymer poly(methyl ethylene phosphate)-*block*-poly(propylene oxide)-*block*-poly(methyl ethylene phosphate) (PMEP-*b*-PPO-*b*-PMEP) was prepared by organocatalyzed ring-opening polymerization of MEP. The cytotoxic features of the resulting formulation were investigated against two different cell lines (HEK-293 and HUVEC) and human red blood cells. The response of the complement system was also evaluated. Results proved the poly(phosphoester)-based

\* Corresponding authors.

formulation was significantly less toxic than that prepared using Pluronic F127 with respect to all the tested cell lines and, more importantly, hemolysis assay and complement system activation tests demonstrated its very high hemocompatibility. The potentially biodegradable poly(phosphoester)-based cubosomes represent a new and versatile platform for preparation of functional and smart nanocarriers.

© 2020 Published by Elsevier Inc.

## 1. Introduction

In recent years, nanotechnologies provided an extraordinary boost to the chemistry of materials and, among the various fields in which they have been applied, nanomedicine is certainly one of the most investigated [1]. Possibly, the main result pursued by researchers working in this arena is the formulation of safe nanoparticles [2] able to precisely deliver drugs and/or imaging agents to pathological tissues, thus maximizing therapeutic effects while simultaneously reducing side effects, also in the perspective of personalized medicine. Yet, independently by all the efforts made so far, only a few nanomedicines have been translated from labs to market [3,4]. One of the reasons for such a negative outcome is the low biocompatibility of certain formulations. To overcome this limitation, formulations need to be engineered using safe building blocks. At the same time, it is necessary to provide nanoparticles with an appropriate surface coverage to avoid recognition from the Mononuclear Phagocyte System to extend their lifetime in the bloodstream [5]. In such a way, the desired therapeutic effect can be exerted at best keeping at minimum the dose of the drug, with the consequent reduction of adverse effects.

Cubosomes are soft nanoparticles characterized by a lyotropic liquid crystalline core prepared to exploit the natural self-assembly ability in water of several lipids (e.g., monoolein or phytantriol). They are often referred to as the non-lamellar analog of liposomes. Indeed, they are constituted by a three-dimensional, curved, and non-intersecting lipid double layer that, differently from liposomes, extends in space superimposed over an infinite periodic minimal surface of cubic symmetry, originating a network of two unconnected water channels [6]. Since they can host hydrophobic drugs and imaging probes, cubosomes are sometimes proposed as theranostic tools and, more in general, for application in the drug delivery field [6–10]. It is here worth mentioning that cubosomes may host larger amounts of hydrophobic drugs with respect to liposomes, because they possess a larger hydrophobic (normalized) volume [11]. Cubosomes are traditionally prepared by fragmenting in water a liquid crystalline bicontinuous bulk phase by high-pressure homogenization or high-speed shearing (top-down approach) or by dissolving the lipids in water with the aid of a hydrotrope (bottom-up approach) [6]. In both cases, a dispersant is generally added to the aqueous solution to stabilize the nanoparticles in water against flocculation. Generally, the used dispersant belongs to the family of non-ionic poly(ethylene oxide)-poly(propylene oxide)-poly(ethylene oxide) tri-block copolymers known as Pluronic, being the F127 the most representative. These copolymers interact with biological molecules of different kinds and are proposed as drug delivery carriers [12–15]. However, Pluronic are not biodegradable *in vivo* and activate the complement (which is part of the immune system) in the blood, they might cause cardiopulmonary distress in sensitive patients [16]. Other dispersant for the stabilization of cubosomes in water were less frequently reported in literature [16–20]. In some cases, it was found that the newly proposed stabilizers used as substitute of PF127 make the cubosome formulation less cytotoxic [21,22].

Here, we present novel cubosomes with improved biocompatibility and the potential to be fully biodegradable by the use of an amphiphilic poly(phosphoester) (PPE) analog of Pluronic F127

(PF127). PPEs are polyesters, based on phosphoric acid derivatives that possess the remarkable characteristic of being highly stable but also degradable on demand [23,24]. Especially synthetic PPEs have been studied by Wurm's group intensely as alternatives for poly(ethylene glycol) in drug delivery applications [25].

This article presents detailed physicochemical and cytotoxic analyses of PPE-based cubosomes and compared them with traditional cubosomes stabilized by PF127, to assess their possible application as biodegradable drug delivery system. With the chemical versatility of PPEs, this strategy opens a new platform for the design of bicontinuous cubic liquid crystalline nanoparticles with additional chemical functionality and a controlled degradation pattern.

## 2. Materials and methods

### 2.1. Materials

The main component of the cubosomes, glycerol monooleate (MO, 1-monooleoylglycerol, RYLO MG 19 PHARMA, 98.1 wt%) was kindly provided by Danisco A/S (Denmark). Sodium citrate dihydrate (99.0%), citric acid (99.9%), sodium dihydrogen phosphate (99.9%), sodium hydrogen phosphate (99.9%), sodium chloride (99.9%), potassium chloride (99.9%), and quercetin ( $\geq 95.0\%$ ) were purchased from Sigma-Aldrich. Fresh distilled water purified using a Milli-Q system (Millipore) was used for preparing each sample and it was filtered with a 0.22  $\mu\text{m}$  pore size hydrophilic filter prior to any use.

The Human Embryonic Kidney 293 (HEK-293) and the Human Umbilical vein/vascular endothelium (HUVEC) cell lines were purchased from ATCC (American Type Culture Collection, Manassas, Virginia United States). The CellTox™ Green Cytotoxicity Assay kit and the Apo-ONE® Homogeneous Caspase-3/7 Assay kit were purchased from Promega (Madison, WI). For fluorescence microscopy cells were stained with MitoTracker® Red CMXRos and Weat Germ Agglutinin (WEG) Conjugates Alexa Fluor® 350 conjugate (Invitrogen, Thermo Fischer Scientific, Waltham, Massachusetts, USA).

$^1\text{H}$  and  $^{31}\text{P}$  Nuclear Magnetic Resonance Spectroscopy. For nuclear magnetic resonance (NMR) analyses,  $^1\text{H}$  and  $^{31}\text{P}$  NMR spectra were recorded on a Bruker AVANCE III 500 spectrometer operating with 500 MHz and 202 MHz frequencies, respectively.

Size Exclusion Chromatography. Size exclusion chromatography (SEC) measurements were performed in DMF containing 0.25  $\text{g L}^{-1}$  of lithium bromide at 50 °C and a flow rate of 1  $\text{mL min}^{-1}$  with an Agilent 1100 Series as an integrated instrument, including a PSS HEMA column (106/105/104  $\text{g mol}^{-1}$ ), a UV (275 nm) and a refractive index (RI) detector. Calibration was carried out using poly(ethylene glycol) standards provided by Polymer Standards Service.

### 2.2. Polyphosphoester synthesis

Monomer Synthesis: 2-Methoxy-2-oxo-1,3,2-dioxaphospholane (MEP). A flame-dried 1000 mL three-neck flask, equipped with a dropping funnel, was charged with 2 chloro-2-oxo-1,3,2-dioxaphospholane (50 g, 0.35 mol) dissolved in dry THF (300 mL). A solution of dry methanol (11.24 g, 0.35 mol) and dry pyridine (27.72 g,

0.35 mol) in dry THF (45 mL) was added dropwise to the stirring solution of COP at  $-20\text{ }^{\circ}\text{C}$  under argon atmosphere. During the reaction, hydrogen chloride was formed and precipitated as pyridinium hydrochloride. The reaction was stirred at  $4\text{ }^{\circ}\text{C}$  overnight. The salt was removed by filtration and the filtrate concentrated *in vacuo*. The residue was purified by distillation at reduced pressure to give a fraction at  $89\text{--}97\text{ }^{\circ}\text{C}/0.001\text{ mbar}$ , obtaining the clear, colorless, liquid product MEP (25.54 g, 0.19 mol, yield: 53%).  $^1\text{H}$  NMR (500 MHz, DMSO  $d_6$ ):  $\delta$  4.43 (m, 4H), 3.71 (d, 3H).  $^{13}\text{C}\{\text{H}\}$  NMR (125 MHz, DMSO  $d_6$ ):  $\delta$  66.57, 54.72.  $^{31}\text{P}\{\text{H}\}$  NMR (202 MHz, DMSO  $d_6$ ):  $\delta$  17.89.

**Polymerization of MEP.** *N*-cyclohexyl-*N'*-(3,5-bis(trifluoromethyl)phenyl)thiourea (TU) was synthesized according to the literature procedure [26]. TU (268 mg,  $7.2\cdot 10^{-4}$  mol) and the poly(propylene oxide)<sub>68</sub>-macroinitiator (75  $\mu\text{mol}$ , 300 mg, PPO-diol of molar mass  $4,000\text{ g mol}^{-1}$  was used) were placed in a Schlenk tube and freeze-dried with benzene prior use. 5 mL of dry dichloromethane and freshly distilled MEP (1.83 g,  $15\cdot 10^{-3}$  mol) were added to the mixture. The solution was cooled down to  $0\text{ }^{\circ}\text{C}$ , then the polymerization was initiated by the rapid addition of 0.12 mL DBU (113 mg,  $7.2\cdot 10^{-4}$  mol) to the stirred solution. The polymerization was terminated after 90 min by the addition of ca. 1 mL acetic acid in dichloromethane ( $1\text{ mol L}^{-1}$ ). The polymer was purified by precipitation from dichloromethane into ice-cold ethyl acetate twice and finally into ice-cold diethyl ether, followed by dialysis against deionized water overnight (MWCO: 3500). The polymer was obtained after freeze-drying in quantitative yield.

### 2.3. Pendant drop surface tension measurements

The PPE surface tension was measured using a tensiometer (Sinterface Technologies, Germany) equipped with a recording camera, from the shape of a pendant drop of  $20\text{ mm}^3$  at different concentrations of the polymer in an aqueous solution (in the range  $0.01\text{--}180\text{ }\mu\text{M}$ ). The shape was obtained using the Gauss-Laplace equation, a relationship between the curvature of a liquid meniscus and the surface tension,  $\gamma$ , that can be determined by the Gauss-Laplace equation to the coordinates of a drop. The fitting was performed using the PAT fitting software. The surface tension for each concentration was measured after 8000 s of equilibrium time at least.

### 2.4. Cubosome formulation

To obtain the cubosomes formulation, at first, MO was melted at  $40\text{ }^{\circ}\text{C}$  (drug loaded cubosomes were prepared by adding quercetin to the melted MO). A clear solution of PPE polymer was then added to the lipid phase and the mixture was ultrasonicated usually for 2 cycles of 5 min (Amplitude 40%, 1 s ON and 1 s OFF) using a tip-sonicator equipped with a controller Sonics Vibra Cells, both from Chemical Instruments AB (Sweden). Cubosomes formulations here investigated had the following composition in wt % (the name of the corresponding sample is in parenthesis): MO/PF127/Water = 3.3/0.3/96.4 (Cubo-0.3F127) and MO/PPE/Water = 3.3/0.3/96.4, 3.3/0.6/96.1, 3.3/0.9/95.8, 3.3/1.2/95.5 (Cubo-0.3PPE, Cubo-0.6PPE, Cubo-0.9PPE, and Cubo-1.2PPE, respectively).

### 2.5. Encapsulation efficiency

After loading with quercetin, formulations Cubo-0.3F127 and Cubo-0.6PPE were dialyzed into a tubing cellulose membrane (14 kDa molecular weight cutoff, purchased from Sigma Aldrich) against 2 L of water at room temperature for 2 h (water was changed after 1 h). The adsorption spectra of quercetin ( $\lambda_{\text{abs}} = 373\text{ nm}$ ) were acquired using a Win-Cary Varian UV-Vis double-beam

spectrophotometer in EtOH. A standard calibration curve was built up to evaluate the loading of the antioxidant adopting a linear regression analysis (correlation coefficient,  $R^2 = 0.9999$ ). The quercetin-loaded formulations (before and after dialysis) were then dissolved in EtOH and placed in quartz cuvette (1 cm of optical path). The encapsulation efficiency (%) of quercetin into the formulation was calculated exploiting the following expression:

$$EE(\%) = \frac{\text{mass of drug after dialysis}}{\text{mass of drug before dialysis}} \cdot 100$$

### 2.6. Dynamic light scattering and electrophoretic mobility experiments

The cubosome formulations were diluted 1:50 in water at least 24 h after preparation and before any measurement. The mean nanoparticles size (diameters) was characterized employing Dynamic Light Scattering (size and polydispersity index, Pdl) and Electrophoretic Mobility ( $\zeta$ -potential), using a ZetaSizer Nano ZS by Malvern Instruments (Malvern, UK) at ( $25.0 \pm 0.1$ )  $^{\circ}\text{C}$  (backscattering angle  $173^{\circ}$ , 4 mW He-Ne laser at 663 nm). Size, Pdl, and  $\zeta$ -potential of each sample was collected at least 5–6 times. The stability of the formulations was also evaluated measuring these parameters up to five months while keeping the samples at  $25\text{ }^{\circ}\text{C}$ . The formulation Cubo-0.6PPE was studied at two different pHs (3.4 and 7.4) by diluting the dispersion prepared in water into the desired buffer 1:50 before performing the DLS and  $\zeta$ -potential measurements.

### 2.7. Electron microscopy at cryogenic temperature (cryo-TEM)

The cubosomes were imaged by cryo-TEM, using a JEM-2200FS transmission electron microscope (JEOL), optimized for cryo-TEM at the National Center for High Resolution Electron Microscopy (nCHREM) at Lund University. The instrument is equipped with a field-emission electron source, a cryo pole piece in the objective lens and an in-column energy filter (omega filter). Zero-loss images were recorded at an acceleration voltage of 200 kV on a bottom-mounted TemCam-F416 camera (TVIPS) using SerialEM under low-dose conditions. Each sample was prepared using an automatic plunge freezer system (Leica Em GP) with the environmental chamber operating at  $25.0\text{ }^{\circ}\text{C}$  and 90% of relative humidity. A 4  $\mu\text{L}$  droplet of the cubosomes formulation was deposited on a lacey formvar carbon-coated grid (Ted Pella) and was blotted with filter paper to remove excess fluid. The grid was then plunged into liquid ethane (around  $-183\text{ }^{\circ}\text{C}$ ) to ensure the rapid vitrification of the sample in its native state. The specimens were thereafter stored in liquid nitrogen ( $-196\text{ }^{\circ}\text{C}$ ) and before imaging transferred into the microscope using a cryo transfer tomography holder (Fischione, Model 2550).

### 2.8. Small angle X-ray scattering (SAXS)

SAXS experiments were performed at the SAXSLab instrument (JJ-Xray, Denmark) at Lund University equipped with a 30 W Cu X-RAY TUBE for GeniX 3D and a 2D 300 K Pilatus detector (Dectris). The measurements were acquired with a pin-hole collimated beam with the detector positioned asymmetrically to yield a single measurement  $q$ -range of  $0.012\text{--}0.67\text{ }\text{\AA}^{-1}$ . The sample-to-detector distance was 480 mm in all experiments.

The magnitude of the scattering vector is defined by  $q = (4\pi \sin\theta)/\lambda$ , where  $\lambda$  equals to  $1.54\text{ }\text{\AA}$ , Cu  $K\alpha$  wavelength, and  $\theta$  is half of the scattering angle. The  $d$  spacing was calculated using the following expression:

$$d = \frac{2\pi}{q} \quad (1)$$

Then, the lattice parameter,  $a$ , was obtained by Eq. (2) and Eq. (3) for the bicontinuous cubic and hexagonal phases, respectively.

$$a = d \cdot \sqrt{h^2 + k^2 + l^2} \quad (2)$$

$$a = d \cdot \frac{2}{\sqrt{3}} \sqrt{h^2 + k^2 + hk} \quad (3)$$

Here,  $h$ ,  $k$  and  $l$  are the Miller indexes that describe the crystalline planes. The values of  $a$  were also used to calculate the water channel radius ( $r_w$ ) of the bicontinuous cubic phase (Eq. (4)) or of the hexagonal phase (Eq. (5)):

$$r_w = \sqrt{\frac{A_0}{-2\pi\chi}} \cdot a - l \quad (4)$$

$$r_w = a \cdot \sqrt{1 - \varphi_{lipid}} \cdot \left(\frac{\sqrt{3}}{2 \cdot \pi}\right)^{\frac{1}{2}} \quad (5)$$

where  $\chi$  and  $A_0$  are, respectively, the Euler characteristic and the surface area of the IPMS geometry (Pn3m,  $\chi = -2$ ,  $A_0 = 1.919$ ), and  $l$  is the MO hydrophobic chain length at 25 °C (17 Å). The lipid fraction,  $\varphi_{lipid}$ , was calculated using the following equation (Eq. (6)), where  $w_{MO}$ ,  $d_{MO}$ ,  $w_{water}$  and  $d_{water}$  are the weight and density of MO and water respectively:

$$\varphi_{lipid} = \frac{\frac{w_{MO}}{d_{MO}}}{\frac{w_{MO}}{d_{MO}} + \frac{w_{water}}{d_{water}}} \quad (6)$$

The temperature in the analysis chamber was controlled using a Julabo T Controller CF41 from Julabo Labortechnik GmbH (Germany). The T range measurements were acquired after equilibrating the sample for 1 h at the given temperature.

The angular scale was calibrated using silver behenate, CH<sub>3</sub>-(CH<sub>2</sub>)<sub>20</sub>-COOAg, as a standard.

To evaluate the effect of the pH on the formulation Cubo-0.6PPE, few drops of the buffer (citrate or PBS) were added to the cubosomes dispersion until the target pH was reached. The mixture was then let equilibrate for 30 min prior to any measurements.

### 2.9. Cytotoxicity and apoptosis assays

HEK cells were grown in DMEM medium (Euroclone, Milan, Italy) supplemented with 10% fetal bovine serum (Euroclone, Milan, Italy) and 1% penicillin/streptomycin antibiotics (Euroclone, Milan, Italy) at 37 °C in a humidified incubator with 5% CO<sub>2</sub>. HUVEC cells were maintained in F-12 K medium, adding appropriate components, as recommended by the manufacturer. HEK-293 and HUVEC cells were seeded at a density of  $5 \times 10^4$  cells/well in 96-multiwell plate (Corning, New York, USA). After 24 h, formulations Cubo-0.3F127 and Cubo-0.6PPE were added in the culture medium at MO concentrations of 10, 25, 50, 75, 100 µg/mL. After 24, 48 and 72 h of incubation, CellTox™ Green Cytotoxicity Assay kit (Promega Madison, WI) was used to quantify cytotoxicity, and Apo-ONE® Homogeneous Caspase-3/7 Assay kit (Promega Madison, WI) was used to determine caspase-3/7 activity according to the manufacturer's instructions. The fluorescence was determined by GloMax® Discover Microplate Reader instrument (Promega Madison, WI). All data collected are reported as the mean and standard deviation of three independent experiments.

### 2.10. Hemolysis assay

Red blood cells were freshly isolated and analyzed as previously reported [27]. The whole blood sample was freshly obtained from the experimenter (female healthy volunteer, SB) upon written informed consent. Briefly, the erythrocytes were separated from the whole blood by centrifugation at 1500 rpm for 10 min, washed three times, and diluted with saline solution (0.9% NaCl). 50 mL of the erythrocyte stock dispersion was added to 950 mL of saline containing different concentrations of formulations Cubo-0.3F127 and Cubo-0.6PPE (MO concentrations of 10, 25, 50, 75, 100 µg/mL). Saline solution (0.9% NaCl) and distilled water were employed respectively as the negative control (0% lysis) and positive control (100% lysis). After 1 h of incubation, the absorbance of the supernatant separated upon centrifugation at 10 000 rpm for 5 min was recorded at 560 nm UV-vis using GloMax® Discover Microplate Reader instrument (Promega Madison, WI).

### 2.11. Complement activity assay

Human serum (0.1 mL) was incubated with or without Cubo-0.3F127 or Cubo-0.6PPE (see section 2.4) at the final concentration of 660 µg/mL for 2 h at 37 °C; at the end, the reaction was blocked adding EDTA at the final concentration of 20 mM. The residual hemolytic activity of the classical pathway of the C system was then evaluated incubating different dilution (1:50, 1:100, 1:200, 1:400) of treated human serum with IgM-sensitized sheep red blood cells (50 mL at  $1.5 \times 10^7$ ) in glucose veronal-buffered saline for 30 min at 37 °C; hemoglobin released from lysed red blood cells was evaluated reading the supernatant after centrifugation at 415 nm [28].

### 2.12. Cell fluorescence imaging

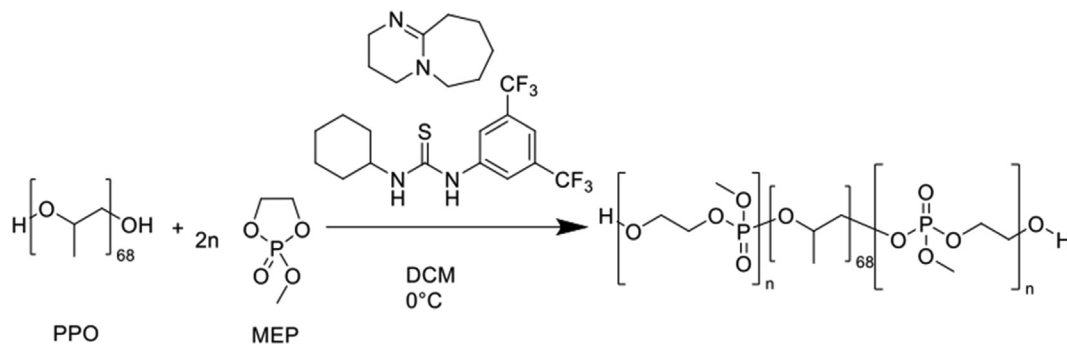
HUVEC cells were seeded in slides (20 × 20) coated with 50 µg/mL human fibronectin (Corning, New York, USA) at a density of  $2.5 \times 10^5$  onto 6-well plate (Corning, New York, USA). Cells were incubated for 24 h in medium alone (control) or in presence of formulations Cubo-0.3F127 or Cubo-0.6PPE at the MO concentration of 100 µg/mL. Wheat Germ Agglutinin Conjugates Alexa Fluor® 350 conjugate was used at a concentration of 5 µg/mL at 37 °C for 20 min to stain cell membranes. MitoTracker® Red CMXRos probe was used at a concentration of 200 nM at 37 °C for 20 min to reveal the mitochondria distribution. Cells were washed twice with D-PBS buffer (Euroclone, Milan, Italy) and fixed with paraformaldehyde (PFA) 4% (MERCK, Darmstadt Germania) for 30 min. The slides were mounted using Vectashield mounting medium for fluorescence with DAPI (Vector Laboratories Inc. Burlingame, CA) to stain cellular nuclei. Fluorescent images of cells were acquired by using an inverted microscope with a CCD camera, and the objectives lens 20X (Axioplan2, with Axiocam MRC, ZEISS Oberkochen Germany).

## 3. Results and discussion

### 3.1. Poly(phosphoester) synthesis

For the preparation of a PPE-based pluronic mimic, we used poly(propylene oxide)68 (with a molar mass of 4000 g/mol) as a difunctional initiator for the organocatalyzed ring-opening polymerization of MEP (Scheme 1 and Experimental for details).

TU and DBU were used as the organocatalytic system and a PPE polymer with the composition PMEP<sub>105</sub>-*b*-PPO<sub>68</sub>-*b*-PMEP<sub>105</sub> ( $M_n = 33,000$  g/mol – from <sup>1</sup>H NMR) was obtained. The degree of polymerization of MEP was determined from the <sup>1</sup>H NMR spectrum



**Scheme 1.** Synthesis of  $\text{PMEP}_{105}\text{-}b\text{-PPO}_{68}\text{-}b\text{-PMEP}_{105}$  triblock copolymer by organocatalyzed ring-opening polymerization.

(Fig. S1) by comparing the resonances of the PPO macroinitiator at 1.1 ppm (methyl side chain) with the doublet of the methoxy side chains of PMEP at 3.8 ppm. SEC molar masses were strongly underestimated with  $M_n = 3500$  g/mol (vs. PEG standards, as reported previously for similar polymers on our setup) but a monomodal molar mass distribution with a dispersity  $D = 1.4$  (from SEC in DMF) was determined.

The critical micelle concentration (CMC) of the PPE in water was extrapolated from a series of measurements at increasing concentration of the polymer using a pendant-drop tensiometer. From the Gauss-Laplace fitting a CMC value of  $1.92 \mu\text{M}$  was obtained.

### 3.2. Cubosome characterization

The cubosome formulations here investigated were prepared by dispersing the molten MO in an aqueous dispersion of PF127 (Cubo-0.3F127) or the newly synthesized PPE (Cubo-0.3PPE, Cubo-0.6PPE, Cubo-0.9PPE, and Cubo-1.2PPE), as described in Section 2.4. The PPE was used as a stabilizing agent for the nanoparticles in substitution of the commonly used PF127. To verify the possibility of forming cubosomes using the PPE, investigate its stabilizing properties, and observe if and how it could alter the morphology and the topology of these nanoparticles, different samples were prepared at increasing concentration of PPE (from 0.3 to 1.2 wt%, see Section 2.4). The macroscopic appearance of all the samples was that of milky, highly fluid aqueous solutions as typically observed for this kind of formulations. The presence of cubosomes was proven by cryo-TEM and SAXS experiments.

In Fig. 1 are reported the cryo-TEM images of samples Cubo-0.6PPE and Cubo-1.2PPE, emblematic for all the formulations

stabilized by the PPE. As can be seen, they consisted in aqueous dispersions of spherical nanoparticles exhibiting a dense inner matrix characterized by a honeycomb structure. It is worth noticing that, although cubosomes appeared as nanoparticles having cubic morphology in numerous scientific articles, they were also often observed as round shaped, as in the present case. In Fig. 1B it can be also noticed the presence of small objects presenting the so-called interlamellar attachments, which are considered intermediates in the transition from lamellar to reverse bicontinuous cubic structures [29]. Remarkably, cryo-TEM images did not show the presence of the small unilamellar vesicles (SUVs) usually found in coexistence with cubosome nanoparticles stabilized by PF127 (see also Fig. S2). Since MO does not form SUVs in excess of water, the existence of these aggregates can be attributed to the presence of the stabilizing agent. In turn, the observed absence of SUVs in the samples here under investigation may suggest a different type of interaction among the PPE and MO with respect to PF127. The topology of the nanoparticles' inner core was assessed by SAXS. The diffraction patterns reported in Fig. 2 revealed that nanoparticles in formulations Cubo-0.3PPE to Cubo-1.2PPE were constituted by a pure Pn3m bicontinuous cubic phase, while formulation Cubo-0.3F127 was characterized by the coexistence of both the Pn3m and the Im3m phases.

Pioneering SAXS experiments on cubosomes by Nakano *et al.* demonstrated that interaction of the poly-(propylene oxide) block of P127 with the nanoparticle internal bicontinuous cubic phase causes a Pn3m-to-Im3m inter-cubic phase transition [30]. While the PPE shares the same hydrophobic block of PF127, no Bragg peaks belonging to other phases different from the Pn3m can be observed in all the formulations stabilized with the PPE here

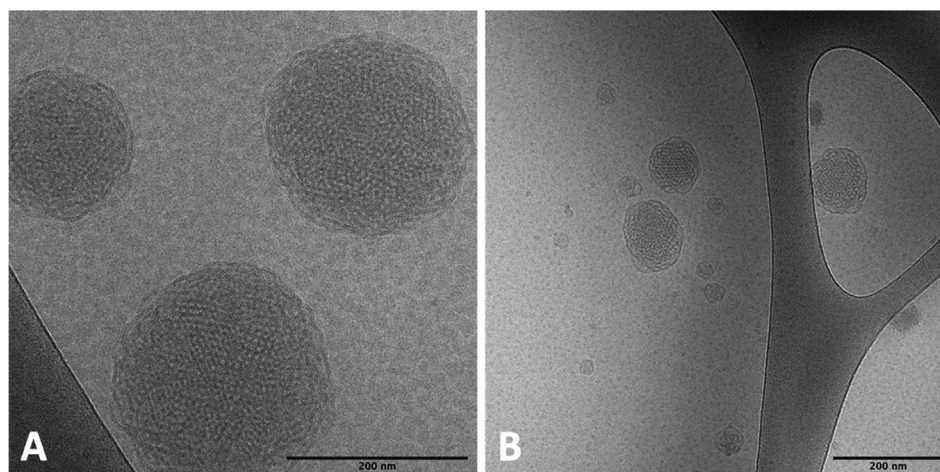


**Fig. 1.** Cryo-TEM images of formulations Cubo-0.6PPE (A) and Cubo-1.2PPE (B).



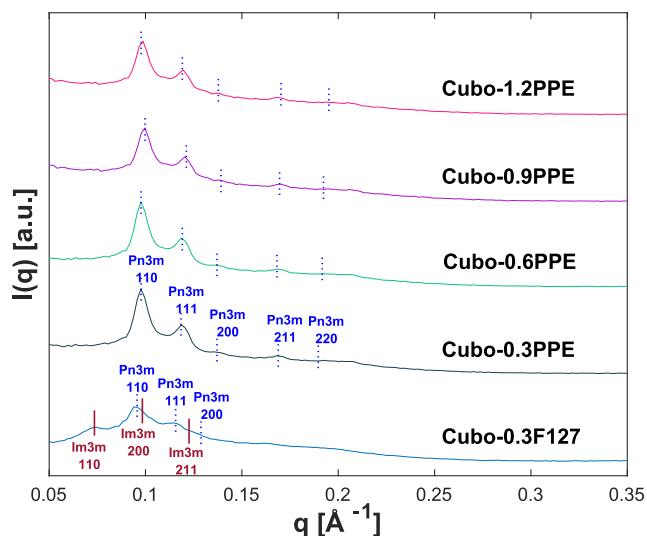


**Fig. 2.** SAXS diffractograms at 25 °C of the investigated cubosomes formulations. On the top of the corresponding Bragg peaks, the Miller indices are also reported along with the indication of the phase. Formulation Cubo-0.3F127 was stabilized using Pluronic F127, while formulations Cubo-0.3PPE to Cubo-1.2PPE were stabilized using increasing concentrations of the newly synthesized PPE polymer (see also Section 2.4).

investigated. This finding strongly suggests that the hydrophilic arms of the stabilizing polymer may have a role in the inter-cubic phase transition process and reinforce the idea that the PPE interacts with MO aggregates differently from PF127. From data reported in Table 1, it can be also observed that the Pn3m phase characterizing the cubosomes has a slightly smaller lattice parameter, 91.2 Å rather than 95.8 Å, when PPE is used to replace PF127 as stabilizer. However, the tiny variation of the observed lattice parameter while varying the PPE content along the Cubo-0.3PPE, Cubo-0.6PPE, Cubo-0.9PPE, and Cubo-1.2PPE sample series is very close to the experimental error and it seems not significant. Moreover, the presence of the PPE into the formulation influences slightly the lattice parameters of the Pn3m phase in comparison with cubosomes stabilized by PF127 (Table 1).

As reported in Table 1, DLS experiments showed that increasing amounts of the PPE lead to smaller nanoparticles with low polydispersity index, and that all the formulations were characterized by a high negative  $\zeta$ -potential (around  $-50$  mV), much larger than that recorded for the formulation Cubo-0.3F127. The origin of the negative  $\zeta$ -potential sometimes observed at interfaces constituted by non-ionic molecules is still not fully understood. However, impurities or partial hydrolysis of monoolein can be safely ruled out in explaining the recorded negative  $\zeta$ -potential. Indeed, also cubosomes prepared using pure monoolein (>99%) [31] or phytantriol [32] (a polar lipid that does not contain hydrolysable ester bonds) show high negative  $\zeta$ -potential. Rather, this fact may be justified assuming a hydroxide ions adsorption at the lipid/water interface

originating a polarized outer layer surrounding the nanoparticles (a well-known phenomenon occurring at oil/water interfaces) [33,34]. If this is correct, the substitution of the Pluronic with the PPE may play a fundamental role in a different hydroxide ions adsorption at the cubosome/water interface, and could be accounted for the increase of the  $\zeta$ -potential reported in Table 1.

Measurements of pH evidenced that formulations are slightly acidic, decreasing from pH = 6.50 (Cubo-0.3PPE) to pH = 6.27 (Cubo-1.2PPE) while increasing the PPE content (see Table S1). Remarkably, pH halved upon one-month aging in case of cubosomes stabilized by the PPE, while it remained constant during this time frame when PF127 was used. Such a result is not surprising since PPE degradation originates phosphates that can provoke the detected drop of pH.

To understand how pH affects the physicochemical features of cubosomes stabilized by the new polyphosphoester polymer, the formulation Cubo-0.6PPE was diluted in two different buffers. PBS buffer at pH 7.4 (100 mM) and a citrate buffer at pH 3.4 (100 mM) were chosen to simulate the pH of a biological environment and the strong acidic character after one month of formulation ageing. Fig. 3 summarizes the effect of pH on the cubosomes nanostructure. The initial pH of the formulation was 6.4 and the SAXS experiment revealed that cubosome nanostructure consisted solely of the cubic Pn3m phase. Whenever the sample is diluted in the PBS buffer (pH 7.4), no significant differences were noticed in comparison with the SAXS pattern at pH 6.4. Differently, when exposed to pH 3.4 the SAXS pattern evidenced the presence of both the Im3m and the Pn3m cubic bicontinuous phases (respectively showing lattice parameters of  $120.3 \pm 0.6$  and  $92.0 \pm 0.4$ , and water channel radii of  $19.7 \pm 0.2$  and  $19.0 \pm 0.2$ ). Due to the complex interaction of PPE with the lipid bilayer, the motivation for the inter-cubic phase transition at low pH was not fully understood, and requires further investigations. Contrarily, the internal phase of nanoparticles in Cubo-0.3F127 did not change when formulation was diluted with the citrate buffer at pH 3.4.

The mean nanoparticles size in the Cubo-0.6PPE formulation did not vary significantly at the investigated pHs.  $D$  values of  $158.2 \pm 1.9$  (Pdl =  $0.11 \pm 0.01$ ) and  $164.8 \pm 1.2$  (Pdl =  $0.10 \pm 0.01$ ) were respectively found at pH 3.4 and 7.4. On the other hand, a drop in the  $\zeta$ -potential values was observed ( $-6.1 \pm 0.6$  and  $-10.2 \pm 0.8$  at pH 3.4 and 7.4, respectively), possibly due to the shielding effect caused by the presence of ions in the buffers.

Investigation of nanoparticle size, polydispersity index, and  $\zeta$ -potential over the time showed that only formulation Cubo-0.6PPE possesses good performances in terms of colloidal stability since no phase separation was noticed after more than 5 months (see Fig. S3 a,b), while others formulations degraded after 4 weeks. Based on the stability tests, further experiments were conducted only on formulation Cubo-0.6PPE. Particularly, the lyotropic behavior of the internal phase of the nanoparticles in formulation Cubo-0.6PPE was checked upon temperature change by SAXS (Fig. 4).

In cubic bicontinuous liquid crystalline systems, the lipid hydrophobic chains become less ordered while increasing

**Table 1**

Phase, lattice parameter ( $a$ ), water channel radius ( $r_w$ ), average diameter of the nanoparticles ( $D$ ), polydispersity index (Pdl), and  $\zeta$ -potential of all the cubosomes formulations investigated at 25 °C. Data are reported as mean  $\pm$  SD.

Sample	Phase	$a$ (Å)	$r_w$ (Å)	$D$ (nm)	Pdl	$\zeta$ -potential (mV)
Cubo-0.3F127	Pn3m	$95.8 \pm 0.8$	$20.4 \pm 0.5$	$141 \pm 1$	$0.11 \pm 0.02$	$-25 \pm 1$
	Im3m	$126.4 \pm 0.6$	$21.8 \pm 0.5$			
Cubo-0.3PPE	Pn3m	$92.6 \pm 0.5$	$19.2 \pm 0.1$	$200 \pm 3$	$0.23 \pm 0.01$	$-45 \pm 1$
Cubo-0.6PPE	Pn3m	$91.2 \pm 0.6$	$18.6 \pm 0.1$	$160 \pm 1$	$0.09 \pm 0.01$	$-47 \pm 1$
Cubo-0.9PPE	Pn3m	$90.7 \pm 0.5$	$18.4 \pm 0.1$	$148 \pm 1$	$0.12 \pm 0.02$	$-51 \pm 2$
Cubo-1.2PPE	Pn3m	$90.8 \pm 0.4$	$18.5 \pm 0.1$	$143 \pm 2$	$0.11 \pm 0.02$	$-48 \pm 2$

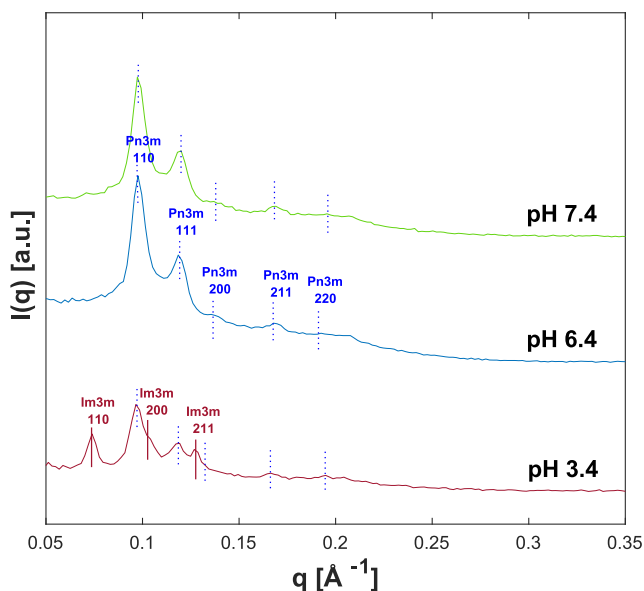


Fig. 3. SAXS diffractograms at 25 °C of the formulation Cubo-0.6PPE at various pH.

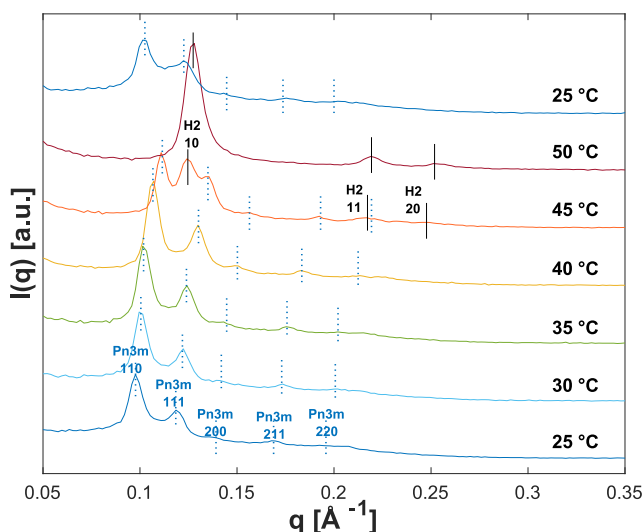


Fig. 4. SAXS diffractograms of formulation Cubo-0.6PPE collected in the temperature range between 25 and 50 °C. On the top of the corresponding Bragg peaks, the Miller indices are also reported along with the indication of the phase.

Table 2

Phase, lattice parameter ( $a$ ), water channel radius ( $r_w$ ), of formulation Cubo-0.6PPE collected at different temperatures. Data at  $T = 25^*$  were calculated after cooling the sample down from 50 to 25 °C. Data are reported as mean  $\pm$  SD.

T (°C)	Phase	$a$ (Å)	$r_w$ (Å)
25	Pn3m	91.2 $\pm$ 0.6	18.6 $\pm$ 0.1
30	Pn3m	89.1 $\pm$ 0.3	17.8 $\pm$ 0.1
35	Pn3m	87.9 $\pm$ 0.3	17.4 $\pm$ 0.1
40	Pn3m	83.9 $\pm$ 0.2	15.8 $\pm$ 0.1
45	Pn3m	80.4 $\pm$ 0.3	14.4 $\pm$ 0.1
50	H <sub>2</sub>	57.1 $\pm$ 0.1	30.1 $\pm$ 0.2
50	H <sub>2</sub>	54.4 $\pm$ 3.2	29.4 $\pm$ 0.2
25*	Pn3m	90.8 $\pm$ 1.1	18.4 $\pm$ 0.4

temperature [30], thus provoking a more negative curvature of the lipid/water interface. Consequently, the lattice parameter of the cubosomes decreases as reported in Table 2. As shown in Fig. 3,

the Pn3m bicontinuous phase is retained up to 40 °C, while the diffraction pattern at 45 °C evidenced the simultaneous occurrence of a reverse hexagonal (H<sub>2</sub>) phase. The cubic-to-hexagonal phase transition at high temperature is a well-known phenomenon for MO-based liquid crystalline systems, but typically occurs at much higher temperature, around 90 °C according to the MO/W binary phase diagram [35]. However, it was established that the lyotropic behavior of dispersed cubic nanoparticles is different from that of the parent bulk phase. Specifically, experiments performed up to 95 °C on MO-based cubosomes dispersion stabilized with 1 wt% of PF127, demonstrated that the cubic-to-hexagonal transition do not occur [36]. Therefore, being the hydrophobic moiety of the PPE and PF127 polymers almost identical, the alteration of the cubosomes lyotropic behavior upon increasing the temperature here recorded could be taken as a further evidence that the hydrophilic arms of the PPE strongly interact with the lipid interface. On the other hand, when the formulation was cooled down to ambient temperature, the Pn3m phase was reestablished, indicating the absence of hysteresis.

Since the cubosome formulation here under investigation is proposed as a drug carrier, the encapsulation of a hydrophobic payload was also studied. Quercetin, a hydrophobic natural antioxidant, was chosen as a drug model and its encapsulation was evaluated in Cubo-0.6PPE and, for the sake of comparison, in Cubo-0.3F127. After an excess of quercetin was added to the formulations, the latter were dialyzed to remove the non-encapsulated antioxidant.

The encapsulation efficiency was studied via UV-Vis spectroscopy after disruption of the formulation in EtOH, in which all the components of the dispersion are soluble. Cubo-0.3F127 and Cubo-0.6PPE presented the same EE% (respectively 95.3  $\pm$  4.5 and 95.4  $\pm$  3.8) and almost the same concentration of drug ( $(7.0 \pm 0.4) \times 10^{-4}$  M and  $(6.0 \pm 0.3) \times 10^{-4}$  M, respectively). This fact is not surprising, since the encapsulation of a hydrophobic drug basically depends on the amount of lipid used to prepare the formulation (identical in Cubo-0.3F127 and Cubo-0.6PPE).

### 3.3. In vitro toxicity studies

A significant question of the current applications of cubosomes in medicine is the issue of safety. Although this is not a strong concern for preclinical studies using small animals, it is fundamental for the translation into clinical practice when the toxicity of these bicontinuous cubic liquid crystalline nanoparticles needs to be carefully evaluated. It was previously speculated that MO, a membrane lipid, could promote bio-adhesion and internalization of PF127, which is used to stabilize the formulation. After passage through the cell membrane, PF127 inevitably ends up in contact with the intracellular space and could induce damage toward mitochondrial and nuclear membranes, leading to cell death [37]. Therefore, the rationale behind replacing PF127 with PPE to stabilize the formulation is the reduced exposure of intracellular space to toxic agents.

Nowadays, biological aspects of interactions between cubosomes and cells are becoming less and less obscure, and experimental evidence showed that cytotoxicity differed significantly in their response *in vitro*, depending on the cellular line investigated [38–40]. The present study aimed to compare the cytotoxicity of PF127- (Cubo-0.3F127) and PPE-stabilized (Cubo-0.6PPE) MO-based cubosomes after exposure to two different cell lines. The concentrations chosen encompassed the range at which cytogenotoxic responses were previously observed and taken into consideration the expected medical applications *in vivo*. Indeed, previous *in vivo* studies on this kind of nanoparticles stabilized by Pluronic F108 showed that a MO concentration lower than 60  $\mu$ g per mL of plasma is required to prevent hemolysis [41].

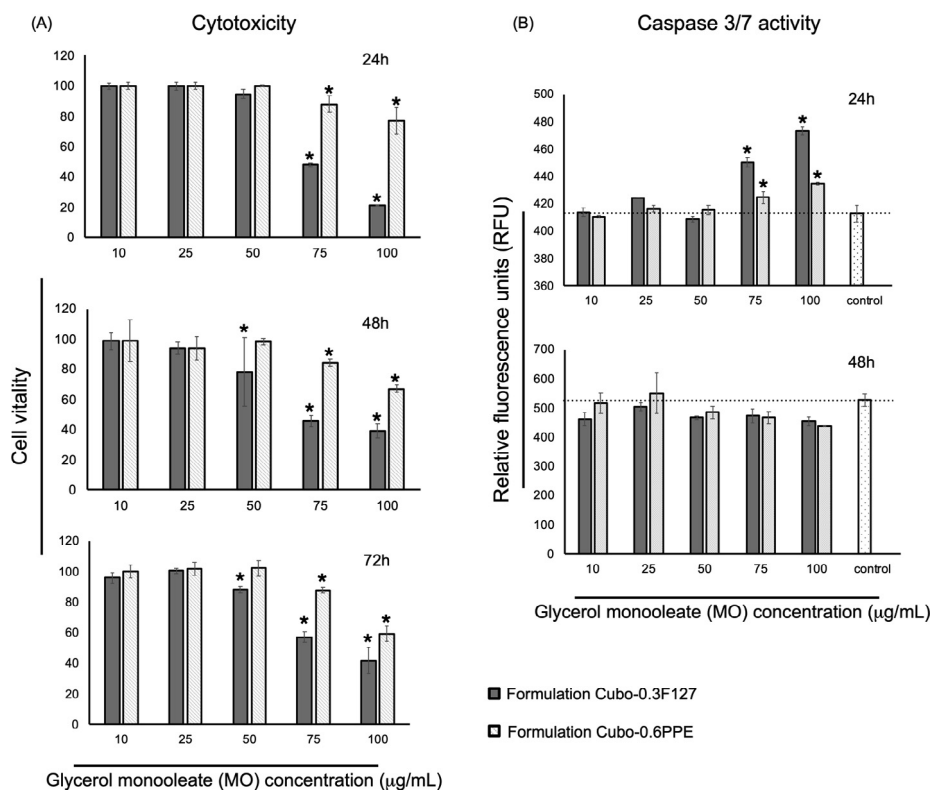


**Fig. 5.** (A) Cellular viability of Human Embryonic Kidney (HEK) 293 cells incubated with formulations Cubo-0.3F127 and Cubo-0.6PPE at different concentrations for 24, 48, and 72 h. Data are shown as mean  $\pm$  SD of 3 individual experiments. (B) Effects on caspase 3/7 activity in HEK-293 cells induced by treatment with formulations Cubo-0.3F127 and Cubo-0.6PPE. Enzymatic activities of caspase 3/7 after 24 and 48 h treatment of HEK-293 cells with medium as control, formulations Cubo-0.3F127 and Cubo-0.6PPE at different concentrations. The caspase activity is expressed as the relative fluorescence unit (RFU), measured after 30 min by the Glomax MultiDetection System instrument (Promega Madison, WI). \* $P < 0.05$ .

Fig. 5 shows the cell viability of a HEK-293 cell line after the treatment with all the formulations here under investigation. Cytotoxicity was evaluated by an assay measuring changes in membrane integrity that occur as a result of cell death. The viability analysis displayed the highest cytotoxic activity in the cells treated with formulation Cubo-0.3F127 with respect to formulation Cubo-0.6PPE. There is no loss of cell viability up to 50  $\mu\text{g/mL}$ , and this value is in line with other studies that analyzed the toxicity of MO-based cubosomes with the Hek293 cell line.

The induction of cytotoxicity after the exposure at a higher concentration was particularly marked with formulation Cubo-0.3F127 (Fig. 5A). Along with the loss of cell viability, it was noted a significant increase in the caspase 3/7 activity in the cells treated with formulation Cubo-0.3F127 compared to formulation Cubo-0.6PPE. These studies revealed an intriguing feature: the HEK-293 cell line increased their caspase 3/7 activity in a transient manner (24 h) after the exposure at higher concentrations. Indeed, it was not observed any effect on caspase 3/7 activity at longer exposure time (Fig. 5B).

Besides, it was detected that the formulation Cubo-0.3F127 exposure induced significant cytotoxicity in the HUVECs cell line at the highest concentration (100  $\mu\text{g/mL}$ ), whereas when formulation Cubo-0.6PPE was used the HUVECs viability (Fig. 6A) was not affected. It deserves noticing that, apparently, Cubo-0.3F127 at a concentration of 100  $\mu\text{g/mL}$  was less cytotoxic after 48 h rather than 24 h cell treatment. It can be speculated that this finding is related to the uptake of nanoparticles, and their persistence at cellular level. Understanding of the toxicity mechanism will require further investigation. Of interest, formulation Cubo-0.3F127 induced a significant increase in the caspase 3/7 activity after 24 h of exposure compared to formulation Cubo-0.6PPE as

previously described for the HEK-293 cells (Fig. 6B). In parallel, the cellular morphology of HUVECs was examined through fluorescence microscopy. The effects of Cubo-0.3F127 on cell morphology were consistent with their reported ability to cause cell death (Fig. 6C).

After the general cytotoxic evaluation of our formulation Cubo-0.3F127 and Cubo-0.6PPE, we performed a hemolysis assay that we conceived as a proof-of-concept to preliminarily assess (*in vitro*) hemocompatibility of the new nanocarriers. As can be seen in Fig. 7, it is noteworthy that in samples treated with formulation Cubo-0.6PPE, the percentage of hemolysis rate was lower than the 5% allowed according to ISO/TR 7406 (samples with a hemolytic ratio of less than 5% are considered nonhemolytic) up to MO concentration of 50  $\mu\text{g/mL}$ . Overall, we observed the presence of significant amounts of hemoglobin in the supernatant of samples treated with formulation Cubo-0.3F127 compared to formulation Cubo-0.6PPE. These features may contribute to improving the drawbacks of conventional cubosomes formulations, and therefore will require further investigations.

The capacity to limit the activation of the complement system is another pivotal characteristic of nanostructures [42,43]; in fact, deposition of complement components on their surface induce particle degradation and fast elimination caused by enhanced phagocytosis. Formulations Cubo-0.3F127 or Cubo-0.6PPE (660  $\mu\text{g/mL}$ ) have been incubated with human serum for 2 h at 37  $^{\circ}\text{C}$ . The residual activity of the complement system was measured using a hemolytic assay rather than the quantification of activation products by ELISA [16]. Indeed, quantification of the complement activation products C5a and C5b-9 by ELISA is often used to evaluate capacity of the nanoparticles to activate the complement system. However, this analysis can be influenced by the

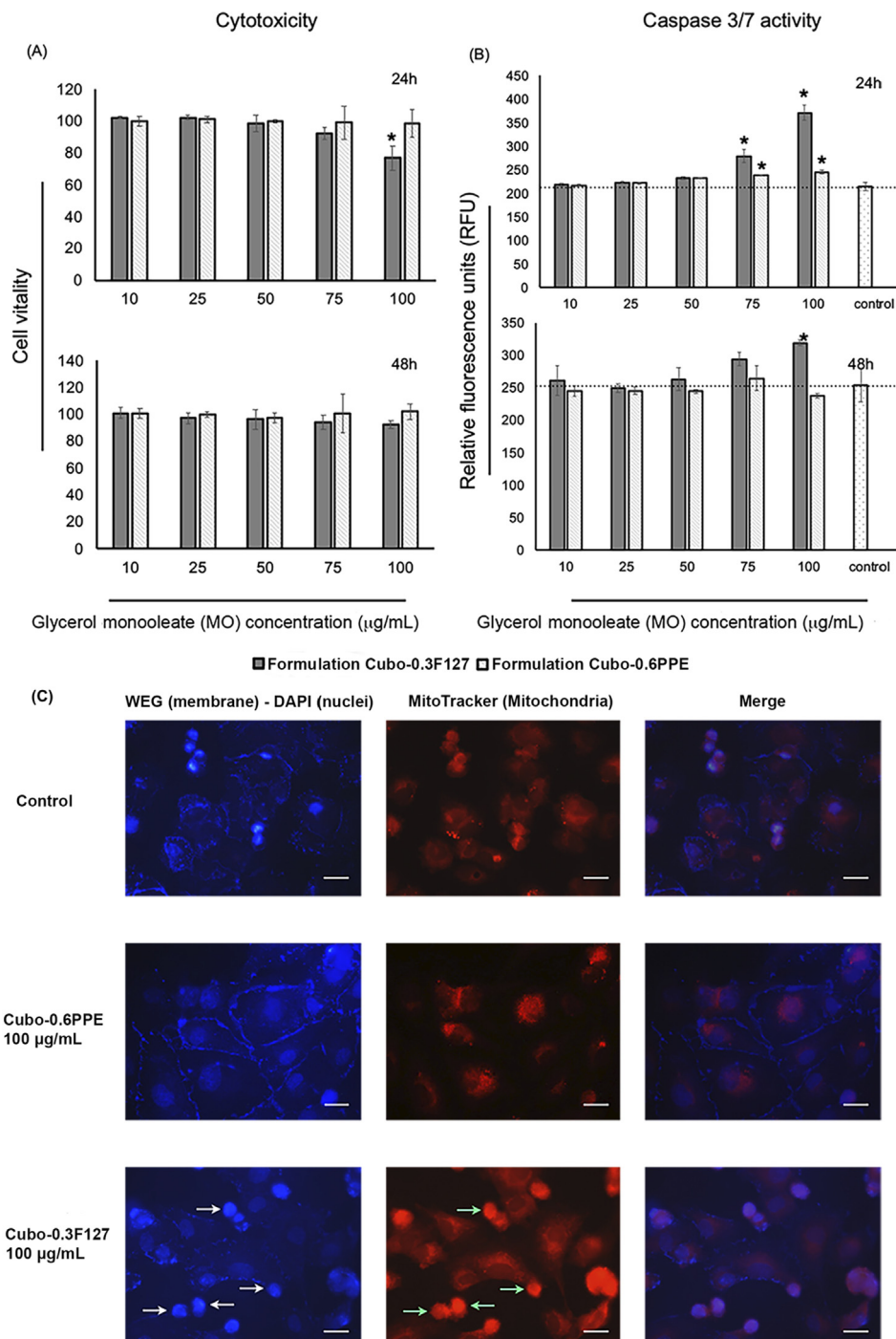


**Fig. 6.** (A) Cellular viability of Human Umbilical Vein Embryonic Cells (HUVECs) incubated with formulations Cubo-0.3F127 and Cubo-0.6PPE at different concentrations for 24 and 48 h. Data are shown as mean  $\pm$  SD of 3 individual experiments. (B) Effects on caspase 3/7 activity in HUVECs cells induced by treatment with formulations Cubo-0.3F127 and Cubo-0.6PPE. Enzymatic activities of caspase 3/7 after 24- and 48-hours treatment of HUVECs cells with medium as control, formulations Cubo-0.3F127 and Cubo-0.6PPE at different concentrations. The caspase activity is expressed as the relative fluorescence unit (RFU), measured after 30 min by the Glomax MultiDetection System instrument (Promega Madison, WI). \* $P < 0.05$ . (C) Fluorescence microscopy images. HUVECs were incubated for 24 h in medium alone (control) or in presence of formulations Cubo-0.3F127 or Cubo-0.6PPE at the MO concentration of 100  $\mu\text{g/mL}$ . Cells were subsequently fixed and stained with MitoTracker (mitochondria, red), Wheat Germ Agglutinin (WEG) derivative (membranes, blue) and DAPI (nuclei, blue). Cubo-0.3F127 treated sample contains a number of cells characterized by condensed nuclei. Fluorescent mitochondria images can be correlated with nuclear phenomena made evident by DAPI staining: white arrows indicate the nuclei, and green arrows the colocalized mitochondria. Effects of Cubo-0.3F127 on morphology are consistent with their reported ability to cause cell death. Bar = 50 nm.

amount of molecules adsorbed on the nanoparticles surface, while the residual activity is not. Cubo-0.3F127 activates and partially consumes the complement system in human serum, reducing to

about 60% of the residual activity. On the contrary, Cubo-0.6PPE preparation seems to slightly interact with the complement system and residual activity remains over 90% (Fig. 8).

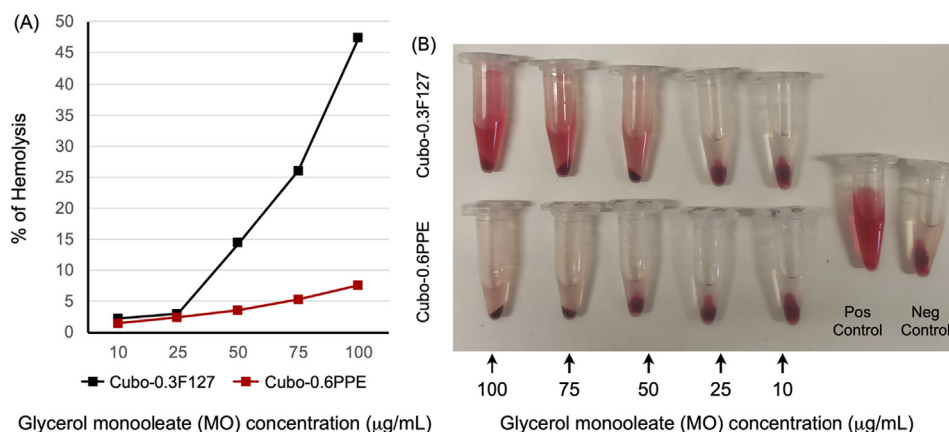


**Fig. 7.** Hemolysis assay on formulation Cubo-0.3F127 and Cubo-0.6PPE. (A) Relative rate of hemolysis in human erythrocytes following 1 h incubation with different concentrations of formulation Cubo-0.3F127 and Cubo-0.6PPE at 37 °C. (B) Photograph of fresh human blood incubated with different concentrations of formulation Cubo-0.3F127 and Cubo-0.6PPE after centrifugation at 10000 rpm for 5 min. Saline solution (0.9% NaCl) and distilled water were employed respectively as the negative control (0% lysis) and positive control (100% lysis). Error bars in (A) are not reported since the standard deviations of triplicate data points of absorbance reading are negligible.

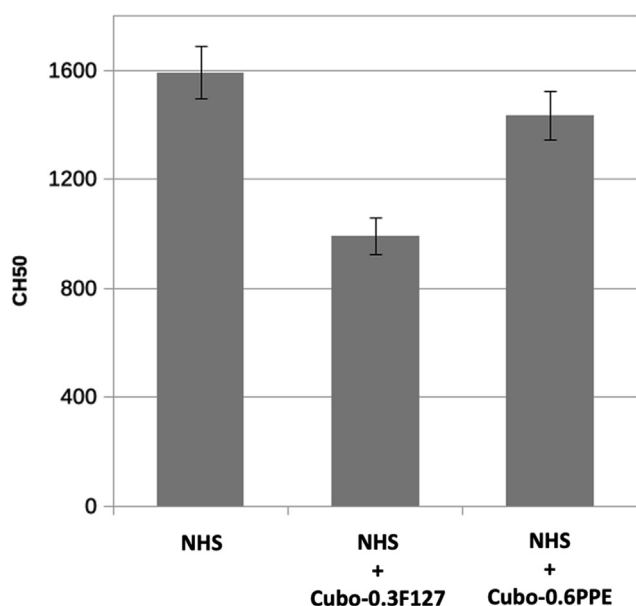


**Fig. 8.** Activation of the complement system in normal human serum (NHS) by formulation Cubo-0.3F127 and Cubo-0.6PPE. Residual activity of the complement system in human serum incubated with formulation Cubo-0.3F127 and Cubo-0.6PPE for 2 h at 37 °C was measured using a hemolytic test. Data (mean ± SD) are expressed as CH50, calculated as the amount (in nL) of treated serum required to induce 50% of red blood cell lysis in the test. NHS vs (NHS + Cubo-0.3F127) showed  $p < 0.01$  while NHS vs (NHS + Cubo-0.6PPE) showed no statistical difference.

#### 4. Conclusions

Nanocarrier cytotoxicity represents one of the most important complications that researchers working in the field of drug delivery have to solve. In the case of cubosomes, such toxicity is exerted mainly towards erythrocytes, as pointed out by several studies [44,45]. To overcome this issue, increasing the cubosomes biocompatibility in general, and with particular reference to their hemocompatibility, a newly synthesized poly-(phosphoester) structurally analog of the traditional PF127, was used to stabilize these nanoparticles dispersion in water. According to the physicochemical experiments here discussed, the PPE effectively stabilized the dispersion against flocculation while preserving the original nanostructure expected for the self-assembly of monoolein in

excess of water. In comparison with PF127-cubosomes, *in vitro* toxicity studies on two different cell lines (HEK-293 and HUVEC) and human erythrocytes proved the higher biocompatibility of PPE-cubosomes and, remarkably, their excellent hemocompatibility. In serum, the capacity to trigger the complement system was particularly high in formulation Cubo-0.3F127, possibly activating the alternative pathway of the complement system, through the binding and the activation of the complement component C3 [46]. On the contrary, formulation Cubo-0.6PPE apparently does not interact with C3 and avoids the typical nucleophilic attack of C3. In conclusion, the reduced capacity of activating the complement system guarantee increased stability and biocompatibility and a lower elimination by phagocytes. It is worth recalling that when in contact with biological fluids such as blood plasma or serum, lyotropic liquid crystalline nanoparticles, (which includes cubosomes and hexosomes, among others) may undergo structural alterations or, in some cases, phase transition. Such aspect, not investigated here, was recently reviewed in detail [39].

Nature and living cells employ several PPEs-based structures, given the high stability of the C–O–P bond. Nevertheless, this bond is degradable on demand through specific enzymes [47,48], depending on factors such as the polymer architecture and its hydrophilicity [49]. On the other hand, PEO-based polymers (i.e. PEG and Pluronic F127) are not a biodegradable and their accumulation inside cells can lead to a cytotoxic effect [50]. For the desired application in nanomedicine, the choice of using PPEs instead of Pluronic as a stabilizer for lyotropic liquid crystalline nanoparticles (such as cubosomes) could avoid the side effects in terms of cytotoxicity, given its intrinsic biodegradability.

Taking into account the possibility of synthesizing polyphosphoesters able to properly stabilize cubosomes also conjugated with imaging or targeting probes, results discussed in this paper pave the way for the development of a new generation of more biocompatible bicontinuous cubic liquid crystalline nanoparticles useful for a wide range of nanomedicine applications.

#### CRediT authorship contribution statement

**Marco Fornasier:** Investigation. **Stefania Biffi:** Investigation, Data curation, Writing - review & editing. **Barbara Bortot:** Investigation, Data curation. **Paolo Macor:** Investigation, Data curation, Writing - review & editing. **Angelika Manhart:** Investigation. **Fredrik R. Wurm:** Supervision, Writing - review & editing. **Sergio Murgia:** Supervision, Funding acquisition, Writing - original draft.

## Declaration of Competing Interest

The authors declare that they have no known competing financial interests or personal relationships that could have appeared to influence the work reported in this paper.

## Acknowledgments

Prof. Tommy Nylander and Prof. Karin Schillén are kindly thanked for precious discussions and suggestions. The authors would like to thank Dr. Anna Karnerup for the precious help for cryo-TEM measurements. SM thanks Fondazione Banco di Sardegna and Regione Autonoma della Sardegna (Progetti Biennali di Ateneo Annualità 2018). MF thanks P.O.R. Sardegna F.S.E. 2014–2020 for funding his Ph.D. Scholarship.

## Appendix A. Supplementary data

Supplementary data to this article can be found online at <https://doi.org/10.1016/j.jcis.2020.07.038>.

## References

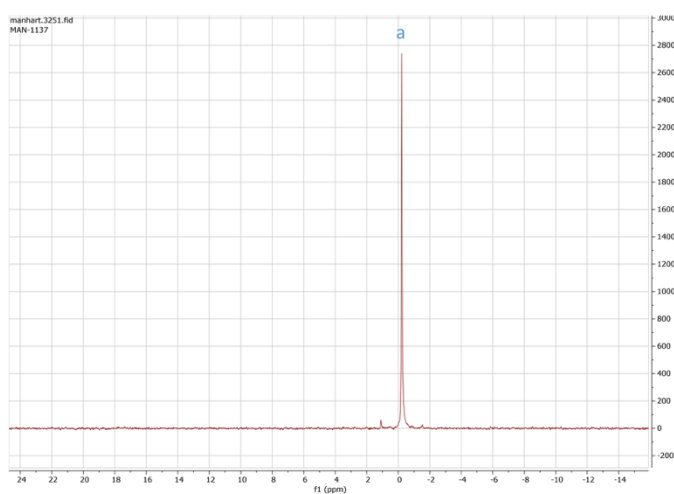
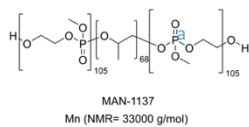
- [1] G. Chen, I. Roy, C. Yang, P.N. Prasad, Nanochemistry and nanomedicine for nanoparticle-based diagnostics and therapy, *Chem. Rev.* 116 (2016) 2826–2885, <https://doi.org/10.1021/acs.chemrev.5b00148>.
- [2] J.K. Fard, S. Jafari, M.A. Eghbal, A review of molecular mechanisms involved in toxicity of nanoparticles, *Adv. Pharm. Bull.* 5 (2015) 447–454, <https://doi.org/10.15171/apb.2015.061>.
- [3] A.C. Anselmo, S. Mitragotri, Nanoparticles in the clinic: An update, *Bioeng. Transl. Med.* 4 (2019) 1–16, <https://doi.org/10.1002/btm2.10143>.
- [4] J. Wolfram, M. Ferrari, Clinical cancer nanomedicine, *Nano Today*, 25 (2019) 85–98, <https://doi.org/10.1016/j.nantod.2019.02.005>.
- [5] J.A. Barreto, W. O'Malley, M. Kubeil, B. Graham, H. Stephan, L. Spiccia, Nanomaterials: applications in cancer imaging and therapy, *Adv. Mater.* 23 (2011) H18–H40, <https://doi.org/10.1002/adma.201100140>.
- [6] J. Zhai, C. Fong, N. Tran, C.J. Drummond, Non-lamellar lyotropic liquid crystalline lipid nanoparticles for the next generation of nanomedicine, *ACS Nano*, (2019), <https://doi.org/10.1021/acsnano.8b07961>.
- [7] R. Mezzenga, J.M. Seddon, C.J. Drummond, B.J. Boyd, G.E. Schröder-Turk, L. Sagalowicz, Nature-inspired design and application of lipidic lyotropic liquid crystals, *Adv. Mater.* 31 (2019) 1–19, <https://doi.org/10.1002/adma.201900818>.
- [8] H.M.G. Barriga, M.N. Holme, M.M. Stevens, Cubosomes: the next generation of smart lipid nanoparticles?, *Angew. Chem. Int. Ed.* 58 (2019) 2958–2978, <https://doi.org/10.1002/anie.201804067>.
- [9] S. Murgia, S. Biffi, R. Mezzenga, Recent advances of non-lamellar lyotropic liquid crystalline nanoparticles in nanomedicine, *Curr. Opin. Colloid Interface Sci.* 48 (2020) 28–39, <https://doi.org/10.1016/j.cocis.2020.03.006>.
- [10] J.A. Prange, S. Aleandri, M. KomisarSKI, A. Luciani, A. Käch, C.D. Schuh, et al., Overcoming endocytosis deficiency by cubosome nanocarriers, *ACS Appl. Bio Mater.* 2 (2019) 2490–2499, <https://doi.org/10.1021/acsabm.9b00187>.
- [11] V. Meli, C. Caltagirone, A.M. Falchi, S.T. Hyde, V. Lippolis, M. Monduzzi, et al., Docetaxel-loaded fluorescent liquid-crystalline nanoparticles for cancer theranostics, *Langmuir* 31 (2015) 9566–9575, <https://doi.org/10.1021/acs.langmuir.5b02101>.
- [12] A.M. Bodratti, P. Alexandridis, Formulation of poloxamers for drug delivery, *J. Funct. Biomater.* 9 (2018), <https://doi.org/10.3390/jfb9010011>.
- [13] E. Tasca, A. Del Giudice, L. Galantini, K. Schillén, A.M. Giuliani, M. Giustini, A fluorescence study of the loading and time stability of doxorubicin in sodium cholate/PEO-PPO-PEO triblock copolymer mixed micelles, *J. Colloid Interface Sci.* 540 (2019) 593–601, <https://doi.org/10.1016/j.jcis.2019.01.075>.
- [14] E.V. Batrakova, A.V. Kabanov, Pluronic block copolymers: Evolution of drug delivery concept from inert nanocarriers to biological response modifiers, *J. Control. Release*, 130 (2008) 98–106, <https://doi.org/10.1016/j.jconrel.2008.04.013>.
- [15] S. Bayati, L. Galantini, K.D. Knudsen, K. Schillén, Effects of bile salt sodium glycodeoxycholate on the self-assembly of PEO-PPO-PEO triblock copolymer P123 in aqueous solution, *Langmuir* 31 (2015) 13519–13527, <https://doi.org/10.1021/acs.langmuir.5b03828>.
- [16] I.D.M. Azmi, P.P. Wibroe, L.P. Wu, A.I. Kazem, H. Amenitsch, S.M. Moghimi, et al., A structurally diverse library of safe-by-design citrem-phospholipid lamellar and non-lamellar liquid crystalline nano-assemblies, *J. Control. Release*, 239 (2016) 1–9, <https://doi.org/10.1016/j.jconrel.2016.08.011>.
- [17] J.Y.T. Chong, X. Mulet, A. Postma, D.J. Keddie, L.J. Waddington, B.J. Boyd, et al., Novel RAFT amphiphilic brush copolymer steric stabilisers for cubosomes: poly(octadecyl acrylate)-block-poly(polyethylene glycol methyl ether acrylate), *Soft Matter*, 10 (2014) 6666–6676, <https://doi.org/10.1039/c4sm01064g>.
- [18] M. Johnsson, J. Barauskas, A. Norlin, F. Tiberg, Physicochemical and drug delivery aspects of lipid-based liquid crystalline nanoparticles: A case study of intravenously administered propofol, *J. Nanosci. Nanotechnol.* 6 (2006) 3017–3024, <https://doi.org/10.1166/jnn.2006.402>.
- [19] J.Y.T. Chong, X. Mulet, D.J. Keddie, L. Waddington, S.T. Mudie, B.J. Boyd, et al., Novel steric stabilizers for lyotropic liquid crystalline nanoparticles: PEGylated-phytanyl copolymers, *Langmuir* 31 (2015) 2615–2629, <https://doi.org/10.1021/la501471z>.
- [20] J.L. Grace, N. Alcaraz, N.P. Truong, T.P. Davis, B.J. Boyd, J.F. Quinn, et al., Lipidated polymers for the stabilization of cubosomes: Nanostructured drug delivery vehicles, *Chem. Commun.* 53 (2017) 10552–10555, <https://doi.org/10.1039/c7cc05842j>.
- [21] J. Zhai, T.M. Hinton, L.J. Waddington, C. Fong, N. Tran, X. Mulet, et al., Lipid-PEG conjugates sterically stabilize and reduce the toxicity of phytantriol-based lyotropic liquid crystalline nanoparticles, *Langmuir* 31 (2015) 10871–10880, <https://doi.org/10.1021/acs.langmuir.5b02797>.
- [22] J. Zhai, R. Suryadinata, B. Luan, N. Tran, T.M. Hinton, J. Ratcliffe, X. Hao, C.J. Drummond, Amphiphilic brush polymers produced using the RAFT polymerisation method stabilize and reduce the cell cytotoxicity of lipid lyotropic liquid crystalline nanoparticles, *Faraday Discuss.* 191 (2016) 545–563, <https://doi.org/10.1039/C6FD00039H>.
- [23] T. Steinbach, F.R. Wurm, Poly(phosphoester)s: a new platform for degradable polymers, *Angew. Chem. Int. Ed.* 54 (2015) 6098–6108, <https://doi.org/10.1002/anie.201500147>.
- [24] M. Worm, B. Kang, C. Dingels, F.R. Wurm, H. Frey, Macromolecular Rapid Communications Acid-labile Amphiphilic PEO- b -PPO- b -PEO Copolymers : Degradable Poloxamer Analogs, (n.d.) 775–780.
- [25] J. Simon, K.N. Bauer, J. Langhanki, T. Opatz, V. Mailänder, K. Landfester, et al., Noncovalent targeting of nanocarriers to immune cells with polyphosphoester-based surfactants in human blood plasma, *Adv. Sci.* 6 (2019), <https://doi.org/10.1002/adv.201901199>.
- [26] B. Clément, B. Grignard, L. Koole, C. Jérôme, P. Lecomte, Metal-free strategies for the synthesis of functional and well-defined polyphosphoesters, *Macromolecules* 45 (2012) 4476–4486, <https://doi.org/10.1021/ma3004339>.
- [27] L. Mazzarino, G. Loch-Neckel, Ldos S. Bubniak, F. Ourique, I. Otsuka, S. Halila, et al., Nanoparticles made from xyloglucan-block-polycaprolactone copolymers: Safety assessment for drug delivery, *Toxicol. Sci.* 147 (2015) 104–115, <https://doi.org/10.1093/toxsci/kfv114>.
- [28] R. Marzari, D. Sblattero, P. Macor, F. Fischetti, R. Gennaro, J.D. Marks, et al., The cleavage site of C5 from man and animals as a common target for neutralizing human monoclonal antibodies: In vitro and in vivo studies, *Eur. J. Immunol.* 32 (2002) 2773–2782, [https://doi.org/10.1002/1521-4141\(200210\)32:10<2773::AID-IMMU2773>3.0.CO;2-G](https://doi.org/10.1002/1521-4141(200210)32:10<2773::AID-IMMU2773>3.0.CO;2-G).
- [29] D. Demurtas, P. Guichard, I. Martiel, R. Mezzenga, C. Hebert, L. Sagalowicz, Direct visualization of dispersed lipid bicontinuous cubic phases by cryo-electron tomography, *Nat. Commun.* 6 (2015) 8915, <https://doi.org/10.1038/ncomms9915>.
- [30] M. Nakano, A. Sugita, H. Matsuoka, T. Handa, Small-angle X-ray scattering and <sup>13</sup>C NMR investigation on the internal structure of “Cubosomes”, *Langmuir* 17 (2001) 3917–3922, <https://doi.org/10.1021/la010224a>.
- [31] S. Murgia, A.M. Falchi, V. Meli, K. Schillén, V. Lippolis, M. Monduzzi, et al., Cubosome formulations stabilized by a dansyl-conjugated block copolymer for possible nanomedicine applications, *Colloids Surfaces B Biointerfaces*, 129 (2015) 87–94, <https://doi.org/10.1016/j.colsurfb.2015.03.025>.
- [32] S.P. Akhlaghi, I.R. Ribeiro, B.J. Boyd, W. Loh, Impact of preparation method and variables on the internal structure, morphology, and presence of liposomes in phytantriol-Pluronic® F127 cubosomes, *Colloids Surfaces B Biointerfaces*, 145 (2016) 845–853, <https://doi.org/10.1016/j.colsurfb.2016.05.091>.
- [33] J.K. Beattie, A.M. Djerdjev, The pristine oil/water interface: Surfactant-free hydroxide-charged emulsions, *Angew. Chem. Int. Ed.* 43 (2004) 3568–3571, <https://doi.org/10.1002/anie.200453916>.
- [34] C.D. Driever, X. Mulet, L.J. Waddington, A. Postma, H. Thissen, F. Caruso, et al., Layer-by-layer polymer coating on discrete particles of cubic lyotropic liquid crystalline dispersions (cubosomes), *Langmuir* 29 (2013) 12891–12900, <https://doi.org/10.1021/la401660h>.
- [35] H. Qiu, M. Caffrey, The phase diagram of the monoolein/water system: Metastability and equilibrium aspects, *Biomaterials* 21 (2000) 223–234, [https://doi.org/10.1016/S0142-9612\(99\)00126-X](https://doi.org/10.1016/S0142-9612(99)00126-X).
- [36] Y. Da Dong, A.J. Tilley, I. Larson, M. Jayne Lawrence, H. Amenitsch, M. Rappolt, et al., Nonequilibrium effects in self-assembled mesophase materials: Unexpected supercooling effects for cubosomes and hexosomes, *Langmuir* 26 (2010) 9000–9010, <https://doi.org/10.1021/la904803c>.
- [37] S. Murgia, A.M. Falchi, M. Mano, S. Lampis, R. Angius, A.M. Carnerup, et al., Nanoparticles from lipid-based liquid crystals: Emulsifier influence on morphology and cytotoxicity, *J. Phys. Chem. B*, 114 (2010), <https://doi.org/10.1021/jp9098655>.
- [38] A.M. Falchi, A. Rosa, A. Atzeri, A. Incani, S. Lampis, V. Meli, et al., Effects of monoolein-based cubosome formulations on lipid droplets and mitochondria of HeLa cells, *Toxicol. Res. (Camb)*, 4 (2015), <https://doi.org/10.1039/c5tx00078e>.
- [39] A. Tan, L. Hong, J.D. Du, B.J. Boyd, Self-assembled nanostructured lipid systems: is there a link between structure and cytotoxicity?, *Adv. Sci.* 6 (2019) 1801223, <https://doi.org/10.1002/adv.201801223>.
- [40] A. Rosa, S. Murgia, D. Putzu, V. Meli, A.M. Falchi, Monoolein-based cubosomes affect lipid profile in HeLa cells, *Chem. Phys. Lipids*, 191 (2015) 96–105, <https://doi.org/10.1016/j.chemphyslip.2015.08.017>.

- [41] S. Biffi, L. Andolfi, C. Caltagirone, C. Garrovo, A.M. Falchi, V. Lippolis, et al., Cubosomes for in vivo fluorescence lifetime imaging, *Nanotechnology* 28 (2017), <https://doi.org/10.1088/1361-6528/28/5/055102>.
- [42] P.P. Wibroe, I.D. Mat Azmi, C. Nilsson, A. Yaghmur, S.M. Moghimi, Citrem modulates internal nanostructure of glyceryl monooleate dispersions and bypasses complement activation: Towards development of safe tunable intravenous lipid nanocarriers, *Nanomed. Nanotechnol. Biol. Med.* 11 (2015) 1909–1914, <https://doi.org/10.1016/j.nano.2015.08.003>.
- [43] I.D. Mat Azmi, L. Wu, P.P. Wibroe, C. Nilsson, J. Østergaard, S. Stürup, et al., Modulatory effect of human plasma on the internal nanostructure and size characteristics of liquid-crystalline nanocarriers, *Langmuir* 31 (2015) 5042–5049, <https://doi.org/10.1021/acs.langmuir.5b00830>.
- [44] J. Barauskas, C. Cervin, M. Jankunec, M. Špandryeva, K. Ribokaitė, F. Tiberg, et al., Interactions of lipid-based liquid crystalline nanoparticles with model and cell membranes, *Int. J. Pharm.* 391 (2010) 284–291, <https://doi.org/10.1016/j.ijpharm.2010.03.016>.
- [45] J.C. Bode, J. Kuntsche, S.S. Funari, H. Bunjes, Interaction of dispersed cubic phases with blood components, *Int. J. Pharm.* 448 (2013) 87–95, <https://doi.org/10.1016/j.ijpharm.2013.03.016>.
- [46] K. Yu, B.F.L. Lai, J.H. Foley, M.J. Krisinger, E.M. Conway, J.N. Kizhakkedathu, Modulation of complement activation and amplification on nanoparticle surfaces by glycopolymer conformation and chemistry, *ACS Nano*. 8 (2014) 7687–7703, <https://doi.org/10.1021/nn504186b>.
- [47] D.F. Xiang, A.N. Bigley, Z. Ren, H. Xue, K.G. Hull, D. Romo, et al., Interrogation of the substrate profile and catalytic properties of the phosphotriesterase from *Sphingobium* sp. strain TCM1: An enzyme capable of hydrolyzing organophosphate flame retardants and plasticizers, *Biochemistry* 54 (51) (2015) 7539–7549, <https://doi.org/10.1021/acs.biochem.5b01144>.
- [48] Y.C. Wang, L.Y. Tang, T.M. Sun, C.H. Li, M.H. Xiong, J. Wang, Self-assembled micelles of biodegradable triblock copolymers based on poly(ethyl ethylene phosphate) and poly( $\epsilon$ -caprolactone) as drug carriers, *Biomacromolecules* 9 (2008) 388–395, <https://doi.org/10.1021/bm700732g>.
- [49] K.N. Bauer, H.T. Tee, M.M. Velencoso, F.R. Wurm, Main-chain poly(phosphoester)s: History, syntheses, degradation, bio- and flame-retardant applications, *Prog. Polym. Sci.* 73 (2017) 61–122, <https://doi.org/10.1016/j.progpolymsci.2017.05.004>.
- [50] S. Schöttler, G. Becker, S. Winzen, T. Steinbach, K. Mohr, K. Landfester, et al., Protein adsorption is required for stealth effect of poly(ethylene glycol)- and poly(phosphoester)-coated nanocarriers, *Nat. Nanotechnol.* 11 (2016) 372–377, <https://doi.org/10.1038/nnano.2015.330>.

# Cubosomes stabilized by a polyphosphoester-analog of Pluronic F127 with reduced cytotoxicity

Marco Fornasier,<sup>a,b</sup> Stefania Biffi,<sup>c</sup> Barbara Bortot,<sup>c</sup> Paolo Macor,<sup>d</sup> Angelika Manhart,<sup>e</sup>  
Frederik R. Wurm,<sup>e,\*</sup> Sergio Murgia<sup>a,b,\*</sup>

<sup>31</sup>P NMR (121 MHz, CDCl<sub>3</sub>, 298K) –  
Polyphosphate PMEP-PPO-PMEP



<sup>1</sup>H NMR (300 MHz, CDCl<sub>3</sub>, 298K) –  
Polyphosphate PMEP-PPO-PMEP

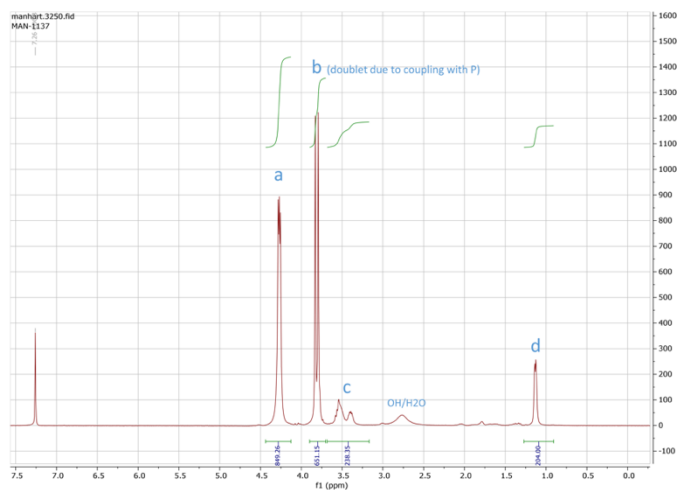
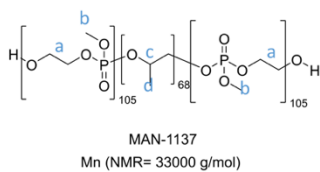
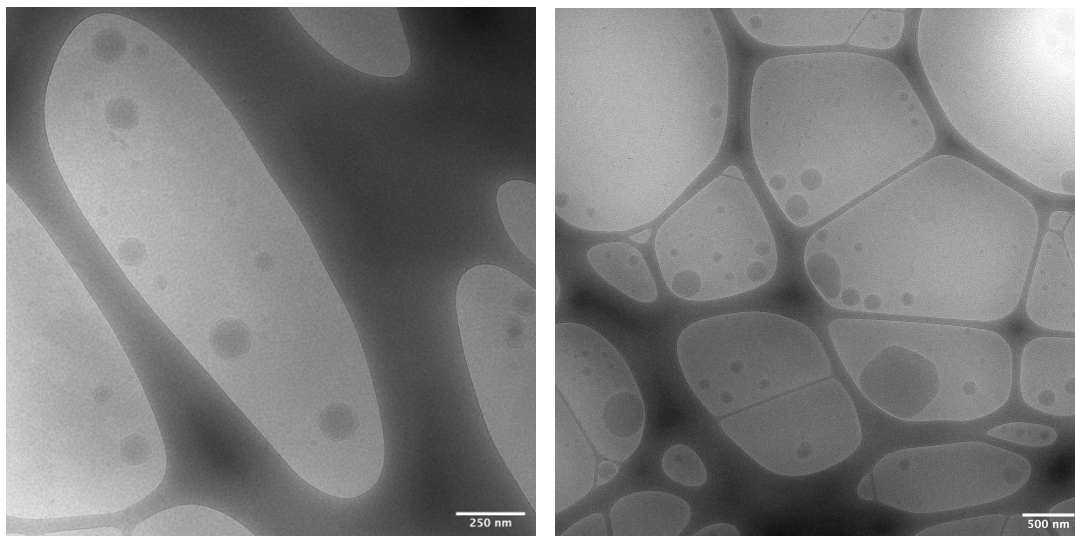
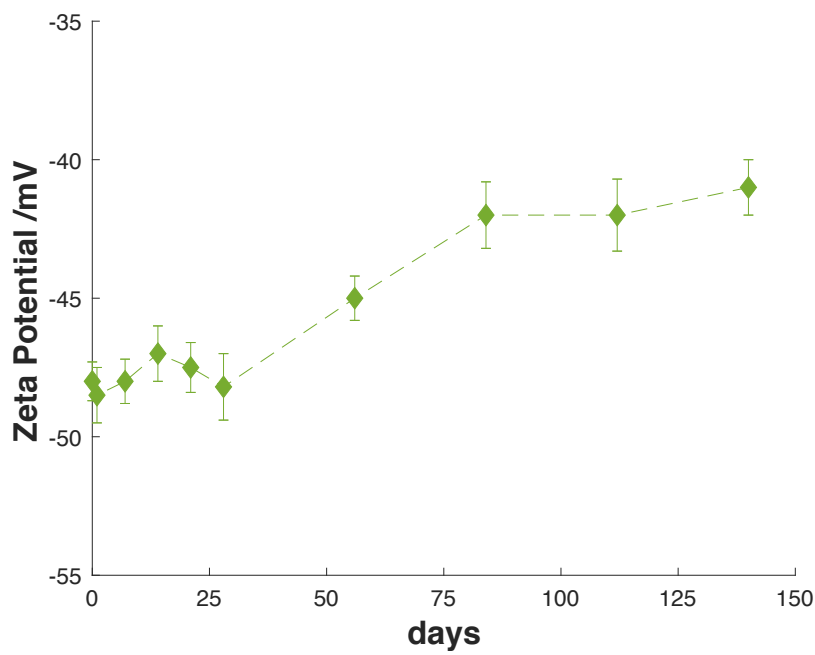
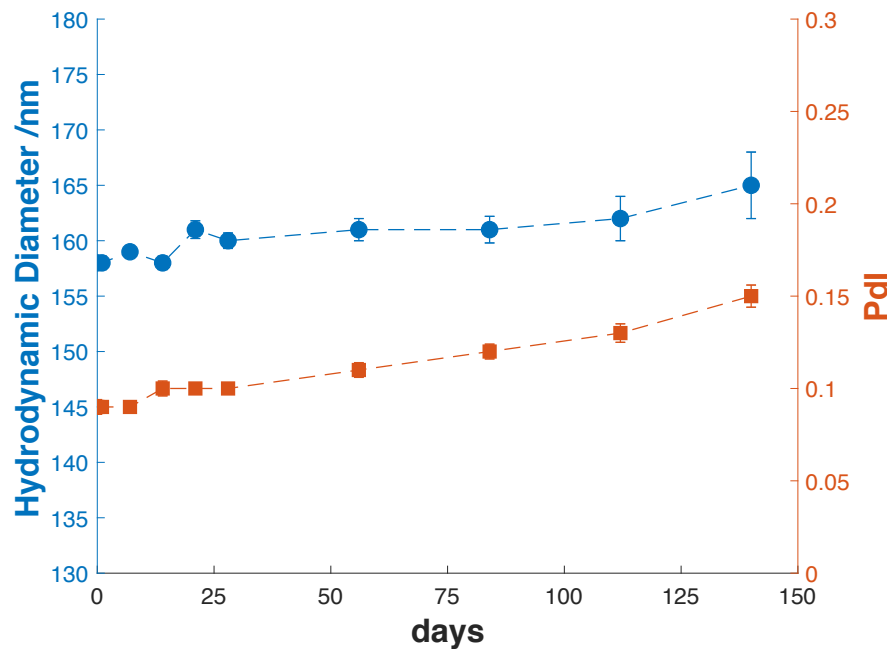


Figure S1.





**Figure S2.** *Cryo-TEM images of formulation Cubo-0.6PPE at different magnification.*



**Figure S3.** Trend of hydrodynamic diameter and PDI (A), and of zeta-potentials (B) of the formulation Cubo-0.6PPE over 5 months. The dashed lines represent a guide for the eye.

**Table S1.** Variation of the pH of the cubosome formulations upon ageing.

<b>Formulation</b>	<b>pH (<math>\pm</math> SD) after 24 h from preparation</b>	<b>pH (<math>\pm</math> SD) after 1 month</b>
Cubo-0.3F127	6.80 $\pm$ 0.02	6.45 $\pm$ 0.02
Cubo-0.3PPE	6.50 $\pm$ 0.01	3.41 $\pm$ 0.01
Cubo-0.6PPE	6.44 $\pm$ 0.02	3.42 $\pm$ 0.01
Cubo-0.9PPE	6.38 $\pm$ 0.01	3.44 $\pm$ 0.01
Cubo-1.2PPE	6.27 $\pm$ 0.02	3.53 $\pm$ 0.01



# Paper IV

*“3-Hydroxycoumarin Loaded Vesicles for Recombinant Human Tyrosinase Inhibition in Topical Applications”*

M. Schlich\*, **M. Fornasier\***, M. Nieddu, C. Sinico, S. Murgia, A. Rescigno;

\*These authors equally contributed to the study.

Colloids and Surfaces B, 2018, 171, 675-681.

**DOI: 10.1016/j.colsurfb.2018.08.008**

Copyright © from Elsevier 2018



## 3-hydroxycoumarin loaded vesicles for recombinant human tyrosinase inhibition in topical applications

Michele Schlich<sup>a,1</sup>, Marco Fornasier<sup>b,1</sup>, Mariella Nieddu<sup>c</sup>, Chiara Sinico<sup>a</sup>, Sergio Murgia<sup>b,\*</sup>, Antonio Rescigno<sup>c</sup>

<sup>a</sup> Department of Life and Environmental Sciences, University of Cagliari, via Ospedale 72, I-09124 Cagliari, Italy

<sup>b</sup> Department of Chemical and Geological Sciences, University of Cagliari and CSGI, s.s. 554 bivio Sestu, I-09042 Monserrato, CA, Italy

<sup>c</sup> Department of Biomedical Sciences, University of Cagliari, s.s. 554 bivio Sestu, I-09042 Monserrato, CA, Italy

### ARTICLE INFO

#### Keywords:

Hyperpigmentation  
Skin disorders  
Liposomes  
Gels  
Transdermal delivery  
Melanoma cells

### ABSTRACT

Tyrosinase is one of the key enzymes in mammalian melanin biosynthesis. Decreasing tyrosinase activity has been targeted for the prevention of conditions related to the hyperpigmentation of the skin, such as melasma and age spots. This paper is devoted to the engineering of vesicle formulations loaded with 3-hydroxycoumarin for topical pharmaceutical applications. At first, it was demonstrated the strong inhibiting ability of 3-hydroxycoumarin against recombinant human tyrosinase. Then, such a drug was effectively encapsulated within liquid or gel-like vesicle formulations, both based on monoolein and lauroylcholine chloride. In vitro skin penetration and permeation studies proved these formulations efficiently overcome the barrier represented by the *stratum corneum*, delivering 3-hydroxycoumarin to the deeper skin layers. The effect of applying for different times the liquid and the gel formulation was also evaluated. Results revealed that application of the gel formulation for 2 h favored the drug accumulation into the skin with low transdermal delivery, thus indicating this combination of administration time and formulation as ideal to locally inhibit tyrosinase activity with minimal systemic absorption. Moreover, when incubated with B16F10 melanoma cells, the liquid vesicle formulations did not show cytotoxic activity.

### 1. Introduction

Lipid-based nanostructured carriers have been extensively investigated in recent years for medicine applications because they present extremely appealing features as drug delivery tools [1–3]. Among these features we can list their biodegradability and biocompatibility, the possibility of carry and release poorly water-soluble drugs, and a morphological and topological diversity that manifests in the various typologies of self-assembled nanoaggregates that can be found in the literature, including the ubiquitous liposomes [4–6] as well as the more exotic hexosomes [7,8] and cubosomes [9–12]. Another important point in favor of this class of aggregates is the potential they have shown as drug nanocarriers useful for all the main administration routes: oral, transdermal, intravenous.

The concept of applying a medication on the skin to achieve either systemic or local effect is of considerable interest for pharmaceutical development. Indeed, dermal/transdermal administration offers the possibility to skip the harsh gastrointestinal environment and avoids

the first pass metabolism, two processes which could severely impact on drug efficacy. Moreover, local administration could reduce the risk of side effects and increase patient acceptability through its intrinsic non-invasiveness and ease of application. However, the large majority of actives does not permeate efficiently within the skin, primarily because of the presence of the *stratum corneum* (SC), a barrier composed of keratinized, dead epithelial cells surrounded by a lipid rich matrix [13,14]. In the attempt to promote SC crossing of poorly diffusing molecules, a vast plethora of nanoparticles, based on different components and with different proposed mechanism of permeation, has been developed in the last decades [15]. More in detail, the topical use of liposomes as drug delivery system dates back to the eighties [16]. Since then, their nanostructure has been upgraded originating innovative nanocarriers, known as niosomes, ethosomes, and transferosomes [17–19] ensuring better performances in terms of dermal or transdermal release of the pharmaceutical payload [20]. Given their ability in transporting drugs through the SC, also hexosomes and cubosomes were proposed as transdermal nanocarriers [21,22], the latter having

\* Corresponding author.

E-mail address: [murgias@unica.it](mailto:murgias@unica.it) (S. Murgia).

<sup>1</sup> These authors equally contributed to this work.

recently demonstrated their potential in photodynamic therapy of melanoma skin cancer [23].

Tyrosinase, (monophenol, *o*-diphenol: oxygen oxido-reductase, EC 1.14.18.1) is an enzyme widely distributed in nature [24], from microorganism [25] to humans, catalyzing both the ortho-hydroxylation of monophenols and the oxidation of ortho-catechols to the corresponding ortho-quinones. Tyrosinase substrates are not limited to mono-phenols and di-phenols, since *o*-aminophenols and aromatic diamines were proven to be substrates of the enzyme [26–28].

Tyrosinase is the key enzyme in the biosynthesis of melanin pigment in animals as the enzyme catalyzes the first two main steps of the melanogenesis: i) the hydroxylation of L-tyrosine to L-dihydroxyphenylalanine (L-DOPA) and ii) the oxidation of L-DOPA to dopaquinone. Then, a cascade of enzymatic and non-enzymatic auto-polymerization reactions lead to the formation of melanin [29]. However, defects in tyrosinase activity could lead to some skin disorders that encompass hyperpigmentation, melasma, age spots, etc. So, tyrosinase activity has been targeted for the treatment of skin disorders related to hyperpigmentation [26].

The discovery of new tyrosinase inhibitors has been for many years the main goal of numerous investigations [30]. In most cases, *in vitro* studies were performed using mushroom tyrosinase (MT) from *Agaricus bisporus*, as this enzyme is easily commercially available although with a very low degree of purity [31]. Although MT and human tyrosinase (HT) share the same bi-cupric cluster, the structure of the two enzymes is quite different, being the first consisting of four subunits while the second is a monomer [30,32]. Despite the huge number of MT inhibitors described [33], very few were tested for their efficacy with the human enzyme [34–36]. Besides, an inhibitor, in addition of being effective at low concentrations, should also possess low or no cellular toxicity when used in humans.

Mono-hydroxycoumarins (hydroxy-1,2-benzopyrones) are common among higher plants, including edible vegetables and fruits, and may have the hydroxyl substituent either on the aromatic ring or on the pyrone ring. Recently, a new activity/relationship study of some hydroxycoumarins and MT was reported [37]. In that study, 3-hydroxycoumarin (3-HC) proved to be an effective MT inhibitor at very low concentration.

Here, for the first time, we describe the interaction of 3-HC with recombinant human tyrosinase (RHT) *in vitro*, and discuss the potential use of a vesicular system endowed of low toxicity and constituted by two penetration enhancers (namely, monoolein and lauroylcholine chloride) [38] for the delivery of 3-HC in the deeper strata of the skin.

## 2. Materials and methods

### 2.1. Materials

Monoolein (MO, 1-monooleoylglycerol, RYLO MG 90-glycerolmonooleate; 98.1 wt% monoglyceride) was kindly provided by Danisco Ingredients, Brabrand, Denmark. Lauroylcholine chloride (LCh) was from TCI Europe. Distilled water, passed through a Milli-Q water purification system (Millipore), was used to prepare the samples. 3-Hydroxycoumarin (3-HC) was purchased from Sigma-Aldrich (Milan, Italy). All substances were used without further purification.

In this study RHT from two suppliers was tested because of RHT is described as inherently inefficient enzyme, with typical small changes in optical density (O. D.) and uncertain degree of purity [39]. RHT (product number: T0206) was purchased by Sigma-Aldrich (Milan, Italy). A second sample of RHT (product number: BML-SE535) was from Enzo (3V-Chimica, Rome, Italy). L-DOPA (3,4-dihydroxy-L-phenylalanine), MBTH (3-methyl-2-benzothiazolinone hydrazone), 3-HC (3-hydroxycoumarin) and all salts used for preparing the buffer solutions were purchased from Sigma-Aldrich and used without any further purification.

### 2.2. Enzyme assay and kinetics

The enzymatic activity of tyrosinase can be followed spectrophotometrically using L-tyrosine or L-DOPA as the substrate. When the enzyme acts on L-tyrosine, it generally shows a lag phase that can cause a considerable lengthening of the measurement times [27]. Therefore, we have chosen to follow the activity of the enzyme with L-DOPA.

Spectrophotometric enzyme assays were based on the reaction of dopaquinone, the product of L-DOPA oxidation, with Besthorn's hydrazone (MBTH) to form a pink adduct, and were carried out as previously described [40] with slight modifications. Briefly, RHT activity was spectrophotometrically determined measuring the amount of adduct formed at 37 °C using 3 mM L-DOPA, 0.5 mM MBTH, in 100 mM sodium phosphate buffer pH 7.3, and monitoring formation of dopaquinone-MBTH adduct at 505 nm ( $\epsilon_{505} = 22.300 \text{ M}^{-1} \text{ cm}^{-1}$ ).

$IC_{50}$  value was determined through a series of measurements of RHT enzyme activity. For all experiments, a high and constant concentration of L-DOPA was used. In each experiment, the amount of inhibitor was steadily increased, and the observed rate of the reaction decreased accordingly. Control experiments were carried out in the absence of tyrosinase. All spectrophotometric data were plotted with Origin 2016 software (Origin Corporation, Northampton, MA, USA). Lineweaver-Burk data and  $IC_{50}$  calculations were analyzed with Grafit 7.0 (Erithacus Software ltd, UK).

### 2.3. Vesicle and vesicle gels preparation

The nanocarriers, empty or loaded with 3-hydroxycoumarin, were prepared dispersing the weighted amount of MO in a solution of LCh in Milli-Q water using an Ultra-Turrax T10 (IKA) device, equipped with a S10N-5 G dispersing tool working at 30,000 rpm. The mixture was then sonicated for 15 min (usually in three cycles of 5 min) obtaining a bluish and transparent solution in case of vesicle or a homogeneous gel. To obtain drug-loaded vesicles, 3-HC was dissolved in melted MO before adding the aqueous solution of LCh. For all samples prepared the MO : LCh ratio (wt/wt) was kept equal to 10 : 1, while throughout the article sample compositions are indicated by the volume fraction of the dispersed phase (DP) in terms of MO + LCh content. Samples composition is given in Table 1.

All samples were analyzed at least 48 h after their preparation.

### 2.4. Drug content

The quantification of 3-HC was performed through a chromatograph Alliance 2690 (Waters, Italy) equipped with a photodiode array detector and an integrating software (Empower 3). The column was a XSelect C18 (3.5  $\mu\text{m}$ , 4.6  $\times$  150 mm, Waters), and the mobile phase was a mixture of water and acetonitrile (45:55) acidified with 0.017% (v/v) acetic acid, eluted at a flow rate of 0.8. mL/min. 3-HC was detected at 306.5 nm wavelength. A standard calibration curve was built up by using standard solutions, and plotted according to the linear regression analysis (correlation coefficient value  $R^2 = 0.999$ ).

**Table 1**  
Samples composition (wt%).

Sample	Monoolein	Lauroylcholine chloride	Water	3-Hydroxycoumarin
DP8	7.0	0.6	92.4	–
DP8 + 3-HC	7.0	0.6	92.3	0.1
DP16	14.5	1.5	84.0	–
DP16 + 3-HC	14.5	1.5	83.9	0.1
DP20	18.2	1.8	80.0	–
DP20 + 3-HC	18.3	1.8	79.3	0.6
DP22	20.0	2.0	78.0	–
DP22 + 3-HC	19.9	2.0	77.3	0.8

## 2.5. Dynamic light scattering

Vesicles sizes and  $\zeta$  potential were measured by means of DLS of DLS and ELS respectively with a ZetaSizer nano ZS (Malvern Instruments, Malvern, UK) at a temperature of  $(25.0 \pm 0.1)$  °C. The samples were diluted 1:50 and backscattered at 173° by a 4 mW He-Ne laser (operative wavelength of 663 nm), taking at least two independent samples. Each sample were analyzed at least 3–5 times.

## 2.6. Small angle X-ray scattering (SAXS)

SAXS experiments were recorded with a S3-MICRO SWAXS camera system (HECUS X-ray System, Graz, Austria) using Cu K $\alpha$  radiation (wavelength = 1.542 Å) provided by a GeniX X-ray Generator, operating at 50 kV and 1 mA. The detection of scattered X-ray in the small-angle region was performed using a 1D-PSD-50 M system (HECUS X-ray Systems, Graz, Austria) containing 1024 channels of width 54.0 m (q-working range, measured in Å,  $0.02 \leq q \leq 0.4$ , where the modulus of the scattering wave vector is  $q = 4\pi \sin(\theta) \lambda^{-1}$ ) [41]. For vesicles and vesicle gel samples thin-walled (2 mm) capillaries for liquids and stainless steel sample holder with thin polymeric sheet (Kapton X-ray film roll TF-475, FluXana GmbH & Co. KG, Germany) were respectively used. Each diffraction pattern was recorded for at least one hour. The camera volume was kept under vacuum during the measurements to minimize scattering from air. The solvent background scattering was subtracted from the intensity and the resulting quantity was normalized and denoted as I(q). The angular scale of the measured intensity was calibrated using Silver Behenate, CH<sub>3</sub>-(CH<sub>2</sub>)<sub>20</sub>-COOAg, as a standard.

## 2.7. In vitro skin penetration and permeation studies

The ability of DP8 and DP16 to permeate through and accumulate in the skin was determined using newborn pig skin, as a representative model of human skin, and Franz vertical cells (diffusion area of 0.785 cm<sup>2</sup>). One-day-old Goland–Pietrain hybrid pigs (~1.2 kg) died of natural causes were provided by a local slaughterhouse. The skin was excised and stored at –80 °C until the day of the experiment. Skin specimens (n = 12 per formulation) were pre-equilibrated with saline (NaCl 0.9% w/v) at 25 °C, then sandwiched between donor and receptor compartments. The receptor was filled with 5.5 mL of saline, continuously stirred and thermostated at  $37 \pm 1$  °C. The amount of formulation to be placed onto the skin surface was carefully measured either by volumetric dosing (400  $\mu$ L for liquid DP8) or by weighing (200 mg for gel DP16). In two different subsets of experiments, the formulations were either left in contact with the skin for all the duration of the study (8 h), or gently wiped off the skin surface after 2 h of non-occlusive contact. At regular intervals, up to 8 h, the receiving solution was entirely withdrawn, replaced with fresh saline to ensure sink conditions and analyzed by HPLC for 3-HC content. After 8 h, the skin surface was gently washed with 1 mL of distilled water and then dried with filter paper. The stratum corneum was removed by stripping with adhesive tape Tesa® AG (Hamburg, Germany). Each piece of adhesive tape was firmly pressed on the skin surface and rapidly pulled off with one stroke. Tape strips and the remaining skin (epidermis and dermis) were cut, placed in glass vials with methanol and subjected to probe sonication for 2 min to extract the drug. The tapes and skin mixtures were filtered out and assayed for drug content by HPLC.

## 2.8. Cell line and culture conditions

B16F10 cell line was obtained from the Interlab Cell Line Collection (ICLC) (IRCCS – IST Istituto Nazionale per la Ricerca sul Cancro, Genova, Italy). B16F10 cells were obtained from mouse melanoma. Subculture of cell line were grown in 75-cm<sup>2</sup> culture flask in phenol red-free Dulbecco's modified Eagle's medium (DMEM, Invitrogen, USA) with high glucose, supplemented with 10% fetal bovine serum (FBS),

2 mM L-glutamine, penicillin (100 U/mL) and streptomycin (100  $\mu$ g/mL) at 37 °C, in 5% CO<sub>2</sub>.

## 2.9. MTT assay for cell viability

The cytotoxic effect of formulation DP8 empty and loaded with 3-HC diluted 1:200, corresponding to 350  $\mu$ g/mL of MO, was evaluated in B16F10 cells using the 3-(4,5-dimethylthiazol-2-yl)-2,5-diphenyltetrazolium bromide (MTT) assay, based on the cleavage of the Tetrazolium salt by mitochondrial dehydrogenases in viable cells [42]. In brief,  $3 \times 10^4$  cells/mL in 100  $\mu$ L of medium was seeded into a 96-well plate and incubated at 37 °C. After 48 h incubation, 5  $\mu$ L/mL of the formulation were added to cultures and incubated at 37 °C for additional 6, 24 and 48 h, respectively. Eight  $\mu$ L portion of MTT solution (5 mg/mL in H<sub>2</sub>O) was then added and left for 4 h at 37 °C. The cells were lysed with 100  $\mu$ L of DMSO and color development was measured at 570 nm with an Infinite 200 auto microplate reader (Infinite 200, Tecan, Austria). The absorbance was proportional to the number of viable cell.

## 2.10. Statistical analysis

Statistical analysis was carried out with the software R, version 2.10.1. Results are expressed as the mean  $\pm$  standard deviation of at least three independent determinations, unless differently stated. Student's *t*-test was used for comparison between two samples, while multiple comparisons of means (Tukey test) were used to substantiate statistical differences between groups. Unless otherwise specified, significance was tested at  $P < 0.05$ .

## 3. Results and discussion

As previously mentioned, 3-HC has been proven to be an excellent inhibitor of tyrosinase from mushrooms. Thus, first of all, we tested the behavior of RHT activity in the presence of 3-HC. Fig. 1 shows the absorption spectra of a reaction mixture containing RHT, L-DOPA and MBTH (3-methyl-2-benzothiazolinone hydrazone). It is evident that, under the conditions described, the presence of 0.05 mM of 3-HC

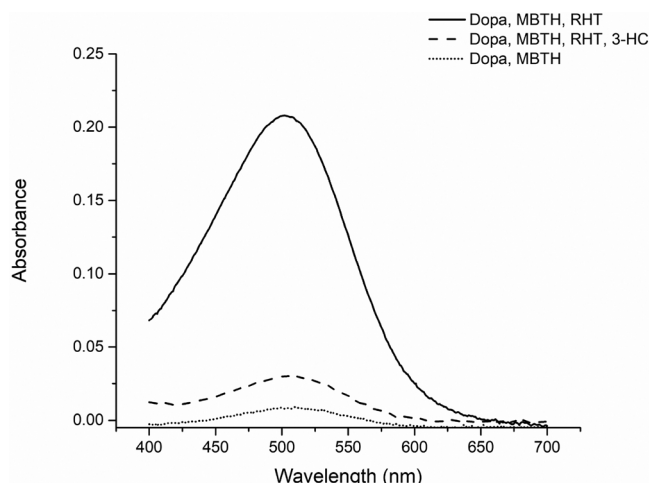


Fig. 1. Enzyme activity was spectrophotometrically determined measuring the amount of adduct formed at 37 °C, using 3 mM L-DOPA, 0.5 mM MBTH, in 100 mM sodium phosphate buffer pH 7.3, and monitoring formation of dopa-quinone-MBTH adduct at 505 nm. The reaction mixture contained 25 units of RHT in one mL of final volume. Scans were recorded after 5 min of incubation time. Solid line (—) represents the catalytic action of RHT on the substrate L-DOPA; dashed line (- -) indicates the same reaction in the presence of 0.05 mM 3-hydroxycoumarin (3-HC); dotted line (····) is the control experiment without enzyme.



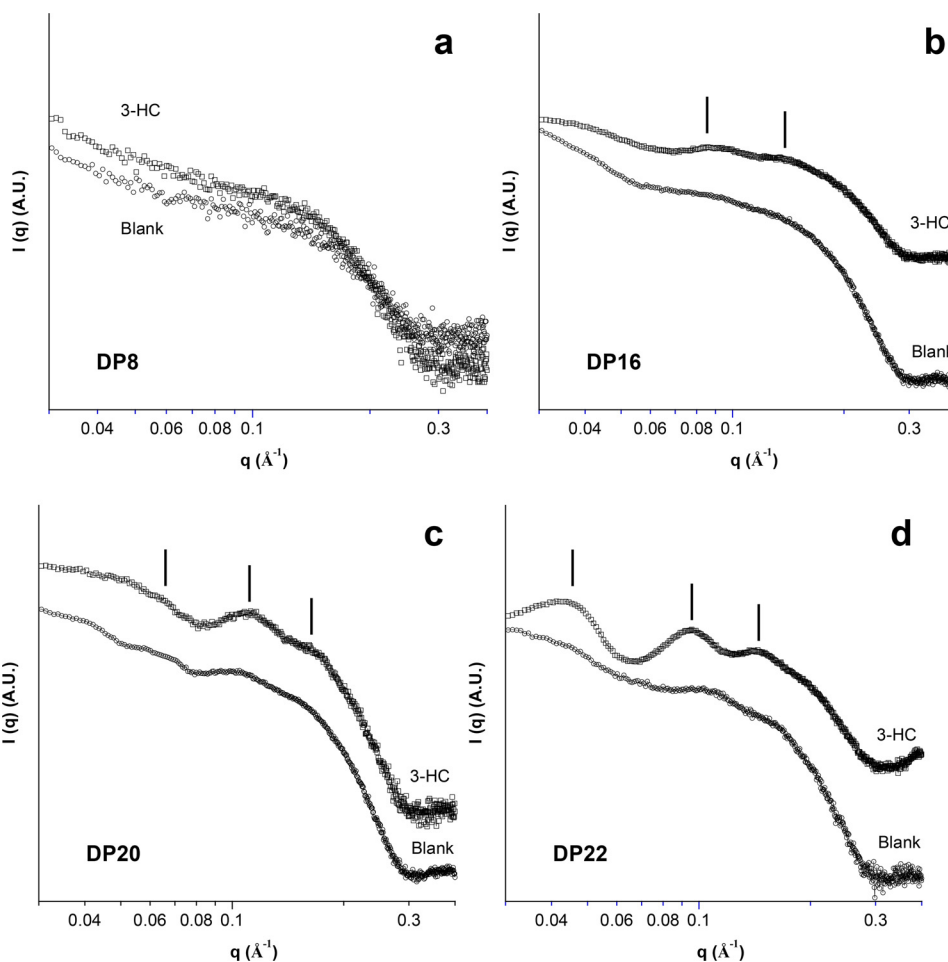


Fig. 2. SAXS patterns (log-log plot) collected at 25 °C of samples DP8, DP16, DP20, and DP22 loaded (3-HC) or not (Blank) with 3-hydroxycoumarin. Also indicated are the quasi-Bragg peaks.

strongly inhibits the transformation of L-DOPA into dopaquinone and therefore the formation of the dopaquinone-MBTH adduct is only about 8% compared to the control after 5 min of incubation time. Following this result, a more in-depth study on the kinetics aspects of the inhibition was carried out, in order to determine the kinetics parameter  $K_m$ ,  $IC_{50}$  and  $K_i$ . The Michaelis constant  $K_m$  is defined as the substrate concentration where the velocity of an enzyme catalyzed reaction is one-half of the maximum velocity. A small  $K_m$  indicates that the enzyme requires a small amount of substrate to become saturated. In contrast, a large  $K_m$  indicates the need for high substrate concentrations to achieve maximum reaction velocity.

The inhibitory constant ( $K_i$ ) and the half maximal inhibitory concentration ( $IC_{50}$ ) of a drug that is known to cause inhibition of an enzyme are correlated to the concentration needed to reduce the activity of that enzyme.  $K_m$  value for L-DOPA was found to be 0.45 mM (0.09 S.E.) when examined by means of the Lineweaver–Burk plot. Such  $K_m$  values is in agreement with similar values reported for HT purified from cultured human melanoma cells [43] (0.5 mM) and the value referred to a RHT produced in insect cells [44] (0.34 mM).

Recent computational analyzes reported that 3-HC is able to enter the catalytic site of MT and directly interact with its surrounding functional groups [37]. Since MT and HT share the same bi-cupric cluster, it can be reasonably assumed that the mechanism of inhibition of RHT by 3-HC is similar, although this speculation requires further structural analysis that goes beyond the aim of this work.

A further reason that makes the use of 3-HC even more interesting is that RHT cannot hydroxylate 3-HC. This is because the hydroxyl-bearing ring of 3-HC is not aromatic and the aromatic ring of the

compound is unsubstituted. Tyrosinases are only capable to ortho-hydroxylate aromatic rings [37].

It is worth reminding that  $IC_{50}$  and  $K_i$  parameters are both measures of an inhibitor's capability to decrease the action of an enzyme, but they are not equivalent. Indeed,  $K_i$  value is a more pure measure since it is a constant for the enzyme-inhibitor complex.  $IC_{50}$  value, in contrast, can vary since it depends on the substrate concentration used in the enzyme inhibition determinations. For this reason,  $IC_{50}$  value was carried out with a high and constant concentration of substrate (3 mM L-DOPA, i.e. about 6.5 times the value of  $K_m$ ). The calculated  $IC_{50}$  value was 0.026 mM. Cheng-Prusoff [45] equation allowed conversion of  $IC_{50}$  value to  $K_i$ . The value found for  $K_i$  was 3.39  $\mu$ M. Taking into account both the  $IC_{50}$  and the  $K_i$  values measured, 3-HC can be definitely considered as an effective HT inhibitor.

Experiments previously described were then replicated with the RHT from the second supplier (date not shown). Although this commercial preparation was shown to be significantly less effective than RHT from Sigma, it was likewise inhibited by 3-HC.

On the basis of these promising results, 3-HC was loaded within a lipid-based nanocarrier to effectively transport and release this molecule within the deeper skin strata with the aim of locally inhibit tyrosinase activity. Among the various nanocarriers useful for such purpose, a recently investigated cationic vesicular system was chosen [38]. Such a non-cytotoxic formulation, prepared by mixing monoolein and lauroylcholine chloride (MO and LCh, respectively, two well-known penetration enhancers), can be readily tuned from a liquid-like unilamellar vesicle dispersion to a very viscous gel-like system by simply varying the dispersed phase composition, a desirable feature for

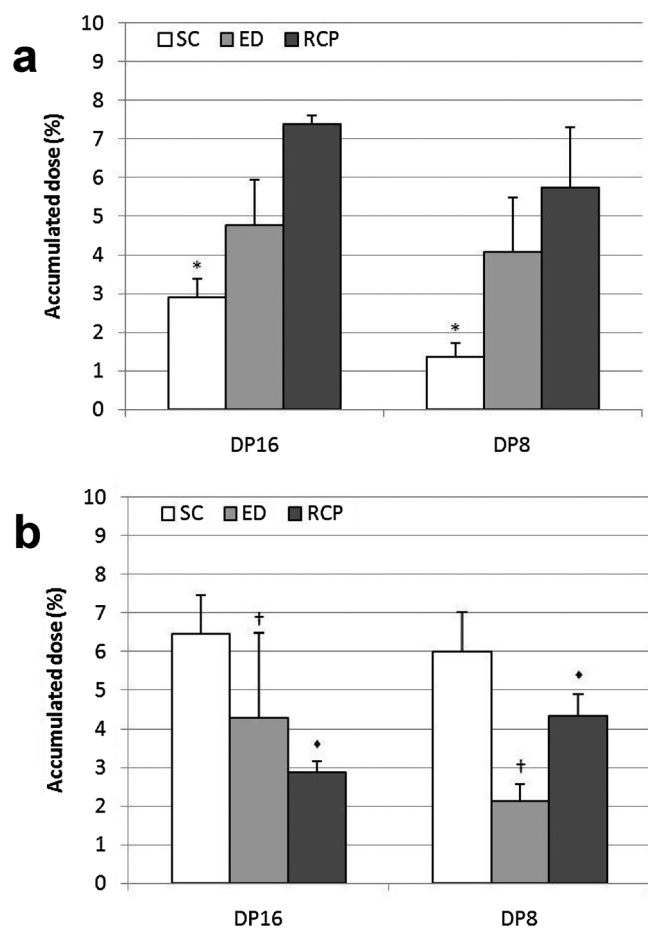


**Fig. 3.** In vitro skin penetration and permeation studies. Bars represent the amount of 3-HC detected in the skin layers (SC, stratum corneum, ED, epidermis and dermis) or receptor compartment (RCP), expressed as % of the dose administered on the skin surface, at the end of the experiment (8 h). a) The formulations were left in contact with the skin for all the duration of the experiment. b) The formulations were removed after 2 h contact with the skin. Results are reported as means  $\pm$  standard deviations of at least 6 independent determinations. Symbols represent significance of differences between the indicated values, evaluated by Student's *t*-test \*  $P < 0.001$ ,  $\diamond P < 0.02$ ,  $\ddagger P < 0.05$ .

pharmaceutical preparations suitable in topical administration. Particularly, it was shown that the nanostructure of the gel-like system is constituted by oligolamellar closely packed vesicles. In addition, the vesicle formulation (dispersed phase, DP, concentration in terms of MO + LCh, approximately equal to 4%) was proven to be effective in releasing diclofenac (used as model drug) to the viable epidermis, with irrelevant transdermal delivery [46]

Here, two different samples were tested for their 3-HC encapsulation efficiency and dermal release. The first, DP8, was prepared at a concentration of the dispersed phase close to the formation of the gel phase (the sample is still a low-viscous liquid). Differently, the second sample, DP16, was formulated at a concentration such that a highly viscous gel forms to investigate the role of the macroscopic viscoelastic behavior of the formulation in the drug release into the skin. Both samples were investigated loaded or not with 3-HC. The drug content in the DP8 and DP16 samples, evaluated by HPLC-UV-vis, was 0.8 mg and 1.0 mg of 3-HC per gram of formulation, respectively.

Concerning the sample DP8, empty and drug loaded vesicles analyzed by DLS showed an average size of  $74 \pm 1$  nm (PDI = 0.21) and  $77 \pm 2$  nm (PDI = 0.25), respectively. Only a slightly larger (not significant) size distribution in the drug-loaded nanoparticles was noticed. Due to the presence of the cationic LCh in the double layer of the nanoparticles, empty and 3-HC loaded vesicles exhibited an average  $\zeta$  potential of  $+41 \pm 2$  mV and  $+43 \pm 2$  mV, respectively.

Lamellarity (i.e., the number of double layers dividing in sub-compartments the interior of the vesicles) is an important issue in vesicle formulations since it can be related to the stability of the system as well as to the drug encapsulation efficiency and release [47]. Therefore, lamellarity was here investigated by SAXS experiments. In SAXS patterns lamellarity manifests with the presence of more or less defined (depending on the number of double layers characterizing the vesicles) quasi-Bragg peaks. Accordingly, SAXS pattern of sample DP8, reported in Fig. 2a, did not show any evidence of quasi-Bragg peaks, a signature of a formulations mainly consisting of unilamellar vesicles. Differently, the scattering profiles of the gel-like DP16 formulation empty or 3-HC loaded, reported in Fig. 2b, were characterized by the appearance of several (very low) quasi-Bragg peaks proving the formation of oligo- or multilamellar vesicles. It is worth recalling here that an increase in lamellarity of vesicular systems typically occurs upon raising the disperse phase content above the critical effective volume fraction, as a convenient way of arranging the additional interface area. This trend was confirmed by the analysis of the scattering profiles of samples DP20 and DP22, reported in Fig. 2c and d. The 3-HC content (when added) in these samples was 1.6 and 2.0 mg per gram of formulation, respectively. All SAXS patterns acquired show almost the same position of the

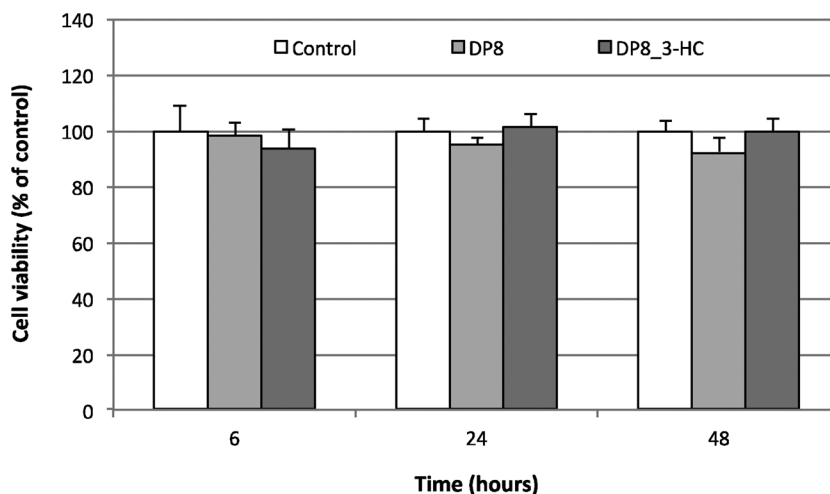


**Fig. 4.** Effect of the formulation DP8 empty or loaded with 3-HC on the viability of B16F10 cell line incubated with the different vesicles for 6, 24, and 48 h. Values represent percentages of viable cells compared to untreated control. Results represent the mean  $\pm$  standard deviation of three independent experiments.

quasi-Bragg peaks, indicating these aggregates are characterized by a similar interbilayer distance (i.e., the distance between two adjacent bilayers). However, as evidenced by the more marked quasi-Bragg peaks, lamellarity appears more pronounced in the systems loaded with 3-HC, suggesting a role of the drug in the multiwalled vesicles formation. Indeed, given its high hydrophobicity, 3-HC certainly locates within the lipid palisade, disturbing the regular alternation of MO and LCh at the interface and very likely modifying the lipid effective packing parameter and the bilayer flexibility, finally, favoring the formation of multilamellar aggregates.

Given the proposed application as topical formulation, shelf life is crucial for the physicochemical characterization of the system. The aqueous DP8 sample could be analyzed by DLS, while the gel DP16 sample, taking into account its rheological nature, was evaluated only by naked eyes for macroscopic phase separation. Particularly, up to 6 weeks after its preparation we did not observe any change neither in size nor in  $\zeta$  potential of DP8 sample, while we found that DP16 sample did not undergo macroscopic phase separation even after 4 months.

To determine the ability of the lipid carriers of delivering 3-HC within and through the skin, *in vitro* penetration and permeation studies through new born pig skin were carried out using Franz vertical diffusion cells. In a first subsets of experiments, the liquid DP8 or gel-like DP16 were spread on the skin specimens and allowed to diffuse under non-occlusive conditions for 8 h, when the experiment was stopped and the skin layers analyzed for 3-HC content (Fig. 3a). DP16 showed a superior ability of accumulating 3-HC in the stratum corneum as compared to DP8. This is not surprising, given the higher concentration of penetration enhancers, able to disturb the dense network of keratin and lipids (free fatty acids, cholesterol, and long chain ceramides) composing the SC, and the increased viscosity of the gel-like system. However, both the formulations showed good skin permeation properties, as witnessed by the high cumulative amount of 3-HC recovered in the receptor compartment and in the deeper skin layers. More in detail, the application of the gel-like DP16 turned in a higher – although not significantly – amount of 3-HC in the receptor solution, in the epidermis and dermis as compared to the liquid DP8. Despite being beneficial for drugs that have to be delivered systemically, this efficient permeation could pose some concerns when the skin itself represents the site of action. Thus, with the aim of reducing the amount of penetrated 3-HC while increasing the local accumulation, a second subset of experiments simulated the case of a shorter application time (2 h), followed by the removal of the excess formulation from the skin surface. Also in this case, the experiment was conducted for 8 h from the application of the 3-HC-containing vehicles on the skin. As expected, a shorter contact time overturned the distribution of the 3-HC, which resulted primarily accumulated in the skin layers (SC being the richest) and, in a notably lower amount, permeated in the receptor compartment (Fig. 3b). The transdermal penetration of the liquid formulation (DP8) appears to be less dependent on the reduction of the contact time compared to the DP16, as the former allows a higher delivery of 3-HC to the receptor medium. Indeed, it can be speculated that DP8 is characterized by a faster process of skin crossing compared to DP16, which requires longer application times to induce a comparable transdermal delivery. To better appreciate the dependence of the distribution upon the contact time, we calculated the ratio between the amount of 3-HC in the combined skin layers against the amount detected in the receptor medium (Skin/Receptor ratio, SR). This parameter could be used as a predictor of the fate of a topically applied drug, where lower values correlate with higher fractions of systemically absorbed drug, while higher values anticipate a local delivery. The calculated SR ratios were  $1.0 \pm 0.5$  (8 h contact) and  $1.9 \pm 0.5$  (2 h contact) for DP8, and  $1.1 \pm 0.2$  (8 h contact) and  $3.8 \pm 1.2$  (2 h contact) for DP16. Therefore, reducing the application time of the formulations from 8 to 2 h significantly increases ( $P < 0.02$ ) the SR values for both the DP8 (about 2-fold) and DP16 (about 4-fold). It has to be noted that the possibility of modulating the SR value by varying the application time

could be directly translated to the clinical setting and home treatment, as the patient could be easily instructed to remove the medication after a given time to optimize the skin accumulation, minimizing the systemic adsorption and the risk of undesired effects.

Finally, the formulation DP8 either empty or loaded with 3-HC was evaluated for cytotoxicity (MTT assay) in B16F10 cell cultures. To this aim, we chose to test the formulation at a therapeutically relevant concentration, basing on the results from enzymatic studies. Keeping constant the concentration of 3-HC, we tested the cell viability at 3 different time points (6, 24 and 48 h) to assess the safety of the formulation in the scenario of a long residence within the deeper skin layers, well after the removal from the skin surface. Fig. 4 shows the viability, expressed as % of the control of mouse melanoma cells after 6 h, 24 h and 48 h incubation in the presence of the two formulations. Inspection of these results clearly evidence that neither the vesicles alone nor those containing the 3-HC exert cytotoxic effects at the concentration investigated.

#### 4. Conclusions

The present study demonstrated the effectiveness of the 3-HC in inhibiting recombinant human tyrosinase, the key enzyme that catalyzes the crucial stages of the cascade of reactions that lead to the biosynthesis of melanin. 3-HC was successfully encapsulated within a vesicle formulation and a vesicle gel formulation, both based on two penetration enhancers, monoolein and lauroylcholine chloride, which efficiently delivered 3-HC to the deeper skin layers. More specifically, the application of the gel DP16 for 2 h produced the highest 3-HC skin accumulation and lowest transdermal delivery, thus representing an ideal candidate to locally inhibit tyrosinase activity with minimal systemic absorption. In addition, the formulation showed non-significant cytotoxicity against B16F10 melanoma cells.

Collectively, these data suggest that the 3-HC-loaded gel could be a promising candidate for pharmaceutical development.

#### Acknowledgments

Sergio Murgia thanks Fondazione Banco di Sardegna and Regione Autonoma della Sardegna (Progetti Biennali d'Ateneo FdS/RAS Annualità 2016, CUP F72F16003060002).

#### References

- [1] D. Peer, J.M. Karp, S. Hong, O.C. Farokhzad, R. Margalit, R. Langer, Nanocarriers as an emerging platform for cancer therapy, *Nat. Nanotechnol.* 2 (12) (2007) 751–760.
- [2] H.Y. Xue, P. Guo, W.C. Wen, H.L. Wong, Lipid-based nanocarriers for RNA delivery, *Curr. Pharm. Des.* 21 (22) (2015) 3140–3147.
- [3] P. Yingchoncharoen, D.S. Kalinowski, D.R. Richardson, Lipid-based drug delivery systems in cancer therapy: what is available and what is yet to come, *Pharmacol. Rev.* 68 (3) (2016) 701–787.
- [4] G. Bozzuto, A. Molinari, Liposomes as nanomedical devices, *Int. J. Nanomed. Nanosurg.* 10 (2015) 975–999.
- [5] F. Cuomo, M. Mosca, S. Murgia, P. Avino, A. Ceglie, F. Lopez, Evidence for the role of hydrophobic forces on the interactions of nucleotide-mono-phosphates with cationic liposomes, *J. Colloid Interface Sci.* 410 (2013) 146–151.
- [6] M.L. Immordino, F. Dosio, L. Cattel, Stealth liposomes: review of the basic science, rationale, and clinical applications, existing and potential, *Int. J. Nanomed.* 1 (3) (2006) 297–315.
- [7] V. Meli, C. Caltagirone, C. Sinico, F. Lai, A.M. Falchi, M. Monduzzi, M. Obiols-Rabasa, G. Picci, A. Rosa, J. Schmidt, Y. Talmon, S. Murgia, Theranostic hexosomes for cancer treatments: an *in vitro* study, *New J. Chem.* 41 (4) (2017) 1558–1565.
- [8] C. Nilsson, B. Barrios-Lopez, A. Kallinen, P. Laurinmaki, S.J. Butcher, M. Raki, J. Weisell, K. Bergstrom, S.W. Larsen, J. Ostergaard, C. Larsen, A. Urtti, A.J. Airaksinen, A. Yaghmur, SPECT/CT imaging of radiolabeled cubosomes and hexosomes for potential theranostic applications, *Biomaterials* 34 (33) (2013) 8491–8503.
- [9] S. Biffi, L. Andolfi, C. Caltagirone, C. Garrovo, A.M. Falchi, V. Lippolis, A. Lorenzon, P. Macor, V. Meli, M. Monduzzi, M. Obiols-Rabasa, L. Petrizza, L. Prodi, A. Rosa, J. Schmidt, Y. Talmon, S. Murgia, Cubosomes for *in vivo* fluorescence lifetime imaging, *Nanotechnology* 28 (5) (2017) 055102.
- [10] V. Meli, C. Caltagirone, A.M. Falchi, S.T. Hyde, V. Lippolis, M. Monduzzi, M. Obiols-Rabasa, A. Rosa, J. Schmidt, Y. Talmon, S. Murgia, Docetaxel-loaded fluorescent

- liquid-crystalline nanoparticles for cancer theranostics, *Langmuir* 31 (35) (2015) 9566–9575.
- [11] S. Murgia, A.M. Falchi, V. Meli, K. Schillen, V. Lippolis, M. Monduzzi, A. Rosa, J. Schmidt, Y. Talmon, R. Bizzarri, C. Caltagirone, Cubosome formulations stabilized by a dansyl-conjugated block copolymer for possible nanomedicine applications, *Colloids Surf. B Biointerfaces* 129 (2015) 87–94.
- [12] R. Negrini, W.K. Fong, B.J. Boyd, R. Mezzenga, pH-responsive lyotropic liquid crystals and their potential therapeutic role in cancer treatment, *Chem. Commun. (Camb.)* 51 (30) (2015) 6671–6674.
- [13] M.M.A. Elsayed, O.Y. Abdallah, V.F. Naggar, N.M. Khalafallah, Lipid vesicles for skin delivery of drugs: reviewing three decades of research, *Int. J. Pharm.* 332 (1–2) (2007) 1–16.
- [14] M.L. Gonzalez-Rodriguez, A.M. Rabasco, Charged liposomes as carriers to enhance the permeation through the skin, *Expert Opin. Drug Deliv.* 8 (7) (2011) 857–871.
- [15] M.S. Roberts, Y. Mohammed, M.N. Pastore, S. Namjoshi, S. Yousef, A. Alinaghi, I.N. Haridass, E. Abd, V.R. Leite-Silva, H. Benson, J.E. Grice, Topical and cutaneous delivery using nanosystems, *J. Control. Release* 247 (2017) 86–105.
- [16] M. Mezei, V. Gulasekharan, Liposomes—a selective drug delivery system for the topical route of administration. Lotion dosage form, *Life Sci.* 26 (18) (1980) 1473–1477.
- [17] G. Cevc, A. Schatzlein, H. Richardsen, Ultradeformable lipid vesicles can penetrate the skin and other semi-permeable barriers unfragmented. Evidence from double label CLSM experiments and direct size measurements, *Biochim. Biophys. Acta* 1564 (1) (2002) 21–30.
- [18] A. Manosroi, P. Khanrin, W. Lohcharoenkal, R.G. Werner, F. Gotz, W. Manosroi, J. Manosroi, Transdermal absorption enhancement through rat skin of gallidermin loaded in niosomes, *Int. J. Pharm.* 392 (1–2) (2010) 304–310.
- [19] E. Toutou, N. Dayan, L. Bergelson, B. Godin, M. Eliaz, Ethosomes - novel vesicular carriers for enhanced delivery: characterization and skin penetration properties, *J. Control. Release* 65 (3) (2000) 403–418.
- [20] C. Sinico, A.M. Fadda, Vesicular carriers for dermal drug delivery, *Expert Opin. Drug Deliv.* 6 (8) (2009) 813–825.
- [21] X. Peng, Y. Zhou, K. Han, L. Qin, L. Dian, G. Li, X. Pan, C. Wu, Characterization of cubosomes as a targeted and sustained transdermal delivery system for capsaicin, *Drug Des. Devel. Ther.* 9 (2015) 4209–4218.
- [22] R. Petrilli, F.S.G. Praça, A.R.H. Carollo, W.S.G. Medina, K.T. De Oliveira, M.C.A. Fantini, M.G.P.M.S. Neves, J.A.S. Cavaleiro, O.A. Serra, Y. Iamamoto, M.V.L.B. Bentley, Nanoparticles of lyotropic liquid crystals: a novel strategy for the topical delivery of a chlorin derivative for photodynamic therapy of skin cancer, *Curr. Nanosci.* 9 (4) (2013) 434–441.
- [23] U. Bazylińska, J. Kulbacka, J. Schmidt, Y. Talmon, S. Murgia, Polymer-free cubosomes for simultaneous bioimaging and photodynamic action of photosensitizers in melanoma skin cancer cells, *J. Colloid Interface Sci.* 522 (2018) 163–173.
- [24] A.M. Mayer, Polyphenol oxidases in plants and fungi: going places? A review, *Phytochemistry* 67 (21) (2006) 2318–2331.
- [25] H. Claus, H. Decker, Bacterial tyrosinases, *Syst. Appl. Microbiol.* 29 (1) (2006) 3–14.
- [26] H. Le-Thi-Thu, G.M. Casañola-Martín, Y. Marrero-Ponce, A. Rescigno, L. Saso, V.S. Parmar, F. Torrens, C. Abad, Novel coumarin-based tyrosinase inhibitors discovered by OECD principles-validated QSAR approach from an enlarged, balanced database, *Mol. Divers.* 15 (2) (2011) 507–520.
- [27] A. Rescigno, E. Sanjust, G. Soddu, A.C. Rinaldi, F. Sollai, N. Curreli, A. Rinaldi, Effect of 3-hydroxyanthranilic acid on mushroom tyrosinase activity, *Biochim. et Biophys. Acta – Gen. Subj.* 1384 (2) (1998) 268–276.
- [28] E. Sanjust, G. Cecchini, F. Sollai, N. Curreli, A. Rescigno, 3-Hydroxykynurenine as a substrate/activator for mushroom tyrosinase, *Arch. Biochem. Biophys.* 412 (2) (2003) 272–278.
- [29] G. Prota, *Melanins and Melanogenesis*, Academic Press, San Diego, 1992.
- [30] Y.J. Kim, H. Uyama, Tyrosinase inhibitors from natural and synthetic sources: structure, inhibition mechanism and perspective for the future, *Cell. Mol. Life Sci.* 62 (15) (2005) 1707–1723.
- [31] A. Rescigno, P. Zucca, A. Flurkey, J. Inlow, W.H. Flurkey, Identification and discrimination between some contaminant enzyme activities in commercial preparations of mushroom tyrosinase, *Enzyme Microb. Technol.* 41 (2007) 620–627.
- [32] M.B. Dolinska, P.T. Wingfield, Y.V. Sergeev, Purification of recombinant human tyrosinase from insect larvae infected with the baculovirus vector, *Curr. Protoc. Protein Sci.* 89 (2017) 6.15.1–6.15.12.
- [33] A. Rescigno, F. Sollai, B. Pisu, A. Rinaldi, E. Sanjust, Tyrosinase inhibition: general and applied aspects, *J. Enzyme Inhib. Med. Chem.* 17 (4) (2002) 207–218.
- [34] M. Hassan, Z. Ashraf, Q. Abbas, H. Raza, S.Y. Seo, Exploration of novel human tyrosinase inhibitors by molecular modeling, docking and simulation studies, *Interdiscip. Sci.* 10 (1) (2018) 68–80.
- [35] J.K. Jhan, Y.C. Chung, G.H. Chen, C.H. Chang, Y.C. Lu, C.K. Hsu, Anthocyanin contents in the seed coat of black soya bean and their anti-human tyrosinase activity and antioxidative activity, *Int. J. Cosmet. Sci.* 38 (3) (2016) 319–324.
- [36] T. Mann, C. Scherner, K.H. Röhm, L. Kolbe, Structure-activity relationships of thiazolyl resorcinols, potent and selective inhibitors of human tyrosinase, *Int. J. Mol. Sci.* 19 (3) (2018).
- [37] S. Asthana, P. Zucca, A.V. Vargiu, E. Sanjust, P. Ruggerone, A. Rescigno, Structure-activity relationship study of hydroxycoumarins and mushroom tyrosinase, *J. Agric. Food Chem.* 63 (32) (2015) 7236–7244.
- [38] R. Angelico, M. Carboni, S. Lampis, J. Schmidt, Y. Talmon, M. Monduzzi, S. Murgia, Physicochemical and rheological properties of a novel monoolein-based vesicle gel, *Soft Matter* 9 (3) (2013) 921–928.
- [39] P.D.S. Enzo, *Life Science, Recombinant Human Tyrosinase*, (2017) (Accessed 24 January 2018), <http://www.enzolifesciences.com/BML-SE535/tyrosinase-human-recombinant-his-tag/>.
- [40] A. Olianias, E. Sanjust, M. Pellegrini, A. Rescigno, Tyrosinase activity and hemocyanin in the hemolymph of the slipper lobster *Scyllarides latus*, *J. Comp. Physiol. B, Biochem. Syst. Environ. Physiol.* 175 (6) (2005) 405–411.
- [41] C. Leggio, L. Galantini, E. Zaccarelli, N.V. Pavel, Small-angle X-ray scattering and light scattering on lysozyme and sodium glycocholate micelles, *J. Phys. Chem. B* 109 (50) (2005) 23857–23869.
- [42] C.D. Schiller, A. Kainz, K. Mynett, A. Gescher, Assessment of viability of hepatocytes in suspension using the MTT assay, *Toxicol. In Vitro* 6 (6) (1992) 575–578.
- [43] B. Jergil, C. Lindbladh, H. Rorsman, E. Rosengren, Dopa oxidation and tyrosine oxygenation by human melanoma tyrosinase, *Acta Derm. Venereol.* 63 (6) (1983) 468–475.
- [44] S. Fogal, M. Carotti, L. Giaretta, F. Lanciai, L. Nogara, L. Bubacco, E. Bergantino, Human tyrosinase produced in insect cells: a landmark for the screening of new drugs addressing its activity, *Mol. Biotechnol.* 57 (1) (2015) 45–57.
- [45] Y.-C. Cheng, W.H. Prusoff, Relationship between the inhibition constant (KI) and the concentration of inhibitor which causes 50 per cent inhibition (I50) of an enzymatic reaction, *Biochem. Pharmacol.* 22 (23) (1973) 3099–3108.
- [46] M. Carboni, A.M. Falchi, S. Lampis, C. Sinico, M.L. Manca, J. Schmidt, Y. Talmon, S. Murgia, M. Monduzzi, Physicochemical, cytotoxic, and dermal release features of a novel cationic liposome nanocarrier, *Adv. Healthc. Mater.* 2 (5) (2013) 692–701.
- [47] M. Fröhlich, V. Brecht, R. Peschka-Süss, Parameters influencing the determination of liposome lamellarity by 31P-NMR, *Chem. Phys. Lipids* 109 (1) (2001) 103–112.

# Paper V

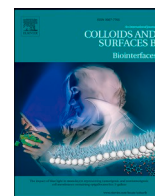
*“Tuning lipid structure by bile salts: hexosomes for topical administration of catechin”*

**M. Fornasier**, R. Pireddu, A. Del Giudice, C. Sinico, T. Nylander, K. Schillén, L. Galantini,  
S. Murgia;

Colloids and Surfaces B, 2021, 199, 111564

**DOI:10.106/j.colsurfb.2021.111564**

Copyright © from Elsevier 2021



## Tuning lipid structure by bile salts: Hexosomes for topical administration of catechin

Marco Fornasier<sup>a,b,c,\*</sup>, Rosa Pireddu<sup>d</sup>, Alessandra Del Giudice<sup>e</sup>, Chiara Sinico<sup>d</sup>, Tommy Nylander<sup>c</sup>, Karin Schillén<sup>c</sup>, Luciano Galantini<sup>e</sup>, Sergio Murgia<sup>a,b,\*</sup>

<sup>a</sup> Department of Chemical and Geological Sciences, University of Cagliari, s.s 554 bivio Sestu, Monserrato, I-09042, Italy

<sup>b</sup> CSGI, Consorzio Interuniversitario per lo Sviluppo dei Sistemi a Grande Interfase, via della Lastruccia 3 Sesto Fiorentino, Florence, I-50019, Italy

<sup>c</sup> Division of Physical Chemistry, Department of Chemistry, Lund University, P.O. Box 124, Lund, SE-221 00, Sweden

<sup>d</sup> Department of Life and Environmental Sciences, University of Cagliari, via Ospedale 72, Cagliari, I-09124, Italy

<sup>e</sup> Department of Chemistry, Sapienza University of Rome, P.le A. Moro 5, Rome, 00185, Italy

### ARTICLE INFO

#### Keywords:

Reverse hexagonal phase  
Skin  
Lipid liquid crystalline nanoparticles  
Natural antioxidants  
Mesophases  
Bile salts

### ABSTRACT

The delivery of bio-active molecules through the skin is challenging given the complex structure of its outer layer, the *stratum corneum*. Here we explore the possibility to encapsulate natural compounds into nanocarriers containing permeation enhancers that can affect the fluidity of the *stratum corneum* lipids. This approach is expected to facilitate dermal or transdermal release. For this purpose, the application of bile salts, which are natural surfactants involved *in vivo* in lipid digestion, was exploited.

Bile salts were added to lipid liquid crystalline nanoparticles (NPs) made of monoolein for antioxidant topical delivery. Monoolein self-assembly behaviour in water was affected by the presence of bile salts molecules, giving a transition from a bicontinuous cubic to unilamellar vesicles dispersion. By adding oleic acid (OA), the change of curvature in the system led to a reverse hexagonal phase. The morphology, structure and size of the nanocarriers was investigated before the nanoparticles were loaded with catechin, a natural antioxidant occurring in plants and food. The encapsulation did not affect significantly the formulation phase behaviour. The formulation loaded with bile salts and catechin was thereafter tested *in vitro* on the skin from new-born pig. The results for two different lipid formulations without bile salts were compared under the same experimental conditions and with the same antioxidant. The formulation with bile salts showed the best performance, allowing a superior permeation of catechin in the different skin layers in comparison with formulations without bile salt.

### 1. Introduction

The skin represents an effective barrier for many organisms, preventing invasion of pathogens and regulating both water content and temperature [1,2]. It consists of several anatomically distinct layers, of which the *stratum corneum* (SC) is the external one. The SC is formed by corneocytes (protein-enriched anucleate cells) and lipid lamellar sheets [3,4]. This architecture, described by P. Elias as the 'bricks and mortar' model [5], strongly restricts the diffusion of drugs and active compounds across the SC, limiting the efficacy of topical delivery of these molecules [6].

Topical formulations containing permeation enhancers are applied to overcome this obstacle: they are able to make the SC more fluid and hence facilitate penetration of the drug [7]. Efficient carriers engineered

for the dermal and transdermal release of active components include lipid dispersions such as liposomes [2,8], ethosomes (phospholipids nanocarriers with a relative high concentration of ethanol) [9,10] and niosomes (non-ionic surfactant-based vesicles) [11–14]. However, most of these carriers have some limitations in terms of drug loading [2].

Many life science applications exploit self-assembly of surfactants and lipids in water. The structure of these aggregates can be tuned by several parameters (*i.e.* temperature, concentration and composition in terms of salt, pH and additives). The particular type of structure formed can be rationalized by using the concept of the critical packing parameter (CPP). It is defined as the ratio between the volume of the hydrophobic tail of the surfactant ( $v$ ), and the product of the surface area of the headgroup ( $a$ ) times the length of the hydrophobic tail ( $l$ ), *i.e.*  $CPP = v/al$  [15]. For values of the packing parameter below 1, direct phases can

\* Corresponding authors at: Department of Chemical and Geological Sciences, University of Cagliari, s.s 554 bivio Sestu, Monserrato, I-09042, Italy.

E-mail addresses: [mformasier@unica.it](mailto:mformasier@unica.it) (M. Fornasier), [murgias@unica.it](mailto:murgias@unica.it) (S. Murgia).

<https://doi.org/10.1016/j.colsurfb.2021.111564>

Received 27 October 2020; Received in revised form 24 December 2020; Accepted 3 January 2021

Available online 6 January 2021

0927-7765/© 2021 Elsevier B.V. All rights reserved.

be formed in water. As it approaches to 1, the lamellar phase become more favorable, whereas reverse phases can be obtained for values higher than 1. Among the latter, the reverse cubic bicontinuous and reverse hexagonal bulk phases can be dispersed in water to obtain non-lamellar liquid crystalline nanoparticles, called cubosomes and hexosomes, respectively [16,17]. They possess a larger hydrophobic volume than their lamellar counterparts (*i.e.* liposomes) of the same size [18]. Herein, hexosomes and cubosomes will be discussed. In the reverse hexagonal phase, a lipid monolayer is curved towards water cylinders organized in a 2-dimensional hexagonal array. In the bicontinuous cubic phase, a curved lipid bilayer is formed in 3 dimensions in such a way that two systems of unconnected water channels are formed, with continuous regions of both water and lipid. The structure formed can be described as an infinite periodic minimal surface [18]. Both cubosomes and hexosomes can be formulated from different lipids, but monoolein-based aggregates are the most used for medical applications, given their low cytotoxicity [18–20]. Monoolein (or glycerol mono-oleate, GMO) forms a reverse hexagonal phase in water above 80 °C, depending on the purity of the sample [21]. Therefore, to favour the cubic bicontinuous-to-reverse hexagonal transition at room temperature, which is needed to formulate hexosomes, lipids such as oleic acid are needed as additives to increase the effective packing parameter.

Both hexosome and cubosome require adding a stabilizing agent to ensure their colloidal stability and avoid aggregation, and amphiphilic non-ionic tri-block copolymers of poly(ethylene oxide) (PEO) and poly(propylene oxide) (PPO), known as poloxamers, are used as the most common stabilizers [18,22]. The hydrophobic PPO middle block is partly buried in the lipid bilayer, whereas the two PEOs hydrophilic end blocks build up a corona surrounding the NP. This corona ensures sterical repulsive forces preventing the aggregation of the dispersed NPs.

Indeed, other kinds of stabilizers can be adopted, such as poly-phosphoesters [23], brush copolymers [24], and polysorbate 80 [25]. Recently, few examples of cubosomes and hexosomes that remain stable in water without adding a stabilizer were reported [26–28].

Several compounds can be added to a formulation to enhance its permeation properties [7,29,30]. Among them, bile salts (BSs) are promising candidates as they are natural surfactants, essential for the lipid digestion *in vivo*. The behaviour of these compounds and some derivatives in several biomedicine relevant systems, such as mixtures containing ionic [31,32] and non-ionic block copolymers [33–37] and lipids [38–40], has been extensively investigated. Moreover, BSs derivatives have been synthesized to obtain drug carriers suitable for delivery in the gastrointestinal tract to enhance the drug bioavailability [41], and as building blocks for supramolecular structures, such as tubules and scrolls [42,43] able to organize into supra-colloidal frameworks [44,45]. Their importance in topical applications has been proven [2,46], as they are considered to be “edge activators”, *e.g.*, bilayer softening components [47], and can confer elastic properties to lipid vesicles [48]. Indeed, the presence of an edge activator into the formulation can increase the penetration of drugs through the skin *strata* [49–51].

To our knowledge, only one experimental investigation has been devoted to explain the effect of a mixture of two BSs (sodium cholate (C) and sodium deoxycholate (DC)) on the structure and morphology of GMO- and phytantriol-based cubosomes [52]. It was found that the bicontinuous cubic Pn3m and Im3m to the lamellar bulk phases and their dispersions (cubosomes and vesicles, respectively) could be formed depending on the concentration and type of BS. However, the topical application of BSs-loaded non-lamellar lipid liquid crystalline dispersions has not yet been explored.

Among the bio-active compounds adopted for topical delivery, natural antioxidants have been widely studied due to their exceptional versatility. Catechin (Cat) is a natural polyphenol, found in several nutritional products. In the last decades, its beneficial properties as antiaging, antidiabetic, antibacterial, neuroprotective, and anti-inflammatory were reported [53–55]. Moreover, some studies

highlighted that Cat has significant skin-photoprotection effect against UV-mediated oxidative stress and sunburns [56]. The application of this antioxidant is challenging due to short half-life *in vivo* and poor bioavailability after oral administration [57]. Therefore, Cat was encapsulated in drug carriers suitable for dermal or transdermal release [55,56,58,59], given that this administration route avoid the harsh environment of the gastrointestinal tract.

The effect of three different BSs, sodium cholate, sodium deoxycholate and sodium taurocholate (TC), on the structure and morphology of GMO-based liquid crystalline nanoparticles have been investigated with the prospect of applying these systems for the topical delivery of Cat. The bile salts used were selected based on their variation of hydrophilicity. After an initial screening, the best formulation in terms of its colloidal stability was loaded with Cat and their antioxidant activity and penetration ability on skin from new-born pigs evaluated *in vitro*.

## 2. Materials and methods

### 2.1. Materials

The building block for the dispersions, RYLO MG 19 PHARMA, glycerol monooleate, 98.1 % wt (GMO), was kindly provided by Danisco Ingredients (Brdrand, Denmark). The bile salts sodium cholate, sodium deoxycholate and sodium taurocholate, as well as catechin (HPLC quality, purity  $\geq 97\%$ ), Pluronic® F108 (here denoted PF108) and oleic acid (GC quality, purity  $\geq 99.0\%$ ) were purchased from Sigma Aldrich. Lauroylcholine chloride (LCh, Titration quality and purity  $> 98\%$ ) was purchased from TCI (Germany). MilliQ water (MilliQ Corporation, Bedford, MA) was used for the preparation of the nanoparticles' solutions.

### 2.2. Loaded and unloaded NPs preparation

The lipid liquid crystalline nanoparticles were prepared by melting GMO with or without oleic acid at 40 °C and thereafter an aqueous solution containing the poloxamer stabilizer PF108 and the BSs was added as described previously [18,22]. The GMO-PF108-BS mixture was thereafter sonicated using a tip sonicator equipped with a controller (Sonics Vibra Cells, both from Chemical Instruments AB, Sweden) for 4 min at 30 % of amplitude and then for 6 min at 40 %, using the pulse in mode ON for 1 s and in mode OFF for 1 s (5 min of total sonication time). After ultrasonication, a milky or bluish dispersion was obtained, depending on the concentration of BSs and OA. To prepare the carriers loaded with the natural antioxidant, Cat was first dispersed in the lipid phase before mixing with the PF108-BS solution. The formulations obtained were stored at 25 °C prior to use and characterized 48 h after preparation. The GMO:PF108 weight ratio was kept at 11:1 and the amount of dispersed phase was 3.6–4.6 wt (%), depending on the amount of BSs and OA added to the formulation. A typical volume for the samples was 2 mL.

The samples of hexosomes without bile salt (used for the *in vitro* studies) were prepared in the same manner, while the vesicles without BSs required the use of LCh instead of PF108.

For detailed compositions of the samples, see the Supplementary Material.

### 2.3. Cryogenic transmission electron microscopy

The morphology of the formulations was analyzed by cryogenic transmission electron microscopy (cryo-TEM) at the National Center for High Resolution Electron Microscopy (nCHREM) at Lund University. The instrument used was a JEM-2200FS transmission electron microscope (JEOL), equipped with a field-emission electron source, a cryopole piece in the objective lens and an in-column energy filter (omega filter). The recording of zero-loss images was acquired at an acceleration voltage of 200 kV on a bottom-mounted TemCam-F416 camera (TVIPS)

using SerialEM under low-dose conditions. Each sample with the lipid nanoparticle dispersions was prepared using an automatic plunge freezer system (Leica Em GP) in an environmental chamber at 25.0 °C and 90 % of relative humidity. A 4 µL droplet of the dispersions of vesicles or hexosomes was deposited on a lacey formvar carbon-coated grid (Ted Pella), and the excess liquid was removed with filter paper after blotting. The grids were plunged into liquid ethane (around -183 °C) to ensure the rapid vitrification of the sample in its native state, and thereafter stored in liquid nitrogen (-196 °C). Before an imaging session, the grids were transferred into the microscope using a cryo-transfer tomography holder (Fischione, Model 2550).

#### 2.4. Dynamic light scattering and electrophoretic mobility measurements

The apparent hydrodynamic diameter ( $D_h$ ) and the zeta ( $\zeta$ ) potential of the particles in the formulation were estimated by DLS measurements and by measurements of the electrophoretic mobility of the particles using a ZetaSizer Nano ZS by Malvern Instruments (now part of Malvern Panalytical) at (25.0 ± 0.1) °C [60], set in a backscattering geometry at a fixed scattering angle of 173°. The nanoparticle dispersions were diluted in water 1:50 and analysed in disposable cuvettes. The values of the intensity-weighted  $D_h$  and polydispersity index (PdI) were extracted from a second order Cumulant analysis. The parameters were collected from at least six independent measurements of 10 runs each.

The electrophoretic mobilities were collected at a fixed scattering angle of 17° using laser Doppler electrophoresis method with disposable folded capillary cells (DTS1070).  $\zeta$  potentials values were estimated from electrophoretic mobility by using Smoluchowski's equation and stated as the average of three consecutive measurements on the same solution together with the estimated standard deviation (SD). Before the measurements, the samples were diluted by a factor of 1:50 in water.

#### 2.5. Small angle X-ray scattering

Small angle X-ray scattering patterns of the formulation were acquired with a SAXSLab Ganesha instrument (JJ-Xray, Denmark), equipped with a 30 W Cu X-ray micro-source (Xenocs, France) and a 2D 300 K Pilatus detector (Dectris, Switzerland). The measurements were performed with a pin-hole collimated beam with the detector positioned asymmetrically at a distance of 480 mm from the sample, to yield azimuthally averaged intensities as a function of the scattering vector ( $q$ ) over the range 0.012 – 0.67 Å<sup>-1</sup>. The magnitude of the scattering vector is defined by  $q = (4\pi\sin\theta)/\lambda$ , where  $\lambda$  equals to 1.54 Å, Cu K $\alpha$  wavelength, and  $\theta$  is half of the scattering angle. The  $q$  scale was calibrated using silver behenate (CH<sub>3</sub>-(CH<sub>2</sub>)<sub>20</sub>-COOAg) as a standard.

Samples were loaded in 1.5 mm quartz capillary cells and placed in a thermostat stage at 25 °C, controlled using a Julabo T Controller CF41 (Julabo Labortechnik GmbH, Germany, and equilibrated for 1800s before any SAXS measurements

The  $d$  spacing was obtained from the positions of the Bragg peaks detected in the patterns ( $q_{peak}$ ) by the following expression:

$$d = \frac{2\pi}{q_{peak}} \quad (1)$$

Then, the lattice parameter of the liquid crystalline phase structure,  $a$ , was calculated from Eqs. 2 and 3 for the bicontinuous cubic and for the hexagonal phases, respectively [61].

$$a = d \cdot \sqrt{h^2 + k^2 + l^2} \quad (2)$$

$$a = d \cdot \frac{2}{\sqrt{3}} \sqrt{h^2 + k^2 + hk} \quad (3)$$

Here,  $h$ ,  $k$  and  $l$  are the Miller indexes that describe the crystalline planes of lattice. The lattice parameter was used to evaluate the water channel radius ( $r_w$ ) of the bicontinuous cubic phase (Eq. 4) or of the hexagonal

phase (Eq. 5):

$$r_w = (a - l) \cdot \sqrt{\frac{A_0}{-2\pi\chi}} \quad (4)$$

$$r_w = a \cdot \sqrt{1 - \varphi_{lipid}} \cdot \left(\frac{\sqrt{3}}{2 \cdot \pi}\right)^{\frac{1}{2}} \quad (5)$$

where  $\chi$  and  $A_0$  are, respectively, the Euler characteristic and the surface area of the IPMS geometry (Pn3m,  $\chi = -2$ ,  $A_0 = 1.919$ ), and  $l$  is the GMO hydrophobic chain length at 25 °C (17 Å). The volume fraction,  $\varphi_{lipid}$ , was calculated using the following equation (Eq. 6), where the parameters  $w_{lipids}$ ,  $d_{lipids}$ ,  $w_{water}$  and  $d_{water}$  are the weight and density of the lipid mixture (GMO + OA) and water respectively:

$$\varphi_{lipid} = \frac{\frac{w_{lipids}}{d_{lipids}}}{\left(\frac{w_{lipids}}{d_{lipids}} + \frac{w_{water}}{d_{water}}\right)} \quad (6)$$

The values of  $d_{lipids} = 0.941 \text{ g cm}^{-3}$  and  $d_{water} = 0.998 \text{ g cm}^{-3}$  were used.

#### 2.6. Encapsulation efficiency

Although Cat is strongly hydrophobic and thus expected to partition mostly in the lipid matrix, the formulations were dialyzed to remove possible traces of the solubilized antioxidant in the aqueous phase. The samples containing Cat were loaded into a dialysis tubing cellulose membrane (14 kDa MW cutoff, purchased from Sigma Aldrich) and dialysed again 2 L of water for 2 h (by replacing the water after 1 h) at room temperature.

The absorption spectra of Cat (with an absorption maximum at 281 nm) were acquired using a Win-Cary Varian UV-vis double beam spectrophotometer in EtOH. The standard calibration curve method was exploited to evaluate the loading of the antioxidant into the formulations via linear regression analysis ( $R^2 = 0.9999$ ). A portion of the lipid formulations loaded with Cat was dissolved in EtOH before and after dialysis and placed in quartz cuvettes (1 cm of optical path).

The encapsulation efficiency (EE %) of the carriers was calculated using the following equation:

$$EE \% = \frac{m_{Cat \text{ after dialysis}}}{m_{Cat \text{ before dialysis}}} \cdot 100 \quad (7)$$

where  $m_{Cat \text{ after dialysis}}$  and  $m_{Cat \text{ before dialysis}}$  represent the mass of Cat evaluated via UV-vis spectroscopy in the samples after and before dialysis, respectively.

#### 2.7. DPPH test

The antioxidant activity of Cat-loaded formulations was assessed by evaluating their ability to scavenge the stable radical 2,2-diphenyl-1-picrylhydrazyl (DPPH). DPPH (0.04 mg/mL) dissolved in methanol was mixed with an appropriate amount of formulation to yield final Cat concentrations in the range 0.01 – 0.1 mg/mL. Empty formulations were also tested as control. Moreover, a negative control was prepared by mixing 990 µL of DPPH solution with 10 µL of water. After 30 min of incubation in the dark at room temperature, the absorbance was read at 517 nm by a Synergy 4 multiplate reader (BioTek, Winooski, USA). The percent antioxidant activity was calculated according to Eq. 8.

$$\text{antioxidant activity (\%)} = \frac{(ABS_{control} - ABS_{sample})}{ABS_{control}} \cdot 100 \quad (8)$$

where  $ABS_{control}$  and  $ABS_{sample}$  are the absorbance of the Cat methanolic solution (control) and of the different Cat-loaded carriers (sample).



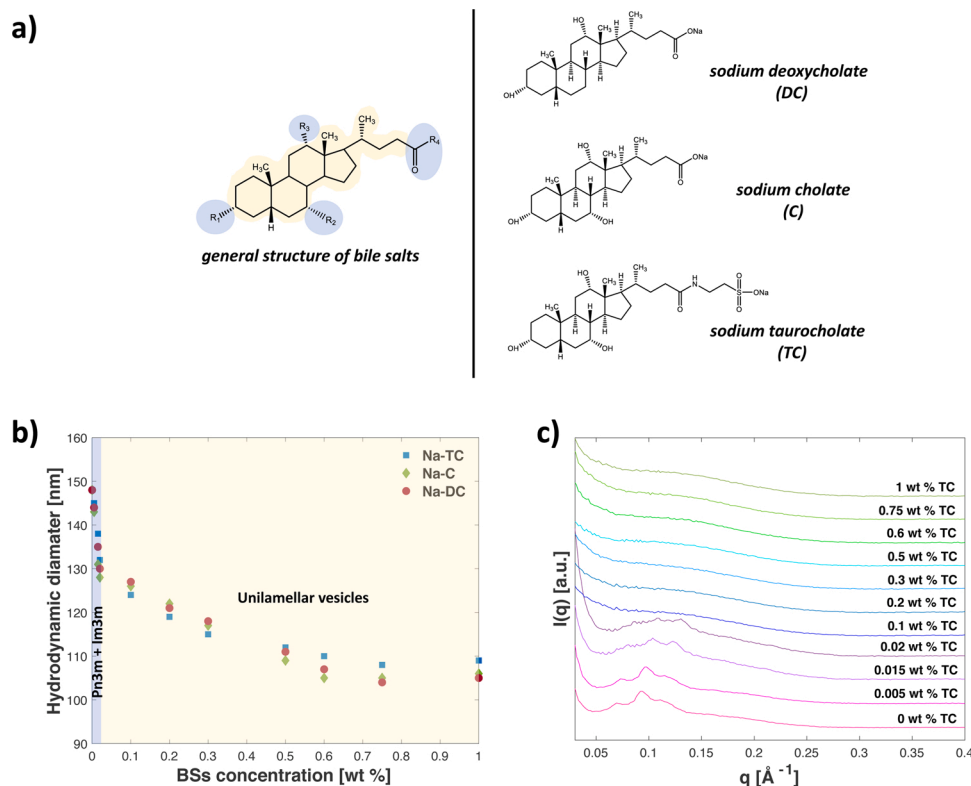


**Fig. 1.** a) Chemical structure of the BSs used in the study. The steroid backbone (light yellow) is highly hydrophobic, while the different substituents (blue) define the hydrophilicity. The main difference between the three sodium bile salts is the substitution in R<sub>4</sub>, equal to a taurine (-C = O-NH-CH<sub>2</sub>-CH<sub>2</sub>-SO<sub>3</sub><sup>-</sup>) in the case of TC and a carboxylate (-COO<sup>-</sup>) for both C and DC. Moreover, DC lacks a -OH in position R<sub>2</sub>. b) The apparent hydrodynamic diameter by DLS is plotted against the BSs concentration (wt % of the dispersion). The errors in the measurements are less than 2 % for each point in the plot. The different structures inferred from SAXS results as a function of BSs content are highlighted as differently colored areas: light blue for the Pn3m + Im3m bicontinuous cubic phase and light green for unilamellar vesicles. c) SAXS patterns acquired for the formulations at 25 °C with increasing content of BSs. The lines on the peaks represent the Im3m (filled lines) and Pn3m (dashed lines) quasi-Bragg peaks. Even though only TC-loaded aggregates were reported in the plot, DC and C followed the same trend without any significant difference (data not shown).

## 2.8. *In vitro* penetration and permeation studies

The ability of BS-loaded formulations to modulate Cat penetration and/or permeation through the skin was evaluated using skin from newborn pigs and the results were compared with the corresponding reference sample without BS. The experiments were performed in Franz vertical cells, exhibiting a diffusion area of 0.785 cm<sup>2</sup>. The skin of one-day-old Goland-Pietrain hybrid pigs (~1.2 kg), died of natural causes and provided by a local slaughterhouse, was excised and stored at -80 °C until the day of the experiment. Skin specimens (n = 6 per formulation) were pre-equilibrated with saline (NaCl 0.9 % w/v) at 25 °C, then put between the donor and the receptor compartments. The receptor was filled with 5.5 mL of saline solution (NaCl 0.9 % w/v), continuously stirred and thermostated at (37 ± 1) °C, to emulate *in vivo* conditions. Exactly 200 µL of each formulation were placed onto the skin surface. At regular intervals, up to 8 h, the receiving solution was entirely withdrawn, replaced with fresh saline to ensure sink conditions and analysed by HPLC for catechin content. After 8 h, the skin surface was gently washed with 1 mL of distilled water and then dried with filter paper. The stratum corneum was removed by stripping with adhesive tape Tesa® AG (Hamburg, Germany). Each piece of adhesive tape was firmly pressed on the skin surface and rapidly pulled off with one stroke. Epidermis was separated from dermis with a surgical scalpel. Skin strata were cut, placed each in a flask with methanol and sonicated for 2 min to extract the accumulated drug. The tape and tissue suspensions were filtered out and assayed for drug content by HPLC.

## 2.9. HPLC method

Cat content was quantified at 222 nm using a chromatograph Alliance 2690 (Waters, Italy). The column was a XSelect HSS T3 (3.5 µm, 4.6 × 100 mm, Waters). The mobile phase was a mixture of acetonitrile, water and acetic acid (40.845:59.15:0.005 v/v), delivered at a flow rate of 0.3 mL/min. A standard calibration curve (R<sup>2</sup> of 0.999) was built up by using working, standard solutions (0.01 – 0.1 mg/mL).

## 2.10. Statistical analysis of data

Results are expressed as the mean ± SD. Multiple comparisons of means (one-way ANOVA with post-hoc Tukey HSD test) were used to substantiate statistical differences between groups, while Student's *t*-test was used to compare two samples. Data analysis was carried out with the software package XLStatistic for Microsoft Excel. Significance was tested at 0.05 level of probability (p).

## 3. Results and discussion

### 3.1. Effect of BSs on the cubosomes dispersion in water

First, a screening was conducted in order to evaluate the effect of the bile salts C, DC and TC on the structure of the GMO-based liquid crystalline nanoparticles. Here, the results in relation to the differences in chemical structures of the BSs used in this study will be discussed (Fig. 1a). The BSs typical facial amphiphilic moiety emerges from the hydroxyl groups-decorated backbone of condensed rings, which allows the molecule to intercalate into lipid bilayers and eventually disrupt them during the digestion [62].

DC and C possess the same substitution in R<sub>4</sub> (DC does not have a O-H group in position R<sub>2</sub>), while TC presents a taurine derivative with a larger polar group (S-O<sub>3</sub><sup>-</sup>). The number of hydroxyl groups and the conjugation with hydrophilic aminoacids determine the hydrophobic/hydrophilic balance on BSs molecules, which decreases in the order deoxycholate > cholate > taurocholate.

The BSs were loaded into the NPs in the range 0–1 wt % of the dispersion, containing 3.6–4.6 wt % of dispersed phase. Then, the (internal) structure and the size (apparent hydrodynamic diameter) of the particles in the formulations were evaluated by SAXS and DLS, respectively.

The D<sub>h</sub> values, upon addition of these BSs in the concentration range 0–1.0 wt %, to the formulation of cubosomes, suggest that the addition of bile salt reduces the size of the particles (Fig. 1b). Starting from a

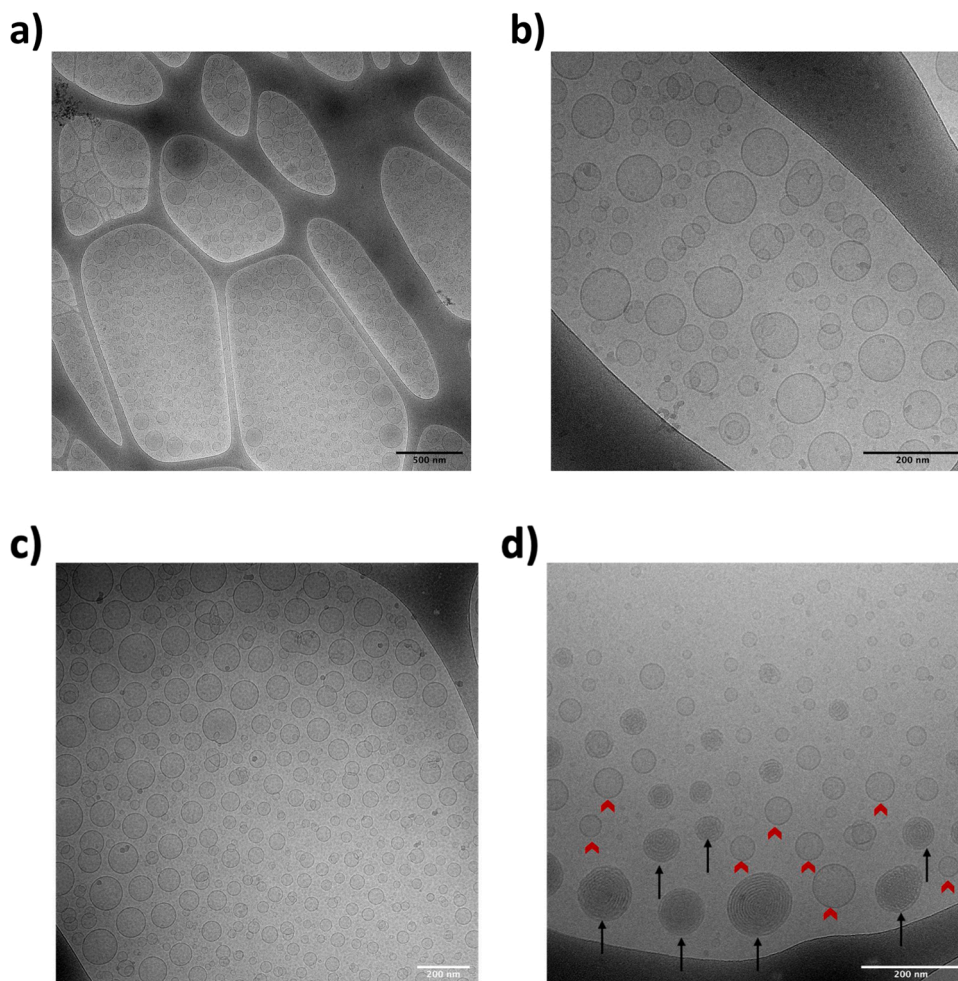


**Fig. 2.** Cryo-TEM images of the formulations investigated. (a) and (b) GMO/TC/PF108/W = 3.3/0.3/0.3/96.1 (wt%) at a magnification of 15k and 60k, respectively. (c) GMO/OA/TC/PF108/W = 3.0/0.2/0.3/0.3/96.2, magnification of 30k. (d) GMO/OA/TC/PF108/W = 3.0/0.5/0.3/0.3/95.9 (wt%), at a magnification of 60k showing hexosomes (black arrows) and vesicles (red arrowheads).

typical value of 148 nm for the cubosomes without BSs, no significant effect on the size was observed up to a BS content of 0.015 wt %. By contrast, a remarkable decrease of the diameter was detected at larger BS concentration down to a plateau at  $D_h$  values of 107–110 nm, which was reached at around 0.6 wt % BS. Similar trends were observed for all of the investigated BSs, with no significant differences.

It is well known that GMO in excess water self-assembles into a bicontinuous cubic Pn3m phase. However, the presence of poloxamers, such as PF108, induces the formation of an additional bicontinuous cubic phase, the Im3m. This phenomenon was explained by Nakano as an interaction between the PPO moiety of the block copolymer and the GMO bilayer [63]. Indexing of the diffraction peaks from the SAXS pattern confirmed the coexistence of Pn3m and Im3m cubic phases in the copolymer-stabilized dispersion in the absence of BSs (Fig. 1c).

The two phases were preserved in the presence of small addition of BSs (< 0.02 wt %) to the formulation, although a slight decrease in the lattice parameters occurred since the diffraction peaks shifted to larger  $q$  values (see Supplementary Material). In parallel a decrease of the peak intensities was detected. A slight decrease in hydrodynamic diameter was also observed. A complete transition from reverse bicontinuous cubic phase to unilamellar vesicles took place above 0.02 wt % BS, as highlighted by the disappearance of the well resolved cubic diffraction that coincides with the appearance of a broad diffuse peak at larger  $q$ , related to the presence of vesicles (Fig. 1c).

The observed strong effect of BSs on the GMO bilayers can be justified considering the capability of the bile salt molecules to intercalate

the bilayer, leaving their charged heads in contact with the bulk water. This reduces the effective packing parameter and hence favours a phase transition from a reverse bicontinuous cubic to a lamellar phase.

We observed that, at the same BS concentration, the different BSs provided formulations with similar structure and size of the particles. However, a relevant effect of the BS type on the polydispersity of the formulations could be observed. In particular, the DC- and C-loaded formulations exhibited higher PDI values ( $0.2 < \text{PDI} < 0.3$ ) compared to the TC-loaded formulations ( $\leq 0.2$ ). Moreover, a visual inspection revealed that both composition and BS type affected the stability of the formulations. Samples containing DC and C below 0.2 and above 0.5 wt % were destabilized after few days, whereas for BSs content between 0.2 and 0.5 wt % the samples lasted for two weeks on average. TC-loaded NPs remained stable for two months at TC content in the range 0.2 – 0.5 wt %, and 2–3 weeks at compositions outside this interval.

According to the electrophoretic mobility measurements, DC- and C-loaded NPs presented an average  $\zeta$  potential of  $(-40 \pm 2)$  mV while the NPs formulated with TC had  $(-50 \pm 1)$  mV. The higher (absolute value)  $\zeta$  potential may explain the higher stability of the TC samples.

It deserves here noticing that, at least to a certain degree, the investigated BSs and PF108 may interact forming complexes, as already reported for different PEO-PPO-PEO block copolymers and another type of BS [33,34,36]. Therefore, a possible reason for the observed loss of colloidal stability when the BS concentration exceeds 0.5 wt % could be due to the reduced amount of PF108 available for the stabilization of the nanoparticles.

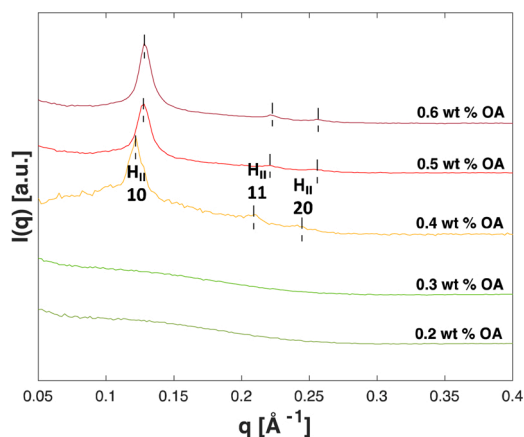


**Fig. 3.** SAXS patterns of GMO/OA/TC/PF108/W systems with increasing concentration of OA at 25 °C. The Bragg peaks related to the reverse hexagonal phase ( $H_{II}$ ) are indicated by vertical black lines.

**Table 1**

Effect of OA concentration on NPs structure. Composition is given in wt %. Lattice parameters and water channel radii were calculated from eq.3 and eq.5.

GMO/OA/TC/PF108/W	Phase	a (Å)	$r_w$ (Å)
3.3/0.2/0.3/0.3/95.9	Vesicles	–	–
3.3/0.3/0.3/0.3/95.8	Vesicles	–	–
3.3/0.4/0.3/0.3/95.7	$H_{II}$	$58.9 \pm 0.2$	$30.4 \pm 0.1$
3.3/0.5/0.3/0.3/95.6	$H_{II}$	$56.7 \pm 0.2$	$29.2 \pm 0.1$
3.3/0.6/0.3/0.3/95.5	$H_{II}$	$55.0 \pm 0.1$	$28.4 \pm 0.1$

Among the stable formulations containing TC, the sample with composition GMO/TC/PF108/W = 3.3/0.3/0.3/96.1 (wt %) was selected for a more detailed characterization due to its stability at intermediate BS content. The morphology of the NPs was studied by cryo-TEM. In the micrographs spherical unilamellar vesicles were observed (Fig. 2a and b), corroborating the previous findings unveiled by SAXS.

### 3.2. Hexosomes containing bile salts

To create formulations based on hexosome dispersions, oleic acid was added to tune the interfacial curvature of the investigated systems. The effect of OA addition to the formulation containing TC was therefore explored in the OA concentration range 0.2 – 0.6 wt %. As revealed by cryo-TEM and SAXS experiments, vesicles were formed up to a content of 0.3 wt % OA, while hexosomes were obtained in the range 0.4 – 0.6 wt % of OA. Further addition of OA led to unstable formulations, undergoing complete macroscopic separation after few minutes. The morphology of the vesicles and hexosomes was studied by means of cryo-TEM (Fig. 2c and d).

Fig. 2c shows a typical micrograph of unilamellar vesicles. A few vesicles were interconnected or fused, highlighting the reduced curvature of the lipid bilayer induced by the presence of TC [49]. Increasing the OA concentration lead to the formation of hexosomes. This is evident from Fig. 2d, which shows a cryo-TEM image for a sample with composition GMO/OA/TC/PF108/W = 3.0/0.5/0.3/0.3/95.9 (wt%), that presents spherical and quasi-spherical particles with an inner-structure characterized by curved striations. These kind of morphologies are commonly reported in other studies of liquid crystalline nanoparticles with a reverse hexagonal phase [64,65]. The presence of unilamellar vesicles can also be discerned in the same micrograph (Fig. 2d).

SAXS patterns of the formulations with different OA concentrations are reported in Fig. 3.

As already mentioned, increasing the OA concentration affected the self-assembly properties of GMO. At 0.2 wt % the amount of OA was not

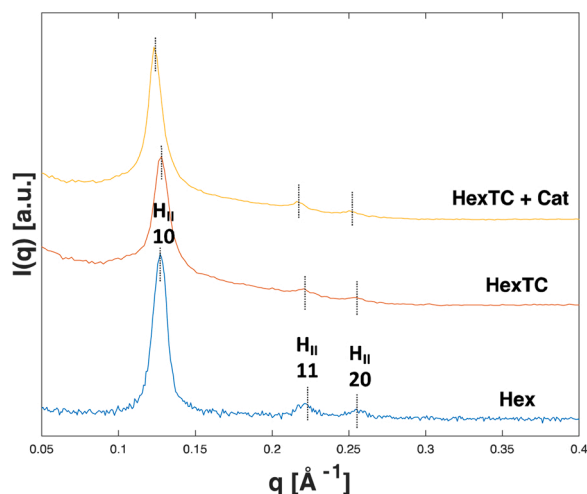


**Fig. 4.** SAXS patterns of the formulation of hexosomes (Hex), TC-loaded hexosomes (HexTC) and TC-loaded hexosomes with catechin encapsulated (HexTC + Cat) at 25 °C.

**Table 2**

Lattice parameters ( $a$ ), apparent hydrodynamic diameters ( $D_h$ ), polydispersity index (PdI) and  $\zeta$  potentials for the loaded and unloaded formulations evaluated by SAXS, DLS, and electrophoretic mobility measurements.

Sample	a (Å)	$r_w$ (Å)	$D_h$ (nm)	PdI	$\zeta$ (mV)
Hex	$56.9 \pm 0.2$	$29.3 \pm 0.1$	$160 \pm 2$	$0.10 \pm 0.02$	$-30 \pm 1$
HexTC	$56.7 \pm 0.2$	$29.2 \pm 0.1$	$157 \pm 1$	$0.13 \pm 0.01$	$-52 \pm 1$
HexTC + Cat	$58.2 \pm 0.7$	$30.0 \pm 0.3$	$158 \pm 1$	$0.14 \pm 0.01$	$-54 \pm 2$

enough to counterbalance the lamellar-forming effect of TC and therefore the SAXS curve reflects a formulation containing only vesicles (Fig. 3). At 0.4 wt % a lamellar-to-hexagonal phase transition was observed. The presence of the reverse hexagonal symmetry was proved by three peaks in the SAXS pattern positioned at  $q$  values in the ratio 1:  $\sqrt{3}$ :  $\sqrt{4}$ . The radius of the water channels calculated from the peak positions was observed to slightly decrease with OA addition (Table 1). Further increasing the amount of OA destabilized the system, with consequent phase separation.

The most stable hexagonal phase dispersion was the one containing 0.5 wt % of OA, which was stable for more than one month as judged by visual inspection.

### 3.3. Encapsulation of catechin into hexosomes

Encapsulation of payloads into a lipid liquid crystalline phase represents an effective method to overcome the poor water solubility of several bio-actives. Here, the encapsulation of a natural antioxidant, Cat, into a non-lamellar lipid phase dispersion was studied to prepare NPs for topical application. Given the hydrophobic character of Cat, the antioxidant was effectively encapsulated into the reverse hexagonal phase of the formulation GMO/OA/TC/PF108/W = 3.0/0.5/0.3/0.3/95.9. This composition was chosen since it has an intermediate OA content among those samples that formed hexosomes. The Cat-loaded formulation (HexTC + Cat) was then compared with two blanks: TC-loaded hexosomes with the same composition (HexTC) and a classical hexosomes (Hex) dispersion (GMO/OA/PF108/W = 3.0/0.5/0.3/96.2) without the BS.

In comparison with the two blank samples, the Cat loading did not significantly affect the structure, size, polydispersity, and  $\zeta$  potential, as shown in Fig. 4 and Table 2.

Regarding the shelf-life of the formulation, the Cat-loaded NPs did not exhibit any phase separation for 1 month after checking the samples

**Table 3**

Parameters obtained from DLS, electrophoretic mobility and encapsulation efficiency measurements on the samples used in the *in vitro* study.

Samples	D <sub>h</sub> (nm)	PdI	ζ (mV)	EE %	Cat Concentration (mg/mL)
HexTC + Cat	158 ± 1	0.14 ± 0.01	-54 ± 2	99.9 ± 0.1	1.00 ± 0.1
Hex + Cat	160 ± 2	0.13 ± 0.01	-29 ± 1	99.5 ± 0.2	0.99 ± 0.1
Ves + Cat	80 ± 3	0.24 ± 0.01	+42 ± 2	97.4 ± 1.2	0.95 ± 0.5

each week by visual inspection.

### 3.4. *In vitro* permeation study on skin from new-born pigs

Based on these results and aiming to a possible topical application of these new NPs, *in vitro* penetration and permeation tests were performed through new-born pig skin, using Franz diffusion cells under non-occlusive conditions.

The capacity of HexTC to deliver Cat into and through the skin during *in vitro* experiments was compared to that of both hexosomes without TC (Hex + Cat) and vesicles formed by GMO and lauroylcholine (Ves + Cat) [8,29,30], which were loaded with the same amount of antioxidant (see Supplementary Material for the SAXS patterns of the empty and Cat-loaded formulations without TC). In Table 3, the general information about these samples is reported.

Results from the (trans)dermal experiments are shown in Fig. 5a. As expected, based on previous studies [8,30], after 8 h of treatment the GMO vesicles (Ves + Cat) increased the skin Cat penetration and accumulation, particularly in the epidermis, as compared to both Hex formulations, while no transdermal release could be observed in the receptor fluids.

Conversely, although the cumulative amount of Cat accumulated in all the three skin layers was lower than that recovered after vesicles application, the conventional hexosomes (Hex) enhanced Cat permeation through the skin. Indeed, 1.15 % of the applied Cat dose was recovered in the receptor compartment after 2 h experiment (data not shown), and 4.56 % after 8 h.

The formulation containing TC, *i.e.*, HexTC, showed a significantly higher drug accumulation in the different skin layers compared to both Hex without TC and vesicles. Indeed, the Cat amount found in the stratum corneum was approximately three and two-fold higher than traditional Hex and vesicle formulations, respectively. Furthermore, also the accumulation in the deeper skin layers as well as the

transdermal permeation increased as can be clearly noticed in Fig. 5a. These data suggest that the HexTC nanoparticles, thanks to the synergic action of the penetration enhancers GMO and OA and the edge activator TC, are able to facilitate the Cat penetration into the stratum corneum, where it creates a depot by which slowly diffuses through the skin layers.

### 3.5. *In vitro* antioxidant activity

Finally, to evaluate the effect of Cat encapsulation on its intrinsic antioxidant activity, a DPPH assay experiment was performed. Fig. 5b presents the antioxidant activity of the different Cat formulations expressed as % inhibition of the DPPH radical as compared to a Cat in methanol solution. In order to verify a possible antioxidant activity of the formulation components, the formulations without Cat were also tested. Results showed that in the range between 20–100 µg/mL of Cat concentration, all the tested formulations exert a high and statistically equivalent antioxidant activity with a DPPH radical inhibition of ~ 88 %. These outcomes demonstrate that Cat preserves its strong antioxidant activity after hexosome encapsulation, while the formulation components did not affect it.

## 4. Conclusions

Administration of drugs or bio-actives on skin represents a convenient and non-invasive therapeutic route, although it can be challenging to overcome the skin barrier, especially the *stratum corneum*. Previously, vesicles were widely studied for this task, formulated with permeation enhancers and edge activators [8,10,66–68]. However, vesicular carriers have limitations in terms of cargo loading that restrict their therapeutical efficacy [2,18].

In this work, we have shown that lipid-based NPs formulation for topical application containing permeation enhancers, such as GMO and OA, and edge activators (*i.e.*, BSs) can tackle the challenges in terms of limited cargo loading and skin penetration. The effect of three bile salts of varying hydrophilicity, *i.e.*, sodium cholate, sodium deoxycholate and sodium taurocholate were evaluated by using SAXS, DLS and cryo-TEM with the purpose of formulating the most stable composition. A natural antioxidant, catechin, was loaded into hexosomes. The *in vitro* penetration tests showed that the presence of BSs in the hexosomes enhances the penetration properties, favoring accumulation in the deeper skin layers and transdermal permeation in comparison with the hexosomes and vesicles without BSs. Moreover, DPPH test showed that the antioxidant properties of Cat were retained after encapsulation into the hexosomes.

As a future perspective, formulations of BS gels will be adopted to

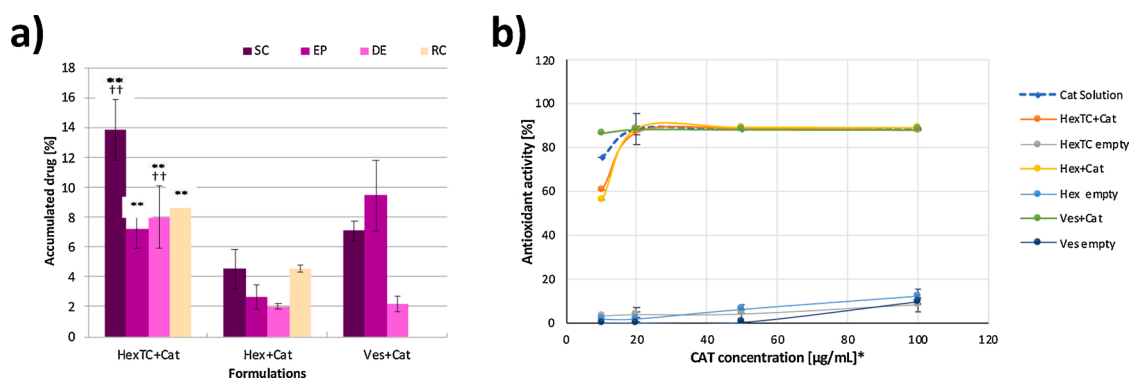


**Fig. 5.** (a) Cumulative amount of Cat retained into and permeated through the skin layers after 8 h-treatment with TC-loaded hexosomes (HexTC + Cat), hexosomes without TC (Hex + Cat) and a GMO-vesicle formulation (Ves + Cat). SC, Ep, D and RC denote stratum corneum, epidermis, dermis and receptor compartment, respectively. Results are reported as means ± SD of at least 6 independent determinations. Symbols represent significance of differences between HexTC and Hex, \*\*  $P < 0.01$ , and between HexTC and Ves, ††  $P < 0.01$ . (b) *In vitro* antioxidant activity of TC-loaded hexosomes (HexTC + Cat), hexosomes without TC (Hex + Cat) and a GMO-based vesicle formulation (Ves + Cat). Results are reported as the mean value ± SD of three separate experiments, each performed in triplicate. \* Empty formulations were also tested as control at the same dilution of Cat loaded formulations.

enhance its applicability compared to liquid formulations, for the reason that a gel is expected to be applied on the skin more easily than a liquid, and hence increase the efficacy of the therapy.

### CRedit authorship contribution statement

**Marco Fornasier:** Conceptualization, Investigation, Methodology, Data curation, Writing - original draft, Writing - review & editing. **Rosa Pireddu:** Investigation, Data curation, Writing - review & editing. **Alessandra Del Giudice:** Investigation, Data curation, Writing - review & editing. **Chiara Sinico:** Resources, Conceptualization, Supervision, Writing - review & editing. **Tommy Nylander:** Resources, Supervision, Writing - review & editing. **Karin Schillén:** Resources, Supervision, Writing - review & editing. **Luciano Galantini:** Resources, Supervision, Writing - review & editing. **Sergio Murgia:** Funding acquisition, Supervision, Resources, Writing - original draft, Writing - review & editing.

### Declaration of Competing Interest

The authors report no declarations of interest.

### Acknowledgements

The authors thank Dr. Anna M. Carnerup for her kind assistance with the cryo-TEM measurements. SAXSLab Sapienza is kindly acknowledged for providing preliminary SAXS analyses. Ph.D. scholarship of M.F. was funded by the project P.O.R. Sardegna F.S.E. 2014-2020. S.M. thanks Fondazione Banco di Sardegna and Regione Autonoma della Sardegna (Progetti Biennali di Ateneo Annualità 2018).

### Appendix A. Supplementary data

Supplementary material related to this article can be found, in the online version, at doi:<https://doi.org/10.1016/j.colsurfb.2021.111564>.

### References

- [1] A. Wolde-Kidan, Q.D. Pham, A. Schlaich, P. Loche, E. Sparr, R.R. Netz, E. Schneck, Influence of polar co-solutes and salt on the hydration of lipid membranes, *Phys. Chem. Chem. Phys.* 21 (2019) 16989–17000, <https://doi.org/10.1039/c9cp01953g>.
- [2] F. Lai, C. Caddeo, M.L. Manca, M. Manconi, C. Sinico, A.M. Fadda, What's new in the field of phospholipid vesicular nanocarriers for skin drug delivery, *Int. J. Pharm.* 583 (2020), <https://doi.org/10.1016/j.ijpharm.2020.119398>.
- [3] M.L. González-Rodríguez, A.M. Rabasco, Charged liposomes as carriers to enhance the permeation through the skin, *Expert Opin. Drug Deliv.* 8 (2011) 857–871, <https://doi.org/10.1517/17425247.2011.574610>.
- [4] S.M. Pyo, H.I. Maibach, Skin Metabolism, Relevance of skin enzymes for rational drug design, *Skin Pharmacol. Physiol.* 32 (2019) 283–293, <https://doi.org/10.1159/000501732>.
- [5] P.M. Elias, Structure and function of the stratum corneum extracellular matrix, *J. Invest. Dermatol.* 132 (2012) 2131–2133, <https://doi.org/10.1038/jid.2012.246>.
- [6] S. Björklund, Q.D. Pham, L.B. Jensen, N.Ø. Knudsen, L.D. Nielsen, K. Ekelund, T. Ruzgas, J. Engblom, E. Sparr, The effects of polar excipients transcuto and dexpanthenol on molecular mobility, permeability, and electrical impedance of the skin barrier, *J. Colloid Interface Sci.* 479 (2016) 207–220, <https://doi.org/10.1016/j.jcis.2016.06.054>.
- [7] Q.D. Pham, S. Björklund, J. Engblom, D. Topgaard, E. Sparr, Chemical penetration enhancers in stratum corneum – relation between molecular effects and barrier function, *J. Control. Release* 232 (2016) 175–187, <https://doi.org/10.1016/j.jconrel.2016.04.030>.
- [8] M. Schlich, M. Fornasier, M. Nieddu, C. Sinico, S. Murgia, A. Rescigno, 3-hydroxycoumarin loaded vesicles for recombinant human tyrosinase inhibition in topical applications, *Colloids Surf. B Biointerfaces* 171 (2018) 675–681, <https://doi.org/10.1016/j.colsurfb.2018.08.008>.
- [9] A. Mistry, P. Ravikumar, Development and evaluation of azelaic acid based ethosomes for topical delivery for the treatment of acne, *Indian, J. Pharm. Educ. Res.* 50 (2016) S232–S243, <https://doi.org/10.5530/ijper.50.3.34>.
- [10] G. Sharma, H. Goyal, K. Thakur, K. Raza, O.P. Katara, Novel elastic membrane vesicles (EMVs) and ethosomes-mediated effective topical delivery of aceclofenac: a new therapeutic approach for pain and inflammation, *Drug Deliv.* 23 (2016) 3135–3145, <https://doi.org/10.3109/10717544.2016.1155244>.
- [11] M.L. Manca, M. Manconi, A. Nacher, C. Carbone, D. Valenti, A.M. MacCioni, C. Sinico, A.M. Fadda, Development of novel diolein-niosomes for cutaneous

- delivery of tretinoin: Influence of formulation and in vitro assessment, *Int. J. Pharm.* 477 (2014) 176–186, <https://doi.org/10.1016/j.ijpharm.2014.10.031>.
- [12] S.R.M. Moghddam, A. Ahad, M. Aqil, S.S. Imam, Y. Sultana, Formulation and optimization of niosomes for topical diacerein delivery using 3-factor, 3-level Box-Behnken design for the management of psoriasis, *Mater. Sci. Eng. C* 69 (2016) 789–797, <https://doi.org/10.1016/j.msec.2016.07.043>.
- [13] L. Tavano, P. Alfano, R. Muzzalupo, B. De Cindio, Niosomes vs microemulsions: new carriers for topical delivery of Capsaicin, *Colloids Surf. B Biointerfaces* 87 (2011) 333–339, <https://doi.org/10.1016/j.colsurfb.2011.05.041>.
- [14] M. Ravaghi, S.H. Razavi, S.M. Mousavi, C. Sinico, A.M. Fadda, Stabilization of natural canthaxanthin produced by Dietzia natronolimnaea HS-1 by encapsulation in niosomes, *LWT - Food Sci. Technol.* 73 (2016) 498–504, <https://doi.org/10.1016/j.lwt.2016.06.027>.
- [15] J.N. Israelachvili, D.J. Mitchell, B.W. Ninham, Theory of self-assembly of hydrocarbon amphiphiles into micelles and bilayers, *J. Chem. Soc. Faraday Trans. 2 Mol. Chem. Phys.* 72 (1976) 1525–1568, <https://doi.org/10.1039/F29767201525>.
- [16] J. Gustafsson, H. Ljusberg-Wahren, M. Almgren, K. Larsson, Submicron particles of reversed lipid phases in water stabilized by a nonionic amphiphilic polymer, *Langmuir* 13 (1997) 6964–6971, <https://doi.org/10.1021/la970566+>.
- [17] C. Neto, G. Aloisi, P. Baglioni, K. Larsson, Imaging soft matter with the atomic force microscope: cubosomes and hexosomes, *J. Phys. Chem. B* 103 (19) (1999) 3896–3899, <https://doi.org/10.1021/jp984551b>.
- [18] S. Murgia, S. Biffi, R. Mezzenga, Recent advances of non-lamellar lyotropic liquid crystalline nanoparticles in nanomedicine, *Curr. Opin. Colloid Interface Sci.* 48 (2020) 28–39, <https://doi.org/10.1016/j.cocis.2020.03.006>.
- [19] S. Biffi, L. Andolfi, C. Caltagirone, C. Garrovo, A.M. Falchi, V. Lippolis, A. Lorenzon, P. Macor, V. Meli, M. Monduzzi, M. Obiols-Rabasa, L. Petrizza, L. Prodi, A. Rosa, J. Schmidt, Y. Talmon, S. Murgia, Cubosomes for in vivo fluorescence lifetime imaging, *Nanotechnology* 28 (2017), <https://doi.org/10.1088/1361-6528/28/5/055102>.
- [20] V. Meli, C. Caltagirone, A.M. Falchi, S.T. Hyde, V. Lippolis, M. Monduzzi, M. Obiols-Rabasa, A. Rosa, J. Schmidt, Y. Talmon, S. Murgia, Docetaxel-loaded fluorescent liquid-crystalline nanoparticles for cancer theranostics, *Langmuir* 31 (2015) 9566–9575, <https://doi.org/10.1021/acs.langmuir.5b02101>.
- [21] H. Qiu, M. Caffrey, The phase diagram of the monoolein/water system: metastability and equilibrium aspects, *Biomaterials* 21 (2000) 223–234, [https://doi.org/10.1016/S0142-9612\(99\)00126-X](https://doi.org/10.1016/S0142-9612(99)00126-X).
- [22] H.M.G. Barriga, M.N. Holme, M.M. Stevens, Cubosomes: the next generation of smart lipid nanoparticles? *Angew. Chemie - Int. Ed.* 58 (2019) 2958–2978, <https://doi.org/10.1002/anie.201804067>.
- [23] M. Fornasier, S. Biffi, B. Bortot, P. Macor, A. Manhart, F.R. Wurm, S. Murgia, Cubosomes stabilized by a polyphosphoester-analog of Pluronic F127 with reduced cytotoxicity, *J. Colloid Interface Sci.* 580 (2020) 286–297, <https://doi.org/10.1016/j.jcis.2020.07.038>.
- [24] J.Y.T. Chong, X. Mulet, A. Postma, D.J. Keddie, L.J. Waddington, B.J. Boyd, C. J. Drummond, Novel RAFT amphiphilic brush copolymer steric stabilisers for cubosomes: poly(octadecyl acrylate)-block-poly(polyethylene glycol methyl ether acrylate), *Soft Matter* 10 (2014) 6666–6676, <https://doi.org/10.1039/c4sm01064g>.
- [25] M. Valldeperas, A.P. Dabkowska, G.K. Pålsson, S. Rogers, N. Mahmoudi, A. Carnerup, J. Barauskas, T. Nylander, Interfacial properties of lipid sponge-like nanoparticles and the role of stabilizer on particle structure and surface interactions, *Soft Matter* 15 (2019) 2178–2189, <https://doi.org/10.1039/c8sm02634c>.
- [26] U. Bazylińska, J. Kulbacka, J. Schmidt, Y. Talmon, S. Murgia, Polymer-free cubosomes for simultaneous bioimaging and photodynamic action of photosensitizers in melanoma skin cancer cells, *J. Colloid Interface Sci.* 522 (2018) 163–173, <https://doi.org/10.1016/j.jcis.2018.03.063>.
- [27] F. Müller, A. Salonen, O. Glatter, Phase behavior of Phytantriol/water bicontinuous cubic Pn3m cubosomes stabilized by Laponite disc-like particles, *J. Colloid Interface Sci.* 342 (2010) 392–398, <https://doi.org/10.1016/j.jcis.2009.10.054>.
- [28] J. Zhai, L. Waddington, T.J. Wooster, M.I. Aguilar, B.J. Boyd, Revisiting  $\beta$ -casein as a stabilizer for lipid liquid crystalline nanostructured particles, *Langmuir* 27 (2011) 14757–14766, <https://doi.org/10.1021/la203061f>.
- [29] R. Angelico, M. Carboni, S. Lampis, J. Schmidt, Y. Talmon, M. Monduzzi, S. Murgia, Physicochemical and rheological properties of a novel monoolein-based vesicle gel, *Soft Matter* 9 (2013) 921–928, <https://doi.org/10.1039/c2sm27215f>.
- [30] M. Carboni, A.M. Falchi, S. Lampis, C. Sinico, M.L. Manca, J. Schmidt, Y. Talmon, S. Murgia, M. Monduzzi, Physicochemical, cytotoxic, and dermal release features of a novel cationic liposome nanocarrier, *Adv. Healthc. Mater.* 2 (5) (2013) 692–701, <https://doi.org/10.1002/adhm.201200302>.
- [31] K. Schillén, L. Galantini, G. Du, A. Del Giudice, V. Alfredsson, A.M. Carnerup, N. V. Pavel, G. Masci, B. Nyström, Block copolymers as bile salt sequestrants: intriguing structures formed in a mixture of an oppositely charged amphiphilic block copolymer and bile salt, *Phys. Chem. Chem. Phys.* 21 (2019) 12518–12529, <https://doi.org/10.1039/c9cp01744e>.
- [32] M.C. Di Gregorio, M. Gubitosi, L. Travaglini, N.V. Pavel, A. Jover, F. Mejjide, J. Vázquez Tato, S. Sennato, K. Schillén, F. Tranchini, S. De Santis, G. Masci, L. Galantini, Supramolecular assembly of a thermoresponsive steroidal surfactant with an oppositely charged thermoresponsive block copolymer, *Phys. Chem. Chem. Phys.* 19 (2017) 1504–1515, <https://doi.org/10.1039/c6cp05665b>.
- [33] S. Bayati, L. Galantini, K.D. Knudsen, K. Schillén, Effects of bile salt sodium glycodeoxycholate on the self-assembly of PEO-PPO-PEO triblock copolymer P123 in aqueous solution, *Langmuir* 31 (2015) 13519–13527, <https://doi.org/10.1021/acs.langmuir.5b03828>.

- [34] S. Bayati, C. Anderberg Haglund, N.V. Pavel, L. Galantini, K. Schillén, Interaction between bile salt sodium glycodeoxycholate and PEO-PPO-PEO triblock copolymers in aqueous solution, *RSC Adv.* 6 (2016) 69313–69325, <https://doi.org/10.1039/c6ra12514j>.
- [35] E. Tasca, A. Del Giudice, L. Galantini, K. Schillén, A.M. Giuliani, M. Giustini, A fluorescence study of the loading and time stability of doxorubicin in sodium cholate/PEO-PPO-PEO triblock copolymer mixed micelles, *J. Colloid Interface Sci.* 540 (2019) 593–601, <https://doi.org/10.1016/j.jcis.2019.01.075>.
- [36] S. Bayati, L. Galantini, K.D. Knudsen, K. Schillén, Complexes of PEO-PPO-PEO triblock copolymer P123 and bile salt sodium glycodeoxycholate in aqueous solution: a small angle X-ray and neutron scattering investigation, *Colloids Surfaces A Physicochem. Eng. Asp.* 504 (2016) 426–436, <https://doi.org/10.1016/j.colsurfa.2016.05.096>.
- [37] A.J. Clulow, B. Barber, M. Salim, T. Ryan, B.J. Boyd, Synergistic and antagonistic effects of non-ionic surfactants with bile salt + phospholipid mixed micelles on the solubility of poorly water-soluble drugs, *Int. J. Pharm.* 588 (2020), <https://doi.org/10.1016/j.ijpharm.2020.119762>.
- [38] M. Cárdenas, K. Schillén, V. Alfreðsson, R.D. Duan, L. Nyberg, T. Arnebrant, Solubilization of sphingomyelin vesicles by addition of a bile salt, *Chem. Phys. Lipids* 151 (2008) 10–17, <https://doi.org/10.1016/j.chemphyslip.2007.09.002>.
- [39] S.J. Marrink, A.E. Mark, Molecular dynamics simulations of mixed micelles modeling human bile, *Biochemistry* 41 (2002) 5375–5382, <https://doi.org/10.1021/bi015613i>.
- [40] P. Garidel, A. Hildebrand, K. Knauf, A. Blume, Membranolytic activity of bile salts: influence of biological membrane properties and composition, *Molecules* 12 (2007) 2292–2326, <https://doi.org/10.3390/12102292>.
- [41] C. Faustino, C. Serafim, P. Rijo, C.P. Reis, Bile acids and bile acid derivatives: use in drug delivery systems and as therapeutic agents, *Expert Opin. Drug Deliv.* 13 (2016) 1133–1148, <https://doi.org/10.1080/17425247.2016.1178233>.
- [42] L. Galantini, M.C. di Gregorio, M. Gubitosi, L. Travaglini, J.V. Tato, A. Jover, F. Meijide, V.H. Soto Tellini, N.V. Pavel, Bile salts and derivatives: rigid unconventional amphiphiles as dispersants, carriers and superstructure building blocks, *Curr. Opin. Colloid Interface Sci.* 20 (2015) 170–182, <https://doi.org/10.1016/j.cocis.2015.08.004>.
- [43] M.C. Di Gregorio, L. Travaglini, A. Del Giudice, J. Cautela, N.V. Pavel, L. Galantini, Bile salts: natural surfactants and precursors of a broad family of complex amphiphiles, *Langmuir* 35 (2019) 6803–6821, <https://doi.org/10.1021/acs.langmuir.8b02657>.
- [44] J. Cautela, B. Stenqvist, K. Schillén, D. Belić, L.K. Månsson, F. Hagemans, M. Seuss, A. Fery, J.J. Crassous, L. Galantini, Supracolloidal atomium, *ACS Nano* 14 (11) (2020) 15748–15756, <https://doi.org/10.1021/acsnano.0c06764>.
- [45] J. Cautela, V. Lattanzi, L.K. Månsson, L. Galantini, J.J. Crassous, Sphere–tubule superstructures through supramolecular and supracolloidal assembly pathways, *Small* 14 (2018) 1–10, <https://doi.org/10.1002/sml.201803215>.
- [46] S.C. Shin, C.W. Cho, K.H. Yang, Development of lidocaine gels for enhanced local anesthetic action, *Int. J. Pharm.* 287 (2004) 73–78, <https://doi.org/10.1016/j.ijpharm.2004.08.012>.
- [47] E.H. Lee, A. Kim, Y.K. Oh, C.K. Kim, Effect of edge activators on the formation and transfection efficiency of ultradeformable liposomes, *Biomaterials* 26 (2005) 205–210, <https://doi.org/10.1016/j.biomaterials.2004.02.020>.
- [48] G. Ceve, Transfersomes, liposomes and other lipid suspensions on the skin: permeation enhancement, vesicle penetration, and transdermal drug delivery, *Crit. Rev. Ther. Drug Carrier Syst.* 13 (3–4) (1996), <https://doi.org/10.1615/CritRevTherDrugCarrierSyst.v13.i3-4.30>.
- [49] G.M. El Zaafarany, G.A.S. Awad, S.M. Holayel, N.D. Mortada, Role of edge activators and surface charge in developing ultradeformable vesicles with enhanced skin delivery, *Int. J. Pharm.* 397 (2010) 164–172, <https://doi.org/10.1016/j.ijpharm.2010.06.034>.
- [50] G.M.M. El Maghraby, A.C. Williams, B.W. Barry, Interactions of surfactants (edge activators) and skin penetration enhancers with liposomes, *Int. J. Pharm.* 276 (2004) 143–161, <https://doi.org/10.1016/j.ijpharm.2004.02.024>.
- [51] Y.-K. Oh, M.Y. Kim, J.-Y. Shin, T.W. Kim, M.-O. Yun, S.J. Yang, S.S. Choi, W.-W. Jung, J.A. Kim, H.-G. Choi, Skin permeation of retinol in Tween 20-based deformable liposomes: in-vitro evaluation in human skin and keratinocyte models, *J. Pharm. Pharmacol.* 58 (2006) 161–166, <https://doi.org/10.1211/jpp.58.2.0002>.
- [52] A. Sadeghpour, M. Rappolt, S. Misra, C.V. Kulkarni, Bile salts caught in the act: from emulsification to nanostructural reorganization of lipid self-assemblies, *Langmuir* 34 (2018) 13626–13637, <https://doi.org/10.1021/acs.langmuir.8b02343>.
- [53] L. Wu, Q.L. Zhang, X.Y. Zhang, C. Lv, J. Li, Y. Yuan, F.X. Yin, Pharmacokinetics and blood-brain barrier penetration of (+)-Catechin and (-)-Epicatechin in rats by microdialysis sampling coupled to high-performance liquid chromatography with chemiluminescence detection, *J. Agric. Food Chem.* 60 (2012) 9377–9383, <https://doi.org/10.1021/jf301787f>.
- [54] C. Ramassamy, Emerging role of polyphenolic compounds in the treatment of neurodegenerative diseases: a review of their intracellular targets, *Eur. J. Pharmacol.* 545 (2006) 51–64, <https://doi.org/10.1016/j.ejphar.2006.06.025>.
- [55] Y.H. Lin, M.J. Tsai, Y.P. Fang, Y.S. Fu, Y. Bin Huang, P.C. Wu, Microemulsion formulation design and evaluation for hydrophobic compound: catechin topical application, *Colloids Surf. B Biointerfaces* 161 (2018) 121–128, <https://doi.org/10.1016/j.colsurfb.2017.10.015>.
- [56] R.K. Harwansh, P.K. Mukherjee, A. Kar, S. Bahadur, N.A. Al-Dhabi, V. Duraipandiyani, Enhancement of photoprotection potential of catechin loaded nanoemulsion gel against UVA induced oxidative stress, *J. Photochem. Photobiol. B, Biol.* 160 (2016) 318–329, <https://doi.org/10.1016/j.jphotobiol.2016.03.026>.
- [57] Y. Cai, N.D. Anavy, H.H. Sherry Chow, Contribution of presystemic hepatic extraction to the low oral bioavailability of green tea catechins in rats, *Drug Metab. Dispos.* 30 (2002) 1246–1249, <https://doi.org/10.1124/dmd.30.11.1246>.
- [58] K.P. Meena, M.R. Vijayakumar, P.S. Dwibedy, Catechin-loaded Eudragit microparticles for the management of diabetes: formulation, characterization and in vivo evaluation of antidiabetic efficacy, *J. Microencapsul.* 34 (2017) 342–350, <https://doi.org/10.1080/02652048.2017.1337248>.
- [59] Q. Song, D. Li, Y. Zhou, J. Yang, W. Yang, G. Zhou, J. Wen, Enhanced uptake and transport of (+)-catechin and (-)-epigallocatechin gallate in zebrafish intestinal caco-2 cells, *Int. J. Nanomedicine* 9 (2014) 2157–2165, <https://doi.org/10.2147/IJN.S59331>.
- [60] J. Janiak, S. Bayati, L. Galantini, N.V. Pavel, K. Schillén, Nanoparticles with a bicontinuous cubic internal structure formed by cationic and non-ionic surfactants and an anionic polyelectrolyte, *Langmuir* 28 (2012) 16536–16546, <https://doi.org/10.1021/la303938k>.
- [61] C.V. Kulkarni, W. Wachter, G. Iglesias-Salto, S. Engelskirchen, S. Ahualli, Monoolein: a magic lipid? *Phys. Chem. Chem. Phys.* 13 (2011) 3004–3021, <https://doi.org/10.1039/c0cp01539c>.
- [62] L.M. de Buy Wenniger, T. Pusch, U. Beuers, Bile Salts, 2nd ed., Elsevier Inc., 2013 <https://doi.org/10.1016/B978-0-12-378630-2.00031-1>.
- [63] M. Nakano, A. Sugita, H. Matsuoaka, T. Handa, Small-angle X-ray scattering and <sup>13</sup>C NMR investigation on the internal structure of “cubosomes”, *Langmuir* 17 (2001) 3917–3922, <https://doi.org/10.1021/la010224a>.
- [64] V. Meli, C. Caltagirone, C. Sinico, F. Lai, A.M. Falchi, M. Monduzzi, M. Obiols-Rabasa, G. Picci, A. Rosa, J. Schmidt, Y. Talmon, S. Murgia, Theranostic hexosomes for cancer treatments: an in vitro study, *New J. Chem.* 41 (2017) 1558–1565, <https://doi.org/10.1039/c6nj03232j>.
- [65] C. Caltagirone, M. Arca, A.M. Falchi, V. Lippolis, V. Meli, M. Monduzzi, T. Nylander, A. Rosa, J. Schmidt, Y. Talmon, S. Murgia, Solvatochromic fluorescent BODIPY derivative as imaging agent in camptothecin loaded hexosomes for possible theranostic applications, *RSC Adv.* 5 (2015) 23443–23449, <https://doi.org/10.1039/c5ra01025j>.
- [66] Y.K. Song, C.K. Kim, Topical delivery of low-molecular-weight heparin with surface-charged flexible liposomes, *Biomaterials* 27 (2006) 271–280, <https://doi.org/10.1016/j.biomaterials.2005.05.097>.
- [67] A. Hussain, A. Samad, M. Ramzan, M.N. Ahsan, Z. Ur Rehman, F.J. Ahmad, Elastic liposome-based gel for topical delivery of 5-fluorouracil: in vitro and in vivo investigation, *Drug Deliv.* 23 (2016) 1115–1129, <https://doi.org/10.3109/10717544.2014.976891>.
- [68] S. Doppalapudi, A. Jain, D.K. Chopra, W. Khan, Psoralen loaded liposomal nanocarriers for improved skin penetration and efficacy of topical PUVA in psoriasis, *Eur. J. Pharm. Sci.* 96 (2017) 515–529, <https://doi.org/10.1016/j.ejps.2016.10.025>.

# Supplementary Material

## Tuning lipid structure through bile salts: hexosomes for topical administration of catechin

*Marco Fornasier,<sup>1,2,5,\*</sup> Rosa Pireddu,<sup>3</sup> Alessandra Del Giudice,<sup>4</sup> Chiara Sinico,<sup>3</sup> Tommy  
Nylander,<sup>5</sup> Karin Schillén,<sup>5</sup> Luciano Galantini,<sup>4</sup> Sergio Murgia<sup>1,2,\*</sup>*

<sup>1</sup> *Department of Chemical and Geological Sciences, University of Cagliari, s.s 554 bivio Sestu, Monserrato I-09042, Italy*

<sup>2</sup> *CSGI, Consorzio Interuniversitario per lo Sviluppo dei Sistemi a Grande Interfase, via della Lastruccia 3 Sesto Fiorentino, Florence, I-50019, Italy*

<sup>3</sup> *Department of Life and Environmental Sciences, University of Cagliari, via Ospedale 72, Cagliari I-09124, Italy*

<sup>4</sup> *Department of Chemistry, Sapienza University of Rome, P.le A. Moro 5, Rome 00185, Italy*

<sup>5</sup> *Division of Physical Chemistry, Department of Chemistry, Lund University, P.O. Box 124, Lund, SE-221 00, Sweden*

**Table SI-1.** Compositions for the system GMO/BS/PF108/W reported as wt %.

<b>sample</b>	<b>Monoolein GMO</b>	<b>Bile salts BS</b>	<b>Pluronic F108 PF108</b>	<b>Water W</b>	<b>Phase*</b>
1	3.3	0	0.3	96.4	Pn3m Im3m
2	3.3	0.005	0.3	96.395	Pn3m Im3m
3	3.3	0.015	0.3	96.385	Pn3m Im3m
4	3.3	0.02	0.3	96.38	Vesicles
5	3.3	0.1	0.3	96.3	Vesicles
6	3.3	0.2	0.3	96.2	Vesicles
7	3.3	0.3	0.3	96.1	Vesicles
8	3.3	0.5	0.3	95.9	Vesicles
9	3.3	0.6	0.3	95.8	Vesicles
10	3.3	0.75	0.3	95.65	Vesicles
11	3.3	1	0.3	95.4	Vesicles

\* determined by SAXS measurements



**Table SI-2.** Lattice parameters ( $a$ ) and water channel radii ( $r_w$ ) of the bicontinuous cubic phase dispersions up to 0.02 wt % of TC evaluated by SAXS.

sample	TC [wt %]	Phase	$a$ [Å]	$r_w$ [Å]
1	0	Im3m	$127.6 \pm 1.0$	$22.0 \pm 0.3$
		Pn3m	$94.0 \pm 0.9$	$19.7 \pm 0.4$
2	0.005	Im3m	$120.2 \pm 1.6$	$19.7 \pm 0.5$
		Pn3m	$91.2 \pm 0.6$	$18.7 \pm 0.2$
3	0.015	Im3m	112.5	17.4
		Pn3m	$87.2 \pm 0.4$	$17.1 \pm 0.2$
4	0.02	Im3m	104.6	14.9
		Pn3m	$82.4 \pm 0.2$	$15.2 \pm 0.1$

**Table SI-3.** Composition of the sample for the *in vitro* study.

Formulation	Composition (wt %)
Hex + Cat	GMO/OA/PF108/W = 3.0/0.5/0.3/96.2
Ves + Cat	GMO/LCh/W = 3.3/0.3/96.4

The samples were prepared using the same protocol described in the Material and Methods (in the case of the vesicles formulation (Ves), an aqueous solution of lauroylcholine chloride (LCh) was used instead of one of Pluronic F108).

## SAXS measurements of the samples used in the *in vitro* study

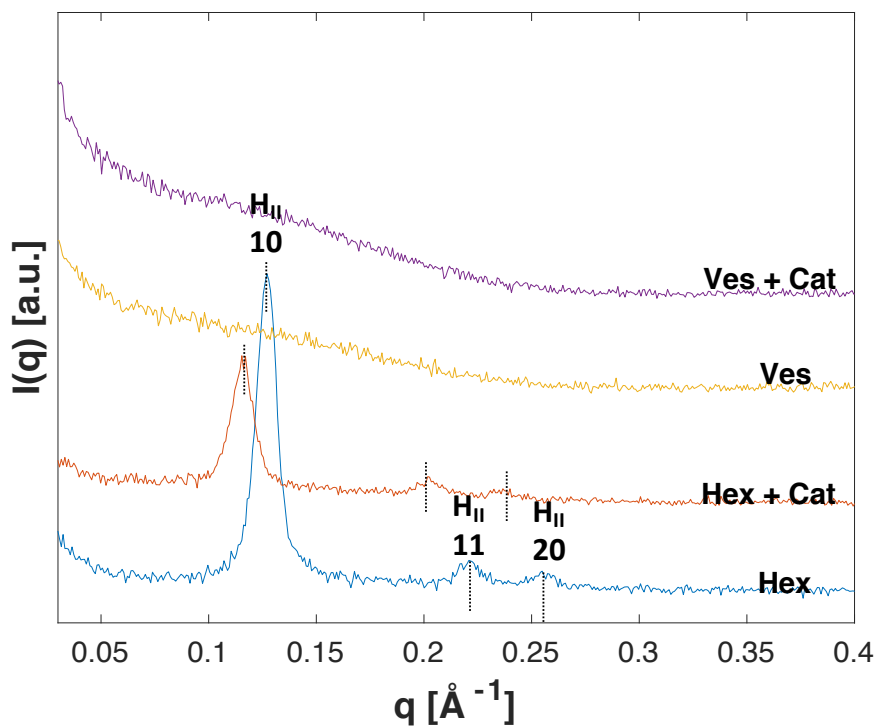


**Figure SI-1.** SAXS patterns of the hexosomes (Hex) and vesicles (Ves) empty and loaded with catechin (Cat) used for the permeation study *in vitro* on new-born pig skin. The Miller's indexes are reported above each peak related to a crystalline plane of an inverse hexagonal phase ( $H_{II}$ ). Each scattering curve was recorded for 2 hours at 25 °C.

**Table SI-4.** Phase, lattice parameters and water radii for the samples reported in Figure SI-1.

sample	Phase	a (Å)	$r_w$ (Å)
Hex	$H_{II}$	$56.9 \pm 0.2$	$29.3 \pm 0.1$
Hex + Cat	$H_{II}$	$61.8 \pm 0.4$	$31.8 \pm 0.2$
Ves	Vesicular	-	-
Ves + Cat	Vesicular	-	-

# Paper VI

*“Surface-modified nanoerythroosomes for potential optical imaging diagnostics”*

**M. Fornasier**, A. Porcheddu, A. Casu, S. R. Raghavan, P. Jönsson, K. Schillén, S. Murgia;

Journal of Colloid and Interface Science, 2021, 582, 246-253.

**DOI: [10.1016/j.jcis.2020.08.032](https://doi.org/10.1016/j.jcis.2020.08.032)**

Copyright © from Elsevier 2020



Contents lists available at ScienceDirect

Journal of Colloid and Interface Science

journal homepage: [www.elsevier.com/locate/jcis](http://www.elsevier.com/locate/jcis)

## Surface-modified nanoerythroosomes for potential optical imaging diagnostics



Marco Fornasier<sup>a,c,\*</sup>, Andrea Porcheddu<sup>a</sup>, Anna Casu<sup>b</sup>, Srinivasa R. Raghavan<sup>d</sup>, Peter Jönsson<sup>e</sup>, Karin Schillén<sup>e</sup>, Sergio Murgia<sup>a,c,\*</sup>

<sup>a</sup> Department of Chemical and Geological Sciences, University of Cagliari, s.s. 554 bivio Sestu, I-09042 Monserrato, Cagliari, Italy

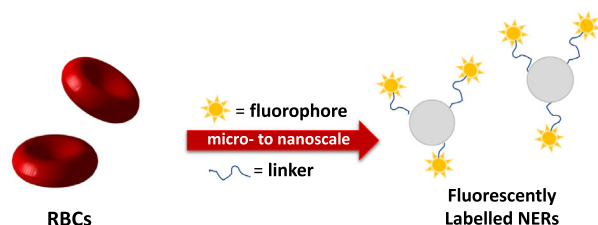
<sup>b</sup> Translational Research Institute–AdventHealth, Orlando, FL, USA

<sup>c</sup> CSGI, Consorzio Interuniversitario per lo Sviluppo dei Sistemi a Grande Interfase, Via della Lastruccia 3, I-50019 Sesto Fiorentino, Florence, Italy

<sup>d</sup> Department of Chemical & Biomolecular Engineering, University of Maryland, College Park, MD 20742, USA

<sup>e</sup> Division of Physical Chemistry, Department of Chemistry, Lund University, P.O. Box 124, SE-22100 Lund, Sweden

### GRAPHICAL ABSTRACT



### ARTICLE INFO

#### Article history:

Received 26 April 2020

Revised 3 August 2020

Accepted 8 August 2020

Available online 14 August 2020

#### Keywords:

Cu-free click chemistry

Fluorescence

Red blood cells

Ghosts

Vesicles

### ABSTRACT

Nanoerythroosomes (NERs), vesicle-like nanoparticles derived from red blood cells, represent a new and interesting vector for therapeutic molecules and imaging probes, mainly thanks to their high stability and excellent biocompatibility. Aiming to present a proof-of-concept of the use of NERs as diagnostic tools for *in vitro/in vivo* imaging purposes, we report here several functionalization routes to decorate the surfaces of NERs derived from bovine blood with two different fluorophores: 7-amino-4-methylcumarin and dibenzocyclooctinecyanine5.5. Notably, the fluorophores were cross-linked to the NERs surface with glutaraldehyde and, in the case of dibenzocyclooctinecyanine5.5, also using a click-chemistry route, termed strain-promoted azide-alkyne cycloaddition. The physicochemical characterization highlighted the high stability of the NERs derivatives in physiological conditions. Furthermore, the loading efficiency of the fluorophores on the NERs surface was evaluated using both UV–Vis spectroscopy and fluorescence microscopy.

© 2020 Elsevier Inc. All rights reserved.

### 1. Introduction

The development of a robust therapeutic and diagnostic tools based on nanoparticles to manage diseases is a current goal in nanomedicine. These nanocarriers can significantly enhance the

bioavailability of drugs and probes while minimizing the pharmacological side effects. Many carriers, such as cubosomes [1–5], hexosomes [6,7], silica nanoparticles [8,9], and vesicles [10–15], have been studied over the past years, and their efficacy via many administration routes has been proven.

Recent advances have opened the possibility of using cellular carriers such as erythrocytes, exosomes, leukocytes, and cancer cells [11,16–20]. These carriers meet several criteria desirable in clinical applications, such as biocompatibility and their unharmed

\* Corresponding author at: Department of Chemical and Geological Sciences, University of Cagliari, s.s. 554 bivio Sestu, I-09042 Monserrato, Cagliari, Italy.

E-mail addresses: [mfornasier@unica.it](mailto:mfornasier@unica.it) (M. Fornasier), [murgias@unica.it](mailto:murgias@unica.it) (S. Murgia).

degradation products. Among the possible carriers, the so-called ghosts have gained attention as a valid alternative to other vectors. Ghosts can be obtained from red blood cells (RBCs) by removing the inner content (mostly hemoglobin) via hypotonic conditions. Unfortunately, due to their micrometric size, they exhibit fast *in vivo* clearance [11,21]. In 1994, Gaudreault and collaborators reported the first example of ghost nanoderivatives, named nanoerythroosomes (NERs) [22,23]. Being essentially vesicles (100–150 nm) derived by shearing (e.g., extrusion or sonication) of RBCs' ghosts, NERs do not show toxicity against different cell lines, and they are non-immunogenic in autologous administration [16,20,21,24,25]. The composition of the membrane gives NERs high versatility, both in the types of molecules that can be encapsulated and in the functionalization of their surface [21,26,27]. However, the high-shear process during NERs preparation can induce modification of the shell composition, especially removal of membrane proteins [26]. Interestingly, a recent work from Bóta et al. showed that addition of specific phospholipids originates a polygonal proteins scaffold that enhances the nanoerythroosomes stiffness and allows tailoring of these nanocarriers [28].

The coupling of targeting agents or imaging probes onto the surfaces of nanocarriers is a strategical step to minimize the leaching of these molecules (compared to merely encapsulating the molecules in the lumen of the nanocarriers). In this regard, *Click Chemistry* has proven to be a powerful tool in chemistry for gaining insight into biology, and nanomedicine. Exploiting a reaction among an azide and an alkyne catalyzed by copper (Cu, copper-catalyzed azide alkyne cycloaddition, CuAAC) species, it is possible to obtain a stable covalent 1,2,3-triazole ring conjugate. Such azide-alkyne cycloaddition has found a wide variety of practical applications across many different scientific sectors, especially in cell membrane functionalization [29–31]. The presence of Cu catalysts could affect the cell microenvironment, and a Cu-free click-chemistry route called “strain-promoted azide-alkyne cycloaddition” (SpAAC) represents a superior alternative. In this latter case, the reaction is promoted by a strain on the alkyne or azide, without any Cu catalysts. The benefits of SpAAC include biocompatibility, stability, specificity, and bio-orthogonality [4,30,32,33]. The SpAAC is preferable whenever a small concentration of Cu can affect protein folding or cell function [33,34].

Fluorescence light has been widely used in medical imaging [35–37]. The proper choice of a fluorescent probe is crucial, since UV–Vis and near-infrared (NIR) emitters can be adopted for imaging applications *in vitro* and *in vivo*, respectively. In the latter case, features such as minimal autofluorescence and adsorption in tissue are advantages of the so-called “NIR window”, within the range 650–900 nm. Consequently, fluorophores emitting in the NIR region are a valuable asset for *in vivo* diagnostics [3,38]. Moreover, compared with visible light, NIR fluorescence wavelengths allow high-sensitivity real-time image guidance in different surgery protocols [35–37,39].

So far, the application of NERs as probes for optical imaging has barely been studied [24,40,41]. Therefore we explored the possibility of using this kind of nanovectors as imaging tools for *in vitro*/*in vivo* applications by labelling their surface with two fluorescent dyes (a coumarin and a cyanine derivative). Specifically, labelling was realized by using the cross-linking method with glutaraldehyde, and the first example of SpAAC Click Chemistry applied to NERs.

## 2. Material and methods

### 2.1. Materials

Bovine blood was obtained from Istituto Zooprofilattico della Sardegna and withdrawn from a healthy two-years-old cow, dur-

ing a routine clinical examination. Na-EDTA (1.5 mg per mL of blood) was added to blood samples to avoid coagulation of RBCs, thereafter the samples were stored at 4 °C before any manipulation. The blood was used no longer than 2 h after withdrawal.

Glutaraldehyde 50% v/v, 7-amino-4-methylcoumarin (AMC), 3-azido-1-propylamine were purchased from TCI Chemicals (Belgium). Sodium chloride, sodium phosphate dibasic, potassium chloride and sodium phosphate monobasic were purchased from Sigma Aldrich S.r.l. (Italy). The fluorophore dibenzocyclooctinecyanine5.5 (DBCO-Cy5.5) was purchased from Lumiprobe GmbH (Germany).

Fresh distilled water was purified using a Milli-Q system (Millipore Corporation, Bedford, MA, U.S.) for standards preparation, and it was filtered with a 0.22 µm pore size hydrophilic Millipore filter before any use.

### 2.2. Preparation of NERs

The protocol used in this work for the preparation of Nanoerythroosomes was derived from the one proposed by Raghavan and collaborators [25]. It can be divided into four steps (three centrifugation steps and one ultrasonication process) described as following. The first step is the extraction of the red blood cells: blood (usually 80 mL and divided in four fractions of 20 mL each) was diluted with 30 mL of cold phosphate-buffered saline (PBS) solution at pH 7.4 and centrifuged at 1859 g at 4 °C for 15 min. The light-yellow supernatant (mainly plasma) was removed, the red pellet at the bottom of the tube (RBCs) was washed with 30 mL of cold PBS solution at pH 7.4 and then dispersed. This step was repeated until the supernatant appeared colorless and transparent, usually three times. In the second step, the RBCs were lysed in a hypotonic environment. After the removal of the supernatant, they were dispersed in 30 mL of cold hypotonic solution 0.5% wt of NaCl and incubated for 30 min in a cold bath. The dark red solution (derived from the release of hemoglobin) was then centrifuged at 10,706g for 15 min at 4 °C. The supernatant was removed, and the pellet was resuspended and washed with cold PBS solution at pH 7.4 and dispersed in the medium. This step was repeated until the pellet appeared cream-colored or light yellow (usually three times), to remove most of hemoglobin from RBCs. In the third step, microerythroosomes (MERs) were formed: the pellet obtained in the previous step was dispersed in 30 mL of cold PBS solution at pH 7.4 and centrifuged at 24,088g for 15 min at 4 °C. The supernatant was removed, the pellet was resuspended in PBS and dispersed again. This step was repeated three times. Finally, in the fourth and final step, nanoerythroosomes were formed. The cream-color pellet was resuspended in 3 mL of PBS 10 mM at pH 7.4 and sonicated for 5 min using a tip-sonicator and the temperature of the dispersion was controlled using a water bath. The pulse of the sonicator was set to 90% of amplitude, having 1 s of sonication (ON) and 1 s of break (OFF). The solution was then filtered three times through a 2.7 µm pore size membrane from Millipore. After an additional 10 min of sonication with the same set-up as before, a bluish and homogeneous colloidal dispersion of NERs was obtained.

### 2.3. Functionalization of NERs surface by cross-linking

The first surface functionalization to fluorescently label the NERs is based on a cross-linking method using glutaraldehyde [23]. 100 µL of 0.5% v/v solution of glutaraldehyde was added to 1 mL of NERs formulation in 1 mL of PBS at pH 7.4. Then 1 mg of the fluorescent dye AMC was added to the solution under mild stirring at room temperature in the dark for 1 h. A solution of glycine 15% v/v in PBS at pH 7.4 was added to stop the reaction and the formulation was stored at 25 °C overnight. The day after, the formulation appeared as a light yellow solution, and it was purified from

the free fluorophore by dialysis, loading 2 mL of formulation into a dialysis tubing cellulose membrane (14 kDa molecular weight cut-off, purchased from Sigma Aldrich) and dialyzing it against 2 L of PBS pH 7.4 for 2 h by replacing the buffer after 1 h at room temperature in the dark. The formulation NER-F1 was thereafter stored at 25 °C until use.

#### 2.4. Functionalization of NERs surface with cross-linking and SpAAC method

By implementing Click Chemistry into the previous functionalization, we were able to obtain the formulation NER-F2 as follows. 100  $\mu$ L of 0.5% v/v solution in PBS of glutaraldehyde 5  $\mu$ L of 3-azido-1-propylamine were added to 1 mL of NERs formulation in another 1 mL of PBS at pH 7.4. It was let under mild stirring for 1 h in the dark at room temperature. The bright pink solution was dialyzed to remove the free 3-azido-1-propylamine, following the procedure described in the previous section. Then, 1 mg of DBCO-Cy5.5 was added to the formulation and it was let under mild stirring overnight at room temperature in the dark. The formulation appeared as a light purple/blue solution with some dark blue precipitate (the fluorophore) at the bottom of the tube. 2 mL of the formulation was loaded into a dialysis tubing cellulose membrane (14 kDa MW cutoff, purchased from Sigma Aldrich) and dialyzed again 2 L of PBS pH 7.4 for 2 h (by replacing the buffer after 1 h) at room temperature in the dark. NER-F2 was stored at 25 °C.

#### 2.5. Dynamic light scattering and electrophoretic light scattering

The three samples, NERs, NER-F1 and NER-F2 were diluted 1:50 with PBS pH 7.4 solution prior to any measurement and were analyzed within 24 h after preparation. Their hydrodynamic size was measured by Dynamic Light Scattering using a ZetaSizer Nano ZS instrument (Malvern Instruments/Malvern Panalytical), Malvern, U.K.) at a temperature of  $25.0 \pm 0.1$  °C [42]. The instrument is equipped with a 4 mW He-Ne laser (operating at a wavelength of 633 nm) and the light scattering measurements were performed in a backscattering geometry at a scattering angle of 173°. The same instrument was used for the determination of the  $\zeta$ -potential (using the Smoluchowski's equation) from measurements of the electrophoretic mobility in DTS1070 disposable folded capillary cells at the scattering angle of 13°. The intensity-weighted hydrodynamic diameter ( $D_h$ ) and the polydispersity index (Pdl) extracted from a second-order Cumulant analysis as well as the  $\zeta$ -potential are reported as averages of six consecutive measurements.

#### 2.6. Effect of sonication on NERs size

We studied how the sonication time affects NER's size. After each sonication cycle (5, 6, 8, 10, 15, 20 and 30 min), a portion of the dispersion was diluted with the buffer (1:50) and then the hydrodynamic diameter was determined using DLS.

#### 2.7. Cryogenic transmission electron microscopy

The morphology of the NERs was examined using a JEM-2200FS transmission electron microscope (JEOL) specially optimized for cryo-TEM at the National Center for High Resolution Electron Microscopy (nCHREM) at Lund University. It is equipped with a field-emission electron source and an in-column energy filter (omega filter). The images were recorded under low-dose conditions with 15 eV slit width in place, adopting an acceleration voltage of 200 kV on a bottom-mounted TemCam-F416 camera (TVIPS) using SerialEM. Each sample was prepared using an automatic

plunge freezer system (Leica Em GP) with the environmental chamber operated at 21.0 °C and 90% of relative humidity. A droplet (4  $\mu$ L) of the NERs formulation was deposited on a lacey formvar carbon-coated grid (Ted Pella) and was blotted with filter paper to remove excess fluid. The grid was then plunged into liquid ethane (around  $-183$  °C) to ensure the rapid vitrification of the sample in its native state. Prior to the Cryo-TEM measurements, the specimens were stored in liquid nitrogen ( $-196$  °C) before imaging microscope using a cryo-transfer tomography holder (Fischione Model 2550).

#### 2.8. Photophysical measurements

NER-F1 and NER-F2 were studied through ultraviolet-visible (UV-Vis) absorption and steady-state fluorescence spectroscopy using a Win-CaryVarian UV-Vis double-beam spectrophotometer and a Win-CaryVarian Fluorimeter respectively, after dilution 1:10 and 1:500. The absorption spectra of the two fluorophores were measured in 1 cm quartz cuvettes from which the background was subtracted by using the pure solvent. The fluorescence signal was measured using 5.0 and 2.5 slits aperture, for excitation and emission respectively. AMC was excited at 351 nm and DBCO-Cy5.5 at 680 nm. The dyes loading was measured three times using the calibration curve methods in the UV-Vis range:

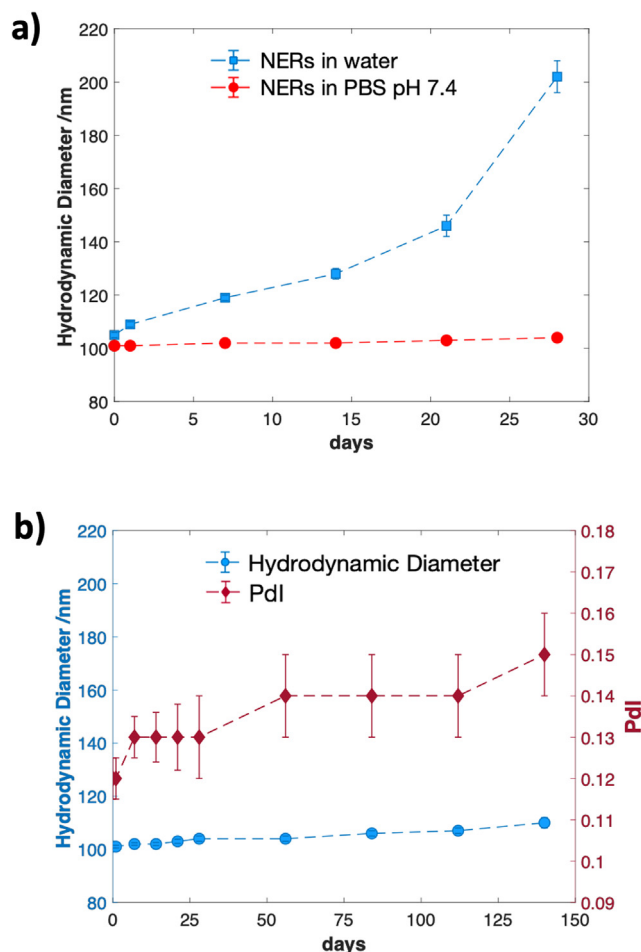


**Fig. 1.** (a) The apparent hydrodynamic diameter ( $D_h$ ) of the NER particles in water as a function of time after preparation. (b) Stability of the NERs in PBS pH 7.4 in terms of  $D_h$  and polydispersity index (Pdl) of the formulation over 5 months. The dashed lines are guides for the eyes. Both  $D_h$  and Pdl were obtained from a second-order Cumulant analysis of the measured intensity-intensity autocorrelation functions.

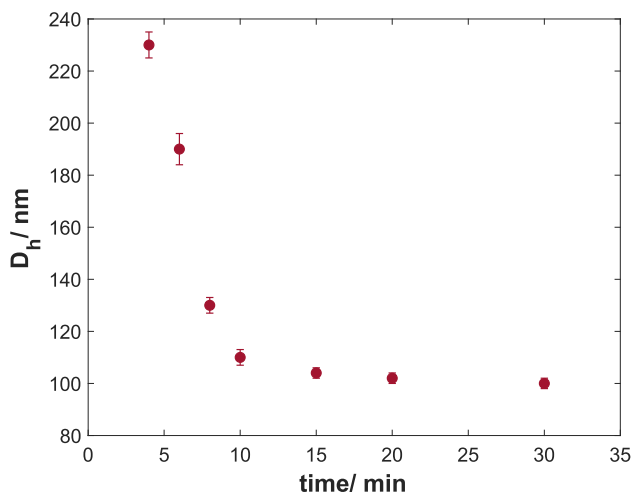


**Fig. 2.** Evaluation of sonication time on the apparent hydrodynamic diameter ( $D_h$ ) of the NERs.

the measurements were performed in MeOH/H<sub>2</sub>O: 3/1 buffered at pH 7.4 for the free AMC and NER-F1. Since the solubility of DBCO-Cy5.5 in DMSO, the analyses for NER-F2 were performed in a DMSO/H<sub>2</sub>O: 3/1 mixture buffered at pH 7.4. The free dyes excitation and emission spectra were acquired in MeOH and DMSO (data not shown).

### 2.9. Fluorescence single molecule microscopy

The DBCO-Cy5.5-labelled NERs were studied with a Nikon Apo TIRF 100× magnification oil immersion objective on a customized Nikon Eclipse Ti Eclipse microscope equipped with a Photometrics Prime 95B scientific CMOS. The DBCO-Cy5.5-labelled NERs were diluted 1:100 in PBS and added to a cover glass slide (25 mm diameter, No 1, VWR), resulting in approximately 500 NERs in the image field of view. The sample was illuminated using an Oxix diode laser operating at a wavelength of 638 nm (180 mW). The acquired images were 600 pixels by 600 pixels with a pixel size of 0.11 μm by 0.11 μm and were acquired at an exposure time of 100 ms. The individual NER-F2 particles were detected using the MATLAB script pkfnd.m (<http://site.physics.georgetown.edu/matlab/code.html>)

after background subtraction. Photobleaching steps were obtained by continuously taking images until the particles bleached.

### 3. Results and discussion

The RBC vesicles were obtained from a total bovine blood sample according to a procedure that slightly alters that reported by Raghavan et al. [25]. It consisted of several centrifugation and washing steps to purify the RBCs. The centrifugation steps are required first to separate the blood cells from plasma. Then, by tuning the concentration of the hypotonic solution from 0.85% w/v to 0.5% w/v, the membranes of the RBCs were osmolyzed to ensure the complete release of the hemoglobin content. The membrane materials are finally resealed in an isotonic environment (PBS buffer 10 mM at pH 7.4) and ultrasonicated to obtain the nanoderivatives, i.e. the NERs. Initially, large aggregates (ca. 3–4 μm) were observed by DLS, even after 20 min of sonication (data not shown). Therefore, an extrusion method was implemented in the preparation of the nanoparticles, in order to remove larger aggregates. After extrusion through a filter (2.7 μm pore size), the dispersion was ultrasonicated again to reduce the size to ca. 100 nm. The appearance of the dispersion after the final sonication step was transparent and bluish.

As it is possible to obtain NERs both in water and buffers, we evaluated their stability over one month in terms of their hydrodynamic diameter ( $D_h$ ) in each media using DLS. As reported in Fig. 1a, the apparent hydrodynamic diameter in water and physiological buffer at 25 °C is initially ca. 100 nm, while the ζ-potentials −18 mV and −30 mV were respectively recorded for NERs dispersed in water or PBS buffer.

By aging, the sample in water exhibited an increasing trend in terms of size and polydispersity. On the contrary, the size and polydispersity of NERs in 1x PBS pH 7.4 (10 mM) remained stable without any significant changes over one month (between measurements, the NERs were stored at 25 °C), most likely because of the higher negative surface charge of NERs in PBS buffer that better prevents flocculation of the nanoparticles. For this reason, PBS was used as a buffer to investigate further NERs morphology, stability, and physicochemical features.

First, the long-time stability of the NER particles in this formulation was followed in terms of  $D_h$  over five months (Fig. 1b). As reported above, the sample was stored at 25 °C

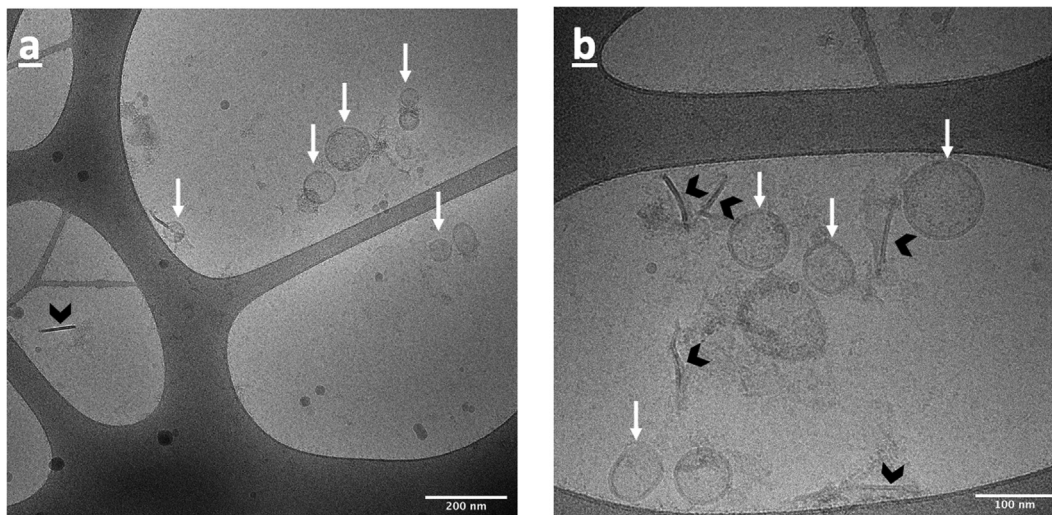
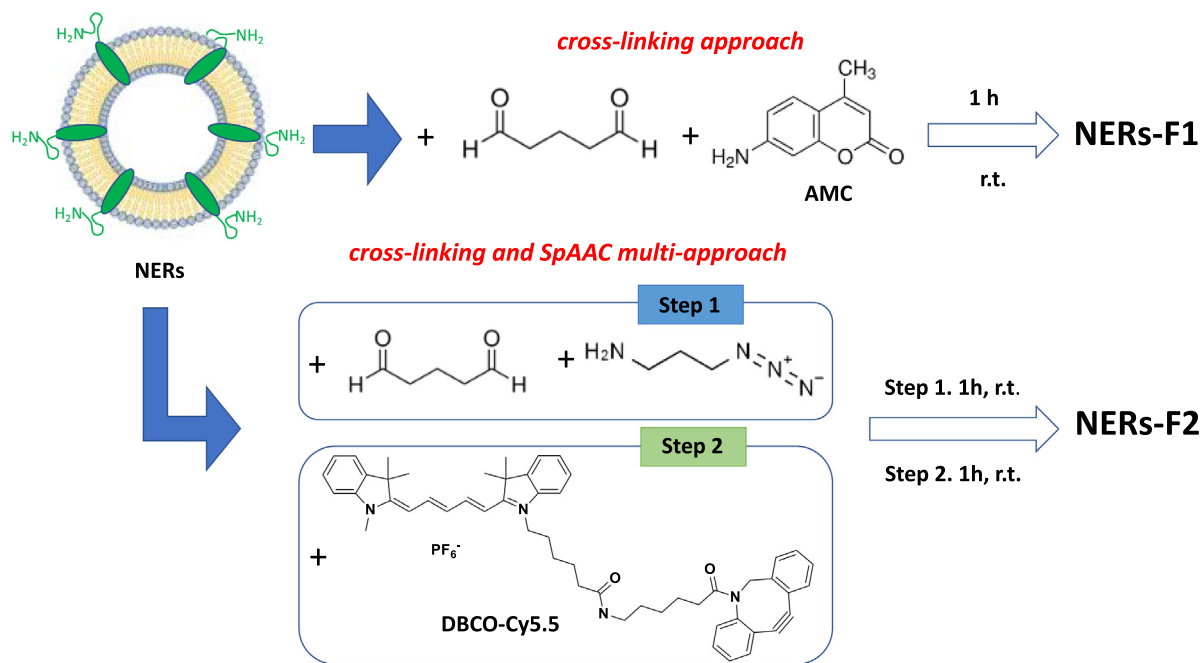


**Fig. 3.** NERs cryo-TEM image in PBS buffer at pH 7.4 10 mM at two different magnitudes (a at ×40k and b at ×80k). Several membranes not reassembled into vesicles are indicated by black arrowheads. The white arrows point toward spherical unilamellar vesicles.



**Scheme 1.** Surface modification to obtain NERs-F1 and NERs-F2.

**Table 1**

Hydrodynamic diameters ( $D_h$ ), polydispersity index (Pdl) and  $\zeta$ -potentials of the unlabeled and labelled formulations.

Formulation	$D_h$ [nm]	Pdl	$\zeta$ -potential [mV]
NERs	101 ± 1	0.12 ± 0.01	-31.2 ± 1.1
NERs-F1	120 ± 4	0.20 ± 0.01	-23.2 ± 2.1
NERs-F2	127 ± 4	0.18 ± 0.02	-24.0 ± 2.3

between each measurement. As noticed, the hydrodynamic diameter and the accompanied polydispersity index remained almost constant during the investigated temporal range, hence indicating that aging did not affect the dispersion significantly in terms of size. It is worth noticing that the polydispersity indices measured for the formulations here investigated are in good agreement with those reported in literature in similar systems [25,40].

The size of the vesicles strongly depends on the sonication conditions adopted during the sample preparation. Therefore, the effect of sonication time on the size was investigated sonicating the sample for 5, 6, 8, 10, 15, 20, and 30 min after the extrusion procedure.

As shown in Fig. 2, after 5 min, the NER particles showed a quite large size. While increasing the sonication time, their size decreased, reaching a plateau at 10 min. These features were not reduced further by longer sonication times, probably because the cytoskeleton material constituting the NERs membrane does not allow a further reduction of the bilayer curvature.

Cryo-TEM images reported in Fig. 3a and b showed that the NERs exhibit in 1x PBS at pH 7.4 mostly unilamellar vesicles with spherical shape (white arrows) coexisting with some membranes not reassembled into vesicles (black arrowheads). Although no direct evidence can be obtained from this formulation, it was already reported that the morphology of these nanoparticles in

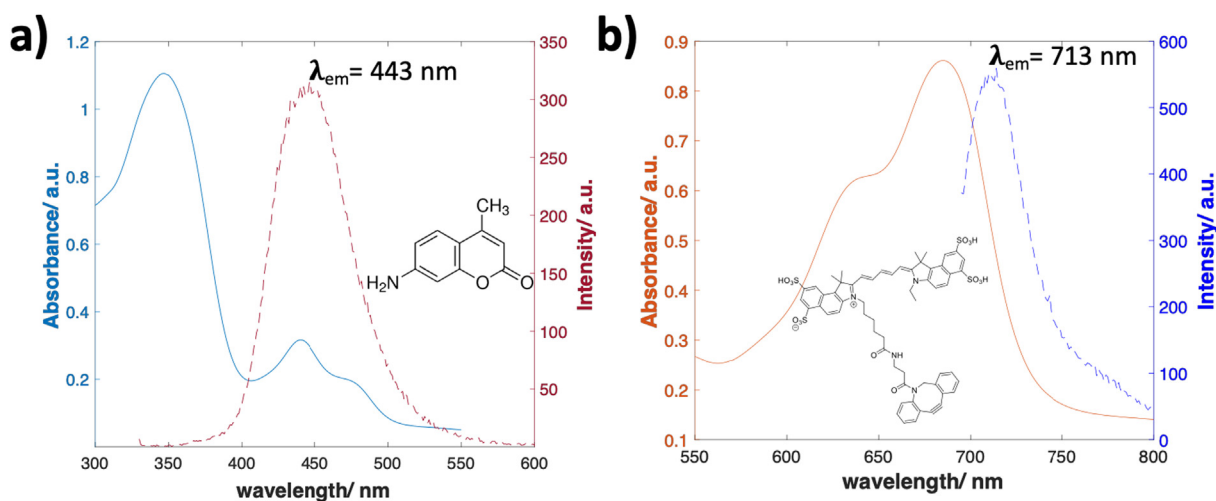


**Fig. 4.** Absorption and emission spectra for NERs-F1 (a) and NERs-F2 (b) after dilution 1:500 in PBS pH 7.4 medium.



hypertonic conditions is reminiscent of that exhibited by RBCs, showing the same biconcave structure [25]. This finding suggests that, after the hypotonic lysis, the membrane may reassemble in its native conformation. However, a membrane flipping during the reconstituting process cannot be fully excluded. In addition, the sonication process could solubilize some membrane proteins that aggregates in solution with their lipid surroundings [26], originating part of the particulate material observed in Fig. 3a and b.

The retention of membrane structures, e.g. proteins, lipids, and glycolipids, on NERs surface and the possible use of their  $-\text{NH}_2$  terminal groups for a functionalization process was already hypothesized and exploited by Lejeune, who applied the cross-linking method to decorate the NERs surface with daunorubicin [23]. Accordingly, glutaraldehyde was here used as a cross-linker to have a first layer on which the fluorophores (i) AMC and (ii) DBCO-Cy5.5 were attached using SpAAC Click Chemistry to obtain NERs-F1 and NERs-F2, respectively (Scheme 1).

The reactions required dark conditions to avoid glutaraldehyde polymerization. These labelled NER particles had an apparent  $D_h$  around 120 nm and were characterized by a slightly larger Pdl with respect to bare NERs (see Table 1).

Moreover, a decrease of the  $\zeta$ -potential values for both NERs-F1 and NERs-F2 was recorded compared to unlabeled NERs, a finding certainly related to the functionalization of the membrane proteins that removes charged groups in the electric double layer.

AMC is a commercial dye that absorbs at 350 nm and emits at 430 nm in MeOH, whereas the DBCO-Cy5.5 fluorophore absorbs the radiation in the red (680 nm) and has a fluorescence emission around 710 nm in DMSO. The maxima of absorption in the UV-Vis region for both dyes, 350 nm for AMC and 680 nm for DBCO-Cy5.5, respectively (Fig. 4a and b), were used to quantify the fluorophores covalently linked to the surface of NERs using the curve calibration method.

The concentration of the dyes was found to be  $(5.2 \pm 0.8) \times 10^{-5}$  M in the case of AMC and  $(9.2 \pm 0.7) \times 10^{-6}$  M in the case of DBCO-Cy5.5. It is important to address that small membrane fragments or proteins/lipids aggregates could be solubilized during the sonication step. This material in solution can affect the functionalization ratio.

The absorption spectra and the emission fluorescence spectra for the NERs-F1 and NERs-F2 are reported in Fig. 4, where AMC and DBCO-Cy5.5 exhibit an emission band with a maximum at 443 nm and 713 nm, respectively. The small red shift observed for both dyes in comparison with the free dye emission indicates they are experiencing a more polar environment. Also, NERs-F1 and NERs-F2 showed a strong fluorescence emission signal after dilution up to 1:500 in PBS medium. These two fluorescent formulations can be recognized as suitable candidates for optical imaging *in vitro* (NERs-F1) and *in vivo* (NERs-F2).

Since we have already stressed the importance of having an *in vivo* tool for optical imaging, the NERs-F2 formulation was furthermore analyzed using single-molecule fluorescence microscopy at an excitation wavelength of 638 nm (Fig. 5a). Individual NERs-F2 particles could be discerned in the microscopy images and the intensity from two separate measurements gave the fluorescence intensity distribution shown in Fig. 5b.

A typical fluorescence intensity was about 30 counts (Fig. 5b), whereas the average intensity from all 1100 detected NERs-F2 particles was 80 counts. The 30 counts correspond approximately to the fluorescence from one DBCO-Cy5.5 fluorophore, which could be estimated from the abrupt change in intensity when one of the NERs-F2 particles exhibited bleaching (Fig. 5c). This means that the average number of dye molecules is roughly 2.5 per labelled NE2-F2 particle. However, most of the labelled NERs-F2 contains only one fluorophore. This data corresponded to the very low amount of DBCO-Cy5.5 used for the preparation of NERs-F2.

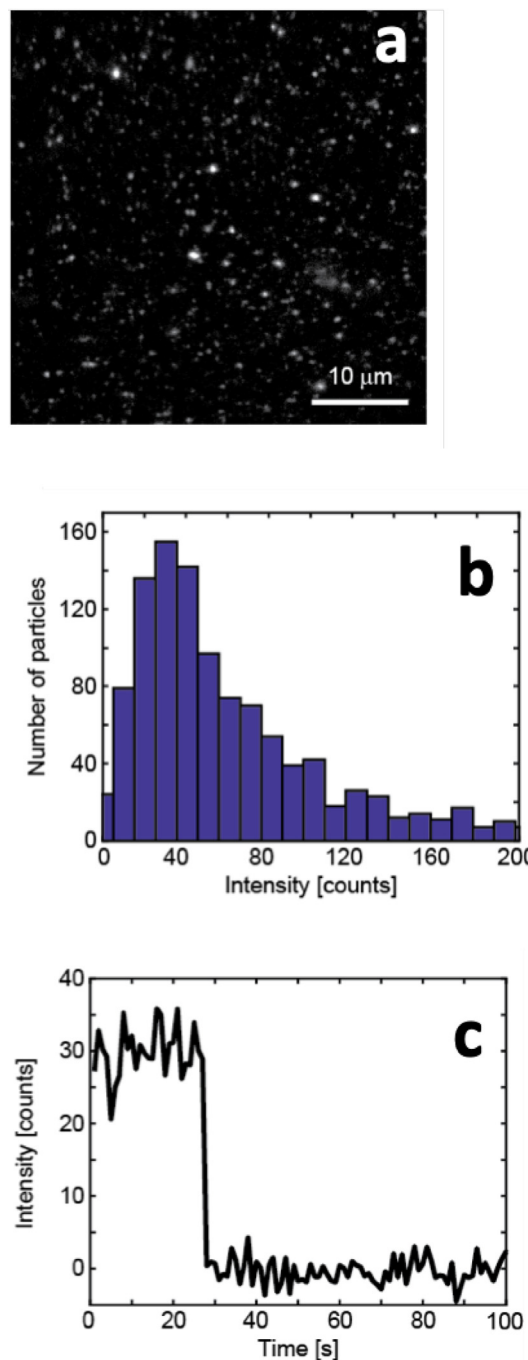


**Fig. 5.** Single-molecule fluorescence imaging of NERs-F2. (a) A representative fluorescence image showing NER-F2 particles absorbed to a glass slide. (b) Histogram of the intensity distribution from individually detected NERs-F2. The data is from two measurements with a total of 1124 detected particles. Approximately 7% of the particles have an intensity larger than 200 counts. (c) The change in intensity when bleaching a representative NER-F2 particle in (a).

Indeed, by increasing the concentration, it would be possible to obtain a higher number of dye molecules per nanoparticle, increasing the fluorescence signal consequently.

#### 4. Conclusions

Given the high demand for finding novel, biocompatible, biodegradable, and non-cytotoxic tools in nanomedicine, the physicochemical properties of unlabeled, and fluorescently labelled nanoerythroosomes (nanoderivatives of bovine red blood

cells) were here investigated. Indeed, NERs are a new class of drug and imaging probe carriers engineered to reduce the biological impact at a minimum, with excellent perspectives in personalized medicine.

NERs applicability in the imaging field has not been established yet. Therefore, different functionalization methods to achieve fluorescent labelling of this kind of nanoparticles were presented in this work. The first case of Click Chemistry on NERs was reported, showing how SpAAC could come in aid to functionalize such kind of nanocarriers. NERs stability was investigated in two different media and over time, highlighting that the physiological PBS was the best buffer to prepare and store the nanoparticles. Given their high colloidal stability and physico-chemical features, NERs represent an interesting alternative to other drug carriers, especially when biocompatibility is an issue. Indeed, they could be harvested directly from a patient blood, thus the immunological response should be negligible. Two different fluorophores were successfully conjugated on NERs surface for imaging applications: AMC and DBCO-Cy5.5. The spectroscopic properties of the labelled formulations showed that in both cases the dyes are experiencing a polar environment, being oriented towards the bulk water. Remarkably, the loading efficiency on NERs surfaces and their fluorescence properties after high dilution ratio (1:500) suggest that fluorescently labelled nanoerythrocytes can be used as a potent imaging tool *in vitro* and *in vivo*.

Drugs can be either encapsulated within the NERs core [43] or conjugated on their surface [23]. Particularly, by combining the versatility of different functionalization routes, e.g. Click Chemistry and cross-linking, with NERs intrinsic biocompatibility, these surface-modified systems could assist in several clinical therapies and imaging applications. However, given the desired application in nanomedicine, these nanovectors should be tested against different cell lines to understand possible difference in terms of uptake in comparison with other soft matter-based formulations. Different groups can be used to conjugate therapeutic molecules or imaging probes to the NERs surface (such as  $-\text{COOH}$ ,  $-\text{OH}$ ,  $-\text{SH}$  and, of course  $\text{NH}_2$ ) [16], and new decoration routes of NERs surface could represent another possible outlook, possibly with targeting agents to achieve selective delivery of therapeutic agents. Nevertheless, surface functionalization should be evaluated with care to avoid activation of the complement with consequent reduction of the NERs permanence in the bloodstream because of RES clearance [44].

#### CRedit authorship contribution statement

**Marco Fornasier:** Investigation, Writing - review & editing. **Andrea Porcheddu:** Investigation, Writing - review & editing. **Anna Casu:** Data curation, Writing - review & editing. **Srinivasa R. Raghavan:** Supervision, Writing - review & editing. **Peter Jönsson:** Investigation, Writing - review & editing. **Karin Schillén:** Supervision, Writing - review & editing. **Sergio Murgia:** Supervision, Funding acquisition, Writing - original draft.

#### Declaration of Competing Interest

The authors declare that they have no known competing financial interests or personal relationships that could have appeared to influence the work reported in this paper.

#### Acknowledgements

The authors thank Dr. Manuel Liciardi and Dr. Giuseppe Argiolas from Istituto Zooprofilattico della Sardegna, who kindly provided the bovine blood samples. They also thank the National

Center for High Resolution Electron Microscopy (nCHREM) at Lund University is kindly thanked for providing access to the executing the Cryo-TEM measurements, and Dr. Anna M. Carnerup for her assistance and advices for these measurements. M.F. Ph.D. scholarship was funded by the project P.O.R. Sardegna F.S.E. 2014–2020. S.M. thanks Fondazione Banco di Sardegna and Regione Autonoma della Sardegna (Progetti Biennali di Ateneo Annualità 2018)

#### References

- [1] H.M.G. Barriga, M.N. Holme, M.M. Stevens, Cubosomes: The next generation of smart lipid nanoparticles?, *Angew Chemie - Int. Ed.* 58 (2019) 2958–2978, <https://doi.org/10.1002/anie.201804067>.
- [2] U. Bazylińska, J. Kulbacka, J. Schmidt, Y. Talmon, S. Murgia, Polymer-free cubosomes for simultaneous bioimaging and photodynamic action of photosensitizers in melanoma skin cancer cells, *J. Colloid Interface Sci.* 522 (2018) 163–173, <https://doi.org/10.1016/j.jcis.2018.03.063>.
- [3] S. Biffi, L. Andolfi, C. Caltagirone, C. Garrovo, A.M. Falchi, V. Lippolis, A. Lorenzon, P. Macor, V. Meli, M. Monduzzi, M. Obiols-Rabasa, L. Petrizza, L. Prodi, A. Rosa, J. Schmidt, Y. Talmon, S. Murgia, Cubosomes for *in vivo* fluorescence lifetime imaging, *Nanotechnology* 28 (2017), <https://doi.org/10.1088/1361-6528/28/5/055102>.
- [4] N. Alcaraz, Q. Liu, E. Hanssen, A. Johnston, B.J. Boyd, Clickable cubosomes for antibody-free drug targeting and imaging applications, *Bioconjugate Chem.* 29 (2018) 149–157, <https://doi.org/10.1021/acs.bioconjchem.7b00659>.
- [5] L. Boge, K. Hallstenson, L. Ringstad, J. Johansson, T. Andersson, M. Davoudi, P.T. Larsson, M. Mahlapuu, J. Håkansson, M. Andersson, Cubosomes for topical delivery of the antimicrobial peptide LL-37, *Eur. J. Pharm. Biopharm.* 134 (2019) 60–67, <https://doi.org/10.1016/j.ejpb.2018.11.009>.
- [6] M.M. Ebersold, M. Petrović, W.K. Fong, D. Bonvin, H. Hofmann, I. Milošević, Hexosomes with undecylenic acid efficient against candida albicans, *Nanomaterials* 8 (2018), <https://doi.org/10.3390/nano8020091>.
- [7] L. Rodrigues, K.N. Raftopoulos, S. Tandrup Schmidt, F. Schneider, H. Dietz, T. Rades, H. Franzyk, A.E. Pedersen, C.M. Papadakis, D. Christensen, G. Winter, C. Foged, M. Hubert, Immune responses induced by nano-self-assembled lipid adjuvants based on a monomycoloyl glycerol analogue after vaccination with the Chlamydia trachomatis major outer membrane protein, *J. Control. Release.* 285 (2018) 12–22, <https://doi.org/10.1016/j.jconrel.2018.06.028>.
- [8] N. Iturriz-Rodríguez, M.A. Correa-Duarte, M.L. Fanarraga, Controlled drug delivery systems for cancer based on mesoporous silica nanoparticles, *Int. J. Nanomed.* 14 (2019) 3389–3401, <https://doi.org/10.2147/IJN.S198848>.
- [9] V. López, M.R. Villegas, V. Rodríguez, G. Villaverde, D. Lozano, A. Baeza, M. Vallet-Regí, Janus mesoporous silica nanoparticles for dual targeting of tumor cells and mitochondria, *ACS Appl. Mater. Interfaces* 9 (2017) 26697–26706, <https://doi.org/10.1021/acsami.7b06906>.
- [10] M. Schlich, M. Fornasier, M. Nieddu, C. Sinico, S. Murgia, A. Rescigno, 3-hydroxycoumarin loaded vesicles for recombinant human tyrosinase inhibition in topical applications, *Colloids Surf. B Biointerfaces* 171 (2018) 675–681, <https://doi.org/10.1016/j.colsurfb.2018.08.008>.
- [11] S. Valkonen, E. van der Pol, A. Böing, Y. Yuana, M. Yliperttula, R. Nieuwland, S. Laitinen, P.R.M. Siljander, Biological reference materials for extracellular vesicle studies, *Eur. J. Pharm. Sci.* 98 (2017) 4–16, <https://doi.org/10.1016/j.ejps.2016.09.008>.
- [12] M. Schlich, C. Sinico, D. Valenti, A. Gulati, M.D. Joshi, V. Meli, S. Murgia, T. Xanthos, Towards long-acting adrenaline for cardiopulmonary resuscitation: Production and characterization of a liposomal formulation, *Int. J. Pharm.* 557 (2019) 105–111, <https://doi.org/10.1016/j.ijpharm.2018.12.044>.
- [13] M. Mamusa, L. Sitia, F. Barbero, A. Ruyra, T.D. Calvo, C. Montis, A. Gonzalez-Paredes, G.N. Wheeler, C.J. Morris, M. McArthur, D. Berti, Cationic liposomal vectors incorporating a bolaamphiphile for oligonucleotide antimicrobials, *Biochim. Biophys. Acta - Biomembr.* 2017 (1859) 1767–1777, <https://doi.org/10.1016/j.bbmem.2017.06.006>.
- [14] M. Mamusa, F. Barbero, C. Montis, L. Cutillo, A. Gonzalez-Paredes, D. Berti, Inclusion of oligonucleotide antimicrobials in biocompatible cationic liposomes: A structural study, *J. Colloid Interface Sci.* 508 (2017) 476–487, <https://doi.org/10.1016/j.jcis.2017.08.080>.
- [15] M. Schlich, F. Longhena, G. Faustini, C.M. O'Driscoll, C. Sinico, A.M. Fadda, A. Bellucci, F. Lai, Anionic liposomes for small interfering ribonucleic acid (siRNA) delivery to primary neuronal cells: Evaluation of alpha-synuclein knockdown efficacy, *Nano Res.* 10 (2017) 3496–3508, <https://doi.org/10.1007/s12274-017-1561-z>.
- [16] H. Zhang, Erythrocytes in nanomedicine: an optimal blend of natural and synthetic materials, *Biomater. Sci.* 4 (7) (2016) 1024–1031, <https://doi.org/10.1039/c6bm00072j>.
- [17] C. Gutiérrez Millán, D.G. Bravo, J.M. Lanao, New erythrocyte-related delivery systems for biomedical applications, *J. Drug Deliv. Sci. Technol.* 42 (2017) 38–48, <https://doi.org/10.1016/j.jddst.2017.03.019>.
- [18] N. Kavita, P. Sayali, S.A. Payghan, Design of three-factor response surface optimization of camouflaged capecitabine nanoerythrocytes, *Asian J. Pharm.* 10 (2016) 306–321.
- [19] V. Balasubramanian, A. Poillucci, A. Correia, H. Zhang, C. Celia, H.A. Santos, Cell membrane-based nanoreactor to mimic the bio-compartmentalization

- strategy of a cell, ACS Biomater. Sci. Eng. 4 (2018) 1471–1478, <https://doi.org/10.1021/acsbomaterials.7b00944>.
- [20] R. Hirlekar, P. Patel, N. Dand, V. Kadam, Drug loaded erythrocytes: as novel drug delivery system, Curr. Pharm. Des. 14 (2008) 63–70, <https://doi.org/10.2174/138161208783330772>.
- [21] K.A. Nangare, S.D. Powar, S.A. Payghan, Nanoerythrocytes: Engineered 2016 (2016) 223–233.
- [22] J. Désilets, A. Lejeune, J. Mercer, C. Gicquaud, Nanoerythrocytes, a new derivative of erythrocyte ghost: IV. Fate of reinjected nanoerythrocytes, Anticancer Res. (2001).
- [23] A. Lejeune, M. Moorjani, C. Gicquaud, J. Lacroix, P. Poyet, C.R. Gaudreault, Nanoerythrocyte, a new derivative of erythrocyte ghost: Preparation and antineoplastic potential as drug carrier for daunorubicin, Anticancer Res. 14 (1994) 915–919.
- [24] X. Han, S. Shen, Q. Fan, G. Chen, E. Archibong, G. Dotti, Z. Liu, Z. Gu, C. Wang, Red blood cell-derived nanoerythrocyte for antigen delivery with enhanced cancer immunotherapy, Sci. Adv. 5 (2019) 1–10, <https://doi.org/10.1126/sciadv.aaw6870>.
- [25] Y.C. Kuo, H.C. Wu, D. Hoang, W.E. Bentley, W.D. D'Souza, S.R. Raghavan, Colloidal properties of nanoerythrocytes derived from bovine red blood cells, Langmuir 32 (2016) 171–179, <https://doi.org/10.1021/acs.langmuir.5b03014>.
- [26] R. Deák, J. Mihály, I. Cs, A. Wacha, G. Lelkes, A. Bóta, Colloids and Surfaces B: Biointerfaces Physicochemical characterization of artificial nanoerythrocytes derived from erythrocyte ghost membranes, 135 (2015) 225–234.
- [27] R. Pouliot, A. Saint-Laurent, C. Chypre, R. Audet, I. Vitté-Mony, R.C. Gaudreault, M. Auger, Spectroscopic characterization of nanoerythrocytes in the absence and presence of conjugated polyethyleneglycols: An FTIR and 31P-NMR study, Biochim. Biophys. Acta – Biomembr. 1564 (2002) 317–324, [https://doi.org/10.1016/S0005-2736\(02\)00465-0](https://doi.org/10.1016/S0005-2736(02)00465-0).
- [28] R. Deák, J. Mihály, I.C. Szgyártó, T. Beke-Somfai, L. Turiák, L. Drahos, A. Wacha, A. Bóta, Z. Varga, Nanoerythrocytes tailoring: Lipid induced protein scaffolding in ghost membrane derived vesicles, Mater. Sci. Eng. C. 109 (2020) 110428, <https://doi.org/10.1016/j.msec.2019.110428>.
- [29] W. Tang, M.L. Becker, “Click” reactions: a versatile toolbox for the synthesis of peptide-conjugates, Chem. Soc. Rev. 43 (2014) 7013–7039, <https://doi.org/10.1039/c4cs00139g>.
- [30] S. Chandrudu, P. Simerska, I. Toth, Chemical methods for peptide and protein production, Molecules 18 (2013) 4373–4388, <https://doi.org/10.3390/molecules18044373>.
- [31] V. Hong, N.F. Steinmetz, M. Manchester, M.G. Finn, Labeling live cells by copper-catalyzed alkyne–azide click chemistry, Bioconj. Chem. 21 (2010) 1912–1916, <https://doi.org/10.1021/bc100272z>.
- [32] J.M. Baskin, J.A. Prescher, S.T. Laughlin, N.J. Agard, P.V. Chang, I.A. Miller, A. Lo, J.A. Codelli, C.R. Bertozzi, Copper-free click chemistry for dynamic in vivo imaging, Proc. Natl. Acad. Sci. U. S. A. 104 (2007) 16793–16797, <https://doi.org/10.1073/pnas.0707090104>.
- [33] J.C. Jewett, C.R. Bertozzi, Cu-free click cycloaddition reactions in chemical biology, Chem. Soc. Rev. 39 (2010) 1272, <https://doi.org/10.1039/b901970g>.
- [34] Y. Takayama, K. Kusamori, M. Nishikawa, Click chemistry as a tool for cell engineering and drug delivery, Molecules 24 (2019) 172, <https://doi.org/10.3390/molecules24010172>.
- [35] S. Keereweer, J.D.F. Kerrebijn, P.B.A.A. van Driel, B. Xie, E.L. Kaijzel, T.J.A. Snoeks, I. Que, M. Hutteman, J.R. van der Vorst, J.S.D. Mieog, A.L. Vahrmeijer, C. J.H. van de Velde, R.J. Baatenburg de Jong, C.W.G.M. Löwik, Optical image-guided surgery—where do we stand?, Mol. Imaging Biol. 13 (2) (2011) 199–207, <https://doi.org/10.1007/s11307-010-0373-2>.
- [36] C. Wang, Z. Wang, T. Zhao, Y. Li, G. Huang, B.D. Sumer, J. Gao, Optical molecular imaging for tumor detection and image-guided surgery, Biomaterials 157 (2018) 62–75, <https://doi.org/10.1016/j.biomaterials.2017.12.002>.
- [37] A.M. De Grand, J.V. Frangioni, An operational near-infrared fluorescence imaging system prototype for large animal surgery, Technol Cancer Res. Treat. 2 (2003) 553–562, <https://doi.org/10.1177/153303460300200607>.
- [38] H.S. Peng, D.T. Chiu, Soft fluorescent nanomaterials for biological and biomedical imaging, Chem. Soc. Rev. 44 (2015) 4699–4722, <https://doi.org/10.1039/c4cs00294f>.
- [39] E.A. Owens, M. Henary, G. El Fakhri, H.S. Choi, Tissue-specific near-infrared fluorescence imaging, Acc. Chem. Res. 49 (2016) 1731–1740, <https://doi.org/10.1021/acs.accounts.6b00239>.
- [40] N. Gupta, B. Patel, K. Nahar, F. Ahsan, Cell permeable peptide conjugated nanoerythrocytes of fasudil prolong pulmonary arterial vasodilation in PAH rats, Eur. J. Pharm. Biopharm. 88 (3) (2014) 1046–1055, <https://doi.org/10.1016/j.ejpb.2014.10.012>.
- [41] J. Agnihotri, S. Saraf, S. Singh, P. Bigoniya, Development and evaluation of anti-malarial bio-conjugates: artesunate-loaded nanoerythrocytes, Drug Deliv. Transl. Res. 5 (2015) 489–497, <https://doi.org/10.1007/s13346-015-0246-y>.
- [42] J. Janiak, S. Bayati, L. Galantini, N.V. Pavel, K. Schillén, Nanoparticles with a bicontinuous cubic internal structure formed by cationic and non-ionic surfactants and an anionic polyelectrolyte, Langmuir 28 (48) (2012) 16536–16546, <https://doi.org/10.1021/la303938k>.
- [43] N. Gupta, B. Patel, F. Ahsan, Nano-engineered erythrocyte ghosts as inhalational carriers for delivery of fasudil: preparation and characterization, Pharm. Res. 31 (6) (2014) 1553–1565, <https://doi.org/10.1007/s11095-013-1261-7>.
- [44] J. Yan, J. Yu, C. Wang, Z. Gu, Red blood cells for drug delivery, Small Methods 1 (2017) 1700270, <https://doi.org/10.1002/smt.201700270>.



# Paper VII

*“Bioimaging Applications of Non-Lamellar Liquid Crystalline Nanoparticles”*

S. Murgia, S. Biffi, **M. Fornasier**, V. Lippolis, G. Picci, C. Caltagirone;

Journal of Nanoscience and Nanotechnology, 2021, 21, 1-18.

**DOI: 10.1166/jnn.2021.19064**

Copyright © from American Scientific Publishers 2020

# Bioimaging Applications of Non-Lamellar Liquid Crystalline Nanoparticles

Sergio Murgia<sup>1,3,\*</sup>, Stefania Biffi<sup>2,\*</sup>, Marco Fornasier<sup>1</sup>, Vito Lippolis<sup>1</sup>,  
Giacomo Picci<sup>1</sup>, and Claudia Caltagirone<sup>1,\*</sup>

<sup>1</sup>*Dipartimento di Scienze Chimiche e Geologiche, Università degli Studi di Cagliari, Cittadella Universitaria, s.s. 554 bivio Sestu, I-09042 Monserrato (CA), Italy*

<sup>2</sup>*Institute for Maternal and Child Health, IRCCS Burlo Garofolo, Trieste, Italy*

<sup>3</sup>*CSGI, Consorzio Interuniversitario per lo Sviluppo dei Sistemi a Grande Interfase, Via della Lastruccia 3, I-50019 Sesto Fiorentino, Florence, Italy*

Self-assembling processes of amphiphilic lipids in water give rise to complex architectures known as lyotropic liquid crystalline (LLC) phases. Particularly, bicontinuous cubic and hexagonal LLC phases can be dispersed in water forming colloidal nanoparticles respectively known as cubosomes and hexosomes. These non-lamellar LLC dispersions are of particular interest for pharmaceutical and biomedical applications as they are potentially non-toxic, chemically stable, and biocompatible, also allowing encapsulation of large amounts of drugs. Furthermore, conjugation of specific moieties enables their targeting, increasing therapeutic efficacies and reducing side effects by avoiding exposure of healthy tissues. In addition, as they can be easily loaded or functionalized with both hydrophobic and hydrophilic imaging probes, cubosomes and hexosomes can be used for the engineering of multifunctional/theranostic nanoplatforms. This review outlines recent advances in the applications of cubosomes and hexosomes for *in vitro* and *in vivo* bioimaging.

**Keywords:** Self-Assembling, Soft Matter, Lipid-Based Nanoparticles, Liquid-Crystalline Nanoparticles, Nanomedicine, Bio-Imaging.

## CONTENTS

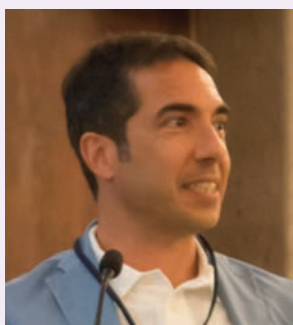
1. Introduction	1
2. Preparation and Characterization of Cubosomes and Hexosomes	4
3. Hexosomes and Cubosomes Based Imaging Agents for <i>In Vitro</i> Applications	5
4. Hexosomes and Cubosomes Based Imaging Agents for <i>In Vivo</i> Applications	11
4.1. Magnetic Resonance Imaging	12
4.2. Single Photon Emission Computed Tomography	13
4.3. Fluorescence Optical Imaging	13
4.4. Multimodal Imaging	13
5. Conclusions	14
Acknowledgments	14
References and Notes	14

## 1. INTRODUCTION

One of the most intriguing physicochemical aspects of amphiphilic lipids, such as monoglycerides or phospholipids, is their self-assembly aptitude in aqueous

solutions [1, 2]. Driven by the hydrophobic effect, which promotes self-assembly to reduce or totally avoid interactions between water and hydrophobic tails, these molecules may aggregate forming nanostructures, known as lyotropic liquid crystalline (LLC) phases, endowed of a long-range order typical of solids but still retaining a certain fluidity typical of liquids. The geometry of the interface that separates the hydrophobic and the hydrophilic domains is helpful in describing the nanostructure of these aggregates [3–5]. Particularly, two contributions characterize such interface: the interfacial curvature associated to the local geometry, and the interfacial topology, describing the global geometry as a function of the interfacial connectivity degree. Importantly, the first contribution can be rationalized in terms of the critical packing parameter ( $P$ ),  $v/a_0l_c$ , where  $v$  is the volume of the hydrophobic chain,  $a_0$  is the headgroup area, and  $l_c$  is the critical hydrocarbon chain length, roughly equal to but less than the fully extended chain length [6, 7]. This simple geometric parameter represents a potent predicting tool since

\*Authors to whom correspondence should be addressed.



**Sergio Murgia** received his Ph.D. degree in Physical Chemistry from the University of Cagliari in 2002. In the period 2003–2006 he was Postdoctoral Fellow at the University of Cagliari, and then Assistant Professor at the same University. Since 2016 he is Associate Professor at the University of Cagliari. His scientific activity is mainly related to the field of soft matter-based colloids. Research topics concern investigation of both the nanostructure and the dynamic behaviour of biocompatible surfactant aggregates, with particular emphasis on those having promising applications as theranostic tools in oncology and diabetes.



**Stefania Biffi** got her Ph.D. in Medicinal Chemistry from the University of Trieste in 2003. From 2003 to 2006, she worked at the Infantile Neuropsychiatry Ward, Institute for Maternal and Child Health, IRCCS Burlo Garofolo, Trieste. From 2006 to 2013 she worked at CBM Scrl (Trieste, Italy) as optical imaging scientist; she also has experience of several years working within an EU-funded consortium undertaking a mobility program as More Experienced Researcher abroad and providing mentoring/tutoring activities for Early Stage and Experienced visiting Researchers. Since 2013 she has been working at the Institute for Maternal and Child Health, IRCCS Burlo Garofolo, as imaging scientist. Her research activity at present is focused on molecular imaging and nanotheranostics applied to study ovarian cancer.



**Marco Fornasier** is a Ph.D. Student in Chemical Sciences and Technologies at University of Cagliari under the supervision of Professor Sergio Murgia since October 2017. He is also a Guest Student at the Physical Chemistry Division of Lund University under the supervision of Professor Tommy Nylander and Professor Karin Schillén. His research activities focus on lipid self-assembly to obtain theranostic nanoparticles such as liposomes, cubosomes, and hexosomes, and gels for application in nanomedicine.



**Vito Lippolis** graduated in chemistry in 1991 at the University of Pisa, Italy, and in the same year gained a diploma in chemistry at the “Scuola Normale Superiore” of Pisa. In 2000, he received his Ph.D. degree from the University of Nottingham, UK, under the supervision of Professor Martin Schröder. In 2001, he was appointed to the chair of Inorganic Chemistry at the University of Cagliari, Italy. He has published about 300 publications and his research interests at the moment mainly include coordination chemistry of macrocyclic ligands and development of molecular sensors and ionophores for heavy metal ions and anions, interaction of chalcogen donor ligands with dihalogens and dihalogen-like acceptors.



**Giacomo Picci** got her Master Degree in Chemistry from the University of Cagliari in 2015 under the Supervision of Professor Claudia Caltagirone. In 2016 started his Ph.D. working on the Supramolecular Chemistry of anionic species and on the development of fluorescent probes for bioimaging application.



**Claudia Caltagirone** got her Ph.D. in Chemistry from the University of Cagliari (Italy) in 2006 under the Supervision of Professor Vito Lippolis. In the same year, she became Lecturer in Inorganic Chemistry at the University of Cagliari. From 2006 to 2008, she spent two years at the University of Southampton (UK) as Academic Visitor working in Philip A. Gale group. Since 2016, she is Associate Professor in Inorganic Chemistry at the University of Cagliari. Her research interests focus on the Supramolecular Chemistry of anionic species and in particular on molecular recognition and sensing and on the development of fluorescent probes of biomedical applications.

it relates the molecular shape with the preferred curvature of the interface. In general, for  $P$  values in between 0.5 and 1, amphiphilic lipids self-assemble forming planar interfaces, while for  $P$  values larger than 1 they form aggregates of the reverse kind [8]. In real systems  $P$  may change according to temperature variations or addition of oils or salts that can modify either the headgroup area or the chain splay, causing phase transitions [9–11].

Therefore, as dictated by the constraints imposed by  $P$ , different types of supramolecular architectures are originated by lipids self-assembly, being the lamellar, hexagonal, and bicontinuous cubic LLC phases the most representative (Fig. 1). Lamellar LLC phases consist of 1D planar, stacked membranes (bilayers) formed by opposing lipid monolayers [12], while in hexagonal LLC phases lipid monolayers envelope water cylinders arranged in a 2D hexagonal array [13, 14]. Differently, in bicontinuous cubic LLC phases a 3D curved, non-intersecting bilayer is folded in space forming two continuous but not interconnected water channels [15, 16]. Remarkably, it was observed that the lipid bilayer in bicontinuous cubic phases is superimposable over the so-called infinite periodic minimal surfaces (IPMSs) [17, 18], and in lipid-based systems three types of IPMSs, describing different cubic space groups, are important: the primitive (body-centered lattice,  $Im3m$ ), the gyroid (body-centered lattice,  $Ia3d$ ), and the double diamond type (primitive lattice,  $Pn3m$ ).

Being lipids ubiquitous constituents of cell membranes, it is not surprising that bicontinuous cubic assemblies have

been found in all kingdoms of life [19]. Indeed, although their role in the cell machinery has not been understood yet, these phases were observed in many different types of cell membranes either under physiological or pathological (infection, tumors) states, or as a result of induced stress (starvation, drug treatments) [20–24].

Lamellar, hexagonal, and bicontinuous cubic LLC phases share an aspect that makes them extremely interesting in pharmaceutical research: they can be dispersed as nanoparticles (NPs) in water. Liposomes are the well-known colloidal dispersions of lamellar phases [25, 26], while the hexagonal and the bicontinuous cubic LLC analogues are, respectively, known as hexosome [27, 28] and cubosomes [1, 29–32]. Often, the latter are referred to as non-lamellar liquid crystalline NPs. Apart from their internal nanostructure, another important difference among these NPs is related to their kinetic stabilization in water against flocculation and consequent phase separation. Indeed, liposomes form stable colloidal dispersions, while stabilization of cubosomes and hexosomes always require the addition of a stabilizing agent (usually a polymer, as will be discussed in the next paragraph) [33–35]. In addition, non-lamellar liquid crystalline NPs differentiate from liposomes because they possess a larger hydrophobic volume. In particular, with respect to unilamellar liposomes, it was calculated that cubosomes have a hydrophobic volume three times larger exposing, at the same time, 40% less of their surface to water [36].

Cubosomes and hexosomes attracted much attention in nanomedicine applications [37–39], especially as drug carriers [40–49], because they can host hydrophobic and hydrophilic drugs, can be doped with imaging agents (see next paragraph), and their surface can be conjugated with targeting agents to properly address the drug and/or the imaging probe to pathological tissues thus reducing unwanted side-effects [50, 51]. Moreover, given the possibility of simultaneously load these NPs with imaging agents and therapeutically active molecules, they are also considered interesting candidates as theranostic nanomedicine [52–54]. Nevertheless, differently from liposome, for which several formulations are already on the market (such as Doxil® or Evacet™, just to name a few) or in clinical trials [55], *in vivo* investigations of hexosomes

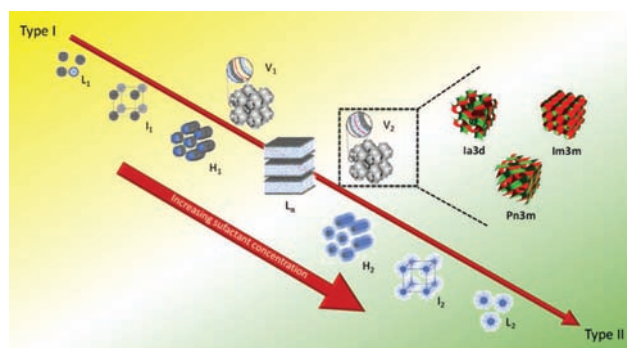


**Figure 1.** Schematic representation of supramolecular architectures originated by lipids self-assembly.



and cubosomes are still at their infancy. Indeed, while the physicochemical characteristics of such NPs are nowadays routinely investigated, their pharmacokinetics, hemato-compatibility, toxicity, and delivery properties remain far from being completely elucidated. Although the cytotoxicity of several cubosomes and hexosomes formulations reported in literature is debated [56–58], others studies evidenced the good performances of non-lamellar liquid crystalline NPs as nanocarriers for molecules with diagnostic and/or therapeutic relevance [59–64]. Therefore, also taking into account their peculiar inner structure, these NPs deserve to be investigated in more depth as alternative to the ubiquitous liposomes.

Several interesting and comprehensive reviews appeared in literature discussing various aspects of non-lamellar LLC NPs [65–67]. In particular the role of LLC NPs for the design of drug delivery systems have been extensively described, however applications for theranostic/imaging have been only marginally considered. This review reports on recent advances in non-lamellar NPs characterized by hexagonal (hexosomes) or bicontinuous cubic (cubosomes) inner structures focusing on their use as analytical tools for *in vitro* and *in vivo* bioimaging. It is important noticing that during the drafting of this review Drummond et al. published a review on the use of these NPs for nanomedicine applications [68].

## 2. PREPARATION AND CHARACTERIZATION OF CUBOSOMES AND HEXOSOMES

Cubosomes and hexosomes are mostly formulated using as molecular building blocks monoolein (2,3-dihydroxypropyl (*Z*)-octadec-9-enoate) or phytantriol (3,7,11,15-tetramethylhexadecane-1,2,3-triol) [65]. Their binary phase diagrams in water are characterized by the existence of LLC phase regions [69–71]. Definitely, at 25 °C and increasing the water content, a lamellar phase and then two bicontinuous cubic phases, respectively the Ia3d and the Pn3m, are found. Remarkably, the Pn3m phase can exist also in excess of water while, increasing the temperature, the cubic nanostructures evolve towards an inverse hexagonal phase. However, the hexagonal phase can also be obtained at room temperature by adding suitable additives, such oleic acid, that can increase *P* thus allowing the cubic-to hexagonal phase transition [72–74].

It deserves noticing that, differently by phytantriol, monoolein can be hydrolyzed by acid hydrolysis reactions or by enzymes (such as carboxylesterases or phosphatases), and it is also prone to degradation because of the unsaturation in the hydrophobic chain. These peculiarities might be important when selecting the lipid for the NPs formulation.

Non-lamellar LLC NPs can be prepared either by a top-down or a bottom up approach. In the former case, the NPs are obtained fragmenting the already prepared bulk

LLC phase, eventually containing the additive, using high-pressure homogenization or high-speed shearing. On the other hand, the bottom-up approach contemplates the formation of the NPs by dissolving hydrophobic additives into the melted monoolein and then adding the aqueous solution containing the dispersant (Fig. 2). Afterward, the energy input required to form the dispersion is typically provided by using ultrasonic homogenizers. Alternatively, cubosome can be prepared by a bottom-up procedure dissolving the lipid by means of a hydrotrope to originate a water like solution to which an aqueous solution containing the dispersant is added. This mixture is then sonicated for several minutes [75, 76]. Additives include pharmaceutically active molecules, imaging probes, as well as molecules that, increasing the hydrophobic chains splay (e.g., capric or oleic acid), may provoke the desired cubic-to hexagonal transition for the formulation of hexosomes [77–79]. On the contrary, sometimes such transition could be unwanted, limiting the amount of additives that can be loaded in the NPs. As anticipated, the formulation of a colloidal LLC stable dispersion requires the presence of a stabilizing agent to avoid flocculation of the NPs. Traditionally, the stabilizing molecule belongs to the class of non-ionic poly(ethylene oxide)-poly(propylene oxide)-poly(ethylene oxide) (PEO-PPO-PEO) tri-block copolymers known as Pluronic, being the F127 and the F108 the most used. The latter differ because of the length of the PEO and PPO segments (PEO<sub>132</sub>-PPO<sub>50</sub>-PEO<sub>132</sub> for F108, and PEO<sub>100</sub>-PPO<sub>65</sub>-PEO<sub>100</sub> for F127), hence because of their Hydrophilic Lipophilic Balance (equal to 22 and 27 for F127 and F108, respectively) [80]. F127 and F108 ensure the steric stabilization of cubosomes or hexosomes anchoring the PPO moiety in the NPs while their PEO segments, oriented towards the solvent, provide the particles with a sort of PEO corona. As an alternative to Pluronic several other steric stabilizers were proposed, including polysorbate 80 (Tween 80, polyoxyethylene (20) sorbitan monooleate) [81], modified cellulose (hydroxypropyl methylcellulose acetate succinate) [82], and poly(octadecyl acrylate)-block-poly(polyethylene glycol methyl ether acrylate) amphiphilic brush copolymers [34], nevertheless Pluronic largely remain the preferred stabilizers in formulating cubosomes and hexosomes. However, colloidal dispersions of non-lamellar LLC NPs can be stabilized in water also without the use of polymers. For instance,  $\beta$ -caseins [83] or laponite [84] disc-like particles were used for such purpose. Another (rare) example is given by polymer-free cubosomes co-stabilized by a mixture of phospholipids and propylene glycol [85]. Here, rather than through steric interactions, collapse of the formulation was avoided by electrostatic repulsion (the measured  $\zeta$ -potential was equal to  $-20$  mV). In addition, being the system engineered for the photodynamic treatment of human melanoma skin cancer, propylene glycol played the double role of hydrotrope and humectant.

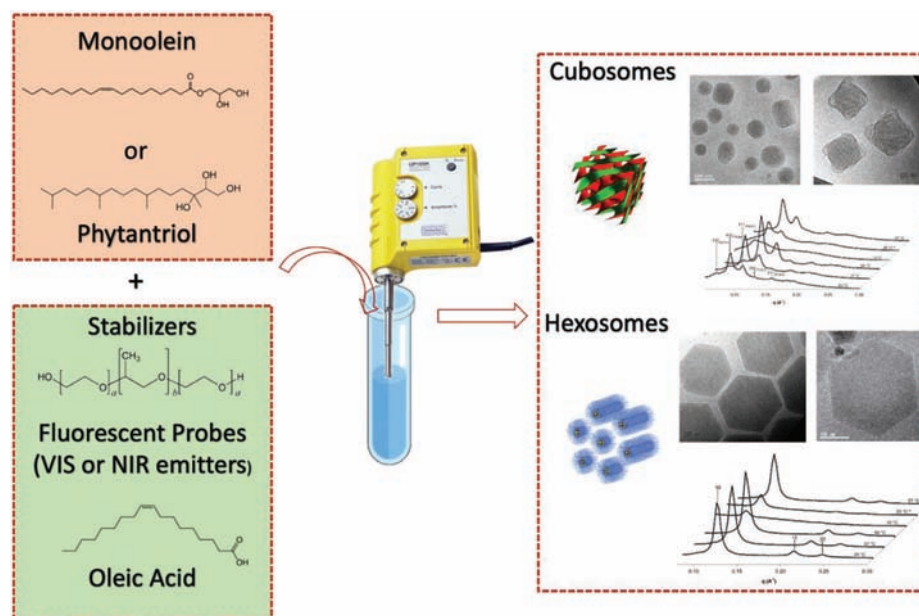


**Figure 2.** Bottom-up approach for the preparation of cubosome and hexosomes formulations.

Although different aspects of these NPs can be investigated using a variety of techniques such as AFM [27], DSC,  $^{23}\text{Na}$  [86–88] and  $^{13}\text{C}$  NMR [89] or ATR-FTIR [90] spectroscopy, the fundamental issue of the internal nanostructure can be properly addressed only by Small Angle X-ray Scattering (SAXS) [75, 91]. Scattering profiles obtained from SAXS experiments allow discriminating among the various LLC phases present in the samples, sometime evidencing the existence of a second phase. For example, the coexistence of the Im3m and the Pn3m phases was observed in the early 2000s in a seminal work by Nakano et al. [92], and attributed to the interaction of the lipid bilayer with the Pluronic F127 used for the cubosomes stabilization. Cubosomes and hexosomes can be directly visualized by transmission (TEM) or scanning (SEM) [93] electron microscopy at cryogenic temperatures [94]. Indeed, to preserve their native nanostructure, samples must be vitrified in liquid ethane at first, and then analyzed under liquid nitrogen to avoid water evaporation under the microscope with consequential damage of the nanostructure. Demurtas et al. recently fully elucidated the 3D organization of cubosomes by cryo-electron tomography and proposed a new model for the mechanism of cubosomes stabilization that involves the interlamellar attachments observed in the outer surface of the NPs, representing the transition state between the LLC internal phase and the usually observed vesicular structures surrounding the NPs [95].

After the complete morphological and topological characterization, cubosomes and hexosomes formulations are usually investigated for their size distribution and  $\zeta$ -potential by Dynamic Light Scattering (DLS). Such technique allows measuring the apparent hydrodynamic

diameter of the NPs and the polydispersity index of the colloidal dispersion. Typically measured size of cubosomes and hexosomes range between 100 and 400 nm. Amazingly, though constituted by non-ionic molecules, these NPs (prepared either with monoolein or phytantriol) display a negative charge, with observed  $\zeta$ -potentials of about  $-20$  mV. Safely excluding the presence of impurities, such charge can be explained calling into play a phenomenon commonly detected at the oil water interfaces, where the specific adsorption of hydroxide ions causes a polarized water layer, in this case, surrounding the NPs [96, 97].

### 3. HEXOSOMES AND CUBOSOMES BASED IMAGING AGENTS FOR *IN VITRO* APPLICATIONS

Cubosomes and hexosomes are versatile NPs and their use has been suggested for various pharmaceutical applications (see, for example, Refs. [98–102]). However, a limited number of papers have been reported so far describing their use for *in vitro* imaging purposes and, in particular, most of the work has been devoted to fluorescence imaging. Indeed, fluorescence is a useful technique that allows for high spatial and time resolution, it is simple and relatively economic, and it is compatible with live cells [103–108].

When designing a fluorescent probe one of the most important aspect is its prompt internalization in cells, as well as its low cytotoxicity. For these reasons the internalization of fluorescent dyes in biocompatible NPs (such as cubosomes and hexosomes) or the labelling of the latter is of high interest.

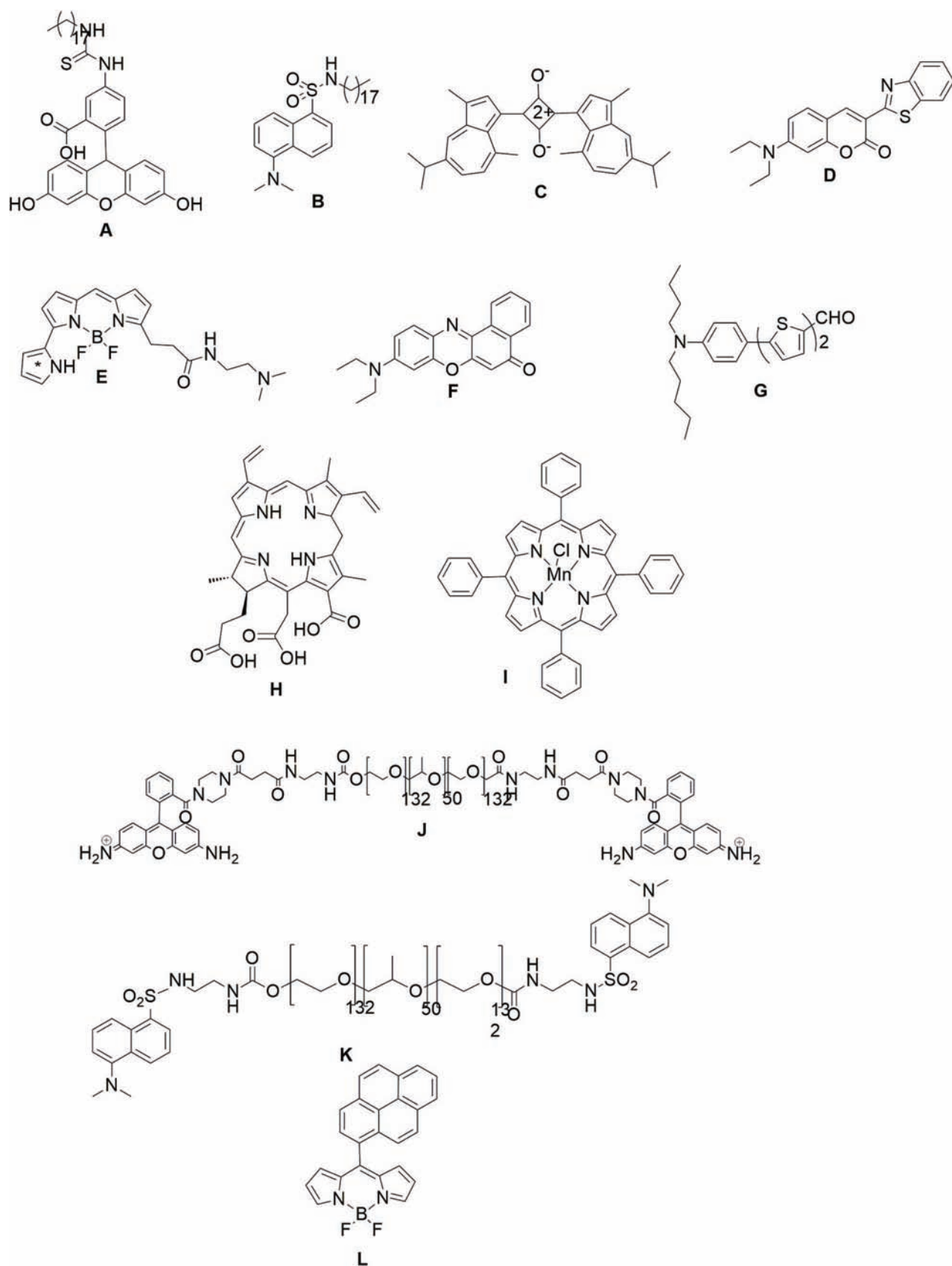


**Figure 3.** Molecular structures of fluorescent probes described in the section above.

As previously stated, most of the cubosomes formulations exploit monoolein (MO) or phythantriol (PHY) as molecular building blocks. For that reason, this paragraph was organized treating separately MO-based and PHY-based non-lamellar NPs.

Relatively few examples of MO-based cubosomes stabilized with Pluronic F108 (PF108) and loaded with different types of fluorophores and drugs were reported. The hydrophobicity of the fluorophore and/or the drug is an essential issue, in order to successfully encapsulate fluorescent probes in the lipid bilayer of the cubosomes. Commercial fluorophores can be functionalized to increase their hydrophobicity, such as fluorescein isothiocyanate and

dansyl chloride derivatized with octadecylamine (**A** and **B**, respectively in Fig. 3) [109].

The cubosomes formulations were also loaded with quercetin, a naturally occurring hydrophobic polyphenolic compound with antioxidant and anticancer activity (**A** in Fig. 4). The formulations containing **A** were successfully internalized in 3T3 fibroblast cells. A diffuse fluorescence was detected in the cytosol and, particularly, in the perinuclear region of living cells after 3 h incubation.

In order to specifically address the NPs towards cancer cells the MO-based cubosomes could be targeted with folic acid, FA (**B**, Fig. 4), since folate receptors are over-expressed on various cancer cells membrane. The targeting

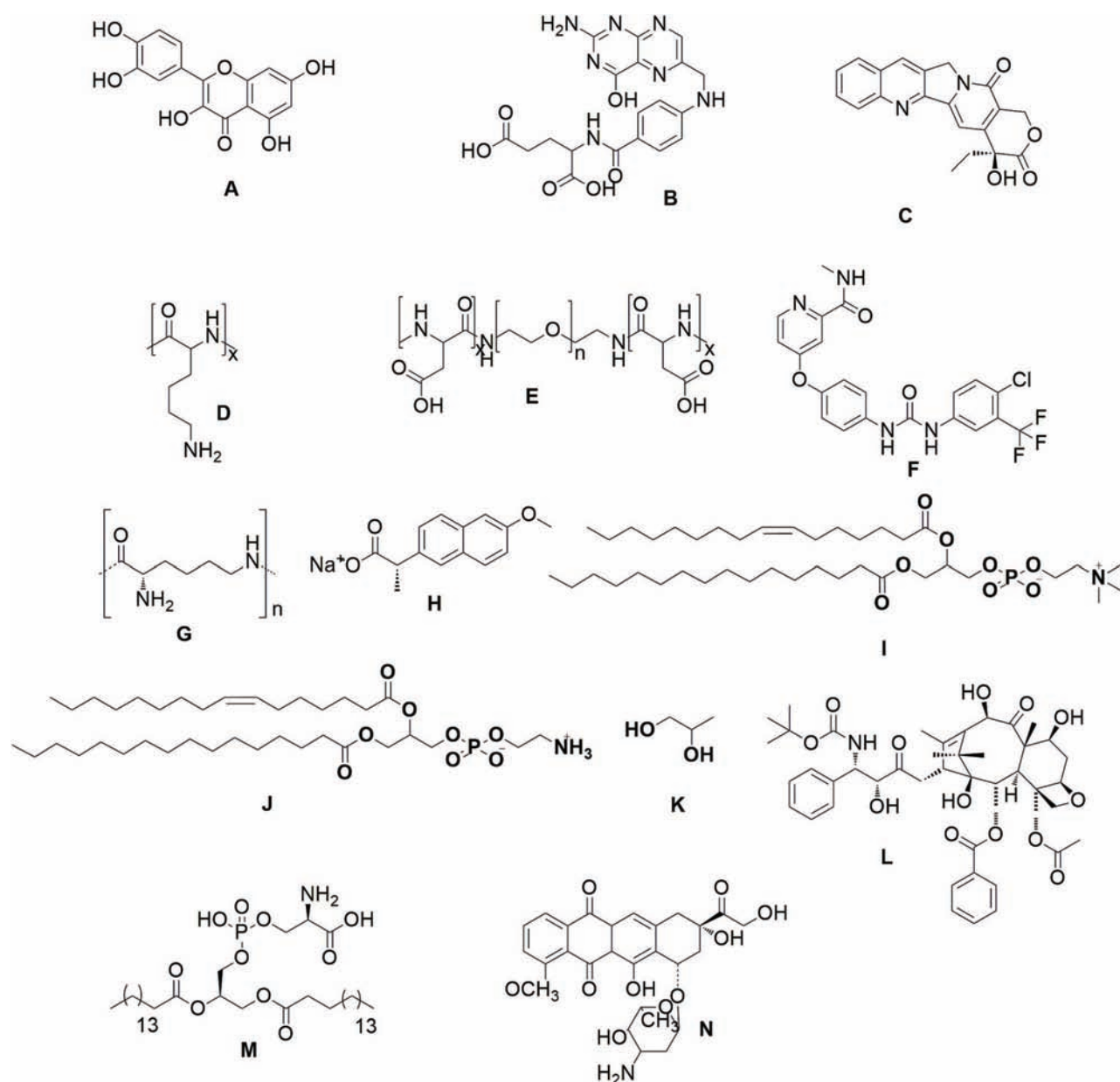


**Figure 4.** Molecular structures of drugs, targeting agents and stabilizers mentioned in the paragraph.

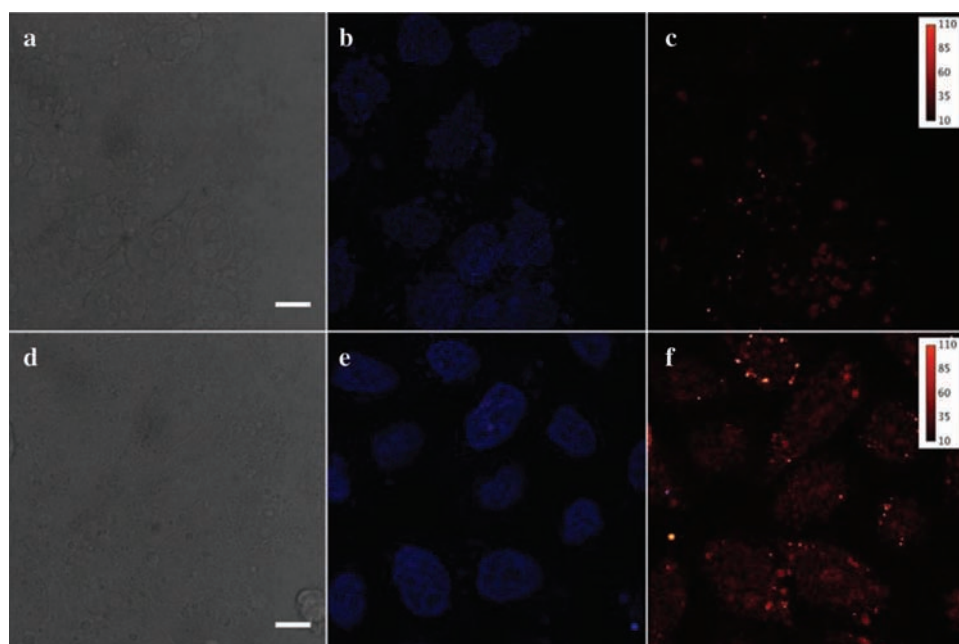


**Figure 5.** Fluorescence microscopy images of HeLa cells treated with probe **C** (a–c) or cubosomes loaded with **C** (d–f). (a, d) Transmission micrographs of cells; scale bar = 10  $\mu\text{m}$ . (b, e) Fluorescence micrographs collected in the 420–480 nm interval where nuclear marker Hoechst emits. (c, f) Fluorescence micrographs collected at >680 nm. Reproduced with permission from [54], Caltagirone, C., et al., **2014**. Cancer-cell-targeted theranostic cubosomes. *Langmuir*, 30(21), pp.6228–6236. Copyright@ACS 2014.

was achieved by conjugating folic acid on the stabilizer PF108 and preparing the cubosomes dispersion using a mixture of PF108/PF108-FA 80:20 [54]. Cubosomes were also loaded with a commercially available near infrared emitting squarain (2,4-di-3-guaiazulenyl-1,3-dihydroxycyclobutenediylum dihydroxide bis(inner salt, **C**, Fig. 3) and camptothecin (**C**, Fig. 4), an anticancer drug [54]. The effective internalization of the formulation in cancer HeLa cells was observed using confocal microscopy. As reported in Figure 5, the dye-treated cells displayed a bright cell-wide emission background and large emitting perinuclear spots that were not observed in the control experiments.

In this paper, the selective cellular uptake was evaluated via integrated optical density (IOD) analysis by evaluating the growth of lipid droplets (LD) in HeLa cells after treatments with targeted and non-targeted cubosomes: at 4 h incubation a superior ability of the targeted NPs to enter cancer cells was highlighted.

An interesting MO-based cubosomes formulation with low hemolytic activity for human hepatocellular carcinoma cells (HepG2) imaging was described by Thapa et al. [40]. Cubosomes were coated by layers of poly-L-lysine (**D** in Fig. 4) and poly(ethylene glycol)-bpoly(aspartic acid) (**E** in Fig. 4) and loaded with Sorafenib (**F** in Fig. 4), an FDA-approved drug for systemic treatment of

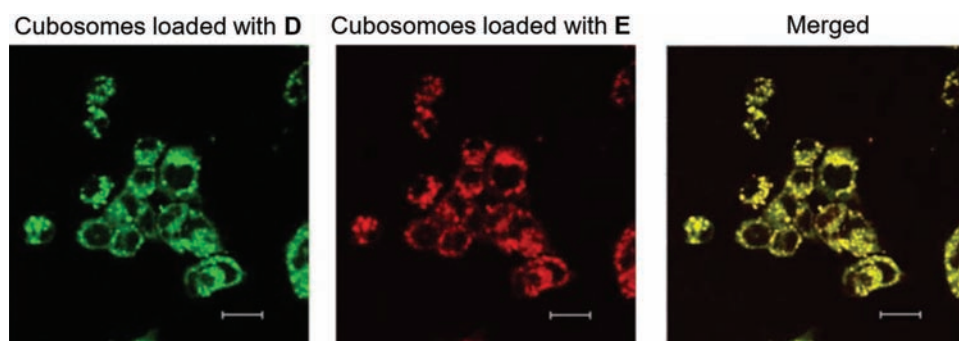


**Figure 6.** Intracellular uptake of cubosomes determined by confocal laser scanning microscopy in HepG2 cells (scale bar, 20  $\mu\text{m}$ ). Cubosomes loaded with fluorophores **D** (green) and **E** (red) were used for the experiment. Adapted with permission from [40], Thapa, R.K., et al., **2015**. Multilayer-coated liquid crystalline nanoparticles for effective sorafenib delivery to hepatocellular carcinoma. *ACS Applied Materials and Interfaces*, 7(36), pp.20360–20368. Copyright@ACS 2015.

hepatocellular carcinoma and coumarin-6 or LysoTracker Red (**D** and **E** in Fig. 3, respectively) as probes. As shown by confocal laser microscopy experiments (Fig. 6), cubosomes were localized in lysosomes, which are organelles that exist at pH 4.5–5.0. It was demonstrated that Sorafenib release from the proposed formulation was more efficient at acidic pHs, and thus lysosomes uptake should enhance the drug release leading to beneficial antitumoral effects.

Kumaraswamy and Singh demonstrated that a MO-based cubosomes coated with layer of  $\epsilon$ -lysine (**G** in Fig. 4) and loaded with sodium Naproxen (**H** in Fig. 4) were able to decrease the drug release rate compared

to uncoated cubosomes [53]. Moreover, both coated and uncoated cubosomes loaded with Nile Red (**F** in Fig. 3) showed strong red fluorescence in HeLa cells after 4 h of incubation. Analysis by confocal microscopy confirmed that cubosomes were effectively internalized and not only adsorbed on the cell surface as most of the Nps were observed between 15 and 30  $\mu\text{m}$  in  $z$  axis scans.

Recently, cubosomes formulation was adopted for the *in vitro* imaging of  $\beta$ -cells. These cells are of particular interest as they are responsible for the production of insulin in pancreas and they are destroyed in Type-1

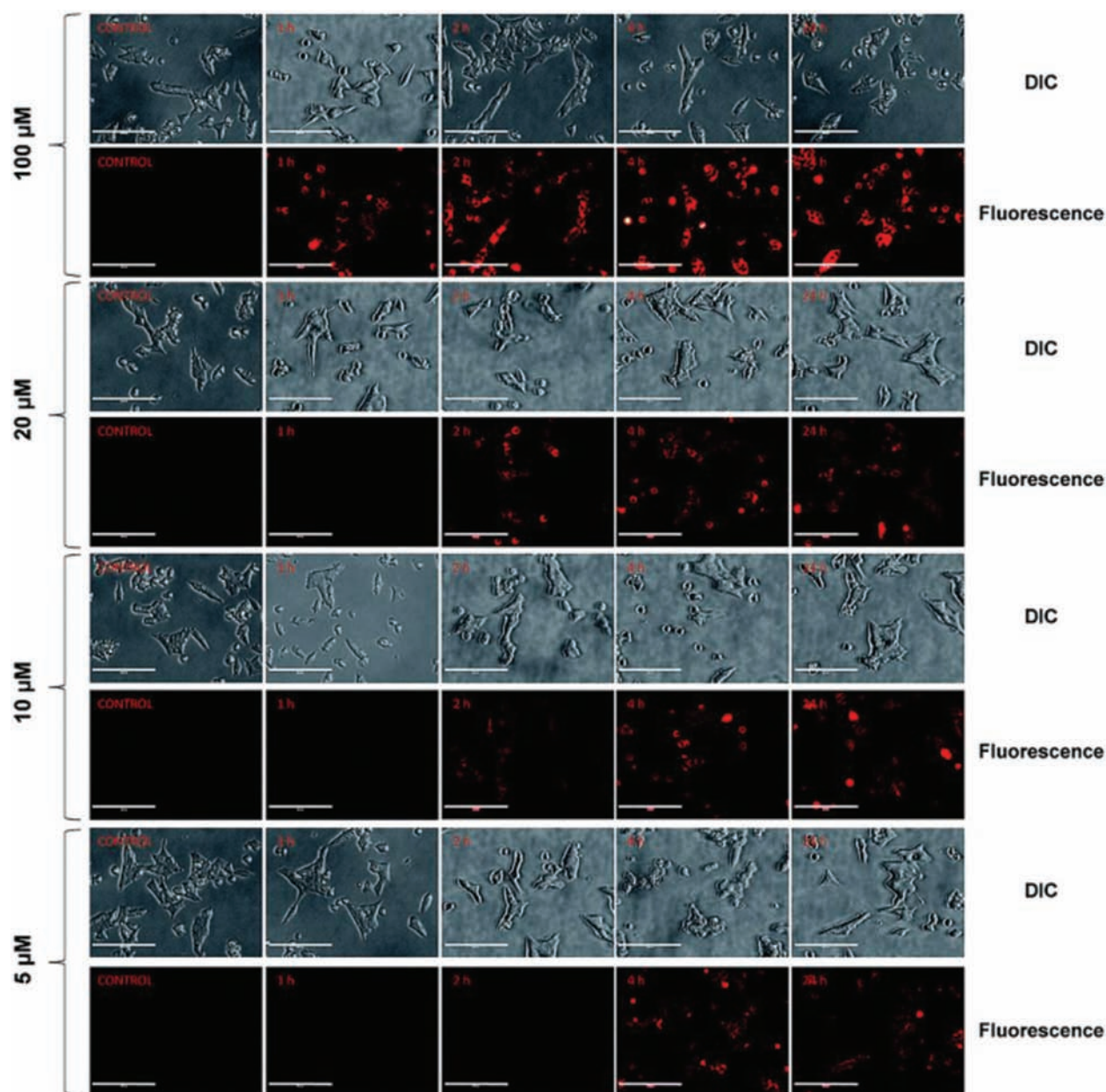


**Figure 7.** *In vitro* imaging of INS-1E cells incubated with or without (control) 5, 10, 20, and 100  $\mu\text{M}$  NPs for 1, 2, 4, and 24 hours. Scale bar corresponds to 10  $\mu\text{m}$ . Adapted from [110], Miceli, V., et al., 2016. *In vitro* imaging of  $\beta$ -cells using fluorescent cubic bicontinuous liquid crystalline nanoparticles. *RSC Advances*, 6(67), pp.62119–62127. Copyright@RSC 2016.

diabetes patients. The MO-based cubosomes loaded with the non-commercial fluorophore (**G** in Fig. 3) were easily internalized by rat pancreatic  $\beta$ -cells (INS-1E). Interestingly, using a probe with a high quantum yield, it was possible to image the cells even at nanomolar concentration of the dye (Fig. 7) [110].

Murgia, Bazylińska and co-workers recently proposed a polymer-free cubosomes dispersion based on MO, phospholipids (**I** and **J** in Fig. 4) as stabilizers, and propylene glycol (**K** in Fig. 4) as hydrotrope. Cubosomes were loaded with the photosensitizers  $Ce_6$  (**H** in Fig. 3) and TPP-Mn (**I** in Fig. 3), selected as delivery vehicles for photodynamic therapy (PDT) [85]. The loaded cubosomes have been tested on malignant melanoma cells derived from lymph node metastasis of skin melanoma (Me45) and melanoma granular fibroblasts (MeWo). Results showed that encapsulated photosensitizer **H** caused over 90% reduction of both Me45 and MeWo cells viability after irradiation. Interestingly, the observed photodynamic action of encapsulated **H** was higher than that of the free photosensitizer tested in a concentration one order of magnitude higher (Fig. 8). On the other hand, photosensitizer **I** showed low cytotoxicity towards both melanoma cell lines tested.

Very recently it was demonstrated an increase in the cellular uptake of fluorescent squaramides when loaded in MO-based cubosomes formulations [111].

With the aim to increase both the concentration of the imaging agent in the NPs and the colloidal stability of the formulation, the innovative strategy of decorating the surface of the cubosomes with a fluorophore by conjugation

to the stabilizer PF108 was recently adopted. Murgia and co-workers prepared targeted theranostic platforms using the commercial block copolymer PF108 and its folate- and rhodamine-conjugated (**J** in Fig. 3) [61] counterparts in a 60/20/20 (wt%) mixture. HeLa cells uptake after 4 h incubation was demonstrated by fluorescent microscopy. A diffuse cytoplasmatic fluorescence was observed in treated cells suggesting cubosomes internalization. Cubosomes were also loaded with Docetaxel (**L** in Fig. 4), one of the most effective anticancer drugs; an increase in its cytotoxicity was demonstrated when it was administrated to HeLa cells via cubosomes. The strategy of decorating cubosomes with the fluorophore was also adopted using PF108 conjugated with dansyl (**K** in Fig. 3), and the *in vitro* imaging on HeLa cells was also demonstrated [112].

PHY-based cubosomes were prepared by Shen and co-workers [113] incorporating 1,2-dihexadecanoyl-sn-glycero-3-phospho-L-serine (**M** in Fig. 4), a derivative of phosphatidylserine (PS), one of the most abundant anionic lipids in the plasma membrane of eukaryotic cells. This molecule is normally confined in cytoplasm, but it is translocated outside the cell membrane in apoptotic cells. Cubosomes targeted with rhodamine-labelled Annexin V (ANX), a protein able to detect phosphatidylserine, and stabilized with Pluronic F127 (PF127) were successfully internalized in HeLa cells stained with plasma membrane green fluorescent protein (PM-GFP) and a red fluorescence on the surface of the apoptotic cell due to rhodamine-loaded cubosomes was observed.

In a more recent paper the same authors described the possibility to apply such cubosomes formulation and the

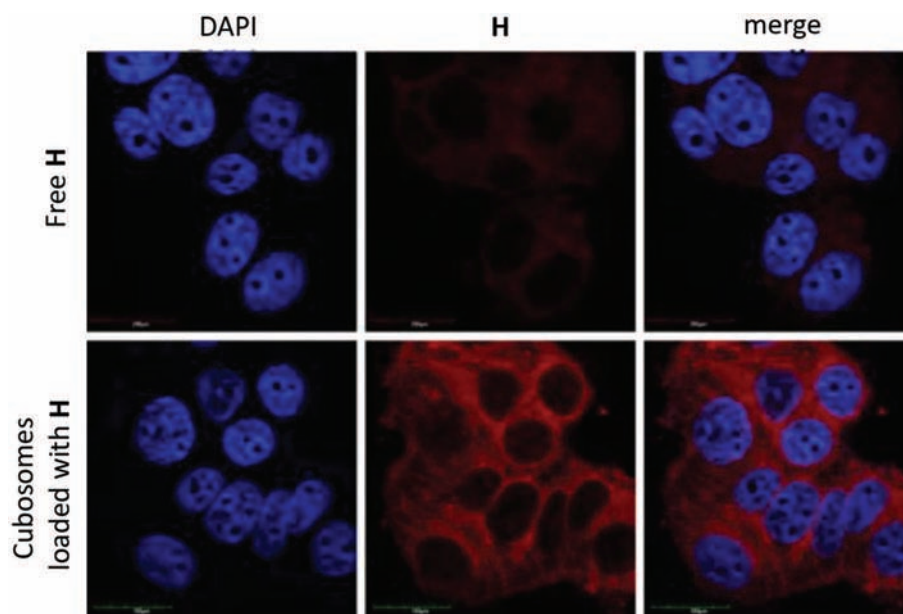


**Figure 8.** Intracellular distribution of photosensitizer **H** delivered with cubosomes stabilised by phospholipids and propylene glycol to the MeWo melanoma cells. DAPI = 4',6-diamidino-2-phenylindole. Adapted with permission from [85], Bazylińska, U., et al., 2018. Polymer-free cubosomes for simultaneous bioimaging and photodynamic action of photosensitizers in melanoma skin cancer cells. *Journal of Colloid and Interface Science*, 522, pp.163–173. Copyright@Elsevier 2018.

analogous MO-based formulation as drug delivery for eyes diseases [114]. Confocal microscopy experiments were carried out to demonstrate the cellular uptake of cubosomes on HeLa cells. It was demonstrated that MO-based cubosomes were not internalized, while the PHY containing formulations were able to penetrate the cell membrane.

To the best of our knowledge, even fewer examples on the use of hexosomes for *in vitro* imaging have been reported so far in the literature. The possible theranostic applications of hexosomes prepared with MO and oleic acid and stabilized with a mixture of PF108 and folate-conjugated PF108 in 80/20 (% wt) mixture was described [115]. Hexosomes were loaded with a pyrene-substituted BODIPY dye (**L** in Fig. 3) and camptothecin (**C** in Fig. 4). Uptake in HeLa cells after 4 h incubation was highlighted (Fig. 9(A)) and demonstrated by colocalization studies with LipidTox dye that after the internalization the hydrophobic fluorophore **L** is released from the hexosomes and localized within the lipid droplets (Fig. 9(B)).

The same approach of decorating the surface of the NPs with the fluorophore (instead of encapsulating it within the lipid bilayer) described above for cubosomes, was successfully realized also for hexosomes [116]. The proposed formulation was prepared using the stabilizer **J** in Figure 3. The effective internalization in HeLa cells was demonstrated by fluorescent microscopy.

Very recently Nazaruk, Gavel and co-workers evaluated the efficiency of drug delivery to cancer cell lines KB, HeLa and T98G by folate-targeted MO-based cubosomes

and MO/tetradecane based hexosomes, loaded with the anticancer drug doxorubicin, DOX (**N** in Fig. 4). The intracellular accumulation rate of different nanocarriers was evaluated by fluorescence and confocal microscopy techniques [117]. The presence of the folate caused an increase of the doxorubicin intake in KB and HeLa cells incubated for 2 h with DOX loaded NPs. The highest drug accumulation in KB and HeLa cells was noticed when folate functionalized DOX loaded cubosomes were internalized while, in the case of folate-targeted hexosomes, DOX intake was lower compared to cubosomes. No changes for the T98G cells were observed for the folate functionalized NPs loaded with doxorubicin compared with the same NPs without folate. Confocal microscopy of the KB, HeLa and T98G cells stained with Phalloidin-fluorescein isothiocyanate incubated for 2 hours with targeted and no-targeted cubosomes and hexosomes loaded with DOX confirmed the highest intracellular accumulation for the drug loaded targeted nanocarrier. Such results are in accordance with previously published studies in which has been described the higher drug delivery capabilities of cubosomes compared to hexosomes [118].

#### 4. HEXOSOMES AND CUBOSOMES BASED IMAGING AGENTS FOR *IN VIVO* APPLICATIONS

The progressive breakthroughs in nanomedicine have supported the development of multifunctional and multimodal NPs that can simultaneously provide imaging contrast, target specific cells, and deliver large

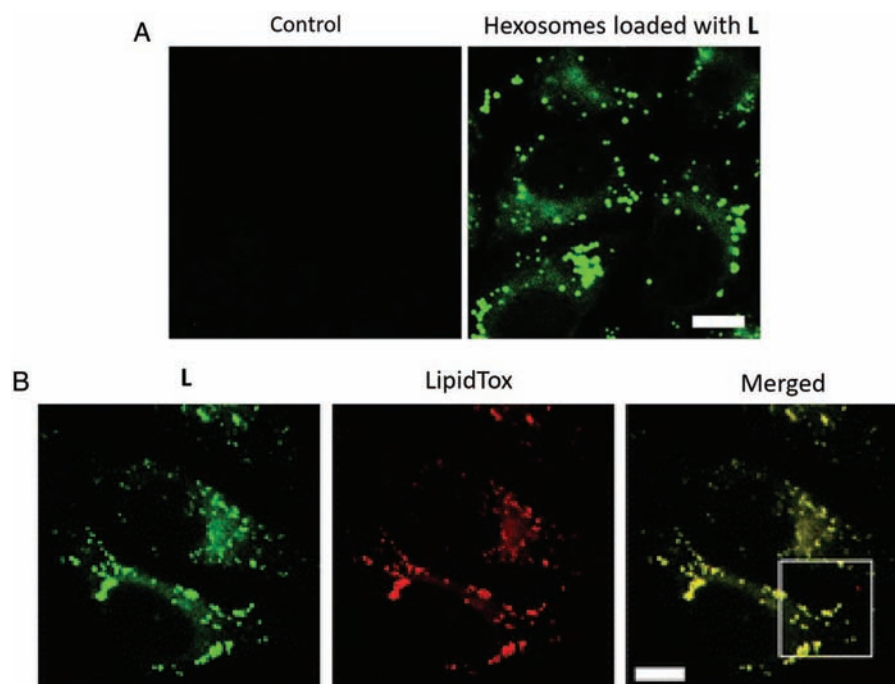


**Figure 9.** Schematic representation of the *in vivo* imaging approaches described in this paragraph.



payloads of drugs impacting the diagnostic and therapeutic strategies [119–121]. In particular, besides storing multiple drug payloads within the NPs core, the conjugation of targeting moieties for specific ‘molecular recognition’ confers an overall improved efficacy, minimizing off-target toxicity [120]. Moreover, the development of multifunctional NPs allows the design of nanoprobes containing more than one-modality-specific contrast agent [119]. Consequently, although therapy was the first medical application of NPs, it has been soon recognized that nanomaterials hold great promise for diagnostic/imaging purposes. Furthermore, based on their ability to encapsulate imaging and therapeutic modalities within a single formulation, NPs hold the greatest promise in the design of theranostic agents for next-generation personalized medicine.

Therapeutic delivery, especially for cancer therapeutics, is to date the key biomedical application of cubosomes and despite numerous *in vitro* examples of hexosomes and cubosome-based drug formulations, the goal of effective *in vivo* imaging applications remains limited [67]. So far, only a few cubosome formulations that provide effective *in vivo* Magnetic Resonance Imaging (MRI) and/or fluorescence contrast enhancement have been reported. In this chapter these imaging approaches will be briefly introduced, and the formulations reported in the literature will be described (Fig. 10).

#### 4.1. Magnetic Resonance Imaging

MRI contrast agents are used clinically to optimize contrast and allow distinguishing more easily healthy tissue from diseased tissue. For instance, contrast-enhanced MRI is an established imaging method for the identification of focal liver lesion compared to normal liver parenchyma [122]. MRI provides anatomical images by measuring the longitudinal and transverse proton ( $^1\text{H}$ ) relaxation times (namely T1 and T2) of water and biological tissues. Clinical contrast agents vary in their properties and consist of either paramagnetic gadolinium ( $\text{Gd}^{3+}$ ) or manganese ( $\text{Mn}^{2+}$ ) chelates, or superparamagnetic iron oxide (SPIO) and ultra-small superparamagnetic iron oxide (USPIO) NPs that catalytically shorten the relaxation times of bulk water protons. Paramagnetic chelates decrease the water spin-lattice relaxation time (T1), consequently showing positive contrast where they are localized, and are referred to as T1 agents. In contrast to paramagnetic chelates, iron oxide NPs decrease the water spin-spin relaxation time (T2), exhibit negative contrast where they are localized, and are referred to as T2 agents.

In recent years, nitroxides have been identified as a promising candidate for MRI contrast agents as they present a paramagnetic electron that enables the shortening of the T1 and T2 of protons. Nitroxide containing LLC NPs have been investigated because of (i) the nitroxide lipid ability to decrease T1 relaxation time that results in

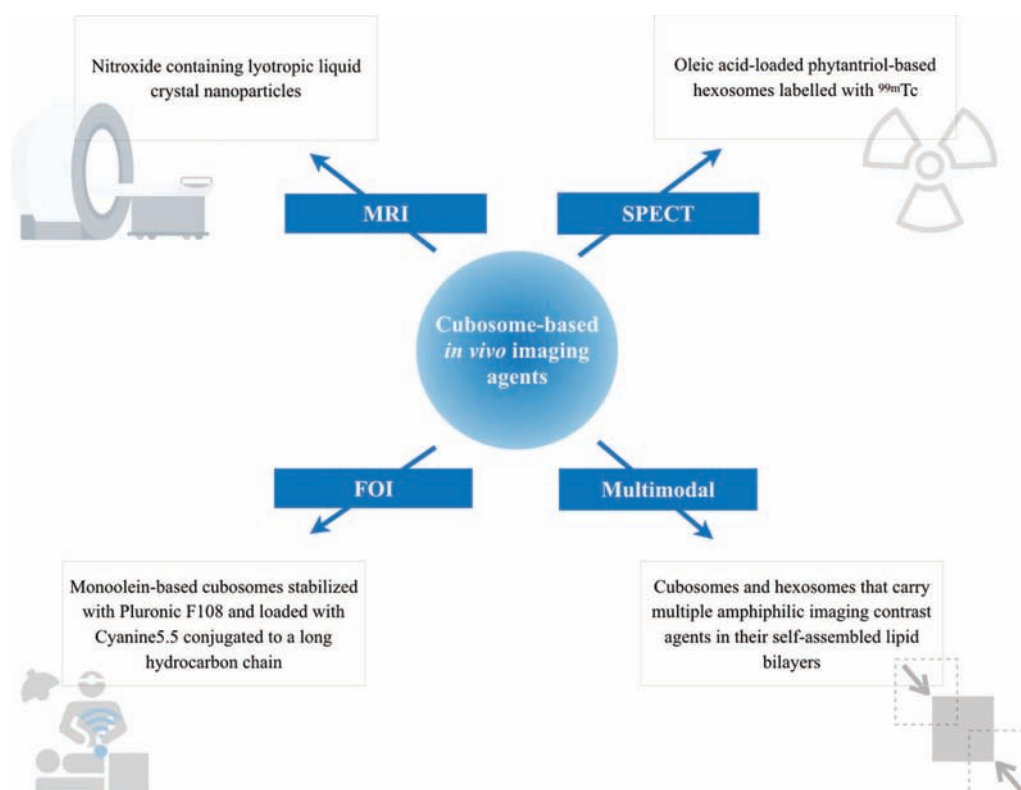


**Figure 10.** Molecular structures of drugs, targeting agents and stabilizers mentioned in the paragraph.

brightening of T1 weighted MRI images; (ii) the potential to function as an MRI contrast agent without containing potentially hazardous heavy metals such as gadolinium; and (iii) the ability to manipulate their physical, chemical, and biological properties to inhibit opsonin binding, enhance bloodstream retention and also protect the nitroxide from reduction [64]. In particular, previous results showed that NPs were better tolerated in cells and live animals when Myverol (a food emulsifier rich in monoacylglycerols) was used as stabilizer. T1 weighted contrast in the liver was rapidly detected after injection, on the contrary negligible contrast was observed in the kidneys over time. A successive study describes a small library of nitroxide lipids with varying tail chemistries, which confer excellent MRI contrast and pharmacokinetic properties to the construct while preserving nitroxide stability [123].

#### 4.2. Single Photon Emission Computed Tomography

Single Photon Emission Computed Tomography (SPECT) relies on the radioactive decay of the gamma-emitting radionuclides administered, e.g., technetium-99m ( $^{99m}\text{Tc}$ ), indium-111 ( $^{111}\text{In}$ ), and iodine-123 ( $^{123}\text{I}$ ). SPECT is one of the two major molecular imaging modalities used in nuclear medicine, and the other is the Positron Emission Tomography (PET) [124]. Among the medical imaging modalities, nuclear imaging provides a unique quantitative potential to measure physiology and biochemical processes and it is often combined with Computer Tomography (CT) that uses X-rays to provide complementary anatomical information. The PET maintains a considerable advantage over SPECT in terms of detection efficiency and spatial resolution. However, the quantitative SPECT imaging holds promise due to its intrinsic advantages compared to PET, due to: (i) the possibility of combining different radionuclides to perform multi-tracer studies simultaneously; (ii) longer half-lives of radionuclides; (iii) radiotracers are readily available and do not require relatively proximity to a medical cyclotron, and (iv) lower cost of the imaging systems.

Nilsson and colleagues have developed a surface chelation method to provide a successful tool for the radiolabeling of oleic acid-loaded phytantriol-based hexosomes, with the  $^{99m}\text{Tc}$  labeling reaction taking place at room temperature [125]. Oleic acid was introduced to provide an accessible carboxylic acid functional group, which facilitated the formation of a conjugate between the hexosomes and the chelating agent SPMTrien. Radiolabeled hexosomes displayed high stability *in vivo* and accumulated in the subcutaneous adipose tissue upon subcutaneous injection, therefore showed high potential as a SPECT imaging agent for the assessment of response to anti-obesity drug treatment.

#### 4.3. Fluorescence Optical Imaging

Fluorescence Optical imaging (FOI) is an emerging imaging modality with high potential for intraoperative

image-guided surgery and endoscopic applications [119, 126]. FOI relies on non-ionizing radiation and uses fluorescent lighting sources to obtain images of organs and tissues. This technique uses exogenous agents relying on the spectral properties of specific probes to improve the signal obtained from endogenous sources of fluorescence and achieve high-contrast imaging.

The first proof of principle for FOI application was provided using fluorescent MO-based cubosomes stabilized with Pluronic F108 and loaded with Cyanine5.5 conjugated to a long hydrocarbon chain. This formulation enabled non-invasive optical imaging in a healthy mouse animal model and following a lifetime analysis approach it was possible to distinguish between cubosome fluorescence and free dye fluorescence (Fig. 11) [126].

#### 4.4. Multimodal Imaging

The imaging modalities currently available vary in sensitivity, spatial/depth resolution and quantitative potential, with each modality having its unique strength and intrinsic limitations. Multi-modality imaging, which involve the incorporation of two or more imaging modalities, has the potential to overcome the inherent limitations of each imaging modality, and allows integration of the strengths of individual modalities. Consequently, multimodal imaging is a central task for clinical imaging research and is bringing together scientists from the far-ranging fields of molecular pharmacology to materials engineering and nanotechnology.

Recently, cubosomes and hexosomes that carry multiple amphiphilic imaging contrast agents in their self-assembled lipid bilayers were developed for dual-modal

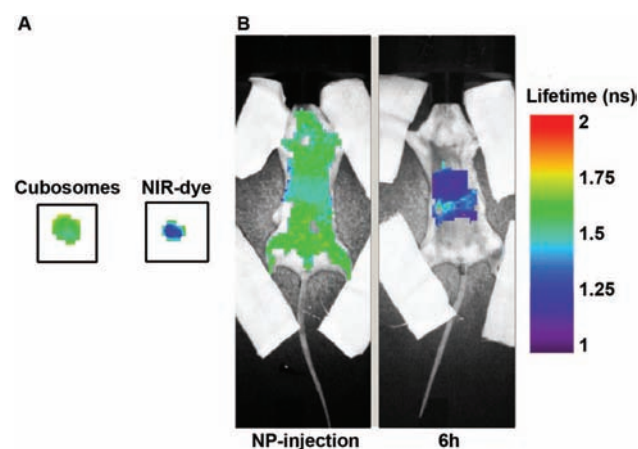


**Figure 11.** Time domain (TD) fluorescence optical imaging analysis of: (A) Equimolar aliquots of the Cy5.5 labeled cubosome formulation and the control NIR-dye; (B) a healthy mouse that received an intravenous injection of the Cy5.5 labeled cubosome formulation. Images were taken a few minutes and 6 h after the injection. For the fluorescence image acquisition a manually-selected region of interests (ROI) encompassing the sample or the mouse whole body was scanned and fluorescence lifetime map was created from temporal point-spread function data acquired using the TD-FOI imaging system.

imaging, and their contrast enhancement efficacy was evaluated combined with biodistribution *in vivo* [62]. FOI *in vivo* showed accumulation of both cubosomes and hexosomes in the liver and spleen of mice up to 20 hours post-injection. Furthermore, *in vivo* MRI data of animals injected with either cubosomes or hexosomes displayed enhanced contrast in the liver and spleen. Of note, the mesophase (i.e., cubic or hexagonal) affected the biodistribution of the NPs formulations. In particular, hexosomes showed higher accumulation in the spleen than the liver compared to cubosomes. Overall, this dual MRI/fluorescent contrast agent has the flexibility to provide unlimited depth penetration, high spatial resolution (based on MRI analysis) and high sensitivity typical of FOI.

## 5. CONCLUSIONS

Ongoing research on cubosomes and hexosomes has validated the high potential of these formulations as advanced bioimaging platforms. Actually, numerous studies showed the possibility of encapsulating (also simultaneously) different types of pharmaceutically active molecules and imaging probes within such non-lamellar lyotropic liquid crystalline nanoparticles, as well as decorating their surface with suitable targeting agents. Furthermore, *in vitro* tests evidenced some aspects of the interactions of these nanoparticles with the cellular machinery, shedding some light on the mechanism at the basis of the cellular internalization. Remarkably, interesting results were achieved when non-commercially available imaging probes were employed, demonstrating the fundamental role of synthetic chemistry in the development of multifunctional nanoparticles. However, as highlighted by this review, only few *in vivo* experiments were performed so far, limiting the translation of cubosomes and hexosomes from laboratories to clinical practice. Therefore, a lot of work still needs to be done to enable the effective use of cubosomes and hexosomes formulations as routine imaging tools in clinics.

**Acknowledgments:** The Authors thank Fondazione Banco di Sardegna and Regione Autonoma della Sardegna (Progetti Biennali di Ateneo Annualità 2016). Claudia Caltagirone, Vito Lippolis and Giacomo Picci thank MIUR for PRIN project 2017EKCS35\_003.

## References and Notes

- Larsson, K., **1989**. Cubic lipid-water phases: Structures and biomembrane aspects. *Journal of Physical Chemistry*, 93(21), pp.7304–7314.
- Larsson, K., **2000**. Aqueous dispersions of cubic lipid-water phases. *Current Opinion in Colloid and Interface Science*, 5(1–2), pp.64–69.
- Hyde, S.T., **1996**. Bicontinuous structures in lyotropic liquid crystals and crystalline hyperbolic surfaces. *Current Opinion in Solid State and Materials Science*, 1(5), pp.653–662.
- Hyde, S.T., **1989**. Microstructure of bicontinuous surfactant aggregates. *Journal of Physical Chemistry*, 93(4), pp.1458–1464.
- Angius, R., Murgia, S., Berti, D., Baglioni, P. and Monduzzi, M., **2006**. Molecular recognition and controlled release in drug delivery systems based on nanostructured lipid surfactants. *Journal of Physics: Condensed Matter*, 18(33), pp.S2203–S2220.
- Israelachvili, J.N., Mitchell, D.J., Ninham, B.W., Israelachvili, J.N., Mitchell, D.J. and Ninham, B.W., **1976**. Theory of self-assembly of hydrocarbon amphiphiles into micelles and bilayers view online. *J. Chem. Soc., Faraday Trans. 2*, 72, pp.1525–1568.
- Mitchell, D.J. and Ninham, B.W., **1981**. Micelles, vesicles and microemulsions. *J. Chem. Soc., Faraday Trans. 2*, 77, pp.601–629.
- Shearman, G.C., Ces, O., Templer, R.H. and Seddon, J.M., **2006**. Inverse lyotropic phases of lipids and membrane curvature. *Journal of Physics Condensed Matter*, 18(28), pp.S1105–S1124.
- Pitzalis, P., Monduzzi, M., Krog, N., Larsson, H., Ljusberg-Wahren, H. and Nylander, T., **2000**. Characterization of the liquid-crystalline phases in the glycerol monooleate/diglycerol monooleate/water system. *Langmuir*, 16(15), pp.6358–6365.
- Murgia, S., Caboi, F. and Monduzzi, M., **2001**. Addition of hydrophilic and lipophilic compounds of biological relevance to the monoolein/water system II-13C NMR relaxation study. *Chemistry and Physics of Lipids*, 110, pp.11–17.
- Monduzzi, M., Lampis, S., Murgia, S. and Salis, A., **2014**. From self-assembly fundamental knowledge to nanomedicine developments. *Advances in Colloid and Interface Science*, 205, pp.48–67.
- Helfrich, W., **1994**. Lyotropic lamellar phases. *Journal of Physics: Condensed Matter*, 6(23A), pp.A79–A92.
- Larsson, K., Fontell, K. and Korg, N., **1980**. Structural relationships between lamellar, cubic and hexagonal phases in monoglycerides-water systems. Possibility of cubic structures in biological systems. *Chemistry and Physics of Lipids*, 27, pp.321–328.
- Amar-Yuli, I., Wachtel, E., Shoshan, E.B., Danino, D., Aserin, A. and Garti, N., **2007**. Hexosome and hexagonal phases mediated by hydration and polymeric stabilizer. *Langmuir*, 23(7), pp.3637–3645.
- Fong, C., Le, T. and Drummond, C.J., **2012**. Lyotropic liquid crystal engineering-ordered nanostructured small molecule amphiphile self-assembly materials by design. *Chemical Society Reviews*, 41(3), pp.1297–1322.
- Murgia, S., Lampis, S., Zucca, P., Sanjust, E. and Monduzzi, M., **2010**. Nucleotide recognition and phosphate linkage hydrolysis at a lipid cubic interface. *Journal of the American Chemical Society*, 132(45), pp.16176–16184.
- Hyde, S.T., **1995**. On swelling and structure of composite materials. Some theory and applications of lyotropic mesophases. *Colloids and Surfaces A: Physicochemical and Engineering Aspects*, 103(3), pp.227–247.
- Hyde, S.T., Andersson, S., Ericsson, B. and Larsson, K., **1984**. A cubic structure consisting of a lipid bilayer forming an infinite periodic minimum surface of the gyroid type in the glycerolmonooleat-water system. *Z. Kristall.*, 168, pp.213–219.
- Hyde, S., Ninham, B.W., Andersson, S., Larsson, K., Landh, T., Blum, Z. and Lidin, S., **1997**. The Language of Shape. Elsevier.
- Deng, Y., Marko, M., Buttle, K.F., Leith, A., Mieczkowski, M. and Mannella, C.A., **1999**. Cubic membrane structure in amoeba (*Chaos carolinensis*) mitochondria determined by electron microscopic tomography. *Journal of Structural Biology*, 127(3), pp.231–239.
- Almshergqi, Z.A., Kohlwein, S.D. and Deng, Y., **2006**. Cubic membranes: A legend beyond the Flatland\* of cell membrane organization. *Journal of Cell Biology*, 173(6), pp.839–844.
- Almshergqi, Z., Hyde, S., Ramachandran, M. and Deng, Y., **2008**. Cubic membranes: A structure-based design for DNA uptake. *Journal of the Royal Society Interface*, 5 pp.1023–1029.

23. Almsherqi, Z., Landh, T., Kohlwein, S.D. and Deng, Y., **2009**. Cubic membranes: The missing dimension of cell membrane organization. *International Review of Cell and Molecular Biology*, 274, pp.275–342.
24. Xiao, Q., Wang, Z., Williams, D., Leowanawat, P., Peterca, M., Sherman, S.E., Zhang, S., Hammer, D.A., Heiney, P.A., King, S.R., Markovitz, D.M., Andre, S., Gabius, H., Klein, M.L. and Percec, V., **2016**. Why do membranes of some unhealthy cells adopt a cubic. *ACS Central Science*, 2, pp.943–953.
25. Immordino, M.L., Dosio, F. and Cattel, L., **2006**. Stealth liposomes: Review of the basic science, rationale, and clinical applications, existing and potential. *International Journal of Nanomedicine*, 1(3), pp.297–315.
26. Etheridge, M.L., Campbell, S.A., Erdman, A.G., Haynes, C.L., Wolf, S.M. and McCullough, J., **2013**. The big picture on small medicine: The state of nanomedicine products approved for use or in clinical trials. *Nanomedicine*, 9(1), pp.1–14.
27. Neto, C., Aloisi, G., Baglioni, P. and Larsson, K., **1999**. Imaging soft matter with the atomic force microscope: Cubosomes and hexosomes. *The Journal of Physical Chemistry B*, 103(19), pp.3896–3899.
28. Boyd, B.J., Whittaker, D.V., Khoo, S.M. and Davey, G., **2006**. Hexosomes formed from glycerate surfactants-Formulation as a colloidal carrier for irinotecan. *International Journal of Pharmaceutics*, 318(1–2), pp.154–162.
29. Gustafsson, J., Ljusberg-Wahren, H., Almgren, M. and Larsson, K., **1996**. Cubic lipid-water phase dispersed into submicron articles. *Langmuir*, 12(20), pp.4611–4613.
30. Gustafsson, J., Ljusberg-Wahren, H., Almgren, M. and Larsson, K., **1997**. Submicron particles of reversed lipid phases in water stabilized by a nonionic amphiphilic polymer. *Langmuir*, 13(6), pp.6964–6971.
31. Murgia, S., Falchi, A.M., Mano, M., Lampis, S., Angius, R., Carnerup, A.M., Schmidt, J., Diaz, G., Giacca, M., Talmon, Y. and Monduzzi, M., **2010**. Nanoparticles from lipid-based liquid crystals: Emulsifier influence on morphology and cytotoxicity. *Journal of Physical Chemistry B*, 114(10), pp.3518–3525.
32. Landh, T., **1994**. Phase behavior in the system pine oil monoglycerides-poloxamer 407-water at 20 °C. *Journal of Physical Chemistry*, 98, pp.8453–8467.
33. Chong, J.Y.T., Mulet, X., Waddington, L.J., Boyd, B.J. and Drummond, C.J., **2012**. High-throughput discovery of novel steric stabilizers for cubic lyotropic liquid crystal nanoparticle dispersions. *Langmuir*, 28(25), pp.9223–9232.
34. Chong, J.Y.T., Mulet, X., Postma, A., Keddie, D.J., Waddington, L.J., Boyd, B.J. and Drummond, C.J., **2014**. Novel RAFT amphiphilic brush copolymer steric stabilisers for cubosomes: Poly(octadecyl acrylate)-block-poly(polyethylene glycol methyl ether acrylate). *Soft Matter*, 10(35), pp.6666–6676.
35. Johnsson, M., Barauskas, J., Norlin, A. and Tiberg, F., **2006**. Physicochemical and drug delivery aspects of lipid-based liquid crystalline nanoparticles: A case study of intravenously administered propofol. *Journal of Nanoscience and Nanotechnology*, 6, pp.3017–3024.
36. Meli, V., Caltagirone, C., Falchi, A.M., Hyde, S.T., Lippolis, V., Monduzzi, M., Obiols-Rabasa, M., Rosa, A., Schmidt, J., Talmon, Y. and Murgia, S., **2015**. Docetaxel-loaded fluorescent liquid-crystalline nanoparticles for cancer theranostics. *Langmuir*, 31(35), pp.9566–9575.
37. Karami, Z. and Hamidi, M., **2016**. Cubosomes: Remarkable drug delivery potential. *Drug Discovery Today*, 21, pp.789–801.
38. Montis, C., Castroflorio, B., Mendoza, M., Salvatore, A., Berti, D. and Baglioni, P., **2015**. Magnetocubosomes for the delivery and controlled release of therapeutics. *Journal of Colloid and Interface Science*, 449, pp.317–326.
39. Negrini, R., Fong, W.-K., Boyd, B.J. and Mezzenga, R., **2015**. PH-responsive lyotropic liquid crystals and their potential therapeutic role in cancer treatment. *Chemical Communications*, 51(30), pp.6671–6674.
40. Thapa, R.K., Choi, J.Y., Poudel, B.K., Hiep, T.T., Pathak, S., Gupta, B., Choi, H.G., Yong, C.S. and Kim, J.O., **2015**. Multilayer-coated liquid crystalline nanoparticles for effective sorafenib delivery to hepatocellular carcinoma. *ACS Applied Materials and Interfaces*, 7(36), pp.20360–20368.
41. Elmaggar, Y.S.R., Etman, S.M., Abdelmonsif, D.A. and Abdallah, O.Y., **2015**. Novel piperine-loaded Tween-integrated monoolein cubosomes as brain-targeted oral nanomedicine in Alzheimer's disease: Pharmaceutical, biological, and toxicological studies. *International Journal of Nanomedicine*, 10, pp.5459–5473.
42. Gontsarik, M., Buhmann, M.T., Yaghmur, A., Ren, Q., Maniura-Weber, K. and Salentinig, S., **2016**. Antimicrobial peptide-driven colloidal transformations in liquid-crystalline nanocarriers. *Journal of Physical Chemistry Letters*, 7(17), pp.3482–3486.
43. Boge, L., Bysell, H., Ringstad, L., Wennman, D., Umerska, A., Cassisa, V., Eriksson, J., Joly-Guillou, M.-L., Edwards, K. and Andersson, M., **2016**. Lipid-based liquid crystals as carriers for antimicrobial peptides: Phase behavior and antimicrobial effect. *Langmuir*, 32(17), pp.4217–4228.
44. Rodrigues, L., Kyriakos, K., Schneider, F., Dietz, H., Winter, G., Papadakis, C.M. and Hubert, M., **2016**. Characterization of lipid-based hexosomes as versatile vaccine carriers. *Molecular Pharmaceutics*, 13(11), pp.3945–3954.
45. Boge, L., Umerska, A., Matougui, N., Bysell, H., Ringstad, L., Davoudi, M., Eriksson, J., Edwards, K. and Andersson, M., **2017**. Cubosomes post-loaded with antimicrobial peptides: Characterization, bactericidal effect and proteolytic stability. *International Journal of Pharmaceutics*, 526(1–2), pp.400–412.
46. Boisen, A., Gibson, B., von Halling Laier, C., Hook, S., Nielsen, L.H., Rades, T. and Moreno, J.A.S., **2019**. Microcontainers for protection of oral vaccines, in vitro and in vivo evaluation. *Journal of Controlled Release*, 294(November 2018), pp.91–101.
47. Wei, Y., Zhang, J., Zheng, Y., Gong, Y., Fu, M., Liu, C., Xu, L., Sun, C.C., Gao, Y. and Qian, S., **2019**. Cubosomes with surface cross-linked chitosan exhibit sustained release and bioavailability enhancement for vinpocetine. *RSC Advances*, 9(11), pp.6287–6298.
48. Angelov, B., Garamus, V.M., Drechsler, M. and Angelova, A., **2017**. Structural analysis of nanoparticulate carriers for encapsulation of macromolecular drugs. *Journal of Molecular Liquids*, 235, pp.83–89.
49. Mionić Ebersold, M., Petrović, M., Fong, W.-K., Bonvin, D., Hofmann, H. and Milošević, I., **2018**. Hexosomes with undecylenic acid efficient against *Candida albicans*. *Nanomaterials*, 8(2), p.91.
50. Barreto, J.A., O'Malley, W., Kubeil, M., Graham, B., Stephan, H. and Spiccia, L., **2011**. Nanomaterials: Applications in cancer imaging and therapy. *Advanced Materials*, 23(12), pp.H18–H40.
51. García, K.P., Zarschler, K., Barbaro, L., Barreto, J.A., O'Malley, W., Spiccia, L., Stephan, H. and Graham, B., **2014**. Zwitterionic-coated “Stealth” nanoparticles for biomedical applications: Recent advances in countering biomolecular corona formation and uptake by the mononuclear phagocyte system. *Small*, 10(13), pp.2516–2529.
52. Murgia, S., Bonacchi, S., Falchi, A.M., Lampis, S., Lippolis, V., Meli, V., Monduzzi, M., Prodi, L., Schmidt, J., Talmon, Y. and Caltagirone, C., **2013**. Drug-loaded fluorescent cubosomes: Versatile nanoparticles for potential theranostic applications. *Langmuir*, 29(22), pp.6673–6679.
53. Deshpande, S., Venugopal, E., Ramagiri, S., Bellare, J.R., Kumaraswamy, G. and Singh, N., **2014**. Enhancing cubosome functionality by coating with a single layer of poly- $\epsilon$ -lysine. *ACS Applied Materials & Interfaces*, 6(19), pp.17126–17133.
54. Caltagirone, C., Falchi, A.M., Lampis, S., Lippolis, V., Meli, V., Monduzzi, M., Prodi, L., Schmidt, J., Sgarzi, M., Talmon, Y.,

- Bizzarri, R. and Murgia, S., **2014**. Cancer-cell-targeted theranostic cubosomes. *Langmuir*, *30*(21), pp.6228–6236.
55. Bozzuto, G. and Molinari, A., **2015**. Liposomes as nanomedical devices. *International Journal of Nanomedicine*, *10*, pp.975–999.
56. Barauskas, J., Cervin, C., Jankunec, M., Špandyreva, M., Ribokaitė, K., Tiberg, F. and Johnsson, M., **2010**. Interactions of lipid-based liquid crystalline nanoparticles with model and cell membranes. *International Journal of Pharmaceutics*, *391*(1–2), pp.284–291.
57. Hinton, T.M., Grusche, F., Acharya, D., Shukla, R., Bansal, V., Waddington, L.J., Monaghan, P. and Muir, B.W., **2014**. Bicontinuous cubic phase nanoparticle lipid chemistry affects toxicity in cultured cells. *Toxicology Research*, *3*(1), pp.11–22.
58. Bode, J.C., Kuntsche, J., Funari, S.S. and Bunjes, H., **2013**. Interaction of dispersed cubic phases with blood components. *International Journal of Pharmaceutics*, *448*(1), pp.87–95.
59. Rosa, A., Murgia, S., Putzu, D., Meli, V. and Falchi, A.M., **2015**. Monoolein-based cubosomes affect lipid profile in HeLa cells. *Chemistry and Physics of Lipids*, *191*, pp.96–105.
60. Falchi, A.M., Rosa, A., Atzeri, A., Incani, A., Lampis, S., Meli, V., Caltagirone, C. and Murgia, S., **2015**. Effects of monoolein-based cubosome formulations on lipid droplets and mitochondria of HeLa cells. *Toxicol. Res.*, *4*, pp.1025–1036.
61. Meli, V., Caltagirone, C., Falchi, A.M., Hyde, S.T., Lippolis, V., Monduzzi, M., Obiols-Rabasa, M., Rosa, A., Schmidt, J., Talmon, Y. and Murgia, S., **2015**. Docetaxel-loaded fluorescent liquid-crystalline nanoparticles for cancer theranostics. *Langmuir*, *31*(35), pp.9566–9575.
62. Tran, N., Bye, N., Moffat, B.A., Wright, D.K., Cuddihy, A., Hinton, T.M., Hawley, A.M., Reynolds, N.P., Waddington, L.J., Mulet, X., Turnley, A.M., Morganti-Kossmann, M.C. and Muir, B.W., **2017**. Dual-modality NIRF-MRI cubosomes and hexosomes: High throughput formulation and in vivo biodistribution. *Materials Science and Engineering: C*, *71*, pp.584–593.
63. Tran, N., Mulet, X., Hawley, A.M., Hinton, T.M., Mudie, S.T., Muir, B.W., Giakoumatos, E.C., Waddington, L.J., Kirby, N.M. and Drummond, C.J., **2015**. Nanostructure and cytotoxicity of self-assembled monoolein-capric acid lyotropic liquid crystalline nanoparticles. *RSC Adv.*, *5*(34), pp.26785–26795.
64. Muir, B.W., Acharya, D.P., Kennedy, D.F., Mulet, X., Evans, R.A., Pereira, S.M., Wark, K.L., Boyd, B.J., Nguyen, T.-H., Hinton, T.M., Waddington, L.J., Kirby, N., Wright, D.K., Wang, H.X., Egan, G.F. and Moffat, B.A., **2012**. Metal-free and MRI visible theranostic lyotropic liquid crystal nitroxide-based nanoparticles. *Biomaterials*, *33*(9), pp.2723–2733.
65. Mulet, X., Boyd, B.J. and Drummond, C.J., **2013**. Advances in drug delivery and medical imaging using colloidal lyotropic liquid crystalline dispersions. *Journal of Colloid and Interface Science*, *393*(1), pp.1–20.
66. Azmi, I.D., Moghimi, S.M. and Yaghmur, A., **2015**. Cubosomes and hexosomes as versatile platforms for drug delivery. *Therapeutic Delivery*, *6*(12), pp.1347–1364.
67. Barriga, H.M.G., Holme, M.N. and Stevens, M.M., **2019**. Cubosomes: The next generation of smart lipid nanoparticles? *Angewandte Chemie—International Edition*, *58*(10), pp.2958–2978.
68. Zhai, J., Fong, C., Tran, N. and Drummond, C.J., **2019**. Non-lamellar lyotropic liquid crystalline lipid nanoparticles for the next generation of nanomedicine. *ACS Nano*, *13*, pp.6178–6206.
69. Qiu, H. and Caffrey, M., **2000**. The phase diagram of the monoolein/water system: Metastability and equilibrium aspects. *Biomaterials*, *21*(3), pp.223–234.
70. Dong, Y.D., Dong, A.W., Larson, I., Rappolt, M., Amenitsch, H., Hanley, T. and Boyd, B.J., **2008**. Impurities in commercial phytantriol significantly alter its lyotropic liquid-crystalline phase behavior. *Langmuir*, *24*(13), pp.6998–7003.
71. Barauskas, J. and Landh, T., **2003**. Phase behavior of the phytantriol/water system. *Langmuir*, *19*(23), pp.9562–9565.
72. Nakano, M., Teshigawara, T., Sugita, A., Leesajakul, W., Taniguchi, A., Kamo, T., Matsuoka, H. and Handa, T., **2002**. Dispersions of liquid crystalline phases of the monoolein/oleic acid/pluronic F127 system. *Langmuir*, *18*(24), pp.9283–9288.
73. Dong, Y.D., Larson, I., Hanley, T. and Boyd, B.J., **2006**. Bulk and dispersed aqueous phase behavior of phytantriol: Effect of vitamin E acetate and F127 polymer on liquid crystal nanostructure. *Langmuir*, *22*(23), pp.9512–9518.
74. Mele, S., Murgia, S. and Monduzzi, M., **2003**. Monoolein based liquid crystals to form long-term stable emulsions. *Colloids and Surfaces A: Physicochemical and Engineering Aspects*, *228*(1–3), pp.57–63.
75. Spicer, T., Hyden, K.L., Lynch, M.L., Ofori-Boateng, A. and Burns, J.L., **2001**. Novel process for producing cubic liquid crystalline nanoparticles (Cubosomes). (4), pp.5748–5756.
76. Rizwan, S.B., Assmus, D., Boehnke, A., Hanley, T., Boyd, B.J., Rades, T. and Hook, S., **2011**. Preparation of phytantriol cubosomes by solvent precursor dilution for the delivery of protein vaccines. *European Journal of Pharmaceutics and Biopharmaceutics*, *79*(1), pp.15–22.
77. Fong, C., Weerawardena, A., Sagnella, S.M., Mulet, X., Waddington, L., Krodziewska, I. and Drummond, C.J., **2010**. Monodisperse nonionic phytanyl ethylene oxide surfactants: High throughput lyotropic liquid crystalline phase determination and the formation of liposomes, hexosomes and cubosomes. *Soft Matter*, *6*, pp.4727–4741.
78. Moghaddam, M.J., de Campo, L., Hirabayashi, M., Bean, P.A., Waddington, L.J., Scoble, J.A., Coia, G. and Drummond, C.J., **2014**. Gadolinium-DTPA amphiphile nanoassemblies: Agents for magnetic resonance imaging and neutron capture therapy. *Biomater. Sci.*, *2*(6), pp.924–935.
79. Moghaddam, M.J., de Campo, L., Waddington, L.J. and Drummond, C.J., **2010**. Chelating phytanyl-EDTA amphiphiles: Self-assembly and promise as contrast agents for medical imaging. *Soft Matter*, *6*(23), p.5915.
80. Kozlov, M.Y., Melik-Nubarov, N.S., Batrakova, E.V. and Kabanov, A.V., **2000**. Relationship between pluronic block copolymer structure, critical micellization concentration and partitioning coefficients of low molecular mass solutes. *Macromolecules*, *33*(9), pp.3305–3313.
81. Diolate, G., Barauskas, J., Misiunas, A., Gunnarsson, T., Tiberg, F. and Johnsson, M., **2006**. “Sponge” nanoparticle dispersions in aqueous mixtures of diglycerol. (27), pp.6328–6334.
82. Uyama, M., Nakano, M., Yamashita, J. and Handa, T., **2009**. Useful modified cellulose polymers as new emulsifiers of cubosomes. *Langmuir*, *25*(20), pp.4336–4338.
83. Zhai, J., Waddington, L., Wooster, T.J., Aguilar, M.I. and Boyd, B.J., **2011**. Revisiting b-casein as a stabilizer for lipid liquid crystalline nanostructured particles. *Langmuir*, *27*(24), pp.14757–14766.
84. Muller, F., Salonen, A. and Glatter, O., **2010**. Phase behavior of phytantriol/water bicontinuous cubic Pn3m cubosomes stabilized by Laponite disc-like particles. *Journal of Colloid and Interface Science*, *342*(2), pp.392–398.
85. Bazylińska, U., Kulbacka, J., Schmidt, J., Talmon, Y. and Murgia, S., **2018**. Polymer-free cubosomes for simultaneous bioimaging and photodynamic action of photosensitizers in melanoma skin cancer cells. *Journal of Colloid and Interface Science*, *522*, pp.163–173.
86. Momot, K.I. and Kuchel, P.W., **2006**. Pulsed field gradient nuclear magnetic resonance as a tool for studying drug delivery systems.
87. Mom, I. and Ku, W., **2006**. Enhancement of Na<sup>+</sup> diffusion in a bicontinuous cubic phase by the ionophore monensin. (8), pp.2660–2666.
88. Larkin, T.J., Garvey, C.J., Shishmarev, D., Kuchel, P.W. and Momot, K.I., **2017**. Na<sup>+</sup> and solute diffusion in aqueous channels

- of Myverol bicontinuous cubic phase: PGSE NMR and computer modelling. *Magnetic Resonance in Chemistry*, 55(5), pp.464–471.
89. Monduzzi, M., Ljusberg-Wahren, H. and Larsson, K., 2000. A 13C NMR study of aqueous dispersions of reversed lipid phases. *Langmuir*, 16(19), pp.7355–7358.
90. Mishraki, T., Ottaviani, M.F., Shames, A.I., Aserin, A. and Garti, N., 2011. Structural effects of insulin-loading into H II mesophases monitored by electron paramagnetic resonance (EPR), small angle X-ray spectroscopy (SAXS), and attenuated total reflection fourier transform spectroscopy (ATR-FTIR). pp.8054–8062.
91. Angelov, B., Angelova, A., Drechsler, M., Garamus, V.M., Mutafchieva, R. and Lesieur, S., 2015. Identification of large channels in cationic PEGylated cubosome nanoparticles by synchrotron radiation SAXS and Cryo-TEM imaging. *Soft Matter*, 11(18), pp.3686–3692.
92. Nakano, M., Sugita, A., Matsuoka, H. and Handa, T., 2001. Small-angle X-ray scattering and <sup>13</sup>C NMR investigation on the internal structure of “Cubosomes.” *Langmuir*, 17(13), pp.3917–3922.
93. Rizwan, S.B., Dong, Y.-D., Boyd, B.J., Rades, T. and Hook, S., 2007. Characterisation of bicontinuous cubic liquid crystalline systems of phytantriol and water using cryo field emission scanning electron microscopy (cryo FESEM). *Micron*, 38(5), pp.478–485.
94. Talmon, Y., 2015. The study of nanostructured liquids by cryogenic-temperature electron microscopy—A status report. *Journal of Molecular Liquids*, 210, pp.2–8.
95. Demurtas, D., Guichard, P., Martiel, I., Mezzenga, R., Hebert, C. and Sagalowicz, L., 2015. Direct visualization of dispersed lipid bicontinuous cubic phases by cryo-electron tomography. *Nature Communications*, 6, p.8915.
96. Driever, C.D., Mulet, X., Waddington, L.J., Postma, A., Thissen, H., Caruso, F. and Drummond, C.J., 2013. Layer-by-layer polymer coating on discrete particles of cubic lyotropic liquid crystalline dispersions (cubosomes). *Langmuir*, 29, pp.12891–12900.
97. Beattie, J.K. and Djerdjev, A.M., 2004. The pristine oil/water interface: Surfactant-free hydroxide-charged emulsions. *Angewandte Chemie—International Edition*, 43(27), pp.3568–3571.
98. Akbar, S., Anwar, A., Ayish, A., Elliott, J.M. and Squires, A.M., 2017. Phytantriol based smart nano-carriers for drug delivery applications. *European Journal of Pharmaceutical Sciences*, 101, pp.31–42.
99. Azmi, I.D.M., Wibroe, P.P., Wu, L.P., Kazem, A.I., Amenitsch, H., Moghimi, S.M. and Yaghmur, A., 2016. A structurally diverse library of safe-by-design citrem-phospholipid lamellar and non-lamellar liquid crystalline nano-assemblies. *Journal of Controlled Release*, 239, pp.1–9.
100. von Halling Laier, C., Gibson, B., van de Weert, M., Boyd, B.J., Rades, T., Boisen, A., Hook, S. and Nielsen, L.H., 2018. Spray dried cubosomes with ovalbumin and Quil-A as a nanoparticulate dry powder vaccine formulation. *International Journal of Pharmaceutics*, 550(1–2), pp.35–44.
101. Salah, S., Mahmoud, A.A. and Kamel, A.O., 2017. Etodolac transdermal cubosomes for the treatment of rheumatoid arthritis: Ex vivo permeation and in vivo pharmacokinetic studies. *Drug Delivery*, 24(1), pp.846–856.
102. Tiberg, F. and Johnsson, M., 2011. Drug delivery applications of non-lamellar liquid crystalline phases and nanoparticles. *Journal of Drug Delivery Science and Technology*, 21(1), pp.101–109.
103. Deng, Y., Xu, A., Yu, Y., Fu, C. and Liang, G., 2019. Biomedical applications of fluorescent and magnetic resonance imaging dual-modality probes. *ChemBioChem*, 20(4), pp.499–510.
104. Germain, R.N., 2012. A decade of imaging cellular in the immune system. *Science*, 1676(June), pp.1676–1682.
105. Jenkins, R., Burdette, M.K. and Foulger, S.H., 2016. Mini-review: Fluorescence imaging in cancer cells using dye-doped nanoparticles. *RSC Advances*, 6(70), pp.65459–65474.
106. Pittet, M.J. and Weissleder, R., 2011. Intravital imaging. *Cell*, 147(5), pp.983–991.
107. Weijer, C.J., 2003. Visualizing signals moving in cells. *Science*, 300(5616), pp.96–100.
108. Li, J., Cheng, F., Huang, H., Li, L. and Zhu, J.J., 2015. Nanomaterial-based activatable imaging probes: From design to biological applications. *Chemical Society Reviews*, 44(21), pp.7855–7880.
109. Murgia, S., Bonacchi, S., Falchi, A.M., Lampis, S., Lippolis, V., Meli, V., Monduzzi, M., Prodi, L., Schmidt, J., Talmon, Y. and Caltagirone, C., 2013. Drug-loaded fluorescent cubosomes: Versatile nanoparticles for potential theranostic applications. *Langmuir*, 29(22), pp.6673–6679.
110. Miceli, V., Meli, V., Blanchard-Desce, M., Bsaibess, T., Pampaloni, M., Conaldi, P.G., Caltagirone, C., Obiols-Rabasa, M., Schmidt, J., Talmon, Y., Casu, A. and Murgia, S., 2016. In vitro imaging of  $\beta$ -cells using fluorescent cubic bicontinuous liquid crystalline nanoparticles. *RSC Advances*, 6(67), pp.62119–62127.
111. Lachowicz, J.I., Picci, G., Coni, P., Lippolis, V., Mamusa, M., Murgia, S., Pichiri, G. and Caltagirone, C., 2019. Fluorescent squaramide ligands for cellular imaging and their encapsulation in cubosomes. *New Journal of Chemistry*, 43, pp.10336–10342.
112. Murgia, S., Falchi, A.M., Meli, V., Schillén, K., Lippolis, V., Monduzzi, M., Rosa, A., Schmidt, J., Talmon, Y., Bizzarri, R. and Caltagirone, C., 2015. Cubosome formulations stabilized by a dansyl-conjugated block copolymer for possible nanomedicine applications. *Colloids and Surfaces B: Biointerfaces*, 129, pp.87–94.
113. Shen, H.H., Lake, V., Le Brun, A.P., James, M., Duff, A.P., Peng, Y., McLean, K.M. and Hartley, P.G., 2013. Targeted detection of phosphatidylserine in biomimetic membranes and in vitro cell systems using annexin V-containing cubosomes. *Biomaterials*, 34(33), pp.8361–8369.
114. Ding, Y., Chow, S.H., Liu, G.S., Wang, B., Lin, T.W., Hsu, H.Y., Duff, A.P., Le Brun, A.P. and Shen, H.H., 2018. Annexin V-containing cubosomes for targeted early detection of apoptosis in degenerative retinal tissue. *Journal of Materials Chemistry B*, 6(46), pp.7652–7661.
115. Caltagirone, C., Arca, M., Falchi, A.M., Lippolis, V., Meli, V., Monduzzi, M., Nylander, T., Rosa, A., Schmidt, J., Talmon, Y. and Murgia, S., 2015. Solvatochromic fluorescent BOD-IPY derivative as imaging agent in camptothecin loaded hexosomes for possible theranostic applications. *RSC Advances*, 5(30), pp.23443–23449.
116. Meli, V., Caltagirone, C., Sinico, C., Lai, F., Falchi, A.M., Monduzzi, M., Obiols-Rabasa, M., Picci, G., Rosa, A., Schmidt, J., Talmon, Y. and Murgia, S., 2017. Theranostic hexosomes for cancer treatments: An in vitro study. *New Journal of Chemistry*, 41(4), pp.1558–1565.
117. Godlewska, M., Majkowska-Pilip, A., Stachurska, A., Biernat, J.F., Gawel, D. and Nazaruk, E., 2019. Voltammetric and biological studies of folate-targeted non-lamellar lipid mesophases. *Electrochimica Acta*, 299, pp.1–11.
118. Gawel, D., Salamończyk, M., Nazaruk, E., Majkowska-Pilip, A. and Godlewska, M., 2018. Electrochemical and biological characterization of lyotropic liquid crystalline phases-retardation of drug release from hexagonal mesophases. *Journal of Electroanalytical Chemistry*, 813(January), pp.208–215.
119. Biffi, S., Voltan, R., Rampazzo, E., Prodi, L., Zauli, G. and Secchiero, P., 2015. Applications of nanoparticles in cancer medicine and beyond: Optical and multimodal in vivo imaging, tissue targeting and drug delivery. *Expert Opinion on Drug Delivery*, 12(12), pp.1837–1849.
120. Biffi, S., Voltan, R., Bortot, B., Zauli, G. and Secchiero, P., 2019. Actively targeted nanocarriers for drug delivery to cancer cells. *Expert Opinion on Drug Delivery*, 16(5), pp.481–496.
121. Di Lorenzo, G., Ricci, G., Severini, G.M., Romano, F. and Biffi, S., 2018. Imaging and therapy of ovarian cancer: Clinical

- application of nanoparticles and future perspectives. *Theranostics*, 8(16), pp.4279–4294.
122. Morana, G., Salviato, E. and Guarise, A., **2007**. Contrast agents for hepatic MRI. *Cancer Imaging*, 7(SPEC. ISS. A), pp.24–27.
123. Bye, N., Hutt, O.E., Hinton, T.M., Acharya, D.P., Waddington, L.J., Mo, B.A., Wright, D.K., Wang, H.X., Mulet, X. and Muir, B.W., **2014**. Nitroxide-loaded hexosomes provide MRI contrast in vivo. *Langmuir: The ACS Journal of Surfaces and Colloids*, 30, pp.8898–8906.
124. Bowen, S.R., Chapman, T.R., Borgman, J., Miyaoka, R.S., Kinahan, P.E., Liou, I.W., Sandison, G.A., Vesselle, H.J., Nyflot, M.J. and Apisarnthanarax, S., **2016**. Measuring total liver function on sulfur colloid SPECT/CT for improved risk stratification and outcome prediction of hepatocellular carcinoma patients. *EJNMMI Research*, 6(1), p.57.
125. Nilsson, C., Barrios-Lopez, B., Kallinen, A., Laurinmäki, P., Butcher, S.J., Raki, M., Weisell, J., Bergström, K., Larsen, S.W., Østergaard, J., Larsen, C., Urtti, A., Airaksinen, A.J. and Yaghmur, A., **2013**. SPECT/CT imaging of radiolabeled cubosomes and hexosomes for potential theranostic applications. *Biomaterials*, 34(33), pp.8491–8503.
126. Biffi, S., Andolfi, L., Caltagirone, C., Garrovo, C., Falchi, A.M., Lippolis, V., Lorenzon, A., Macor, P., Meli, V., Monduzzi, M., Obiols-Rabasa, M., Petrizza, L., Prodi, L., Rosa, A., Schmidt, J., Talmon, Y. and Murgia, S., **2017**. Cubosomes for in vivo fluorescence lifetime imaging. *Nanotechnology*, 28(5).

Received: 10 June 2019. Revised/Accepted: 4 March 2020.

